THE EMISSION TEMPERATURE AND THE NUCLEAR EQUATION OF STATE

By

Hongming Xu

A DISSERTATION

Submitted to
Michigan State University
in partial fulfillment of the requirements
for the Degree of

DOCTOR OF PHILOSOPHY

Department of Physics and Astronomy

1991

ABSTRACT

THE EMISSION TEMPERATURE AND THE NUCLEAR EQUATION OF STATE

BY

Hongming Xu

The relative populations of a large number of particle stable states of intermediate mass fragments were measured with the Oak Ridge Spin Spectrometer for ^{32}S induced reactions on ^{nat}Ag at an incident energy of E/A=22.3 MeV The measured relative populations of these states were compared to those calculated from a thermal model which include sequential feeding from higher lying particle unstable states of heavier nuclei. This comparison indicated an average emission temperature of $T \approx 3-4$ MeV.

To study whether emission temperatures can provide information about the nuclear equation of state and the in-medium nucleon-nucleon cross section, dynamical calculations based on the Boltzmann-Uehling-Uhlenbeck (BUU) equation were performed. Calculations for $^{40}Ca+^{40}Ca$ and $^{40}Ar+^{27}Al$ collisions indicate the cross sections for heavy residues are rather sensitive to both the equation of state at subnuclear density and the in-medium nucleon-nucleon cross section. This dual sensitivity may be reduced or eliminated by measurements of the emission pattern of the coincident light particles. Excitation energies and total angular momenta were also calculated for the residues formed in $^{40}Ar + ^{27}Al$ collisions. These calculations sug-

gest that reaction dynamics, not Coulomb or thermal instabilities, plays the most important role in limiting the production of fusionlike residues at energies E/A $\approx$ 30 MeV.

From the emission rates of nucleons and the thermal excitation energies of heavy residues produced in ^{40}Ar +^{27}Al and ^{40}Ar +^{124}Sn collisions, consistent thermal freeze-out times were obtained. The total excitation energies and temperatures predicted by BUU calculations are comparable with those obtained from experiments. These predicted values for the excitation energies and temperatures are quite sensitive to the equation of state and the impact parameter. Surprisingly, These two observables show little sensitivity to the in-medium nucleon-nucleon cross section.

To my Parents

Meihua and *Shujing*

ACKNOWLEDGMENTS

I am very happy to express my appreciation to my dissertation advisor, Prof. Bill Lynch, for his guidance, encouragement, support, and numerous discussions throughout the course of this dissertation study. His scientific belief and his persistent efforts constitute the essential part of my dissertation, and his knowledge, ability, and standards as a scientific researcher (both experimental and theoretical) have earned my great respect. Hearty thanks go to Prof. Konrad Gelbke for his advice, suggestions, continued interest and valuable contributions to my dissertation. His understanding of people and profession as a researcher have left a deep impression on me.

I am very grateful to Dr. Betty Tsang for her advice, friendship and technical help, particularly during the initial stages of my data analysis. I would like to thank Prof. Pawel Danielewicz and Prof. George Bertsch for many fruitful discussions and encouragement during my theoretical project that forms the second half of my dissertation. I am also indebted to Prof. Mitsuru Tohyama for helpful discussions. It is my great pleasure to thank my fellow graduate students at the cyclotron and the physics department, Pi Bo, Young Cai, Ziping Chen, Yibing Fan, Wenguang Gong, Baoan Li, Yeong Duk Kim, Tapan Nayak, Xun Yang, and Fan Zhu, and to Drs. Nelson Carlin, David Fields, Dave Mikolas, Tetsuya Murakami, and Romualdo deSouza, for their friendship and enjoyable discussions.

I would like to acknowledge the excellent support of the National Superconducting Cyclotron Laboratory and the physics department of Michigan State University. I am particularly grateful to Prof. J.S. Kovacs for bringing me to MSU through the CUSPEA program, and for handling many necessary documents. Special thanks also go to Jackie Bartlett, Rilla McHarris, Babara Pollack, at the NSCL; and Stephanie Holland, at the physics department, for their kind and valuable help. My dissertation committee members, Profs. Bill Lynch, Maris Abolins, George Bertsch, Pawel Danielewicz, Konrad Gelbke, and Mike Thorpe deserve recognition for their services.

Finally, I would like to acknowledge the understanding, support and love of my parents, Meihua and Shujing, who played a special role in raising me up to the point where I was able to select my career. Special thanks also go to my brother and sister, Gouming and Weihong, for their love and friendship.

Contents

List of Tables

List of Figures

Chapter 1

Introduction

I Motivation

Nucleus-nucleus collisions have proven to be an excellent laboratory for the study of statistical and dynamical properties of highly excited nuclear systems. The properties of such systems evolve with incident energy. At incident energies of a few MeV above the Coulomb barrier, the formation of a fully equilibrated compound system (commonly referred to as 'complete fusion') and its subsequent statistical decay is the dominant process for central collisions [More 72, More 75, Frie 83, Sobo 83, Sobo 84]. The statistical decay by emissions of γ, neutrons, and light charged particles as well as fission has been well described by statistical models of compound nuclear decay. At incident energies above E/A $\approx$ 15 MeV, however, the situation becomes more complicated. First, complete fusion of projectile and target becomes less likely, and one observes the onset of preequilibrium emission mechanisms. Second, the limits of stability and the mechanisms for decay of very hot nuclei are not known. This latter issue provides a strong stimulus for the investigations of energetic nucleus-nucleus collisions despite their complexity.

Investigations of nucleus-nucleus collisions have focussed either on the properties of hot fusion-like composite residues consisting of significant fractions of the projec-

tile and target nucleons or on the statistical and dynamical aspects of the hot, but non-equilibrium, initial stages of the reaction. In a practical sense, such a separation is artificial because one can not address issues concerning the properties of hot residues without considering the mechanisms by which they are formed. In this dissertation, both the preequilibrium processes of the initial stages of the reaction and the thermal properties of the composite residues are considered. In the first part of the dissertation, the intrinsic excitation of intermediate mass fragments emitted during the non-equilibrium initial stages of the reaction is determined by measurements of the γ rays from the decay of particle stable states of the fragments. Further discussions of the physics motivation of these measurements are given in subsection A of the introduction. These measurements have shown that the intrinsic excitation at freezeout is surprisingly small. A theoretical investigation of the factors which may affect the intrinsic excitation is the topic of the second half of the dissertation. There we also explore the properties of the residues produced in these reactions. Additional background concerning the properties of such residues is given in subsection B of the introduction.

A Complex Fragment Emission and the Emission Temperature

The emission of low energy intermediate mass fragments (IMF), $3 \leq Z \leq 20$, in processes distinct from fission has been observed for a large variety of nuclear reactions [Lync 87, Gelb 87a, Gelb 87b, Cass 89, Guer 89]. In general, the energy spectra of these fragments exhibit broad maxima at energies close to the exit channel Coulomb barrier and exponential slopes at higher energies. The fragment distributions [Gelb 87a, Mini 82, Finn 82, Hirs 84, Chit 83, Troc 86, Fiel 86a, Fiel 86b, Faty 87b, Sang 87] follow an approximate power-law dependence on fragment mass,

$A^{-\tau}$, in both proton and heavy ion induced reactions, possibly indicating that the mass distributions are determined by a common physical process. For reactions at intermediate energies, E/A=20-500 MeV, the angular distributions are forward peaked indicating that appreciable emission occurs prior to the attainment of statistical equilibrium of the composite projectile-target system [Chit 83, Jaca 83, Fiel 84, Mitt 85, Troc 86, Fiel 86a, Fiel 86b, Kwia 86, Faty 87a, Faty 87b, Poch 85a, Poch 85b, Chit 86, Xu 86, Xu 89, Poch 87, Chen 87a, Chen 87b, Chen 87c,Sain 88] . At backward angles, the angular distributions, particularly for heavier fragments, become more isotropic, consistent with significant contributions from the statistical emission by equilibrated heavy reaction residues that could, for example, be formed in incomplete fusion reactions [Sobo 83, Sobo 84, Kwia 86].

At present, there is no consensus concerning the origin of these fragments. Fragment production has been calculated within statistical [Mini 82, Finn 82, Hirs 84, Fiel 84, Boal 84, Lope 84b, Snep 88, Boal 88b, More 75, Gros 82, Frie 83, Rand 81, Fai 82, Bond 84, Ban 85, Hahn 87, Fiel 87, Gome 88] as well as purely dynamical [Schl 87, Vice 85, Lenk 86, Baue 87, Aich 88, Boal 88b, Sura 89a, Sura 89b, Sura 89c] models. Most models reproduce selected observables such as the fragment mass distribution. Differences between the various fragmentation models reflect, to a great extent, differences in assumptions concerning the densities, internal excitation (characterized by emission temperature) and degree of thermalization which characterized the system at thermal freezeout. For example, IMF emission has been related to the occurrence of adiabatic instabilities [Bert 83, Schl 87, Snep 88, Boal 89a] which may lead to the liquid-gas phase transition of highly excited nuclear matter [Lope 84b, Finn 82, Jacq 84]. Other statistical models [More 75, Fiel 84, Tsan 88, Hahn 87], as well as dynamical models [Boal 89, Boal 89a, Sura 89a, Sura 89b, Sura 89c, Sura 90, Peil 89], which do not incorporate a phase transition have been equally successful at reproduc-

ing many features of the fragment data. To distinguish between different statistical models, one needs to measure experimentally the freezeout densities as well as the emission temperatures, to constrain the assumptions of these fragmentation models.

Since the fragment kinetic energy spectra are sensitive to collective motion, the temporal evolution of the reaction, as well as Fermi motion and Coulomb barrier fluctuations, they do not provide quantitative information concerning the internal excitation energy at the freezeout stage of the reaction [Fiel 84, Frie 83, Bond 78, Ban 85, Stoc 81, Siem 79]. Information about the intrinsic excitation and the degree of thermalization at freezeout may be better obtained from the relative populations of nuclear states of the emitted fragments [Morr 84, Morr 85, Poch 85a, Poch 85b, Chit 86, Xu 86, Poch 87, Chen 87a, Chen 87b, Chen 87c, Bloc 87, Galo 87, Sain 88, Xu 89, Naya 89].

Emission temperatures of T=4-5 MeV were extracted from pairs of widely separated ($\Delta E \geq T$) particle unbound states in ^{4}He, ^{6}Li, and ^{8}Be fragments at angles significantly greater than the grazing angle where contributions from projectile fragmentation are negligible [Poch 85a, Poch 85b, Chit 86, Poch 87, Chen 87a, Chen 87b, Chen 87c, Chen 88a, Sain 88]. The relative populations of these states were found to be surprisingly insensitive to the incident energy over the range of E/A=35-94 MeV [Chen 87a, Chen 87d]. Moreover, these measurements revealed little sensitivity to the gates placed upon the linear momentum transfer to the target residue [Chen 87c] or the associated multiplicity of charged particles emitted at forward angles [Sain 88]. Slightly lower values, T=3 MeV, were extracted [Bloc 87] from the neutron decays of excited states of ^{8}Li emitted in the ^{14}N+ ^{nat}Ag reaction at E/A=35 MeV. In contrast, significantly lower values, T=1 MeV, were extracted [Galo 87] from the neutron decays of excited ^{13}C nuclei emitted close to the grazing angle in the ^{14}N+ ^{165}Ho reaction at E/A=35 MeV. Finally, measurements involving the

γ-ray decays of both low lying [Xu 86, Morr 84, Morr 85, Morr 86] and high lying [Gome 88, Sobo 86] particle stable states have been performed. Before this dissertation started, the emission temperatures obtained from the decay of particle stable states [Morr 84, Morr 85] were reported to be much lower than those obtained from the decay of particle unstable states [Poch 85a]. Some of earliest work done in the dissertation study [Xu 86] demonstrated that these low-lying particle stable states are more difficult to interpret due to sequential feeding from higher lying particle unbound states [Poch 85a, Xu 86, Hahn 87, Fiel 87, Gome 88, Sobo 86]. When the sequential feeding is considered, these low-lying γ-ray measurements are not in contradiction with the emission temperatures extracted from the decay of particle unstable states [Xu 86].

If the populations of excited states can be described in terms of thermal distributions corresponding to a single emission temperature, this temperature can be unambiguously determined by measuring the relative populations of just two states. Indeed, prior to the measurements undertaken in this dissertation and the dissertation of Tapan Nayak [Naya 90], emission temperatures were generally extracted from relative populations of just a few states. On the other hand, the degree of thermalization and the internal consistency of this thermal assumption can only be investigated by measuring a large number of states.

To perform such tests, a large number of particle stable states of intermediate mass fragments were measured in this dissertation for ^{32}S induced reactions on ^{nat}Ag at an incident energy of E/A=22.3 MeV. These measurements were performed at angles back of the grazing angle to avoid large contributions from peripheral processes. Previous particle correlation experiments [Fiel 86b] on this system established that fragments are emitted with a low average multiplicity, $M_{IMF} \leq 1$, for a broad class of violent projectile target collisions representing about 60-70% of the total reaction

cross section. In these reactions, large amounts (200-400 MeV) of energy are converted into intrinsic excitation, and a significant fraction of intermediate mass fragments are emitted prior to the attainment of statistical equilibrium of the composite system [Fiel 86b].

In this dissertation work, the measured relative populations of excited states of intermediate mass fragments are compared with those calculated from a thermal model which includes sequential feeding from higher lying states. The comparison indicates an average emission temperature of $T \simeq 3 - 4$ MeV. These measurements, combined with previous measurements of particle unstable states, provide a picture of a constant or gradually increasing emission temperature with incident energy. The maximum observed emission temperature, is rather small. There are other indications from neutron multiplicity measurements, high energy hard γ-ray measurements, and measurements of charged particle spectra which suggest a similar limitations to the intrinsic excitation of composite residues.

Such observations may relate to the characteristic fragmentation temperature predicted to occur by multiparticle phase space models [Gros 88, Bond 85] when the hot system expands to sufficiently low density. Questions concerning how hot systems expand and cool may be better addressed by dynamic calculations. Surprisingly, these models also predict a low and nearly constant intrinsic excitation at freezeout [Lenk 86, Schl 87, Snep 88, Frie 88, Boal 88a, Boal 88b]. Within these calculations, Both the particle emission and the expansion play roles in cooling the system. To study whether the observed low and slowly varying emission temperatures can teach us anything about the nuclear equation of state or in-medium nucleon-nucleon cross section, we have performed dynamical calculations based on the Boltzmann-Uehling-Uhlenbeck (BUU) equation, which is a theory based on the one-body density matrix. Such calculations have the disadvantages that they do not properly describe many

body correlations and they do not contain sufficient fluctuations to properly predict the emission of intermediate mass fragments, We therefore investigated excitation energies and emission temperatures of the heavy residues predicted by the BUU calculations. We are encouraged to try this approach by the results of molecular dynamical calculations [Lenk 86, Schl 87] which indicate that all reaction products, regardless of their masses, have about the same emission temperature. This suggests that the excitation energies of heavy residues calculated in our study may provide insights concerning the emission temperatures of intermediate mass fragments. Our BUU calculations also allow us to address questions concerning the fusion cross sections, excitation energies and angular momenta for the heavy residues which have not been studied in previous dynamical studies. Further discussion of these questions was given in the following subsection.

B Disappearance of Fusionlike Residues

On rather general grounds, one expects fusion of the projectile and the target nuclei to become less likely with increasing incident energy. Most experimental investigations of the energy dependences of fusion or fusionlike processes have concentrated on measurements of the traditionally well understood residue decay channels leading to the production of the evaporation residues or fission fragments. Such measurements indicate that fusionlike processes, particularly for Ar [Lera 86, Auge 86, Nife85, Fahl 86, Jacq 84, Fabr 87, Bour 85] or Si [Deco 90, Grif 90] induced reactions, decrease rapidly with incident energy when $E/A \geq 20$ MeV, and eventually vanish at around the Fermi energy $E/A \simeq 35 - 40$ MeV.

Fig. 1.1 shows a example of the fission fragment folding angle distribution (the angle between the two fissioning fragments) measured for $^{40}Ar+^{232}Th$ collisions. In such measurements, one sees two peaks in the folding angle distributions at E/A=31

MeV: a large peak at $\theta_{FF} \simeq 170°$, from the decay of target residues in peripheral collisions, and a small one at $\theta_{FF} \simeq 110°$, from central fusionlike collisions. As the energy increases from E/A = 31 MeV to 44 MeV, the peak due to fusionlike reactions decreases with energy and eventually vanishes at E/A=44 MeV.

Total excitation energies and emission temperatures were also extracted from the velocities of the fusion-like residues [Lera 86, Auge 85, Nife85, Bour 85, Gali 88] and coincident light particle spectra [Goni 88, Gali 88, Wada 89, Deco 90], respectively. Light particle evaporation spectra have also been analyzed [Goni 89, Bohn 90, Grif 90] to extract the temperatures and the excitation energies of the residues. These analyses suggested that the maximum excitation energy that a nucleus can sustain, decreases with the mass of the composite system, from $E^*/A \approx$ 5-6 MeV for light systems with total masses A$\leq$ 100, to a value of $E^*/A \approx 3$ MeV for a total mass $A \geq 200$. [Guer 89, Lera 86, Auge 85, Bohn 90, Fahl 86, Bour 85]. If one assumes a level density of $a = A/8$ MeV, the residue temperatures for these heavy systems are comparable to the emission temperatures extracted from the emission of non-equilibrium IMF 's that were discussed in subsection A.

The disappearance of fusionlike cross sections has been most frequently interpreted to be a consequence of the instability of hot nuclei at high temperatures [Finn 82, Lope 84b, Bert 83, Schl 87, Snep 88, Boal 89a, Bord 85, Levi 84, Besp 89, Gros 88]. For example, the static model of Levit and Bonche [Levi 84] predicted a limiting temperature of $T \simeq 5 - 10$ MeV, above which nuclear matter becomes unstable against hydrodynamic expansion. If one assumes a soft nuclear equation of state and a level density of $a = A/8$ MeV, this 'limiting temperature' is consistent with the observed disappearance of fusion-like processes with Ar induced reactions at E/A$\geq$ 35 MeV [Auge 86]. These analyses assume the existence of an equilibrated residue at an excitation predicted by incomplete fusion. To address the validity of this assumption,

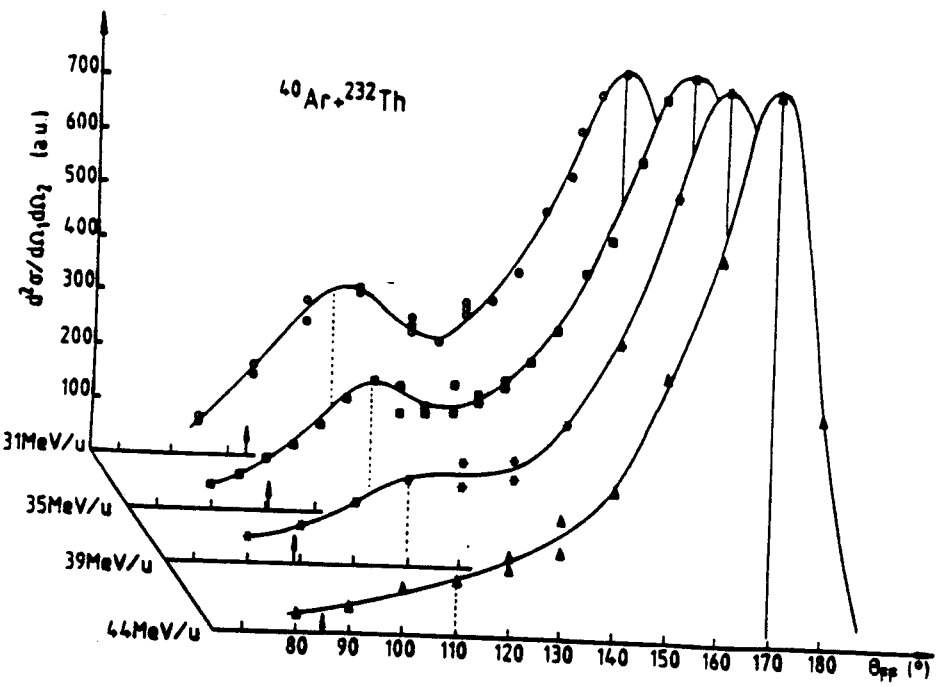

Figure 1.1: Differential cross section of fission products as functions of both the incident energy and the folding angle between the two fission fragments for $^{40}Ar+^{232}Th$ collisions [Conj 85] .

one must also consider the processes which govern the formation of a highly excited composite residue.

Within the presently available microscopic dynamical models, the formation of a fusionlike residue depends on the interplay of the nuclear mean field and the in-medium nucleon-nucleon scattering cross section. Clearly within these models, whether two nuclei fuse or not depends on these ingredients. For example, a larger nucleon-nucleon cross sections would give individual nucleons in the medium more chances to collide with the others. This would result in more stopping and a larger cross section for the formation of heavy composite residues. Therefore a study of, for example, fusion cross section with models having these ingredients may allow one to place limits on these model parameters. Similar questions can be asked about the sensitivity of the residue cross sections or the excitation energies to the nuclear equation of state. Dynamical models based on the Boltzmann-Uehling-Uhlenbeck equation [Bert 84, Bert 87, Aich 85, Bert 88, Rema 86, Baue 87, Baue 88, Moli 85a, Moli 85b, Krus 85,Aich 87, Aich 88, Gale87, Welk 88, Gale90, Peil 89, Cass 88, Cass 89] allow the possibility of investigating these questions. Prior to this dissertation study, however, these issues had not been investigated.

II Organization

This dissertation contains two distinctive parts: The first four chapters deal mainly with an experimental determination of emission temperatures for a large number of particle-stable states. The remaining three chapters describe a theoretical project, designed to address whether one can learn anything concerning the nuclear equation of state at sub-nuclear density from measurements of emission temperatures or heavy residue cross sections. Final conclusions are given in chapter 8. Both parts of

this dissertation are motivated by the idea of testing the concept of thermal freeze-out by emission temperature measurements and by the desire to learn whether such measurements can provide information concerning the nuclear equation of state.

In particular, this dissertation is organized as follows: In Chapter 2, the experimental details, including an overall description of the experimental setup, the background subtraction of coincident γ-rays, as well as the γ-ray calibrations, will be given. In Chapter 3, the inclusive fragment cross sections are presented and fitted with simple parameterizations. The bulk of the particle γ-ray coincidence data are also presented in this chapter.

In Chapter 4, a detailed sequential decay calculation is described. The results of this model calculation are compared with the experimental data and a mean emission temperature is extracted. Summary and conclusions concerning the experimental study are also made in this chapter.

In Chapter 5, a comprehensive description of the improved Boltzmann-Uehling-Uhlenbeck (BUU) equation is provided. In this dissertation study, the BUU equation is improved with a Lattice Hamiltonian method. Such a method gives an excellent conservation of total energy which therefore allows us to study the thermalization and energy deposition which would otherwise be impossible. In this chapter, we will give a detailed descriptions of formal equations, numerical solutions of these equations, and numerical tests of the ground state stability and the conservation of energy.

In Chapter 6, the improved BUU equation is applied to ^{40}Ca+^{40}Ca and ^{40}Ar+^{27}Al collisions in order to address the following two important questions: 1) which observables are most sensitive to the nuclear equation of state at sub-nuclear density; 2) what are the dynamical limits to the formation of heavy residues. We will first discuss the fusion cross sections and their sensitivities to the nuclear equation of state and

the in-medium nucleon-nucleon cross section. We then discuss how one can design an experiment to disentangle these sensitivities. Finally, we examine the various aspects which limit the calculated fusionlike cross sections.

In Chapter 7, we return to address the emission temperature and its possible relation to the nuclear equation of state. For such purposes, we investigate ^{40}Ar+^{27}Al and ^{40}Ar+^{124}Sn collisions to determine the sensitivities to the equation of state. A short summary is given in Chapter 8.

Chapter 2

Experimental Details

After a brief description about the experimental setup in section I, we discuss in detail how to understand the coincident spectra and the background spectra obtained with the NaI(Tl) detectors of the Spin Spectrometer. Since the background yields measured with these detectors are much higher than the yields of the discrete transitions of interest (in some case, background is more than 20 times larger), it is crucial to understand the line-shapes of the spectra. For this purpose, we present, step by step, the calibrations of the line shapes using $\gamma - \gamma$ sources, as well as proton inelastic scattering. The determination of the absolute efficiency and the correction of the line shape distortions due to double hits are also discussed.

I Experimental setup

The experiment was performed at the Holifield Heavy Ion Research Facility of Oak Ridge National Laboratory. Silver targets of natural isotopic abundance were irradiated with ^{32}S ions of 714 MeV energy. Intermediate mass fragments were isotopically identified with five $\Delta E - \Delta E - E$ surface barrier detector telescopes, positioned at the laboratory angles of $\theta_{IMF} = 20°, 25°, 30°, 45°$ and $50°$. The telescopes subtended solid angles of $\Delta\Omega$ = 9.8, 10.1, 15.4, 36.3, and 28.6 msr, respectively. Each telescope con-

sisted of two planar ΔE-detectors with thicknesses between 50 and 100 mm and an E-detector with thickness of 1.5 mm. Cross contaminations between adjacent isotopes were reduced by restricting the analysis to fragments that stopped in the E-detectors of the telescopes thus permitting two independent particle identification gates. This introduced energy thresholds at about E/A=8 MeV for ^{10}B at $\theta_{IMF} = 20°, 25°, 30°$ and at about E/A=7 MeV for $\theta_{IMF} = 45°$ and 50°. In order to reduce computer dead time and speed up data acquisition, a hardware gate was set during the experiment which suppressed triggers of the telescopes generated by light particles $(p, d, .., \alpha)$. These particles are emitted with significantly larger cross sections than intermediate mass fragments which were the focus of the present experiment. In order to make sure that no nuclei with $Z \geq 3$ were rejected, the gates were set such that a small fraction of α-particles were recorded on tape. About 85% of all light particles were rejected by this method.

Coincident γ-rays were detected with the Spin Spectrometer [Jaas 83]. Six of the NaI(Tl) crystals of the Spin Spectrometer were replaced by Compton shielded Germanium detector modules. In addition to the particle γ-ray coincidence events, the Spin Spectrometer was triggered by the detection in one Germanium detector of 0.898 or 1.836 MeV γ-rays from an ^{88}Y source positioned close to the Ag target. With a high probability, a 0.898 (1.836) MeV γ-ray detected in the Germanium ensures the interaction of the companion 1.836 (0.898) MeV γ-ray elsewhere in the the Spin Spectrometer. Using this additional source data, it was possible to monitor the gain shifts of the photomultipliers of NaI(Tl) detectors and make corrections for these gain shifts, run by run, in the off-line analysis.

II Background Subtractions

In the backward hemisphere of the Spin Spectrometer, neutrons could be suppressed by time-of-flight discrimination. The time-of-flight separation of neutrons from γ-rays for detectors in the forward hemisphere of the Spin Spectrometer was considerably worse due to the large cross sections for fast, noncompound neutrons at forward angles. To reduce the systematic errors arising from background subtraction, we consequently restricted our analysis to data taken with the NaI(Tl) modules in the backward hemisphere ($\theta_\gamma \geq 90^\circ$) of the Spin Spectrometer. To illustrate neutron suppression in the backward hemisphere, we show in Fig. 2.1 the relative time spectrum obtained between a solid state particle telescope located at $\theta_{IMF} = 20^\circ$ and a NaI(Tl) γ-ray detector located at $\theta_\gamma = 138^\circ$. The time spectrum clearly exhibits a sharp peak due to prompt γ-rays and a long tail caused predominantly by low energy neutrons emitted from excited target residues. Significant background reductions could be achieved by selecting prompt γ-rays with a narrow time gate. The lower and upper limits of the time gate employed for this particular detector pair are shown by the arrows marked as t_l and t_h ,respectively.

The energy spectra of coincident γ-rays were transformed, event by event, into the rest frames of the detected fragments using relativistic Jacobians and Doppler shift corrections. Since these transformations shift and broaden γ-ray transitions of the target residues, particular attention was paid to identifying and correcting for such effects. For this purpose, background spectra were generated by performing similar transformations to γ-ray spectra measured in coincidence with ^{9}Be nuclei which have no strong transitions at the γ-ray energies of interest. The background spectra were then used in the fitting procedure to extract the yields of γ-rays from the decay of the detected intermediate mass fragments.

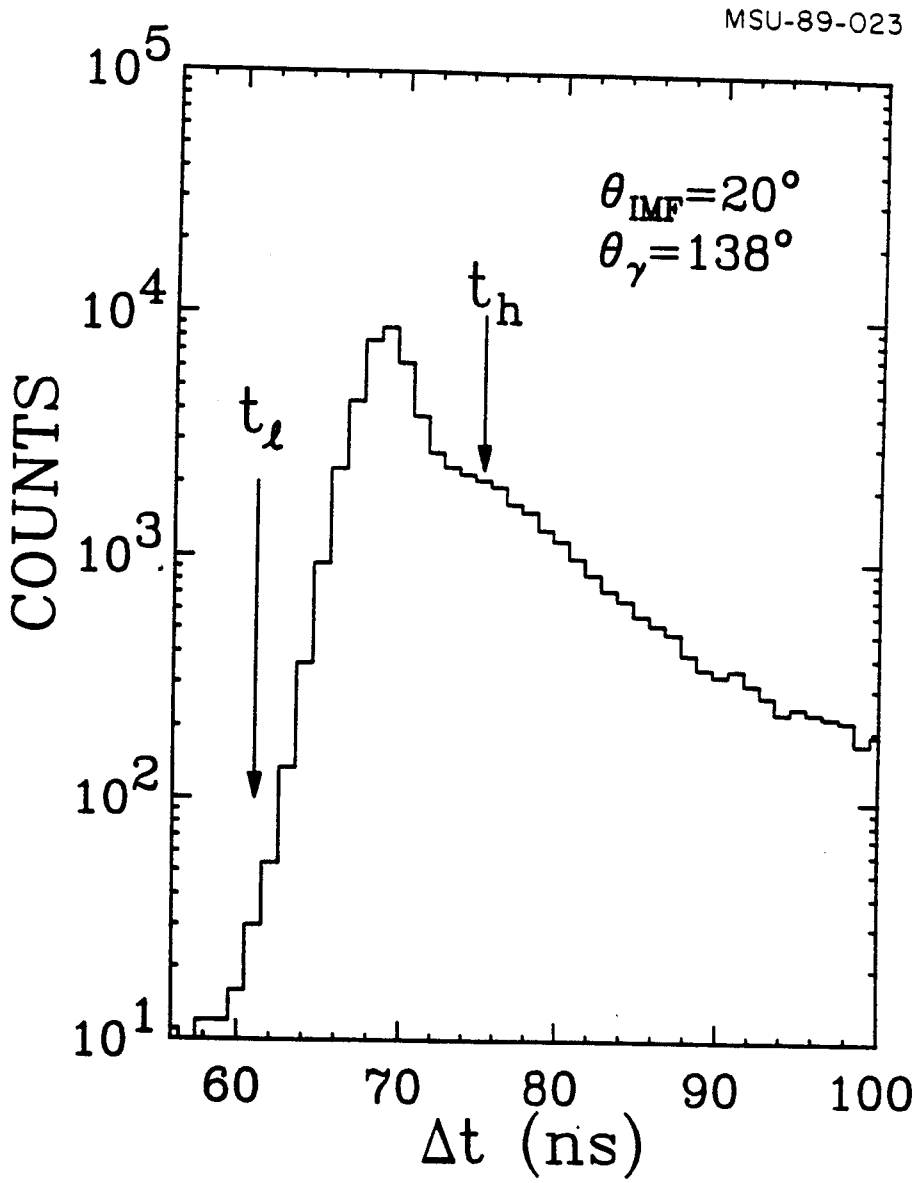

Figure 2.1: Relative time spectrum between a particle detector (at $\theta_{IMF} = 20°$) and a NaI(Tl) γ-ray detector (at $\theta_\gamma = 138°$). The limits of the time gate used for the analysis is indicated by the arrows marked as t_l and t_h.

For illustration, the transformed γ-ray spectra measured in coincidence with ^{11}B, ^{11}C, and ^{12}C fragments are shown in the left hand panels of Figs. 2.2-2.4, respectively. The spectra were summed over all measured particle emission angles and energies and over all γ-ray detectors located in the backward hemisphere. The dashed lines show the corresponding background spectra. On this scale, individual transitions are barely, if at all, visible. A better visual comparison of coincidence and background spectra is possible when smooth analytical functions are subtracted from both of them. The dotted curves correspond to functions of the form

$$f(E_\gamma) = A \cdot \exp(-E_\gamma/\alpha) + B \exp(-E_\gamma/\beta) + C \tag{2.1}$$

where A, B, α, β are constants adjusted by fitting the background and C is a constant offset. The solid and open points in the right hand panels show the coincidence and background spectra after subtraction of these functions. On these scales, the individual γ-ray transitions are clearly discernible. Moreover, spurious structures of the experimental background spectra are small in comparison with the identified peaks of the coincidence spectra. (The subtraction of the function $f(E_\gamma)$ cancels in the final data reduction; this intermediate step only facilitates a detailed comparison of the coincidence and background spectra in regions of high background.)

The yields of γ-rays from the decay of the detected intermediate mass fragment were fitted by folding the detector response function with the energies of known transitions of the detected fragment and adjusting the strengths of the individual transitions and the normalization of the background spectrum. The detector response function was calibrated over the energy range of $E \simeq 0.5-7$ MeV with γ-rays emitted from ^{24}Na,^{60}Co,^{88}Y, and ^{207}Bi radioactive sources as well as γ-rays produced by the inelastic scattering of protons from ^{12}C and^{16}O target nuclei. The response function includes detailed descriptions of the photo-, first and second escape peaks, as well as line shape corrections due to coincidence summing. Finally, the inclusive fragment

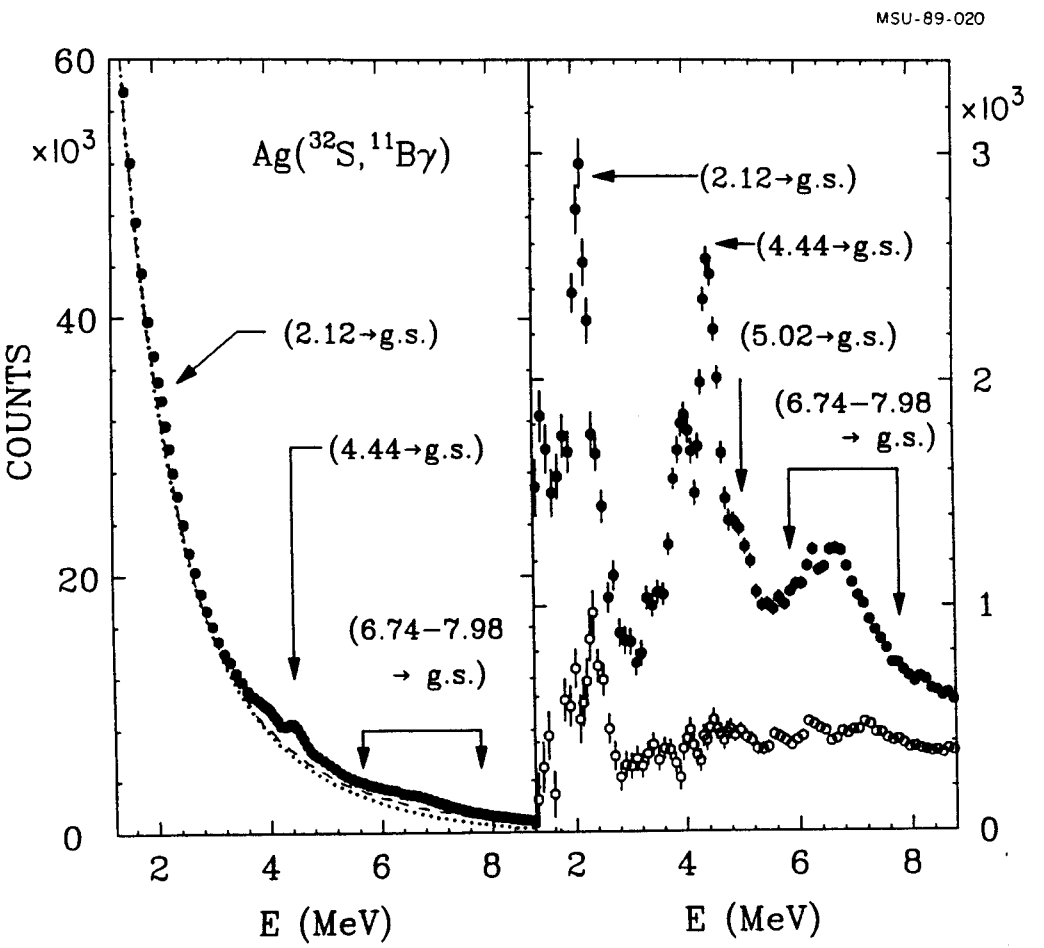

Figure 2.2: Left hand panel: Coincidence (solid line) and background (dashed line) spectra for ^{11}B fragments. The dotted line corresponds to the function of Eq. (2.1). Right hand panel: Coincidence (solid points) and background (open points) spectra after subtraction of the function of Eq. (2.1)The locations of specific γ-ray transitions in ^{11}B are marked by arrows.

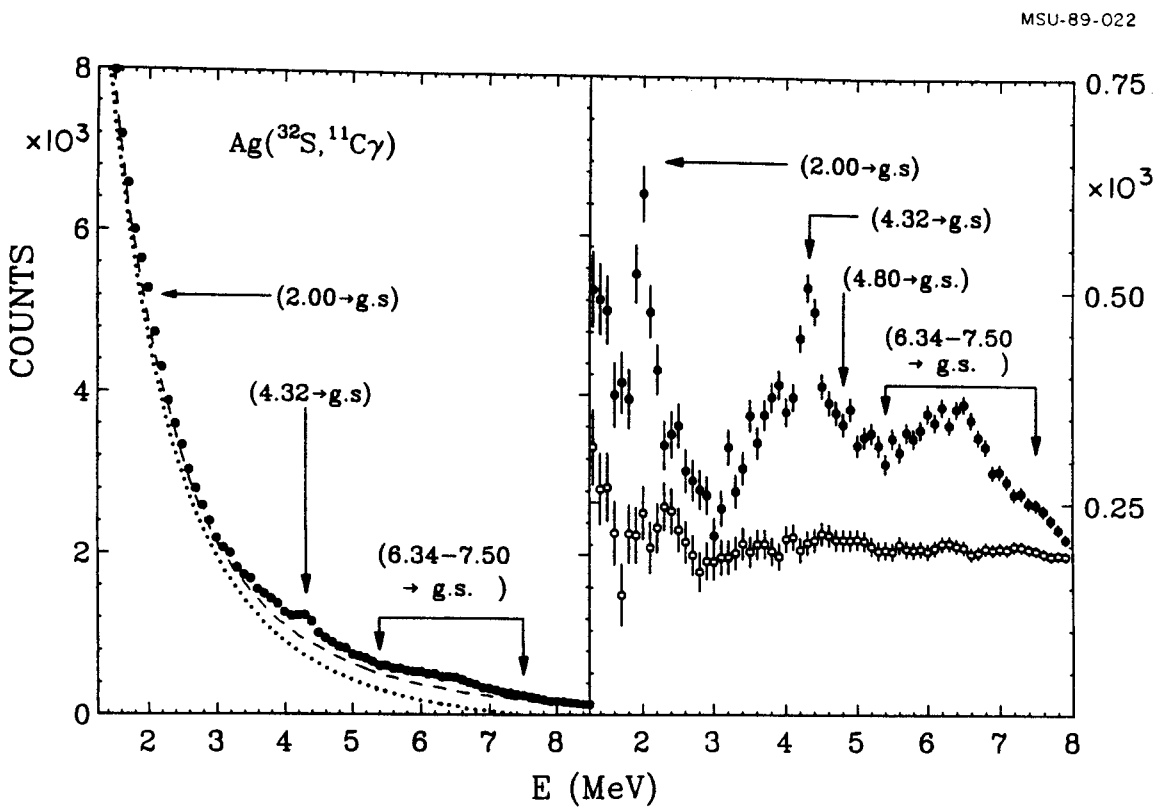

Figure 2.3: Left hand panel: Coincidence (solid points) and background (dashed line) spectra for ^{11}C fragments. The dotted line corresponds to the function of Eq. (2.1). Right hand panel: Coincidence (solid points) and background (open points) spectra after subtraction of the function of Eq. (2.1). The locations of specific γ-ray transitions in ^{11}C are marked by arrows.

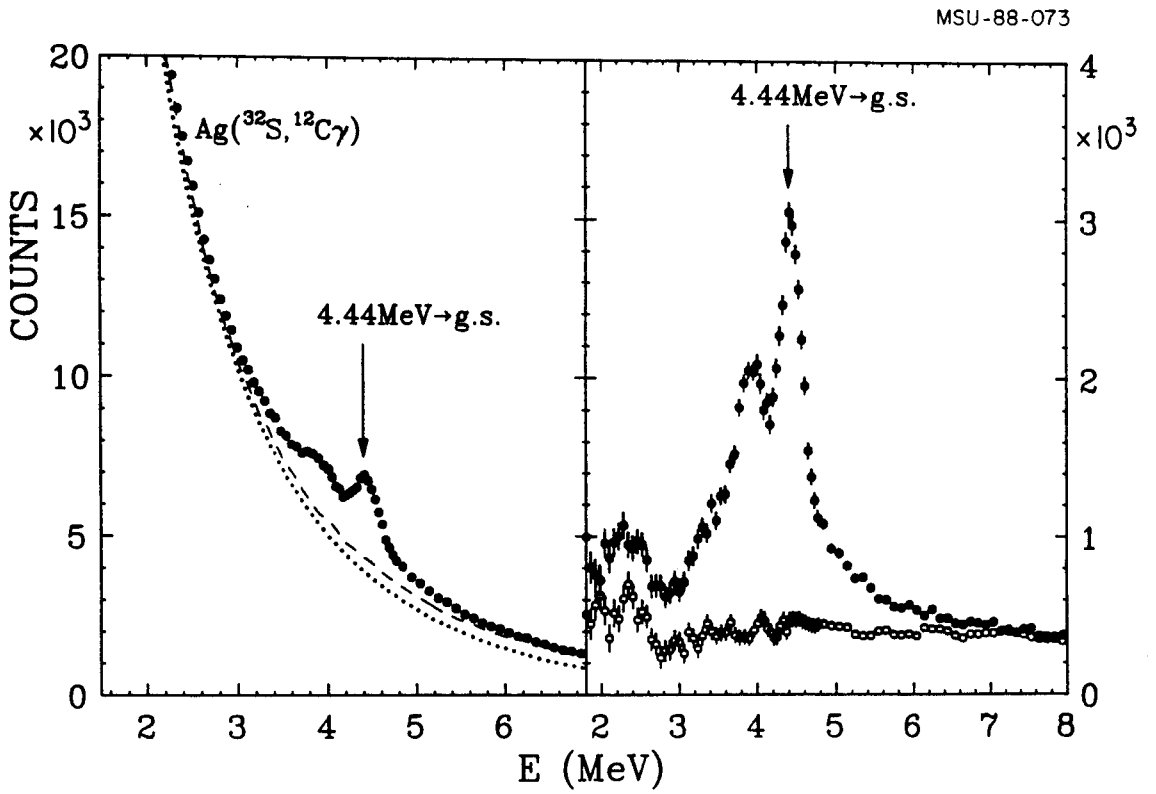

Figure 2.4: Left hand panel: Coincidence (solid points) and background (dashed line) spectra for ^{12}C fragments. The dotted line corresponds to the function of Eq. (2.1). Right hand panel: Coincidence (solid points) and background (open points) spectra after subtraction of the function of Eq. (2.1). The locations of specific γ-ray transitions in ^{12}C are marked by arrows.

yields and the fragment-γ-ray coincidence yields were summed over angle to extract the fraction F_γ of observed fragments which were accompanied by the designated γ-ray. Technical details of the response functions and corrections for the effects of coincident summing are presented in the next section. Here we present a less detailed overview of the analysis procedure.

The effects of coincidence summing are illustrated for the simple case of the 4.44 MeV γ-ray transition of excited ^{12}C fragments, see Fig. 2.4 for the coincidence and background spectra. The final coincidence yield after background subtraction is shown by the solid points in Fig. 2.5. The dashed curve shows the detector response as calibrated via the $^{12}C(\gamma,\gamma')^{12}C$ reaction for which the gamma ray multiplicity is one. This calibration underpredicts the high-energy tail of the line shape for the spectrum measured in the $^{nat}Ag(^{32}S,^{12}C\gamma)$ reaction in which the average γ-ray multiplicity is high. Due to this high γ-ray multiplicity, there is a non-negligible probability that two coincident γ-rays or a γ-ray and a neutron are detected in a single NaI(Tl) module. We denote this effect as 'coincidence summing'; it depends on the associated γ-ray and neutron multiplicities and on the geometry of the experiment, but is independent of the beam intensity. The calculation of the line shape distortion due to coincidence summing will be described in Section III(C). The corrections are illustrated in the lower part of Fig. 2.5. The dashed line shows the response of the detector to a given number of 4.44 MeV γ-rays in the absence of coincidence summing. A fraction, $p(\simeq 0.28)$, of these γ-rays, will interact with the detector in coincidence with a second γ-ray or a neutron from the same reaction. The summed response to the 4.44 MeV γ-ray plus the second γ-ray or neutron is shown by the dashed-dotted curve. The remaining fraction, $1-p$, of the 4.44 MeV γ-rays will interact individually with the detector with the response function measured at low multiplicities and shown by the dotted curve. The total response function, corrected for coincidence

summing, is shown by the solid lines in Fig. 2.5; it corresponds to the sum of the yields represented by the dotted and dashed-dotted curves (See also Eq. (2.19)). This parameter-free correction reproduces the measured coincidence yield rather well. All fitted spectra include corrections due to coincidence summing.

Coincidence summing corrections were also required to extract the γ-ray yields from measurements obtained with the Compton suppressed Germanium detectors of the Spin Spectrometer. Due to the superior resolution of the Germanium detectors, individual γ-ray hits are well separated from summed events and corrections to the line shape are not required. In the Compton suppressed operating mode, however, additional γ-rays or neutrons detected in the Germanium detector or the Compton shield result in a multiplicity dependent loss of efficiency of about 20%. This loss of efficiency are corrected and the data are also included in Figs. 4.4 and 4.5.

Figures 2.6 and 2.7 give examples for more complicated coincidence spectra. The solid points show the final coincidence yields from ^{11}B (2.6) and ^{11}C (2.7) γ-decays, after background subtraction. (The original coincidence and background spectra were already shown in Figs. 2.2 and 2.3.) The photopeak locations of the most important γ-ray transitions are marked by arrows. The lower panels show individual contributions from the most important transitions used in the fits. The most important transitions and branching ratios used in the final fits are shown in the inserts. Clearly, the individual populations of states above about 6 MeV excitation energy are not well determined. In these and other ambiguous cases, we have used the summed strengths of the groups of states indicated in the upper parts of the figures to provide information about the emission temperature.

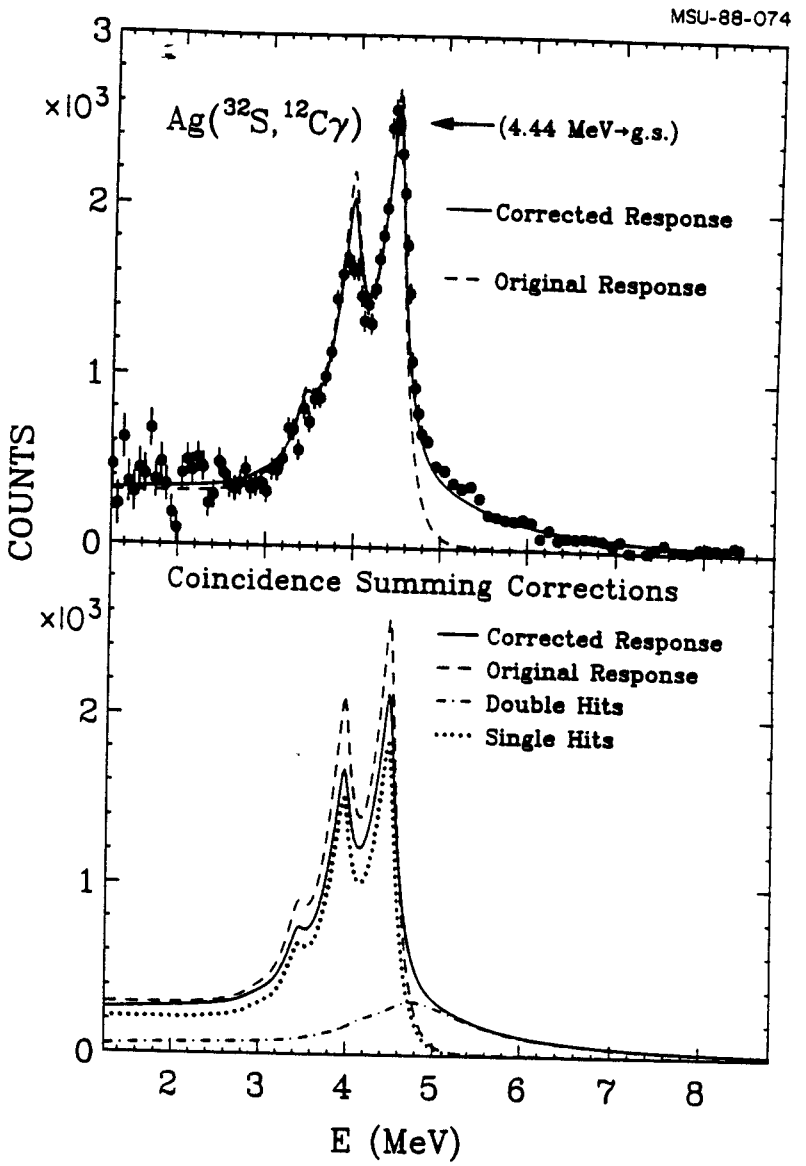

Figure 2.5: Upper panel: Background subtracted coincidence yield (solid points) attributed to γ-ray decays of excited ^{12}C fragments. The location of the photopeak for the decay of the 4.44 MeV states is marked by an arrow. The dashed line shows the original response function determined from the calibration at low γ-ray multiplicity. The solid line shows the final line shape which includes corrections due to coincidence summing. Lower panel: Corrections due to coincidence summing at high γ-ray multiplicity. The solid and dashed lines are the same as in the upper panel. The dotted curve corresponds to the calculated response due to the simultaneous detection of two γ-rays; the dashed-dotted line corresponds to the undistorted response when only the 4.44 MeV γ-ray is detected. The solid line corresponds to the sum of the dotted and dashed-dotted lines.

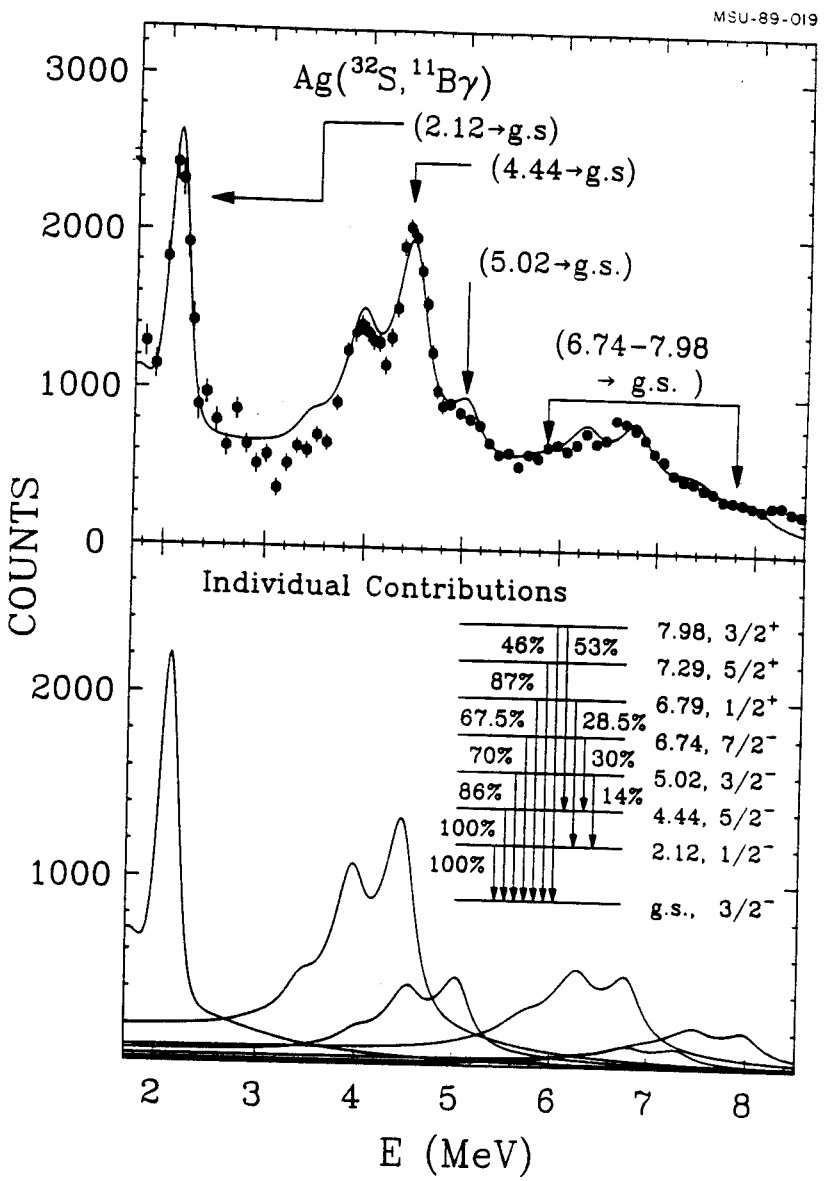

Figure 2.6: Upper panel: Background subtracted coincidence yield (solid points) attributed to γ-ray decays of excited ^{11}B fragments. The solid line shows the fit used for the extraction of the γ-ray fractions,F_γ, listed in 3.2. The locations of several strong transitions are shown by arrows. Lower panel: Contributions from individual transitions. Important transitions and branching ratios are given in the insert.

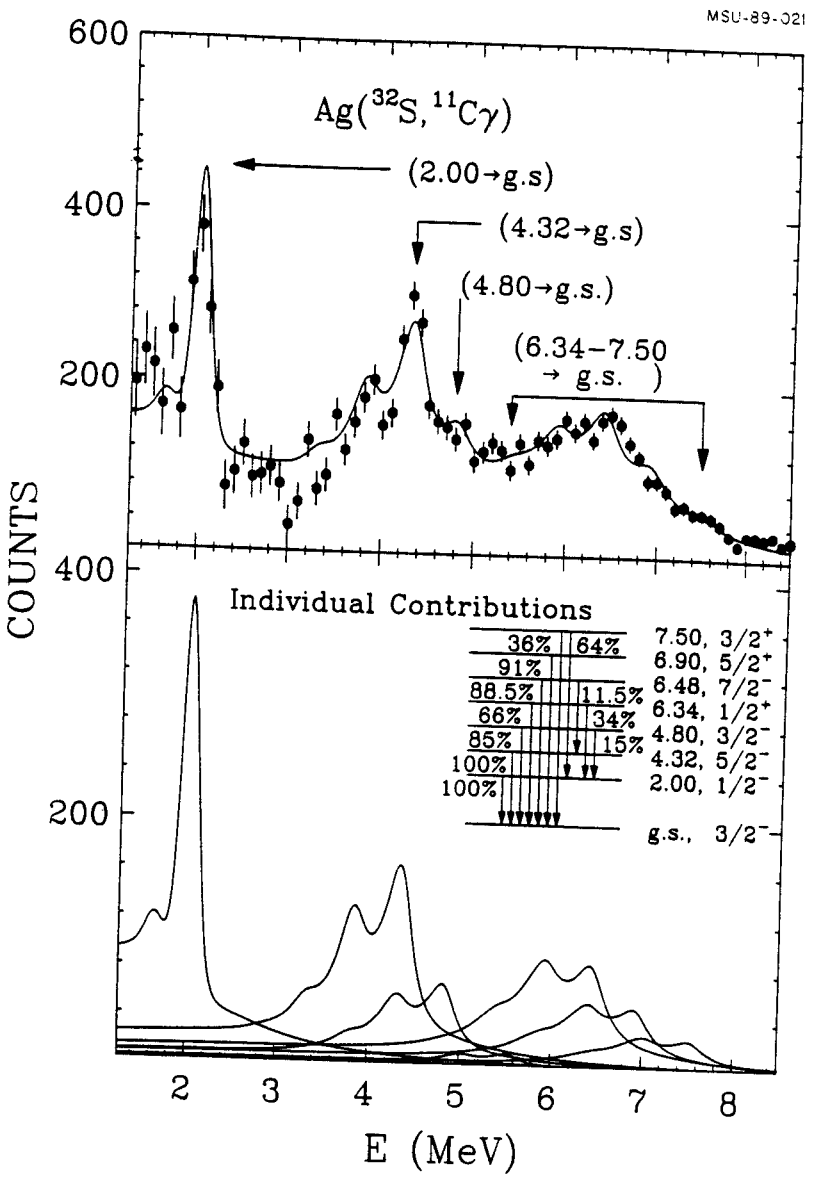

Figure 2.7: Upper panel: Background subtracted coincidence yield (solid points) attributed to γ-ray decays of excited ^{11}C fragments. The solid line shows the fit used for the extraction of the γ-ray fractions,F_γ, listed in 3.2. The locations of several strong transitions are shown by arrows. Lower panel: Contributions from individual transitions. Important transitions and branching ratios are given in the insert.

III γ-ray calibrations

A Line Shape Calibration

The response functions for the individual detector modules of the Spin Spectrometer were calibrated with γ-rays emitted from ^{24}Na,^{60}Co,^{88}Y, and ^{207}Bi radioactive sources as well as γ-rays produced by the inelastic scattering of protons on ^{12}C and ^{16}O nuclei. In total 12 calibration points were measured over the energy range of $E_\gamma \simeq 0.57 - 7$ MeV.

After gain matching of the individual detector modules, the γ-ray spectra were summed over the detectors located in the back hemisphere of the Spin Spectrometer. The summed spectra were then fitted with a parameterized response function. Examples of calibration fits are shown in Fig. 2.8. The fitted response function was parameterized as:

$$\varepsilon_\gamma(E, E_0, A_0) = \sum_{k=0}^{2} A_k[\alpha_k(E, E_k) + \beta_k(E, E_k)], \tag{2.2}$$

with

$$\alpha_k(E, E_k) = \begin{cases} \exp[(L_k/2\sigma_k^2)(L_k + 2E - 2E_k)], & for E \leq E_k - L_k \\ \exp[-(E - E_k)^2/2\sigma_k^2], & for E_k - L_k < E < E_k + U_k \\ \exp[(U_k/2\sigma_k^2)(U_k - 2E + 2E_k)], & for E \geq E_k + U_k \end{cases} \tag{2.3}$$

and

$$\beta_k(E, E_k) = S_k\{\frac{\pi}{2} + \arctan[a_k(E - E_k - b_k)]$$
$$+T_k \arctan[a_k(E - E_k - b_k - c)] - T_K \arctan[a_k(E - E_k - b_k + c)]\} \tag{2.4}$$

In Eqs. (2.2)-(2.4), the indices k = 0, 1, and 2 denote the photo-, first and second escape peaks, respectively; E_0 and E denote the original γ-ray energy and the detector response in MeV; the functions $\alpha_k(E, E_k)$ and $\beta_k(E, E_k)$ parameterize the line shapes of the individual peaks and the Compton backgrounds, respectively. The positions of

the first and second escape peaks were given by:

$$E_k = E_0 - 0.511k. \tag{2.5}$$

The photopeak amplitude, A_0 , was fit to the measured spectrum, and the relative normalizations of the amplitudes, A_1 and A_2 , were determined from the calibrations and could be expressed in the functional form:

$$A_k = C_k A_0\{1 - \exp[(1.56 - E_k)/3.0]\}\Theta(E_k - 1.56), (k = 1, 2), \tag{2.6}$$

where $\Theta(x)$ is the unit step function, $\Theta(x) = 0$ for $x < 0$ and $\Theta(x) = 1$ for $x > 0$, and $C_1 = 0.90$ and $C_2 = 0.18$. The energy dependence of the line shape parameters was determined by the calibrations and could be represented by the functions:

$$L_k = [0.19 + 3.52\exp(-E_k)]\sigma_k, \tag{2.7}$$

$$U_k = [0.47 + 1.22\exp(-E_k/1.91)]\sigma_k, \tag{2.8}$$

$$\sigma_k = (6.8 + 33E_k^{1/2}) \times 10^{-3}, \tag{2.9}$$

$$S_k = \begin{cases} -0.012E_k + 0.075, & for\ E_k < 4.44MeV \\ 0.00345E_k + 0.0063, & for\ E_k \geq 4.44MeV \end{cases} \tag{2.10}$$

$$T_k = 29.5\sigma_k, \tag{2.11}$$

$$a_k = -1.0/(78.7\sigma_k), \tag{2.12}$$

$$b_k = -2.0 - 377.0\sigma_k + 50.0E_k/(1.0 + 9.8E), \tag{2.13}$$

$$c = 72.0\sigma_0. \tag{2.14}$$

Apart from the γ-ray energy E_0 , the calibrated detector response function contains only the adjustable parameter, A_0, which determines the normalization.

B Absolute Efficiency

The relation between the fitted amplitude A_0 and the total number of γ-rays of energy E_0 was calibrated at low energies, $E_\gamma = 0.57 - 2.75$ MeV, via γ-γ coincidence measurements using radioactive sources with coincident transitions. At higher energies,

$E_\gamma \geq 4.4$MeV, the absolute efficiency was obtained from $p-\gamma$ coincidences measured for the inelastic scattering of protons on ^{12}C and^{16}O. If the observed γ-ray peak can be attributed completely to the particle γ-ray coincidence yield, we can define the normalization function $\eta_\gamma(E_0)$ as:

$$\eta_\gamma(E_0) = A_0(E_0)/N(E_0), \tag{2.15}$$

where $A_0(E_0)$ is the amplitude fitted to the spectrum of a γ-ray of energy E_0 (defined as A_0 in Eq. (2.2) and $N(E_0)$ is the total number of emitted γ- rays.

For two coincident γ-rays of energies E_0 and $E_0{}'$, the efficiency for the detection of γ-rays of energy E_0 with the NaI(Tl) detectors of the Spin Spectrometer can be calibrated by determining the amplitude $A_0(E_0)$ for the spectrum measured in coincidence with γ-rays of energy $E_0{}'$ detected with a Compton suppressed Germanium detector module of the Spin Spectrometer. When gated on the γ-ray peak of energy $E_0{}'$ in one (Ge) detector, non-negligible contributions, $A_0(E_0{}')$, of the same energy $E_0{}'$ are observed in the other (NaI) detectors (Fig. 2.8). These contributions,$A_0(E_0{}')$, are entirely due to random coincidences and thus allow us to correct for the random coincidence contributions to the true peak $A_0(E_0)$. Since $A_0(E_0)$ is determined from the spectrum summed over all detectors contained in the backward hemisphere of the Spin Spectrometer, angular correlation effects are effectively integrated out. When such random coincidence effects are important, $\eta_\gamma(E_0)$ is not given by Eq. (2.15). Instead, making the random correction, one has,

$$\eta_\gamma(E_0) = [A_0(E_0) - A_0(E_0{}')\frac{\eta_\gamma(E_0)}{\eta_\gamma(E_0{}')}\frac{P_\gamma(E_0)}{P_\gamma(E_0{}')}]\frac{1}{N_{Ge}(E_0{}')P_{\gamma\gamma}(E_0)}. \tag{2.16}$$

Here, $N_{Ge}(E_0{}')$ denotes the total number of γ-rays of energy $E_0{}'$ detected in the Germanium detector; $P_{\gamma\gamma}(E_0)$ denotes the conditional probability that a γ-ray of energy E_0 is emitted in coincidence with the detected γ-ray of energy $E_0{}'$; typically, $P_{\gamma\gamma}(E_0) = 0.8 - 1.0$; $P_\gamma(E_0)$ and $P_\gamma(E_0{}')$ correspond the single inclusive emission

probabilities for γ-rays of energies E_0 and $E_0{}'$, respectively. The second term in the square brackets corrects for random coincidences. When gated on the other γ-ray peak E_0 (Fig. 2.8, the upper and lower figures in the left-hand column), the true coincidence amplitude for γ-rays of energy $E_0{}'$ and random amplitude for γ-rays of energy E_0 can be extracted. Thus, a corresponding equation for $\eta_\gamma(E_0{}')$ can be established with E_0 and $E_0{}'$ interchanged in Eq. (2.16), allowing the unambiguous determination of $\eta_\gamma(E_0)$ and $\eta_\gamma(E_0{}')$ by an iterative procedure.

For the case of γ-rays emitted in the $^{12}C(p,p'\gamma)$ and $^{16}O(p,p'\gamma)$ reactions, one places a gate on the respective peak in the proton spectrum to determine the number, $N_{p'}$, of inelastically scattered protons. Summing over the NaI(Tl) detectors in the backward hemisphere, one obtains:

$$\eta_\gamma(E_0) = A_0(E_0)/[N_{p'} P_{p\gamma}(E_0)], \tag{2.17}$$

where the amplitude $A_0(E_0)$ is determined from the coincident γ-ray spectrum, corrected for random coincidences; $P_{p\gamma}(E_0)$ is the conditional probability that a γ-ray of energy E_0 is emitted in coincidence with the detected inelastically scattered proton. For the transitions of interest, the conditional probability $P_{p\gamma}(E_0)$ is unity.

Figure 2.9 shows individual points measured for the normalization function. The solid line shows the analytical interpolation used in our analysis,

$$\eta_\gamma(E_0) = 4.11 E_0^{-0.403} \exp[-0.0143(3.912 + \ln E_0)^2 - 0.010(3.912 + \ln E_0)^3]. \tag{2.18}$$

C Coincidence Summing

For the average event analyzed in the present experiment, the individual NaI(Tl) modules in the backward hemisphere trigger with a coincidence probability of about p = 28%. This high probability is due to the rather large multiplicity of γ-rays (and neutrons) emitted from highly excited target residues. Only a fraction, $1 - p$, of

recorded fragment γ-rays will be correspond to single γ-ray interactions for a given detector module; there is the probability, p, for the coincident interaction of a second γ-ray with the same detector module. This 'coincidence summing' effect leads to considerable, multiplicity dependent line shape distortions, see Fig. 2.5 of the main text. These line shape distortions were evaluated by folding the fraction, p, of the original calibration function, Eq. (2.2), with the normalized background function, $B_\gamma(E)$, obtained from an energy spectrum in the backward hemisphere of the Spin Spectrometer which reflects the pulse height distribution for neutrons and γ-rays emitted from target residues. This latter spectrum was gated by the detection of a ^{9}Be fragment in a particle telescope to avoid introducing structures due to discrete γ-rays emitted from the detected fragments. The corrected response function has the form:

$$\varepsilon_\gamma^*(E, E_0, A_0, p) = A_0\{(1-p)\varepsilon_\gamma(E, E_0) + p\int_0^E dE'[\varepsilon_\gamma(E-E', E_0)B_\gamma(E')]\}, \quad (2.19)$$

with

$$\int dE' B_\gamma(E') = 1. \quad (2.20)$$

where $\varepsilon_\gamma(E, E_0)$ is the result of Eq. (2.2) with $A_0 = 1$.

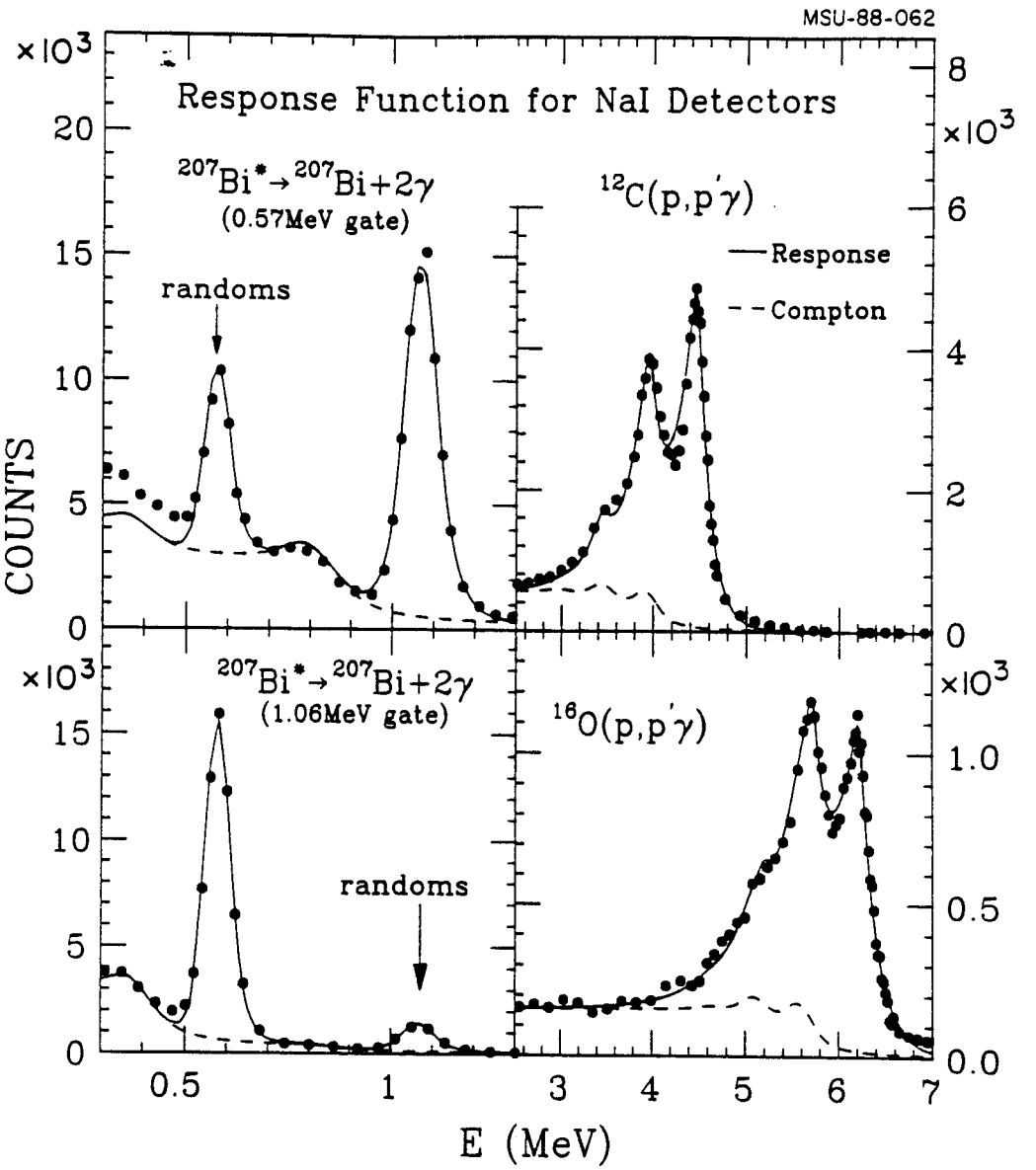

Figure 2.8: Calibrations for the γ-ray response function, $\varepsilon_\gamma(E, E_0, A_0)$, given by Eqs.(2.2)-(2.4). The solid lines show the fitted line shapes; the dashed lines show the calculated Compton background.

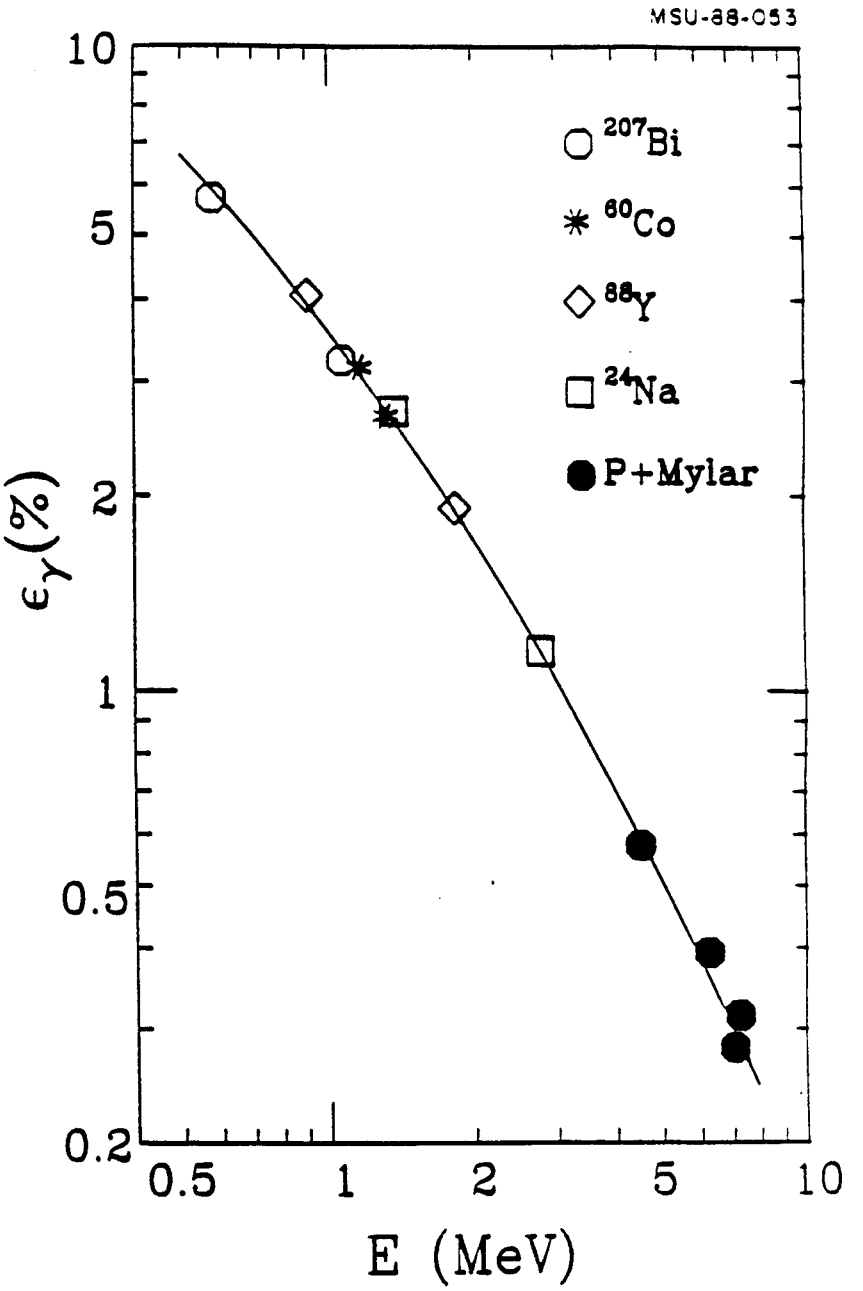

Figure 2.9: Measured values of the normalization function $\eta_\gamma(E_0)$, defined in Eq. (2.15)-(2.17). The solid line corresponds to the analytic interpolation given by Eq. (2.18).

Chapter 3

Data

In this chapter, the data for single particle inclusive spectra and the coincidence γ-ray spectra are presented. In the first section we present the single fragment kinetic energy spectra, and fits to the spectra using a 'moving source' parameterization. The coincident γ-ray data are discussed in the second section.

I Single fragment Inclusive Cross Sections

The inclusive differential cross sections, measured at $\theta_{IMF} = 20°, 25°, 30°, 45°$ and $50°$, are shown in Figs. 3.1-3.5 for isotopes of lithium, beryllium, boron, carbon, nitrogen, and oxygen, respectively. Consistent with previous measurements [Fiel 86a, Fiel 86b], the spectra exhibit broad maxima at energies close to the exit channel Coulomb barrier and rather featureless, nearly exponential slopes at higher energies. These slopes become steeper at larger angles. In the center-of-mass system, the cross sections are peaked at forward angles, indicating emission prior to the establishment of full statistical equilibrium of the composite nuclear system. In order to obtain analytical interpolations of the inclusive cross sections to unmeasured angles and energies, the data were fitted by a parametrization employing the superposition of three Maxwellian distributions ('moving sources'):

$$\frac{d^2\sigma}{d\Omega dE} = \sum_{i=1}^{3} N_i \sqrt{E - U_c} \ \exp\{-[E - U_c + E_i - 2\sqrt{E_i(E - U_c)}\cos\theta]/T_i\} \qquad (3.1)$$

Here, U_c is the kinetic energy gained by the Coulomb repulsion from the heavy reaction residue assumed to be stationary in the laboratory system; N_i is a normalization constant and T_i is the "kinetic temperature" parameter of the i-th source; $E_i = mv_i$, where m is the mass of the emitted fragment and v_i is the velocity of the i-th source in the laboratory system. This choice of parametrization was chosen for simplicity. Fits obtained with this parametrization are shown by the solid lines in Figs. 3.1-3.5; the parameters are listed in Table 3.1. Because of the small angular range covered by the data, substantial ambiguities exist for the individual parameters.

Table 3.1: Parameters used for the fits of the inclusive cross sections with Eq. 3.1. The Coulomb repulsion energies U_c and the temperature parameters T_i are given in units of MeV, and the normalization constants N_i are given in units of $\mu b/(sr\mathrm{MeV}^{3/2})$.

	T_1	v_1/c	N_1	T_2	v_2/c	N_2	T_3	v_3/c	N_3	U_c
^{6}Li	0.156	5.1	73.5	0.095	9.6	219.9	0.025	5.0	226.4	35.0
^{7}Li	0.143	8.6	229.7	0.081	9.6	369.7	0.007	5.0	270.6	34.6
^{8}Li	0.160	5.0	0.1	0.090	11.0	34.3	0.009	13.7	17.1	34.3
^{7}Be	0.161	7.7	65.7	0.085	10.1	73.1	0.018	5.0	41.3	45.4
^{9}Be	0.154	6.8	74.6	0.086	10.0	107.9	0.000	5.0	121.5	44.5
^{10}Be	0.180	5.5	57.7	0.105	10.2	48.9	0.043	10.4	29.7	44.1
^{10}B	0.172	2.5	5675.6	0.097	10.5	92.8	0.001	12.7	42.6	47.0
^{11}B	0.167	4.0	977.7	0.101	10.4	190.3	0.008	11.7	106.8	46.6
^{12}B	0.173	2.7	1494.4	0.102	11.0	21.9	0.014	12.5	12.0	46.3
^{13}B	0.167	3.3	127.4	0.097	12.0	4.8	0.013	13.1	2.3	46.0
^{11}C	0.164	3.5	260.2	0.100	11.2	26.0	0.013	9.0	17.2	58.0
^{12}C	0.165	3.8	1608.1	0.102	10.1	156.9	0.022	8.4	139.0	58.8
^{13}C	0.162	3.5	1787.7	0.100	10.1	107.1	0.037	6.7	98.6	66.8
^{14}C	0.164	3.5	930.5	0.102	10.6	37.5	0.038	10.2	23.7	58.0
^{13}N	0.165	3.6	125.5	0.102	12.3	3.8	0.001	11.4	4.6	69.3
^{14}N	0.169	2.7	11904.2	0.105	10.5	49.5	0.051	7.4	37.0	68.9
^{15}N	0.164	3.2	8122.8	0.106	9.6	123.1	0.051	8.0	79.0	68.5
^{16}N	0.159	3.8	211.4	0.102	11.4	9.6	0.043	10.4	9.5	68.5
^{17}N	0.155	4.5	40.3	0.104	11.9	3.6	0.048	11.6	3.5	67.8
^{15}O	0.164	2.8	2206.9	0.106	11.6	5.6	0.052	7.5	7.0	76.9
^{16}O	0.159	4.2	1254.1	0.107	9.8	66.3	0.057	7.8	55.9	76.5
^{17}O	0.158	3.8	1254.4	0.107	10.1	33.6	0.054	8.3	32.4	76.1
^{18}O	0.158	4.0	557.1	0.103	10.4	19.8	0.051	8.1	19.5	75.7
^{19}O	0.149	5.5	22.1	0.099	12.6	2.0	0.055	11.8	3.1	75.4

II γ-Ray Spectra From Decaying Fragments

A γ-Ray Spectra From Germanium Detectors

Spectra of γ-rays detected in coincidence with isotopes of ^{8}Li, ^{7}Be, ^{10}B, ^{12}B, and ^{13}C are shown by the histograms in Fig. 3.6. To obtain these spectra, the energy spectra of coincident γ-rays were transformed into the rest frames of the coincident particles using relativistic Jacobians and Doppler shift corrections. Since these transformations shift and broaden γ-ray transitions of the target residues, particular attention was paid to identifying and correcting for spurious structures in the γ-ray background. Similar to the analyses of the NaI(Tl) spectra, background spectra were generated by performing Doppler shift transformations on raw γ-ray spectra measured in coincidence with ^{6}Li, ^{9}Be, and ^{11}B nuclei. These nuclei have no strong γ-ray transitions at the γ-ray energies which could be measured with the Germanium detectors; however, these background spectra contained discrete transitions from target residues common to all spectra.

The Doppler shifted background spectra are indicated by the solid dots in the figure. The following transitions were analyzed: ^{8}Li(1^{+}, 0.981 MeV)$\rightarrow \gamma+^{8}$Li($2^{+}, g.s.$), ^{7}Be($\frac{1}{2}^{-}$, 0.429 MeV) $\rightarrow \gamma+^{7}$Be($\frac{3}{2}^{-}, g.s.$), ^{10}B(1^{+}, 2.154 MeV)$\rightarrow \gamma+^{10}$B(0^{+}, 1.740 MeV), ^{13}C($\frac{5}{2}^{+}$, 3.854 MeV)$\rightarrow \gamma+^{13}$C($\frac{3}{2}^{-}$, 3.684 MeV), and overlapping transitions: ^{12}B(2^{+}, 0.953 MeV)$\rightarrow \gamma+^{12}$B($1^{+}, g.s.$), ^{12}B(1^{-}, 2.621 MeV)$\rightarrow \gamma+^{12}$B(2^{-},1.674 MeV). We did not analyze the transition, ^{7}Li($\frac{1}{2}^{-}$, 0.478 MeV)$\rightarrow \gamma+^{7}$Li($\frac{3}{2}^{-}, g.s.$), because the pile-up of two coincident α-particles in the telescopes is misidentified as a ^{7}Li, [Wohn 74], nor the long-lived transition, ^{10}B(1^{+}, 0.718 MeV)$\rightarrow \gamma+^{10}$B($3^{+}, g.s.; \tau = 1.02ns$), [Ajze 86a], because this decay occurs at a considerable distance from the target resulting in major uncertainties in the efficiencies of the γ-ray detectors. The data in Fig. 3.6 were summed over all detectors; the individual detectors provide comparable

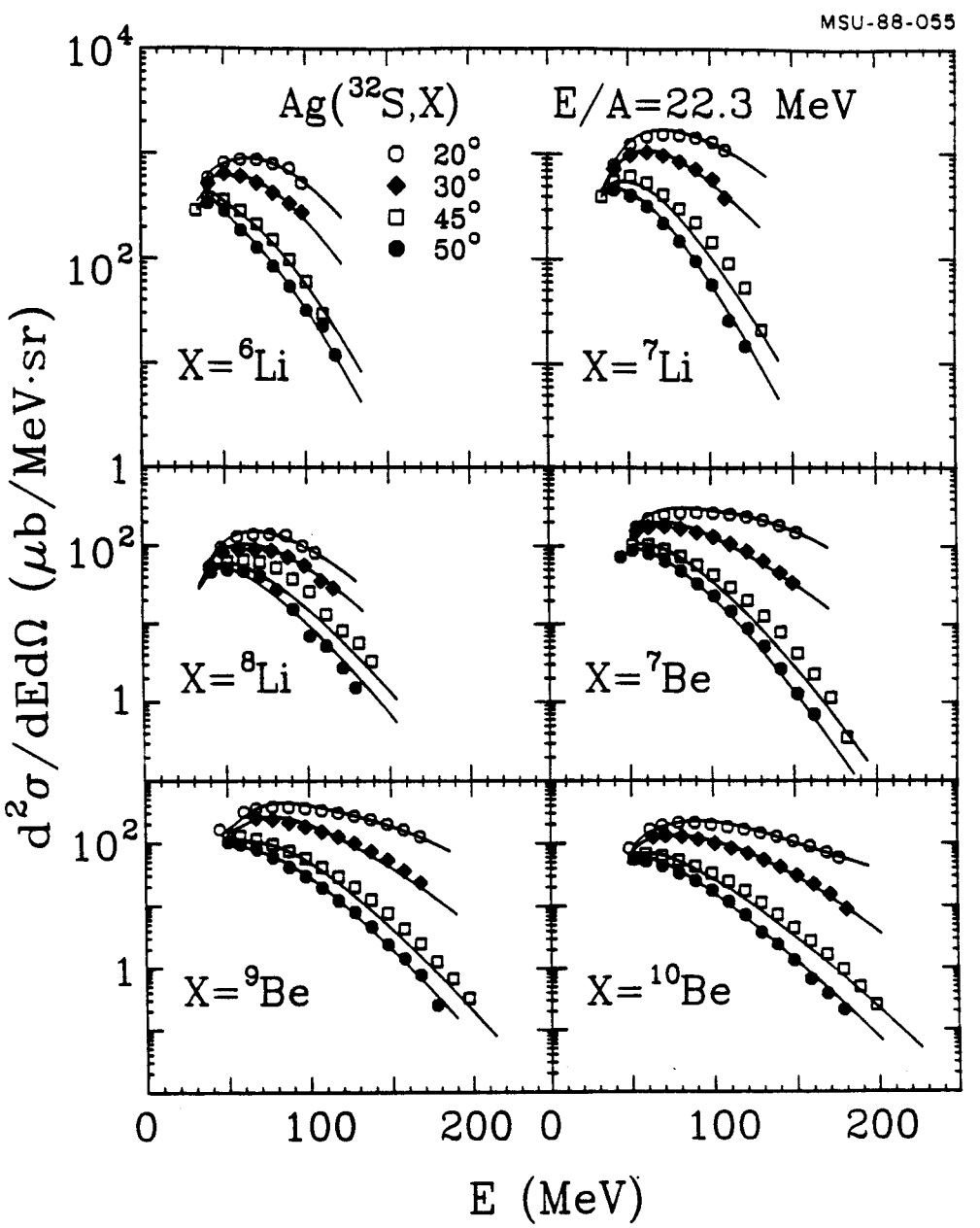

Figure 3.1: Inclusive differential cross sections for lithium and beryllium isotopes; the laboratory detection angles are indicated in the figure. The solid lines represent fits with Eq. (3.1); the parameters are listed in Table 3.1.

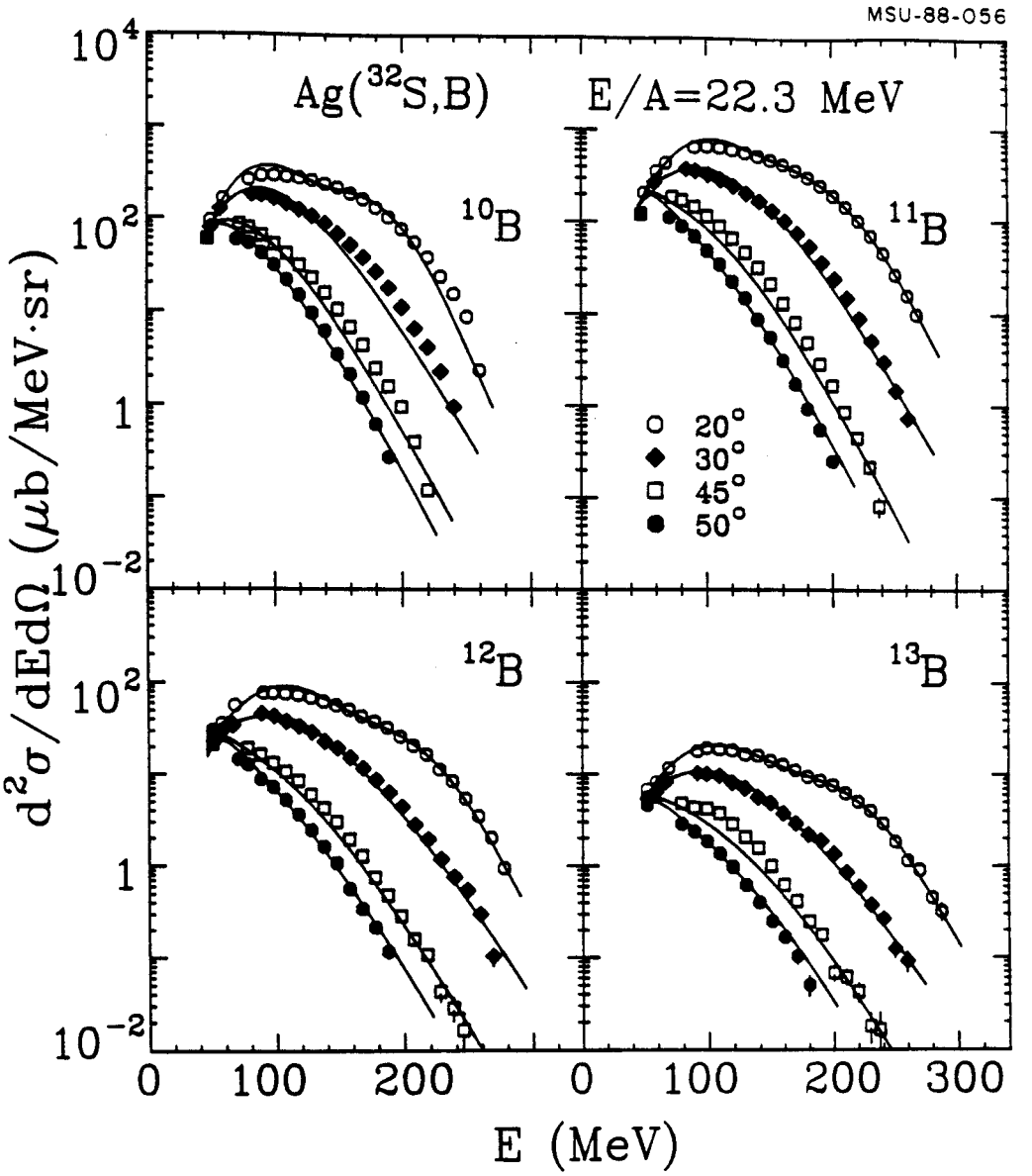

Figure 3.2: Inclusive differential cross sections for boron isotopes; the laboratory detection angles are indicated in the figure. The solid lines represent fits with Eq. (3.1); the parameters are listed in Table 3.1.

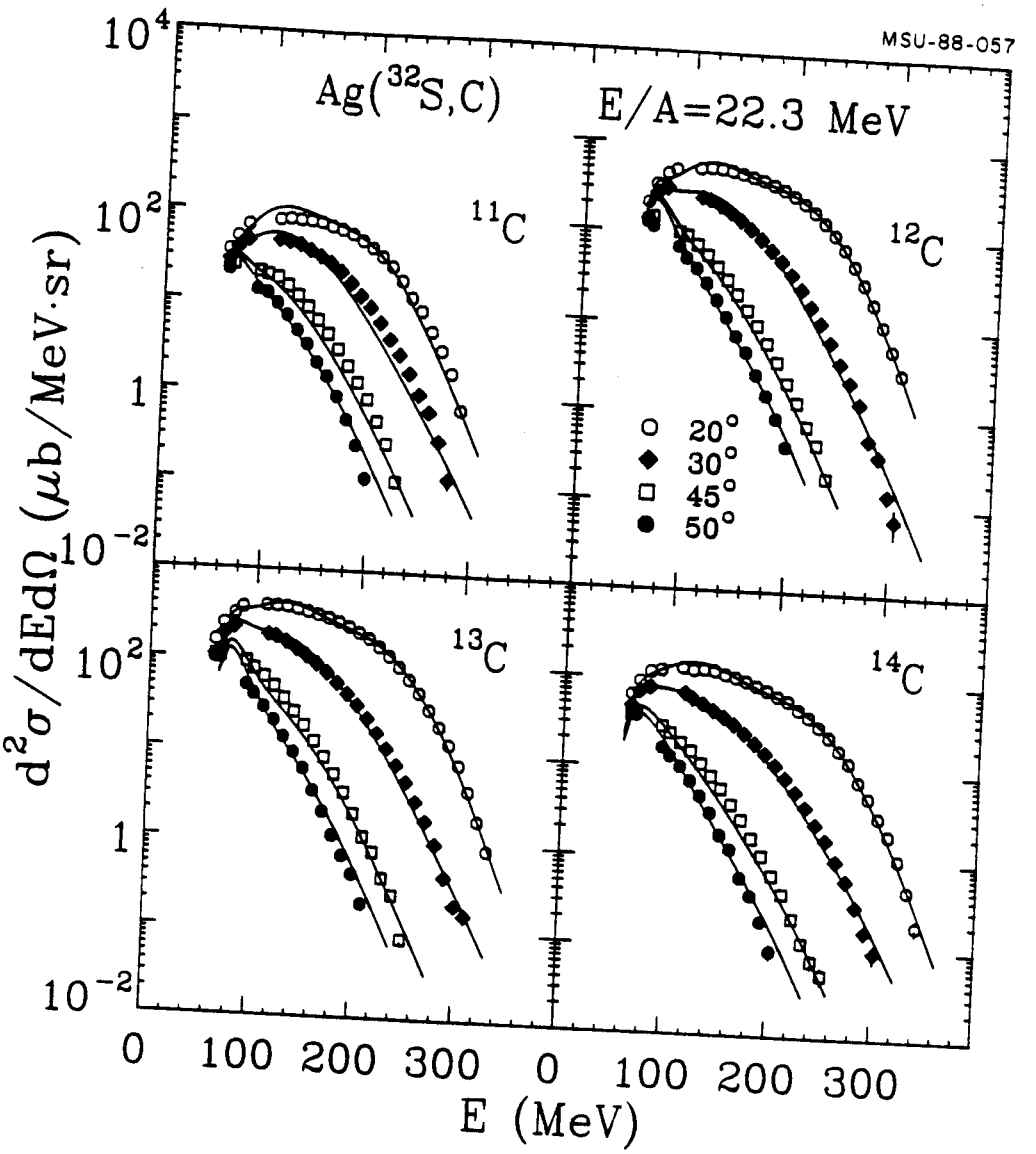

Figure 3.3: Inclusive differential cross sections for carbon isotopes; the laboratory detection angles are indicated in the figure. The solid lines represent fits with Eq. (3.1); the parameters are listed in Table 3.1.

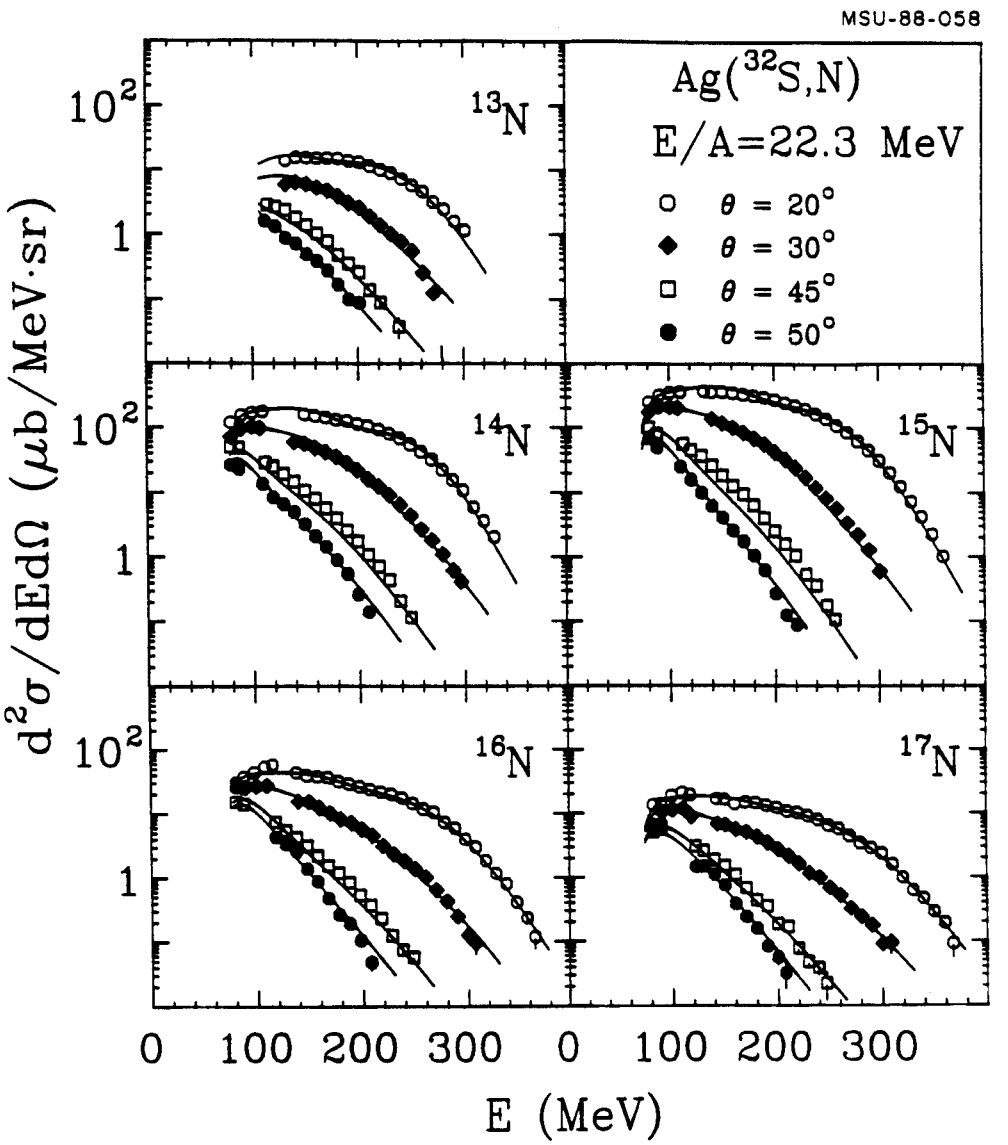

Figure 3.4: Inclusive differential cross sections for nitrogen isotopes; the laboratory detection angles are indicated in the figure. The solid lines represent fits with Eq. (3.1); the parameters are listed in Table 3.1.

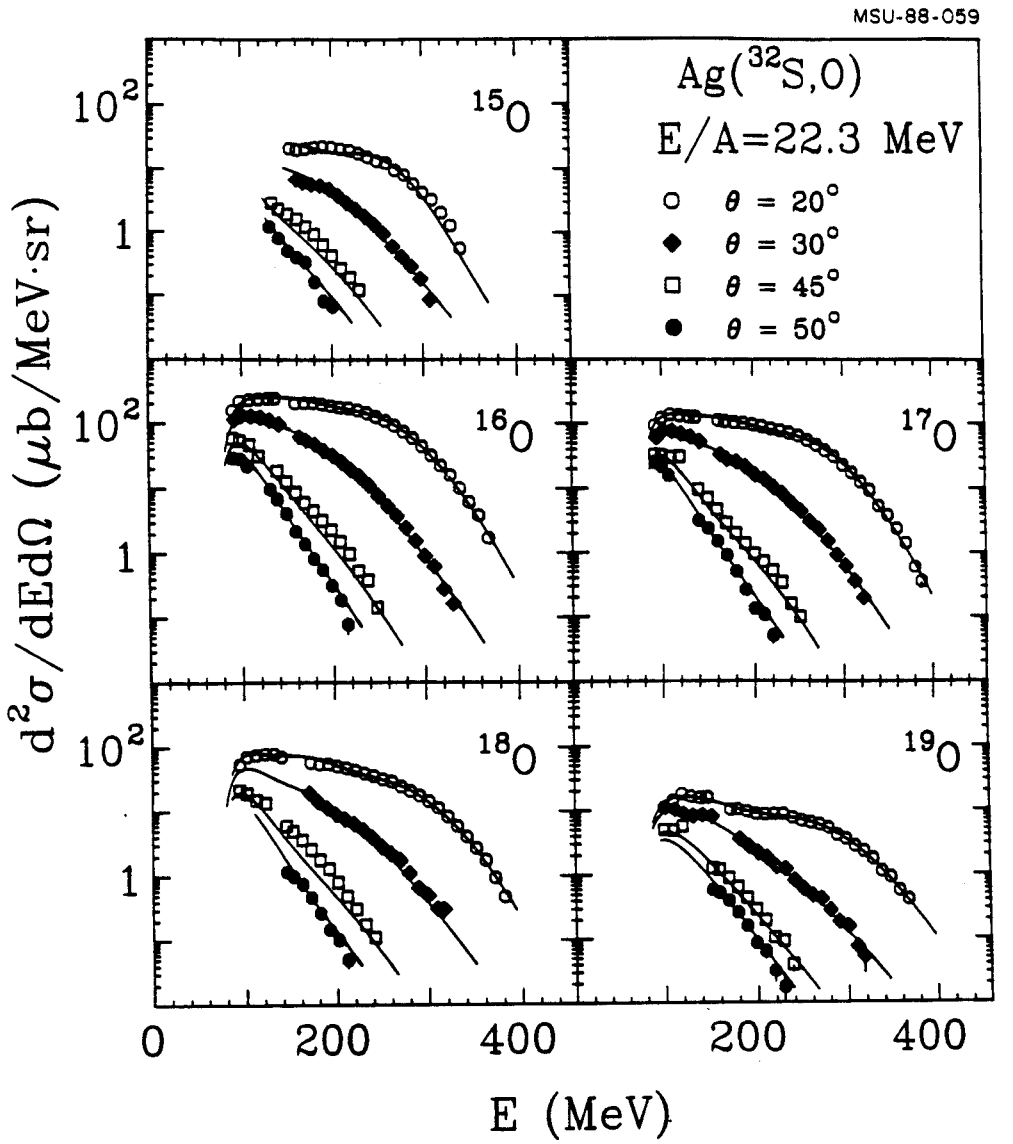

Figure 3.5: Inclusive differential cross sections for oxygen isotopes; the laboratory detection angles are indicated in the figure. The solid lines represent fits with Eq. (3.1); the parameters are listed in Table 3.1.

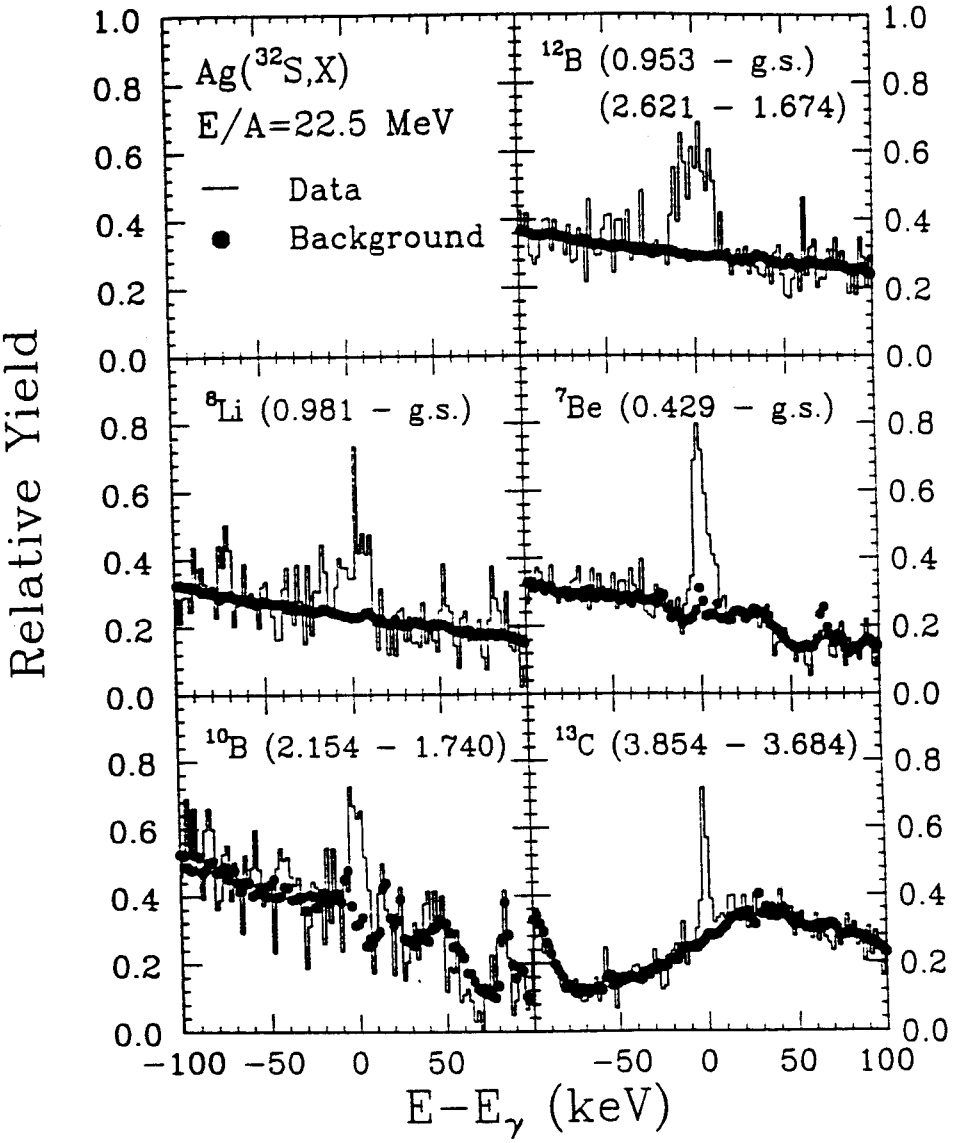

Figure 3.6: Spectra of γ-rays detected in coincidence with isotopes of ^{8}Li, ^{7}Be, ^{10}B, ^{12}B, and ^{13}C produced in ^{32}S from Compton Shielded Germanium detectors.

numerical contributions to the sum. The inclusive fragment yields and fragment-γ-ray coincidence yields were summed over angle and combined to extract the fraction,F_γ, of observed fragments which were accompanied by the designated γ-ray. Spin alignments were assumed to be zero. This introduced a spin alignment dependent uncertainty in F_γ of about 3%. Values for F_γ obtained for these transitions, after correction for the efficiency loss due to the coincidence summing effects are presented in Table 3.2.

B γ-Ray Spectra from NaI Detectors

The γ-ray spectra detected in coincidence with ^{10}Be, ^{12}B, ^{13}C, ^{14}C, ^{14}N, ^{15}N, ^{16}O, and ^{18}O fragments are shown in the left hand panels of Figs. 3.7- 3.14, respectively. The respective background spectra are represented by the dashed lines. The right hand panels show the yields obtained after subtraction of the background spectra. These yields are associated with γ- ray transitions in the detected fragments. The solid lines show the fits used for the extraction of the γ-ray fractions, F_γ. The inserts in the left hand panels show the most important transitions and branching ratios. Photopeak locations of important transitions or groups of transitions are indicated by arrows in the right hand panels. For the actual fits, we used the complete set of transitions and branching ratios from the compilation of ref. [Ajze 84-88]. The γ-ray yields associated with decays of excited ^{11}B, ^{11}C, and ^{12}C transitions were already presented in Figs. 2.5-2.7.

For ^{12}C, ^{13}C, and ^{10}Be fragments we have investigated whether the measured values of F_γ depend on the fragment kinetic energy or scattering angle. Within the experimental uncertainties, no dependence of the F_γ on either quantity was observed. Values for F_γ, listed in Table 3.2, were obtained by combining the data for the various intermediate mass fragment kinetic energies and scattering angles.

The coincident γ-ray spectra can be well understood in terms of known transitions

in the detected fragments. The good agreement of the measured and fitted spectral shapes justifies, *a posteriori*, our treatment of the background associated with emissions from target residues. The only case which shows noticeable deviations from our standard calibration and background subtraction procedures corresponds to the width of the 0.95 MeV γ-ray peak measured in coincidence with ^{12}B fragments, see Fig. 3.8. This peak results from the superposition of the decays $^{12}\mathrm{B}(2^+, 0.953MeV)$ $\rightarrow\gamma+^{12}\mathrm{B}(1^+, g.s.)$ and $^{12}\mathrm{B}(1^-, 2.621MeV) \rightarrow\gamma+^{12}\mathrm{B}(2^-, 1.674MeV)$. For this low energy γ-ray, the line width was somewhat larger than expected from the overall calibration of the response function, suggesting that the resolution of the Spin Spectrometer was slightly worse during the experiment than during the calibration. This degradation of the resolution could possibly arise from the coincidence summing of low energy γ-rays and x-rays which lie below our experimental thresholds and therefore are not taken into account by the coincidence summing corrections described in Appendix C. This resolution problem made the background determination and subsequent subtraction more difficult for γ-ray energies below about 1 MeV. In order to extract the strength of this peak more accurately, the spectrum was fitted by folding the calibrated response function with a Gaussian of 0.14 MeV FWHM (while conserving the integral normalization of the spectrum). The γ-ray fraction extracted from this peak agrees within 10% with that extracted [see Table 3.2] from the γ-ray spectra measured with the Compton shielded Germanium detectors for which the background subtraction was less problematic.

For a considerable number of transitions, the energy resolution of the NaI(Tl) detectors was insufficient to allow reliable determination of the individual γ-ray fractions. In such cases, the γ-ray fractions are only given for groups of transitions which could be determined with good statistical accuracy. Transitions contained within a particular group are identified in Table 3.2 by $\sum 1$, $\sum 2$, ... etc.

There are several sources for the uncertainties in the γ-ray fractions listed in Table 3.2. Because the resolution for low energy γ-rays could not be accurately assessed from the fragment γ-ray coincidence data, the extracted γ-ray fractions have associated uncertainties which could be as large as 10% for γ-ray energies significantly below 3 MeV. Above 3 MeV these uncertainties are less than 2%. Additional uncertainties are associated with low counting statistics, uncertainties in the interpolation of the γ-ray efficiency (see Appendix B), ambiguities in the fitting procedure, and the possibility for misidentification of the mass and charge of the intermediate mass fragment detected in the particle telescope. These uncertainties were estimated and for simplicity, were combined in quadrature to provide the uncertainties listed in Table 3.2. It was particularly difficult to estimate the uncertainty associated with possible errors in the functional form of the background. Upper limits on this uncertainty were obtained by fitting with different background assumptions. With extreme background assumptions, the experimentally determined yield varied by less than 8%. This extreme error estimate, however, was not incorporated into the uncertainties listed in Table 3.2.

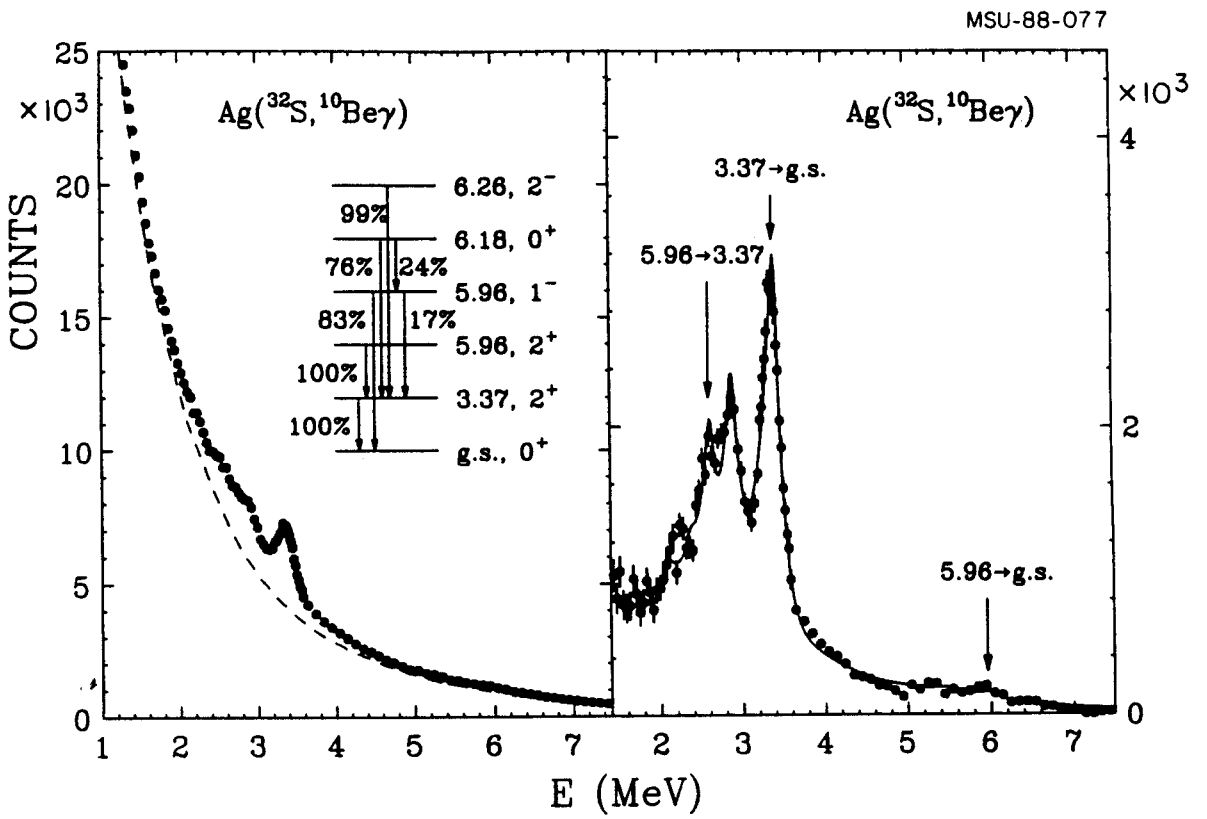

Figure 3.7: γ-ray spectra measured in coincidence with ^{10}Be fragments. The left hand panel shows the raw coincidence spectrum with the background indicated by the dashed line. The right hand panel shows the spectrum associated with γ-ray decays of excited ^{10}Be fragments. The solid line shows the fit used for the extraction of the γ-ray fractions, F_γ , listed in Table 3.2. The insert shows important transitions and branching ratios used for the fit. Photopeak locations of important transitions are indicated by arrows.

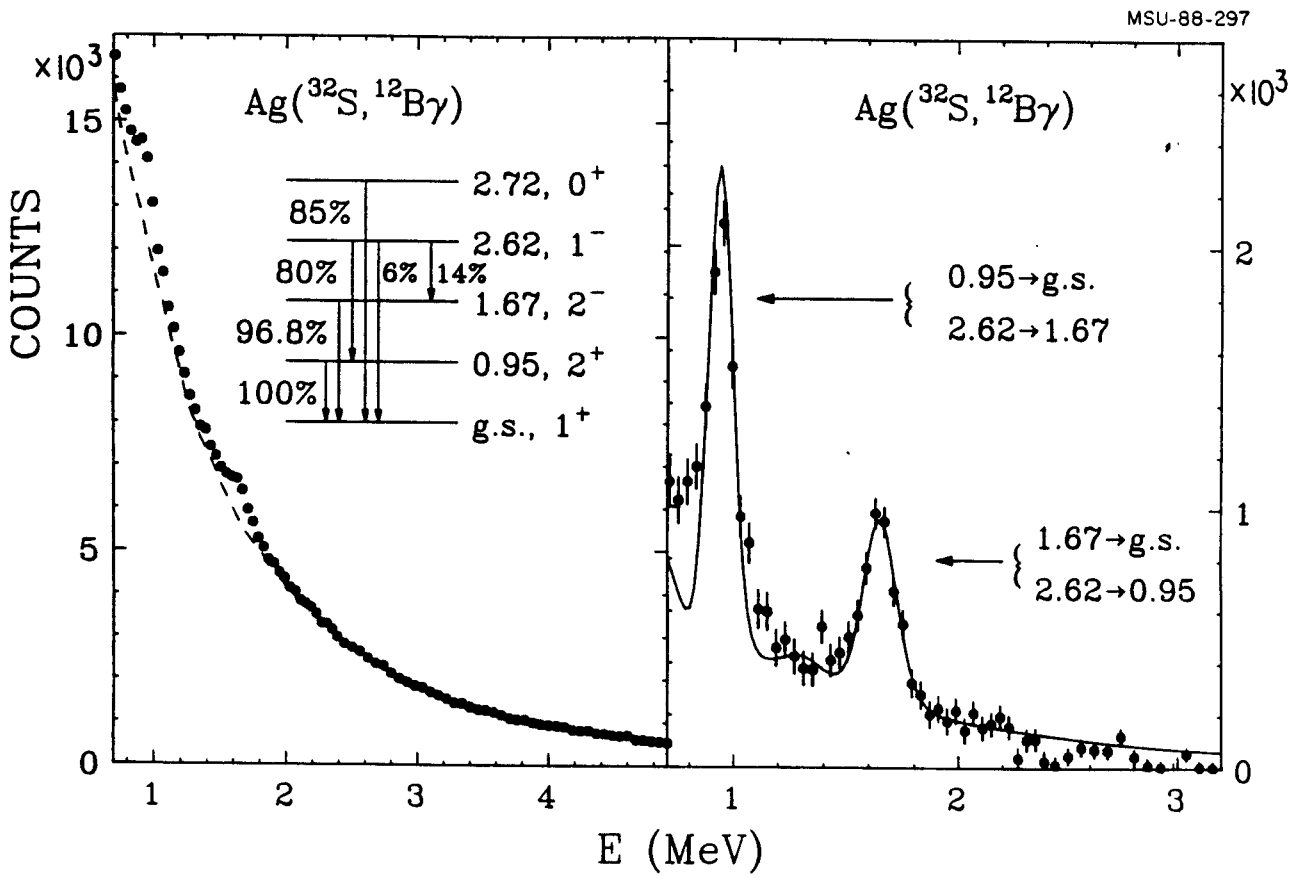

Figure 3.8: γ-ray spectra measured in coincidence with ^{12}B fragments. The left hand panel shows the raw coincidence spectrum with the background indicated by the dashed line. The right hand panel shows the spectrum associated with γ-ray decays of excited ^{12}B fragments. The solid line shows the fit used for the extraction of the γ-ray fractions, F_γ, listed in Table 3.2. The insert shows important transitions and branching ratios used for the fit. Photopeak locations of important transitions are indicated by arrows.

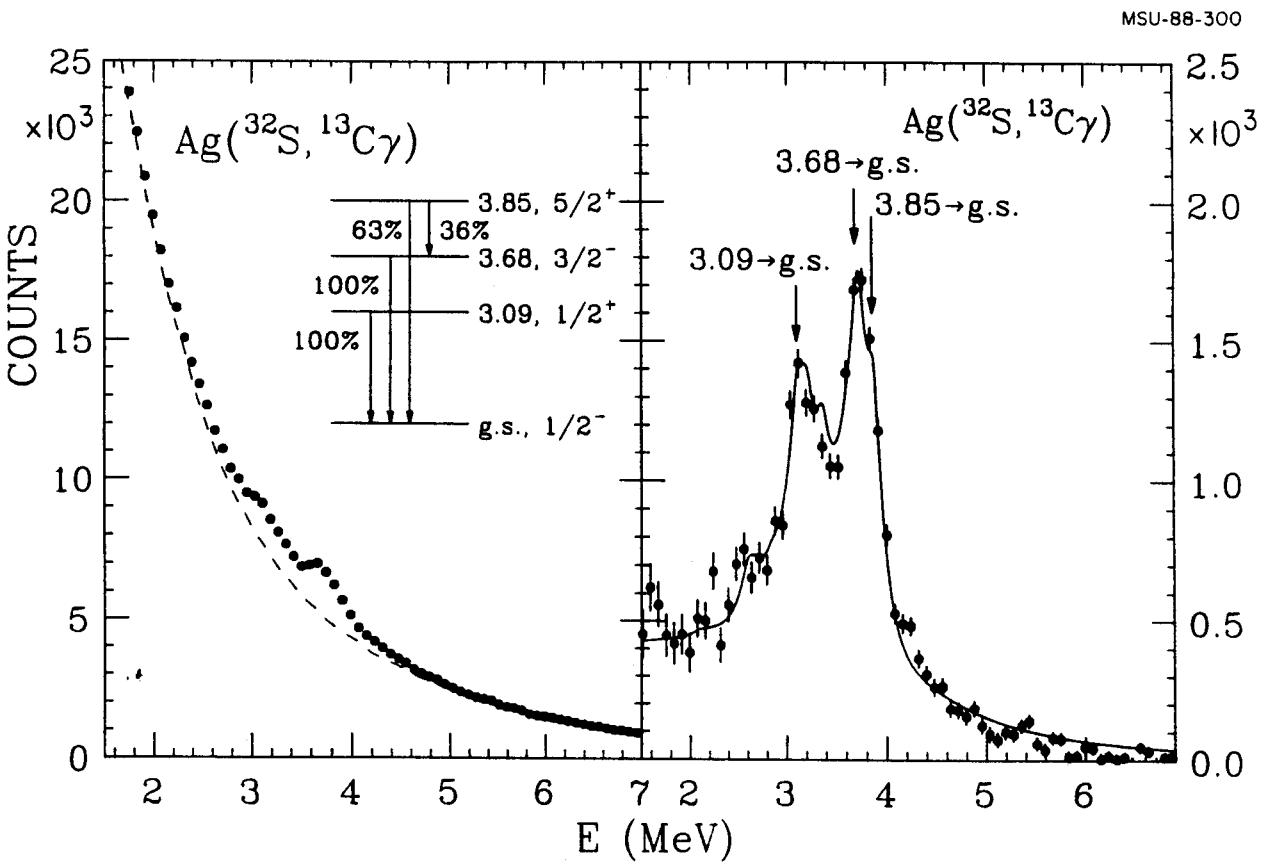

Figure 3.9: γ-ray spectra measured in coincidence with ^{13}C fragments. The left hand panel shows the raw coincidence spectrum with the background indicated by the dashed line. The right hand panel shows the spectrum associated with γ-ray decays of excited ^{13}C fragments. The solid line shows the fit used for the extraction of the γ-ray fractions, F_γ, listed in Table 3.2. The insert shows important transitions and branching ratios used for the fit. Photopeak locations of important transitions are indicated by arrows.

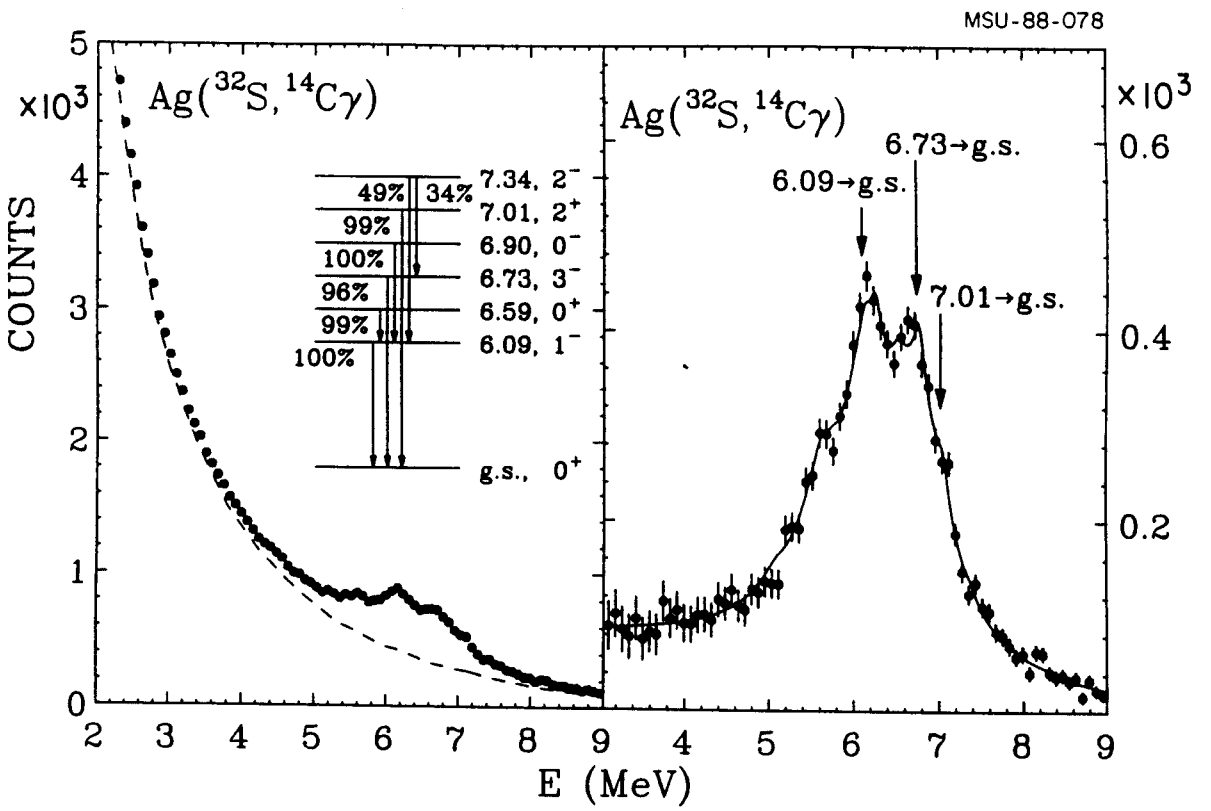

Figure 3.10: γ-ray spectra measured in coincidence with ^{14}C fragments. The left hand panel shows the raw coincidence spectrum with the background indicated by the dashed line. The right hand panel shows the spectrum associated with γ-ray decays of excited ^{14}C fragments. The solid line shows the fit used for the extraction of the γ-ray fractions, F_γ, listed in Table 3.2. The insert shows important transitions and branching ratios used for the fit. Photopeak locations of important transitions are indicated by arrows.

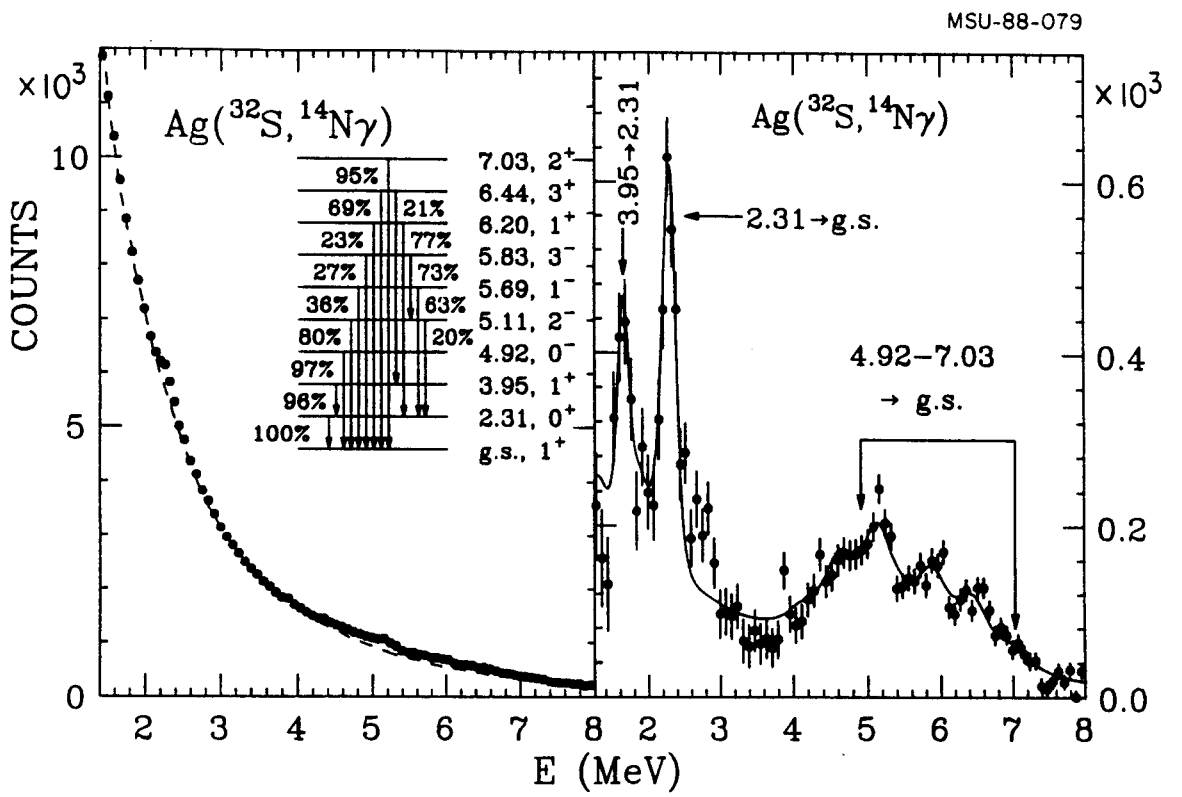

Figure 3.11: γ-ray spectra measured in coincidence with ^{14}N fragments. The left hand panel shows the raw coincidence spectrum with the background indicated by the dashed line. The right hand panel shows the spectrum associated with γ-ray decays of excited ^{14}N fragments. The solid line shows the fit used for the extraction of the γ-ray fractions, F_γ, listed in Table 3.2. The insert shows important transitions and branching ratios used for the fit. Photopeak locations of important transitions are indicated by arrows.

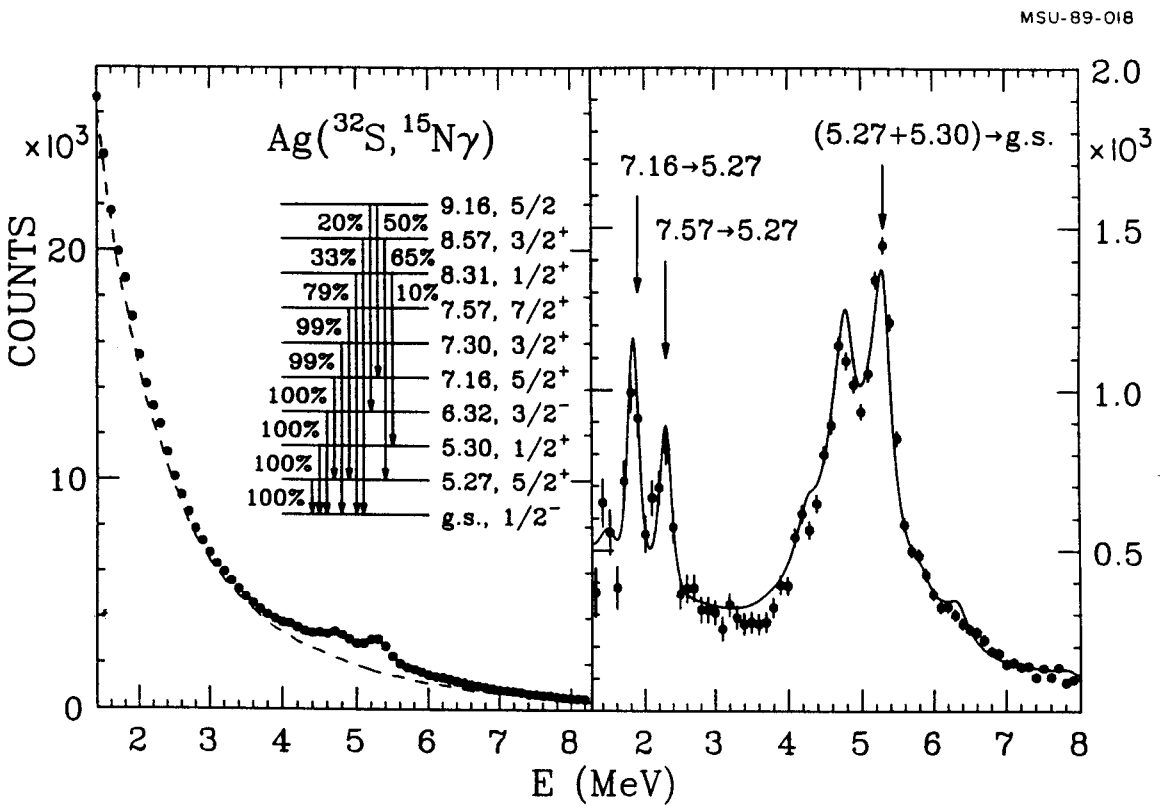

Figure 3.12: γ-ray spectra measured in coincidence with ^{15}N fragments. The left hand panel shows the raw coincidence spectrum with the background indicated by the dashed line. The right hand panel shows the spectrum associated with γ-ray decays of excited ^{15}N fragments. The solid line shows the fit used for the extraction of the γ-ray fractions,F_γ, listed in Table 3.2. The insert shows important transitions and branching ratios used for the fit. Photopeak locations of important transitions are indicated by arrows.

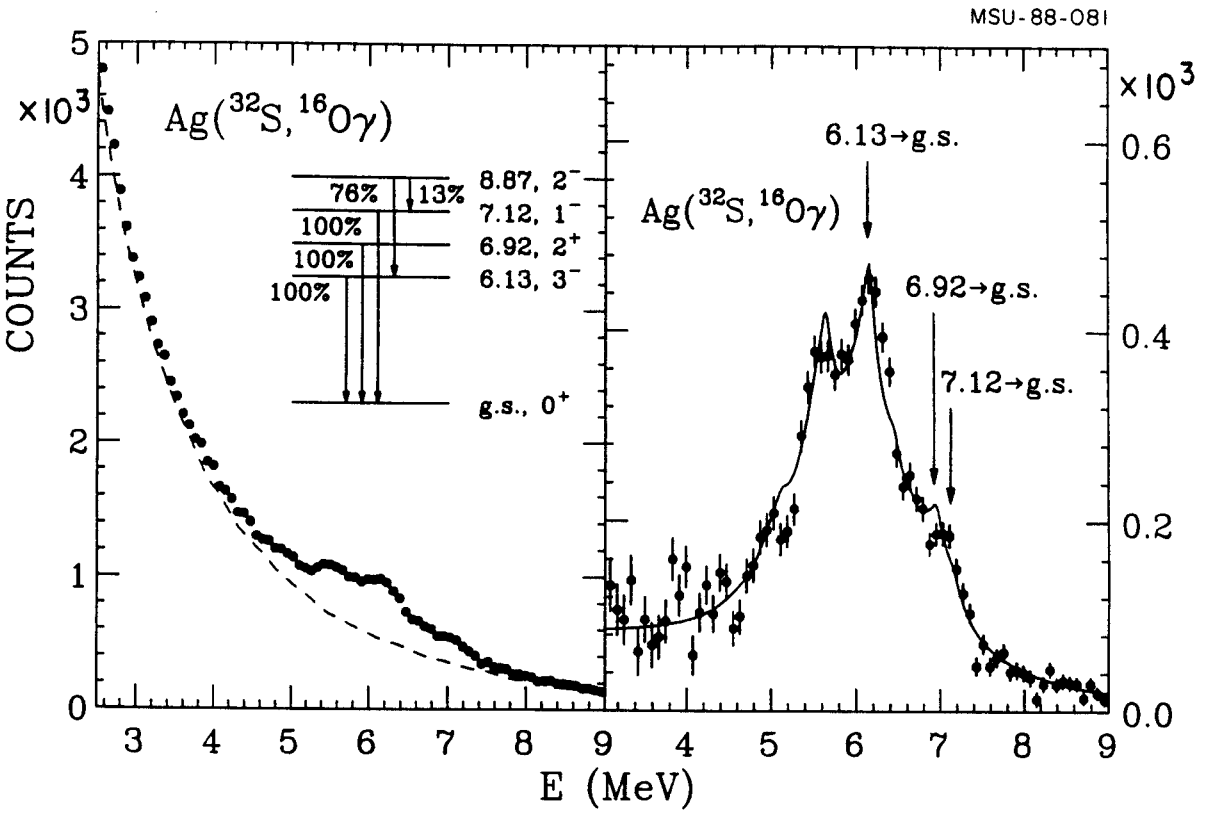

Figure 3.13: γ-ray spectra measured in coincidence with ^{16}O fragments. The left hand panel shows the raw coincidence spectrum with the background indicated by the dashed line. The right hand panel shows the spectrum associated with γ-ray decays of excited ^{16}O fragments. The solid line shows the fit used for the extraction of the γ-ray fractions, F_γ, listed in Table 3.2. The insert shows important transitions and branching ratios used for the fit. Photopeak locations of important transitions are indicated by arrows.

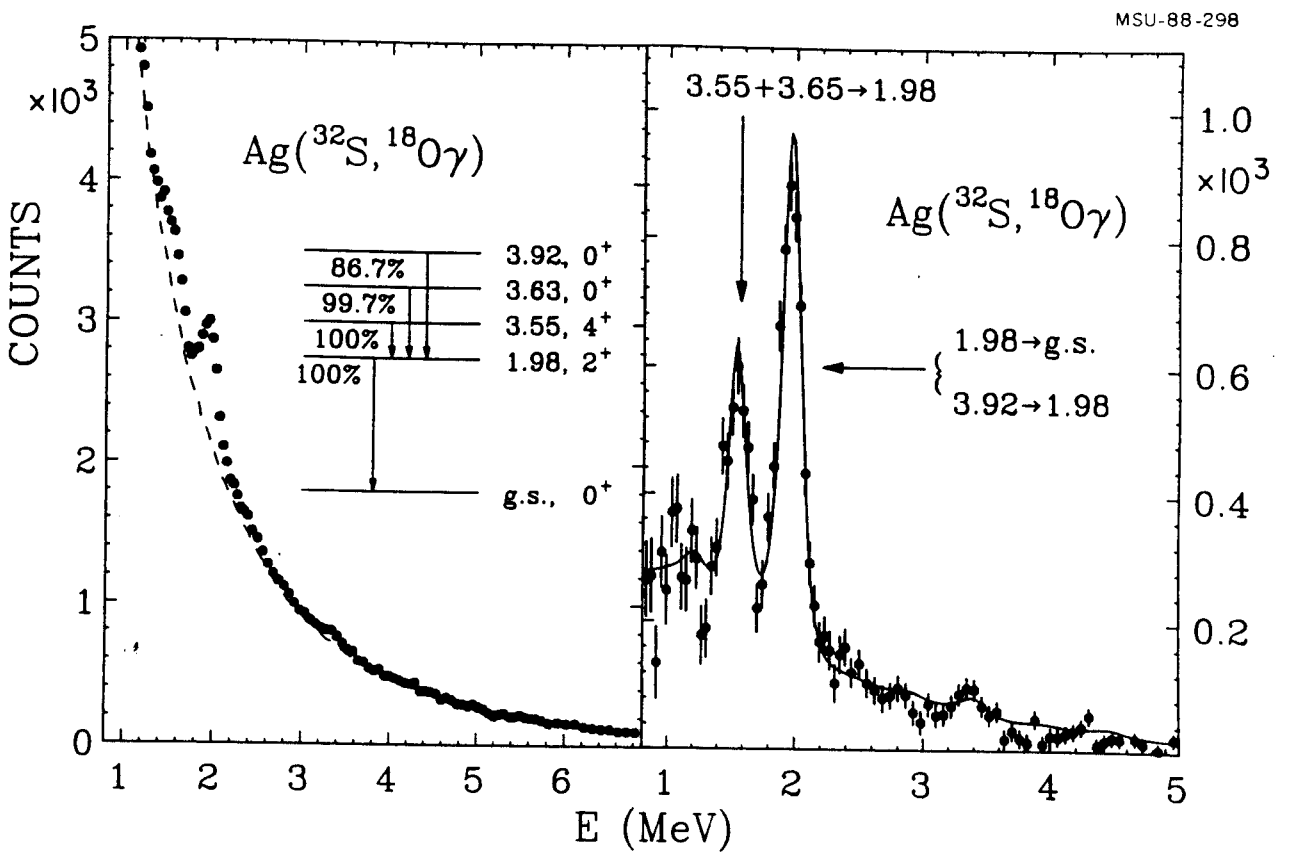

Figure 3.14: γ-ray spectra measured in coincidence with ^{18}O fragments. The left hand panel shows the raw coincidence spectrum with the background indicated by the dashed line. The right hand panel shows the spectrum associated with γ-ray decays of excited ^{12}O fragments. The solid line shows the fit used for the extraction of the γ-ray fractions, F_γ, listed in Table 3.2. The insert shows important transitions and branching ratios used for the fit. Photopeak locations of important transitions are indicated by arrows.

Table 3.2: Extracted fractions, F_γ, of observed fragments which were accompanied by the designated γ-ray transition. Values marked by † are fractions obtained from Germanium detectors corrected for the effects of coincidence summing. For transitions which could not be resolved experimentally, the F_γ-value is given for the summed strength. These transitions and F_γ-values are identified by '$\sum i$', $i = 1, 2, ..., 14$.

Fragment	Transition (J^π, E^*)	F_γ	$\sum i$
^{7}Be	$(\frac{1}{2}^-, 0.429) \rightarrow (\frac{3}{2}^-, 0.0)$	$0.222 \pm 0.017^\dagger$	
^{8}Li	$(1^+, 0.981) \rightarrow (2^+, 0.0)$	$0.204 \pm 0.033^\dagger$	
^{10}Be	$(2^+, 3.37) \rightarrow (0^+, 0.0)$	0.61 ± 0.03	
	$(2^+, 5.96) \rightarrow (2^+, 3.37)$ $(1^-, 5.96) \rightarrow (2^+, 3.37)$	0.16 ± 0.02	$(\sum 1)$
^{10}B	$(1^+, 2.154) \rightarrow (0^+, 1.740)$	$0.082 \pm 0.015^\dagger$	
^{11}B	$(\frac{1}{2}^-, 2.12) \rightarrow (\frac{3}{2}^-, 0.0)$	0.110 ± 0.015	
	$(\frac{5}{2}^-, 4.44) \rightarrow (\frac{3}{2}^-, 0.0)$	0.143 ± 0.016	
	$(\frac{3}{2}^-, 5.02) \rightarrow (\frac{3}{2}^-, 0.0)$	0.059 ± 0.008	
	$(\frac{7}{2}^-, 6.74) \rightarrow (\frac{3}{2}^-, 0.0)$ $(\frac{1}{2}^+, 6.79) \rightarrow (\frac{3}{2}^-, 0.0)$ $(\frac{5}{2}^+, 7.29) \rightarrow (\frac{3}{2}^-, 0.0)$ $(\frac{3}{2}^+, 7.98) \rightarrow (\frac{3}{2}^-, 0.0)$	0.135 ± 0.028	$(\sum 2)$
^{11}C	$(\frac{1}{2}^-, 2.00) \rightarrow (\frac{3}{2}^-, 0.0)$	0.151 ± 0.028	
	$(\frac{5}{2}^-, 4.32) \rightarrow (\frac{3}{2}^-, 0.0)$ $(\frac{1}{2}^+, 6.34) \rightarrow (\frac{1}{2}^-, 2.00)$	0.133 ± 0.016	$(\sum 3)$
	$(\frac{3}{2}^-, 4.80) \rightarrow (\frac{3}{2}^-, 0.0)$ $(\frac{1}{2}^+, 6.34) \rightarrow (\frac{3}{2}^-, 0.0)$ $(\frac{7}{2}^-, 6.48) \rightarrow (\frac{3}{2}^-, 0.0)$ $(\frac{5}{2}^+, 6.90) \rightarrow (\frac{3}{2}^-, 0.0)$ $(\frac{3}{2}^+, 7.50) \rightarrow (\frac{3}{2}^-, 0.0)$	0.062 ± 0.013 0.219 ± 0.032	$(\sum 4)$
^{12}B	$(2^+, 0.953) \rightarrow (1^+, 0.0)$	$0.415 \pm 0.054^\dagger$	$(\sum 5)$
	$(1^-, 2.621) \rightarrow (2^-, 1.674)$	0.43 ± 0.09	$(\sum 5)$
	$(2^-, 1.674) \rightarrow (1^+, 0.0)$ $(1^-, 2.621) \rightarrow (2^+, 0.953)$	0.28 ± 0.04	$(\sum 6)$
^{12}C	$(2^+, 4.44) \rightarrow (0^+, 0.0)$	0.406 ± 0.030	
^{13}C	$(\frac{5}{2}^+, 3.854) \rightarrow (\frac{3}{2}^-, 3.684)$	$0.070 \pm 0.009^\dagger$	
	$(\frac{5}{2}^+, 3.85) \rightarrow (\frac{1}{2}^-, 0.0)$ $(\frac{3}{2}^-, 3.68) \rightarrow (\frac{1}{2}^-, 0.0)$ $(\frac{1}{2}^+, 3.09) \rightarrow (\frac{1}{2}^-, 0.0)$	0.370 ± 0.029	$(\sum 7)$

Table 3.2: (continued)

Fragment	Transition (J^π, E^*)	F_γ	$\sum i$
^{14}C	$(1^-, 6.09) \rightarrow (0^+, 0.0)$ $(3^-, 6.73) \rightarrow (0^+, 0.0)$ $(2^+, 7.01) \rightarrow (0^+, 0.0)$ $(2^-, 7.34) \rightarrow (0^+, 0.0)$	0.481 ± 0.040	$(\sum 8)$
^{14}N	$(0^+, 2.31) \rightarrow (1^+, 0.0)$	0.165 ± 0.030	
	$(1^+, 3.95) \rightarrow (0^+, 2.31)$	0.062 ± 0.040	
	$(0^-, 4.92) \rightarrow (1^+, 0.0)$ $(2^-, 5.11) \rightarrow (1^+, 0.0)$ $(1^-, 5.69) \rightarrow (1^+, 0.0)$ $(3^-, 5.83) \rightarrow (1^+, 0.0)$ $(1^+, 6.20) \rightarrow (1^+, 0.0)$ $(3^+, 6.44) \rightarrow (1^+, 0.0)$ $(2^+, 7.03) \rightarrow (1^+, 0.0)$	0.216 ± 0.021	$(\sum 9)$
^{15}N	$(\frac{5}{2}^+, 5.27) \rightarrow (\frac{1}{2}^-, 0.0)$ $(\frac{1}{2}^+, 5.30) \rightarrow (\frac{1}{2}^-, 0.0)$	0.391 ± 0.042	$(\sum 10)$
	$(\frac{5}{2}^+, 7.16) \rightarrow (\frac{5}{2}^+, 5.27)$ $(\frac{7}{2}^+, 7.57) \rightarrow (\frac{5}{2}^+, 5.27)$	0.165 ± 0.040	$(\sum 11)$
^{16}O	$(3^-, 6.13) \rightarrow (0^+, 0.0)$	0.220 ± 0.025	
	$(2^+, 6.92) \rightarrow (0^+, 0.0)$ $(1^-, 7.12) \rightarrow (0^+, 0.0)$	0.146 ± 0.024	$(\sum 12)$
^{18}O	$(2^+, 1.98) \rightarrow (0^+, 0.0)$ $(2^+, 3.92) \rightarrow (2^+, 1.98)$	0.75 ± 0.07	$(\sum 13)$
	$(4^+, 3.55) \rightarrow (2^+, 1.98)$ $(0^+, 3.63) \rightarrow (2^+, 1.98)$	0.27 ± 0.06	$(\sum 14)$

Chapter 4

Sequential Feeding and the Emission Temperature

The relative populations of states of the emitted fragments provide a measure of the intrinsic excitation energy of the emitting system at freezeout. It is important to know whether this excitation energy is thermally distributed. This can be explored by direct measurements of the relative populations of exited states. However, the observed populations of excited states are influenced by the sequential decay of heavier particle unstable nuclei [Poch 85a, Xu 86, Hahn 87, Fiel 87, Gome 88, Morr 86] and the populations and decays of many of these unbound states are not known experimentally. Since one does not usually know the feeding corrections experimentally, they must be calculated. These calculations [Xu 86, Hahn 87, Fiel 87, Chen 88] usually make the simplifying assumption that the states [Ajze 84, Ajze 85, Ajze 86a, Ajze 86b, Ajze 87, Ajze 88] of primary fragments are populated according to a thermal distribution characterized by a temperature, T. The accuracy of this assumption must be checked by comparing the calculations to the experimental data.

This chapter is organized as follows: In section I, we describe the essence of the sequential feeding calculation and how various fragments and their excited states are included in the calculation. We then present a method for choosing unknown

spectroscopic factors of low lying states, the primary populations of these states, as well as the branching ratios used in the decay calculations. In section II, we compare the results of the calculations to the inclusive elemental yields and to the isotopic yields of the detected fragments. In Section III, the calculated and measured values of the coincident γ-rays are compared. We first compare results for individual transitions. We then discuss a least-χ^2 squares fit method to extract an average emission temperature. Finally, in section IV, the experimental results are summarized and put into perspective with other similar measurements.

I Feeding from Higher Lying States

A Levels and Level Densities

To determine the feeding corrections to the measured γ-ray fractions, we performed sequential decay calculations for an ensemble of nuclei with $3 \leq Z \leq 13$. To facilitate the actual numerical calculations, a lookup table containing excitation energies, spectroscopic factors and different decay channels with corresponding branching ratios for approximately 2600 known levels for isotopes within this charge range [Ajze 84, Ajze 85, Ajze 86a, Ajze 86b, Ajze 87, Ajze 88] was constructed.

Since the spins, isospins and parities of many low-lying particle bound and unbound levels of nuclei with $Z \leq 11$ are known, the information for these lighter nuclei was used in the sequential decay calculations. For known levels with incomplete spectroscopic information, values for the spin, isospin, and parity were chosen randomly according to primary distributions obtained from the non-interacting shell model [Brow 88, Naya 90]. These calculations were repeated with different initialization for the unknown spectroscopic information until the sensitivities of the calculations to these uncertainties could be assessed. The results of the calculations appear to be

insensitive to details in the sampling algorithm, and essentially the same results were obtained in simpler calculations where spins of 0-4 (1/2-9/2) were assumed with equal probability for even A (odd A) nuclei, parities were assumed to be odd or even with equal probability, and the isospins were assumed to be given by the isospin of the ground state. For later reference, this latter distribution of unknown spins is termed a 'flat spin distribution'.

The low-lying discrete levels of heavier nuclei with Z$\geq$12 are not as well known as those of lighter nuclei. To calculate the decay of these heavier nuclei for low excitation energies, $E^* \leq \epsilon_0(A_i, Z_i)$, we used a continuum approximation to the discrete level density [Chen 88], modifying the empirical interpolation formula of ref. [Gilb 65b] to include a spin dependence:

$$\rho(E^*, J_i) = \frac{1}{T_1}\exp[(E^* - E_1)/T_1]\frac{(2J_i+1)\exp[-(J_i+\frac{1}{2})^2/2\sigma_i^2]}{\Sigma(2J_i+1)\exp[-(J_i+\frac{1}{2})^2/2\sigma_i^2]}, \quad \text{for } E^* \leq \epsilon_0, \tag{4.1}$$

where

$$\sigma_i^2 = 0.0888[a_i(\epsilon_0 - E_0)]^{\frac{1}{2}}A_i^{\frac{2}{3}}, \tag{4.2}$$

and $a_i = A_i/8$; J_i, A_i, and Z_i are the spin, mass and charge numbers of the fragment, and the values for $\epsilon_0 = \epsilon_0(A_i, Z_i), T_1 = T_1(A_i, Z_i)$, and $E_1 = E_1(A_i, Z_i)$ were taken from Gilbert and Cameron [Gilb 65b]. For $Z \geq 12$, $E_0 = E_0(A_i, Z_i)$ is determined by matching the level density at ϵ_0 provided by Eq. (4.1) to that provided by Eq. (4.3) given below. [Note: In Eq. (4.1) and also in Eq. (4.7) below, we match the density of levels rather than the density of states because the spins of many of the discrete levels are not known.]

For higher excitation energies in the continuum for all nuclei, we assumed the level density of the form

$$\rho(E^*, J_i) = \rho_1(E^*)\rho_2(J_i, \sigma_i), \tag{4.3}$$

where

$$\rho_1(E^*) = \frac{\exp\{2[a_i(E^* - E_0)]^{1/2}\}}{12\sqrt{2}[a_i(E^* - E_0)^5]^{1/4}\sigma_i}, \tag{4.4}$$

$$\rho_2(J_i, \sigma_i) = \frac{(2J_i + 1)\exp[-(J_i + \frac{1}{2})^2/2\sigma_i^2]}{2\sigma_i^2}, \tag{4.5}$$

$$\sigma_i^2 = 0.0888[a_i(E^* - E_0))]^{1/2}A_i^{2/3}. \tag{4.6}$$

For $Z_i \geq 12$, $E_0 = E_0(A_i, Z_i)$ is determined by matching the level density provided by Eq. (4.1) at ϵ_0 to that provided by Eq. (4.3). At smaller values of Z_i, E_0 is adjusted for each fragment to match the integral of the continuum level density to the total number of tabulated levels according to the equation:

$$\int_{E_0}^{\epsilon_0} dE^* \int dJ\ \rho(E^*, J) = \int_0^{\epsilon_0} dE^* \sum_i \delta(E - E^*), \tag{4.7}$$

where ϵ_0, for these lighter fragments, was chosen to be the maximum excitation energy up to which the information concerning the number and locations of discrete states appears to be complete. An example [Chen 88a] of determining ϵ_0 for the isotope ^{20}Ne is given in figure 4.1.

To reduce the computer memory requirements, the populations of continuum states were stored at discrete excitation energy intervals of 1 MeV for E^* $\leq$15 MeV, 2 MeV for 15$\leq$ E^* $\leq$30 MeV, and 3 MeV for E^* $\geq$30 MeV. The results of these calculations do not appear to be sensitive to these binning widths. In this way, the total number of discrete energy bins including the discrete states came to be about 38,000. Parities of continuum states were chosen to be positive and negative with equal probability. To save both space and time, the isospins of the continuum states were taken to be equal to the isospin of the ground state of the same nucleus.

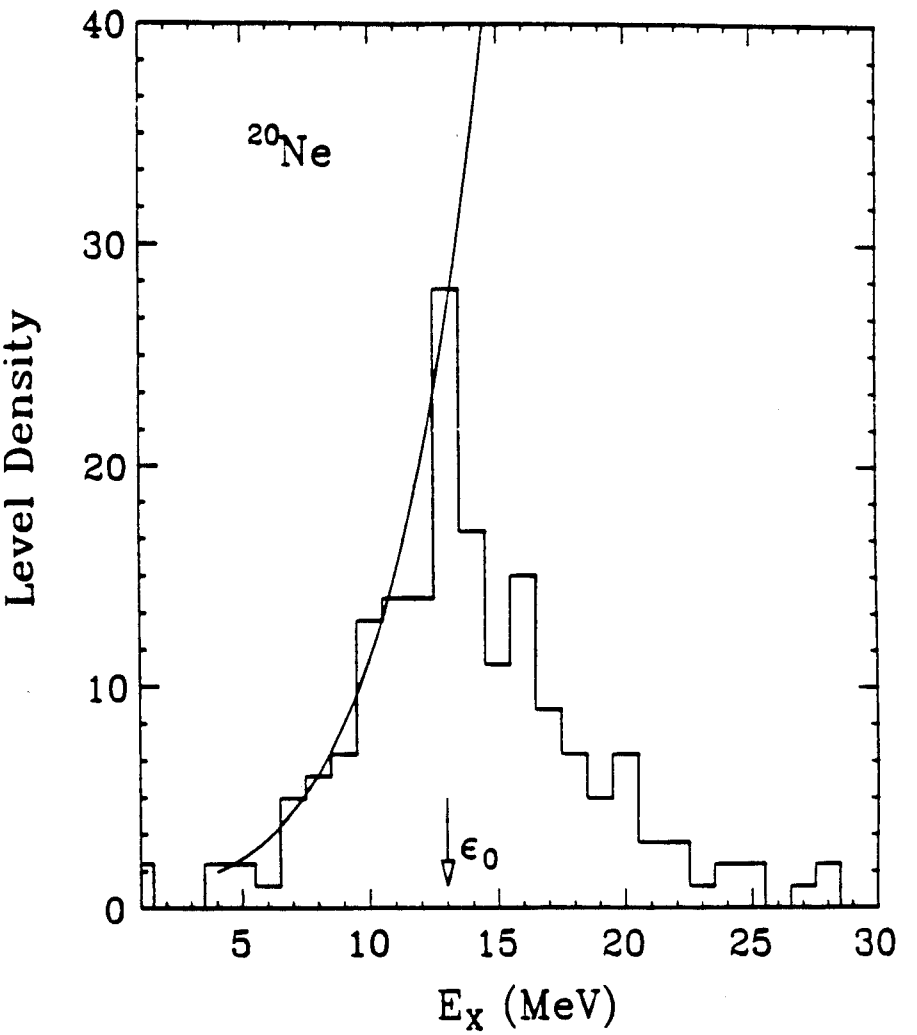

Figure 4.1: The level density of ^{20}Ne as a function of excitation energy [Chen 88a]. The histogram gives the number of known levels whereas the solid curve shows results of level density predicted by eq (4.3).

B Primary Populations

For the ith level of spin J_i we assumed an initial population P_i given by

$$P_i \propto P_0(A_i, Z_i)(2J_i + 1)\exp(-E^*/T), \tag{4.8}$$

where $P_0(A_i, Z_i)$ denotes the population per spin degree of freedom of the ground state of a fragment and T is the emission temperature which characterizes the thermal population of states of a given isotope. (This temperature is associated with the intrinsic excitation of the fragmenting system at breakup and is, in general, different from the "kinetic" temperature which may be extracted from the kinetic energy spectra of the emitted fragments.) The initial populations of states of a given fragment were assumed to be thermal up to excitation energy of $E^*_{\rm cutoff} = \mu A$. This cutoff was introduced to explore the sensitivity of the calculations to highly excited and short-lived nuclei, some of which may be too short-lived to survive the evolution from breakup to freezeout. Calculations were performed for cutoff values of $\mu = 3$ and 5 MeV corresponding to mean lifetime of the continuum states of 230 fm/c and 125 fm/c, respectively [Stok 77]. The calculations were qualitatively similar for the two cutoff energies.

For simplicity, we parameterized the initial relative populations, $P_0(A_i, Z_i)$ by

$$P_0(A, Z) \propto \exp(-fV_C/T + Q/T), \tag{4.9}$$

where V_C is the Coulomb barrier for emission from a parent nucleus of mass and atomic numbers A_p and Z_p and Q is the ground state Q-value

$$V_C = Z_i(Z_p - Z_i)e^2/\{r_0[A_i^{1/3} + (A_p - A_i)^{1/3}]\} \tag{4.10}$$

and

$$Q = [B(A_p - A_i, Z_p - Z_i) + B_i] - B(A_p, Z_p). \tag{4.11}$$

We used a radius parameter of r_0=1.2 fm, A_p=122, Z_p=54 (these values were assumed for compound systems due to incomplete fusion). The binding energies, $B(A,Z)$, of heavy nuclei were calculated from the Weizsäcker mass formula [Marm 69].

$$B(A,Z) = C_0A - C_1A^{2/3} - C_2\frac{Z^2}{A^{1/3}} - C_3\frac{(A-2Z)^2}{A}, \tag{4.12}$$

with C_0=14.1 MeV, C_1=13.0 MeV, C_2=0.595 MeV, and C_3=19.0 MeV. For the emitted light fragments we used the measured binding energies, B_i, of the respective ground states [Waps 85]. At each temperature T, the parameter, f in Eq. (4.9) was adjusted to provide optimal agreement between the calculated final fragment distributions (obtained after the decay of particle unstable states) and the measured fragment distributions. This constraint reduced the possibility of inaccuracies in the predicted primary elemental distributions at high temperatures [Hahn 87, Fiel 87]. The values of f obtained for different T are discussed in the last section of this chapter.

C The Decay Branching Ratios

The branching ratio for a state to decay by different channels has to be known for decay calculations. If known, tabulated branching ratios were used to describe the decay of particle unstable states. If unknown, the branching ratios were calculated from the Hauser-Feshbach formula, with additional constraints on isospins and parities. The branching ratio for a channel c in the original Hauser-Feshbach formula is [Haus 52],

$$\frac{\Gamma_c}{\Gamma} = \frac{G_c}{\sum_i G_i} \tag{4.13}$$

where

$$G_c = \sum_{Z=|S-j|}^{Z=|S+j|} \sum_{l=|J-Z|}^{l=|J+Z|} T_l(E). \tag{4.14}$$

Here, J and j are the spins of the parent and daughter nuclei, Z is the channel spin, S and l are the intrinsic spin and orbital angular momentum of the emitted particle,

and $T_l(E)$ is the transmission coefficient for the lth partial wave. By incorporating parity and isospin conservations, we can write G_c as

$$G_c = < T_{I,D}T_{I,F}T(3)_{I,D}T(3)_{I,F}|T_{I,P}T(3)_{I,P} >^2 \times \sum_{Z=|S-j|}^{Z=|S+j|} \sum_{l=|J-Z|}^{l=|J+Z|} \{[1+\pi_P\pi_D\pi_F(-1)^l]/2\}\ T_l(E). \quad (4.15)$$

The factor, $[1+\pi_P\pi_D\pi_F(-1)^l]/2$ enforces parity conservation and depends on the parities $\pi = \pm 1$ of the emitted fragment and the parent and daughter nuclei. The Clebsch-Gordon coefficient involving $T_{I,P}, T_{I,D}$, and $T_{I,F}$, the isospins of the parent nucleus, daughter nucleus, and emitted particle, likewise allows one to take isospin conservation into account.

For decays from states for which the kinetic energy of the emitted particle is less than 20 MeV and $l \leq 20$, the transmission coefficients were interpolated from a set of calculated optical model transmission coefficients [Brow 88, Naya 90]. For decays from continuum states when the kinetic energy of the emitted particle exceeds 20 MeV, the transmission coefficients were approximated by the sharp cutoff approximation;

$$\begin{aligned} T_l(E) &= 1, \text{ for } l \leq l_0 \\ &= 0, \text{ otherwise,} \end{aligned} \quad (4.16)$$

with

$$l_0 = (2\pi/h)r_0[A_i^{1/3} + (A_p - A_i)^{1/3}]\sqrt{2\mu(E - V_C)}, \quad (4.17)$$

where μ is the reduced mass, and h is Plank's constant.

The calculation was restricted to the particle decays via n, 2n, p, 2p, d, t, ^{3}He, and α channels. The γ-ray decay of particle stable states was taken into account in the calculation of the final particle stable yields.

II Elemental and Isotopic Yields

The measured fragment elemental and isotopic distributions and the calculated distributions for $\mu = 3$ MeV are compared in Figs. 4.2 and 4.3. The solid points correspond to the fragment yields summed over all measured energies and angles. The dashed lines in Fig. 4.2 show the calculated elemental distributions of primary fragments (summation of all particle stable states for all isotopes of a given element) assumed for the temperatures T = 2, 4, and 8 MeV; the parameters, f, are indicated in the figure. The solid lines show the calculated final elemental distributions obtained after the statistical decay of particle unbound fragments. The parameter, f, was adjusted at each temperature so that the calculated final elemental distribution closely follows the trend of the measured elemental distribution. (After choosing appropriate but different values for f, very similar results were obtained for $\mu = 5$ MeV.) Since these parameters, f, have been adjusted to reproduce the elemental yields measured in this experiment, one must be very cautious in applying the results of these calculations to other reactions.

The dashed, solid and dotted histograms in Fig. 4.3 represent final isotopic distributions obtained for the three temperatures, T = 2, 4, and 8 MeV, using the parameters, f, given in Fig. 4.2. In general, the isotopic distributions are fairly well reproduced. For T=2 MeV, however, the calculated isotopic distributions are somewhat narrower than the measured ones and for T=8 MeV, the calculated distributions are somewhat broader than the measured ones. The agreement is slightly better for calculations in the neighborhood of T=4 MeV.

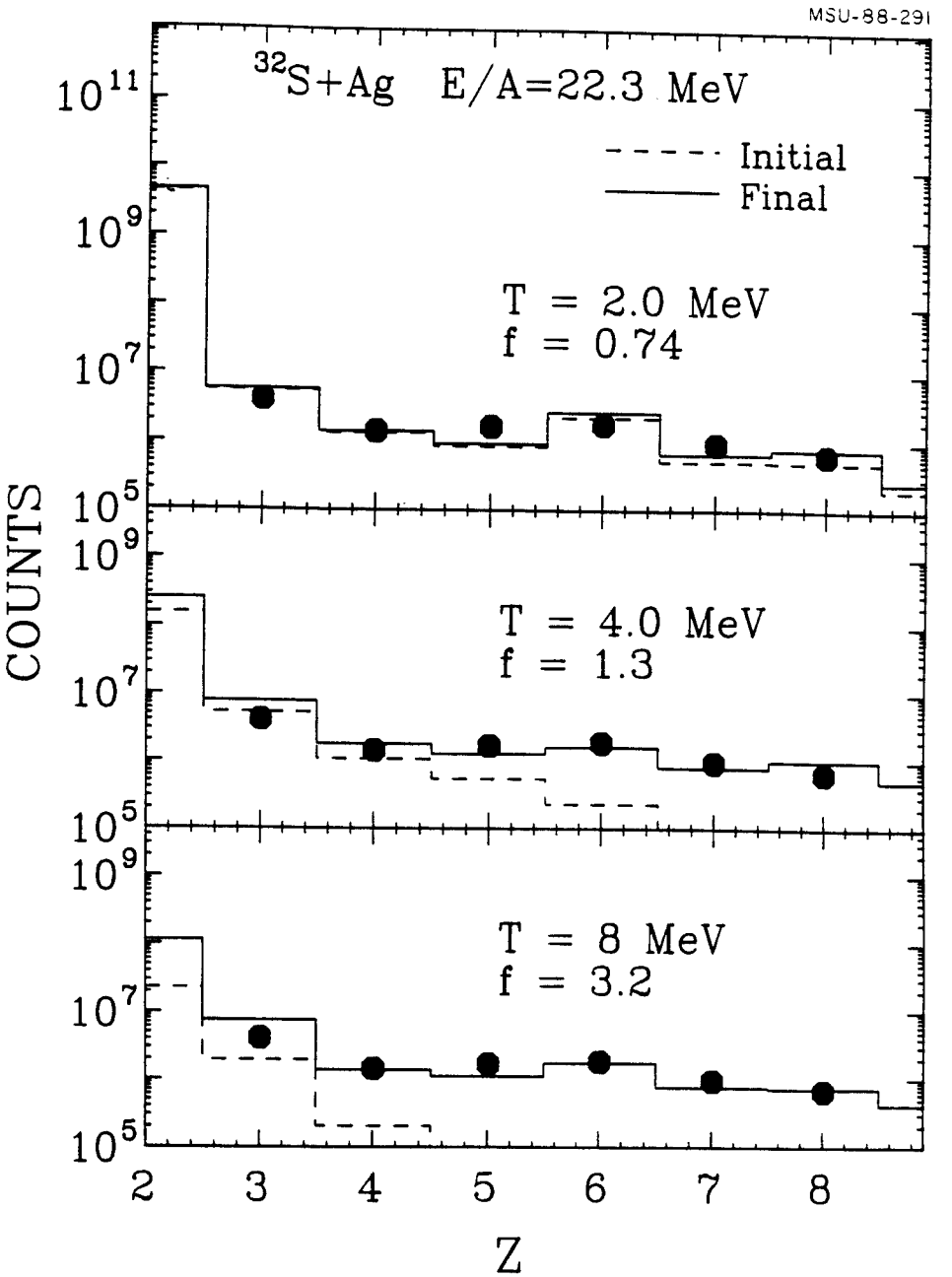

Figure 4.2: Element yields summed over all measured energies and angles. The dashed and solid histograms show the primary and final fragment particle stable yields for the feeding calculations described in the text. The three panels show the results for T = 2, 4, and 8 MeV, respectively. The adjusted values for the parameter, f, in Eq. (4.9) are given in the figure.

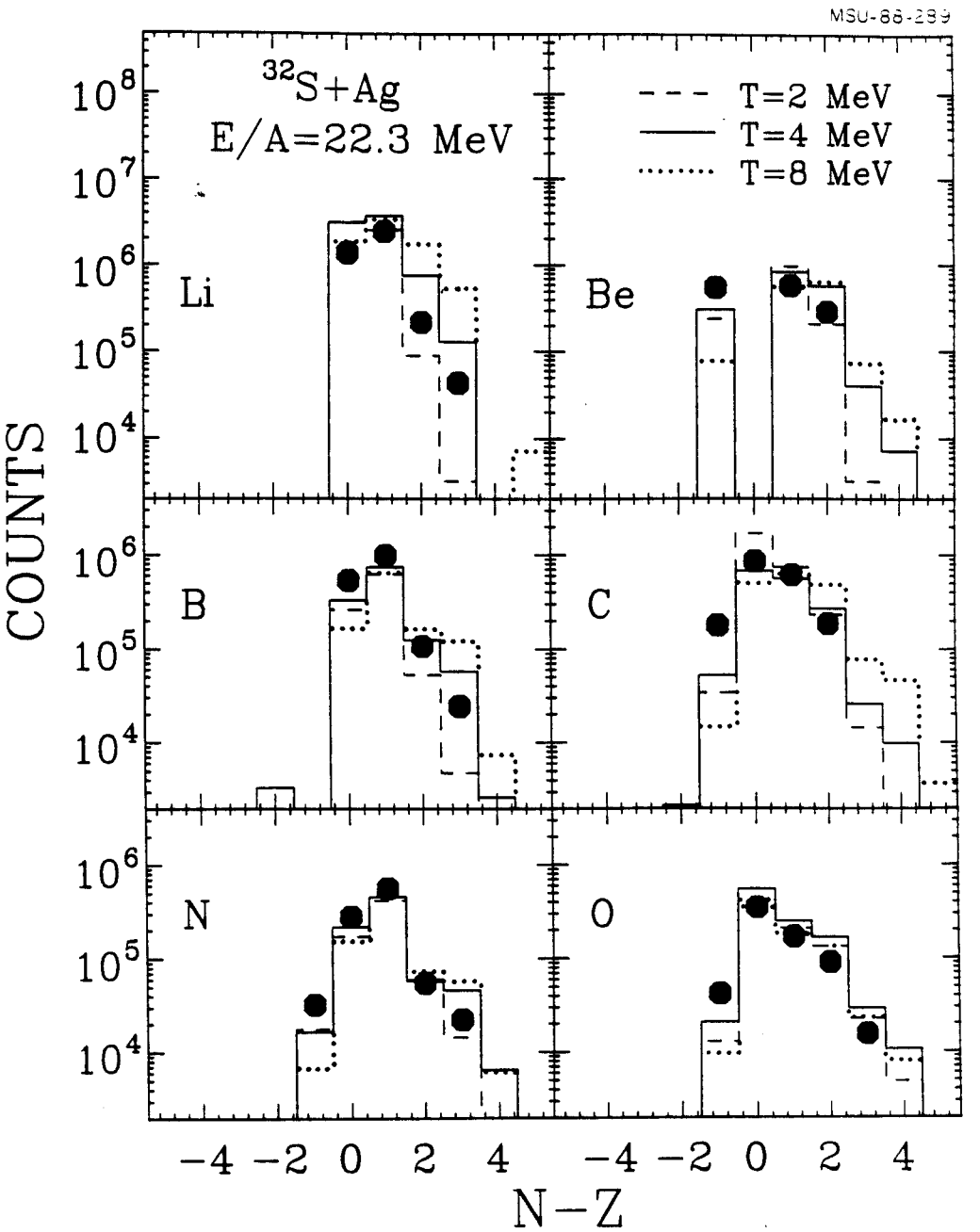

Figure 4.3: Isotope yields summed over all measured energies and angles. The dashed, solid, and dotted histograms show the final fragment distributions for the feeding calculations at T = 2, 4, and 8 MeV, respectively.

III Mean Emission Temperatures

Starting from the initial distribution, Eq.(4.9), we have calculated the fraction, F_γ , of γ-rays emitted in coincidence with a given fragment as a function of the emission temperature, T, which characterizes the ensemble of emitted fragments. The results for an excitation energy cutoff of $\mu = 3$ MeV are presented in Figs. 4.4-4.6 for the transitions given in individual panels. The range of calculated fractions, F_γ , for individual γ-rays are bound by the solid curves in Figures 4.4 and 4.5 for transitions measured in this experiment. The range of calculated values for the relative γ-ray intensities, $R_\gamma = F_{\gamma 1}/F_{\gamma 2}$, are shown by the solid lines in Fig. 4.6 for those fragments for which more than one γ-ray transition were measured. The corresponding calculations for an excitation energy cutoff of $\mu = 5$ MeV are qualitatively very similar and in some cases, indistinguishable.

The spread in calculated values of F_γ's and R_γ's shown in Figs. 4.4-4.6 reflects primarily uncertainties in the spins, isospins and parities of many low lying particle unstable levels which directly feed the particle stable states of interest. The range of calculated values was determined by repeating calculations with different spectroscopic assumptions until the sensitivity of the calculation to those uncertainties could be assessed.

In order to illustrate the modifications due to feeding from particle unbound states, the dashed lines in Figures 4.4-4.6 show the results of calculations which include feeding from higher lying particle stable states, but not from particle unstable states. In all cases, both F_γ's and R_γ's are predicted to be sensitive to feeding from particle unbound states for temperatures higher than approximately 2-3 MeV. (For example, for ^{11}C with μ= 3 MeV and T = 3 MeV, 55% of the yields of the 4.32 MeV excited state and 59% of the ground state yields are predicted to proceed through the sequential

decay of heavier particle unbound nuclei). The ratio R_γ has the advantage of being independent of the total feeding to the ground states of the observed fragments. Since the ground state is fed more strongly than the excited states, the ratios R_γ are slightly less sensitive to the uncertainties in the sequential decay corrections than the fractions F_γ shown in Figures 4.4 and 4.5.

The shaded horizontal bands in Figs. 4.4, 4.5 and 4.6 correspond to the experimental values of F_γ and R_γ, respectively, that are obtained when data for different intermediate mass fragment kinetic energies and scattering angles are combined. In general, the experimental data are larger than the calculations for emission temperatures less than 2 MeV. For most transitions at temperatures of about 3 to 4 MeV, the range of calculated values lie within 20% of the range of experimental values permitted by our estimate of the experimental uncertainties. However, at these and higher temperatures, the calculations are not very sensitive to the temperature, making it impossible to extract reliable upper limits based on individual cases. Some of the transitions, e.g., the fractions F_γ for ^{8}Li$(0.98 \rightarrow g.s.)$, ^{15}N$(5.27 + 5.30 \rightarrow g.s.)$, ^{16}O$(6.13 \rightarrow g.s.)$, and the ratio R_γ $(=F_{\gamma 1}/F_{\gamma 2})$ for ^{11}C$(6.34 - 7.50 \rightarrow g.s.\ /4.32 \rightarrow g.s.)$, deviate significantly from the overall trends, with the ranges of calculated and measured values in disagreement by more than 20% at temperatures of 3-4 MeV. Such discrepancies could be due to inaccuracies in the spectroscopic information that influence strongly the calculations for these nuclei, or could be indicative of non-thermal excited state populations either in these nuclei or in heavier nuclei which feed these transitions by sequential decay processes.

To provide a more quantitative comparison between calculations and experimental data, we have performed a least squares analysis. For each initial temperature in the

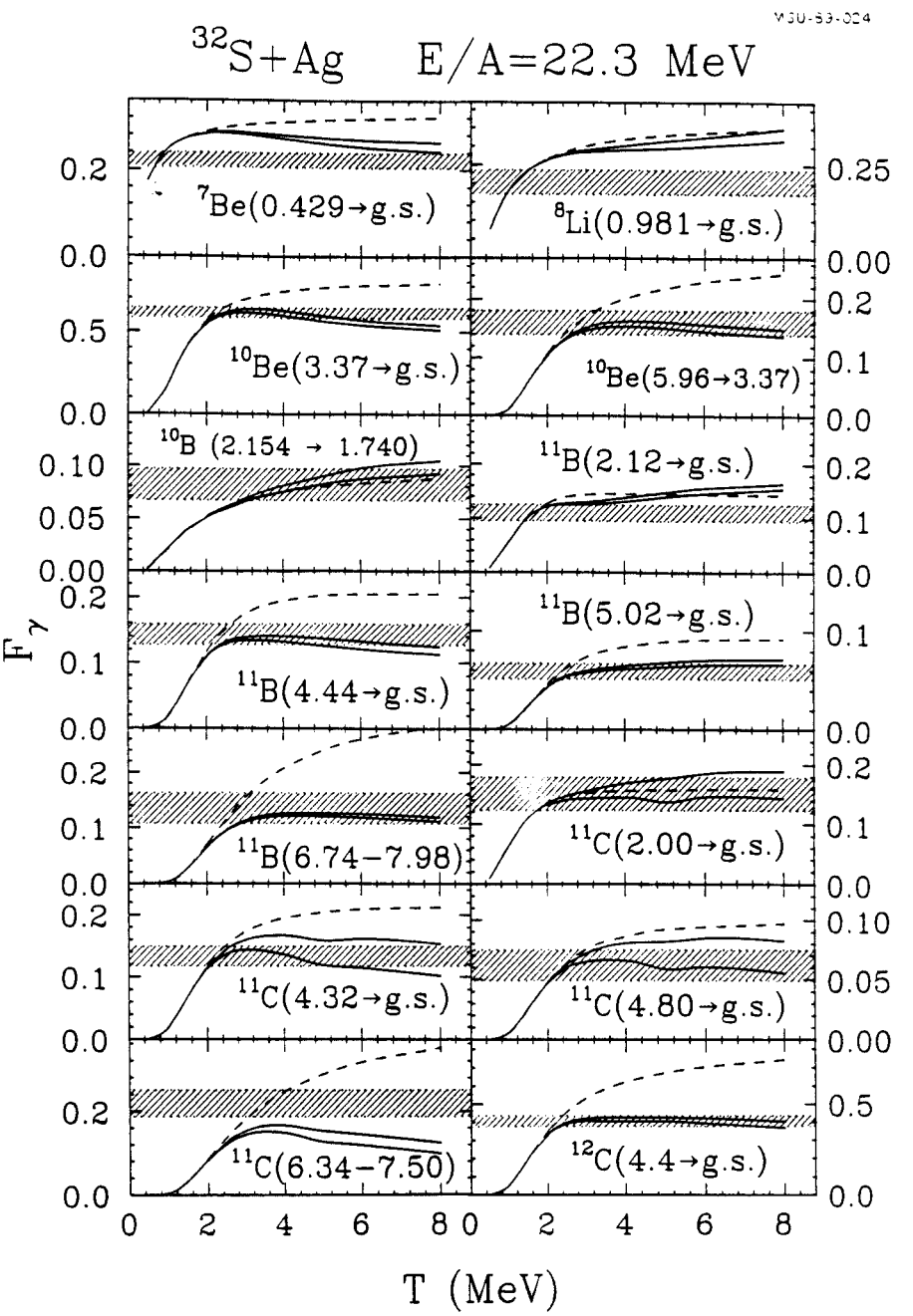

Figure 4.4: The solid curves indicate the range of calculated fractions, F_γ, for fragments decaying through the designated q-ray transition as a function of the emission temperature, T, which characterizes the ensemble of emitted fragments. (The values for F_γ on the curves are one theoretical standard deviation from the average value of F_γ provided by the calculations.) The dashed lines show the fractions calculated when feeding from particle stable states is included, but not feeding from particle unbound states. The horizontal bands indicate the measured values.

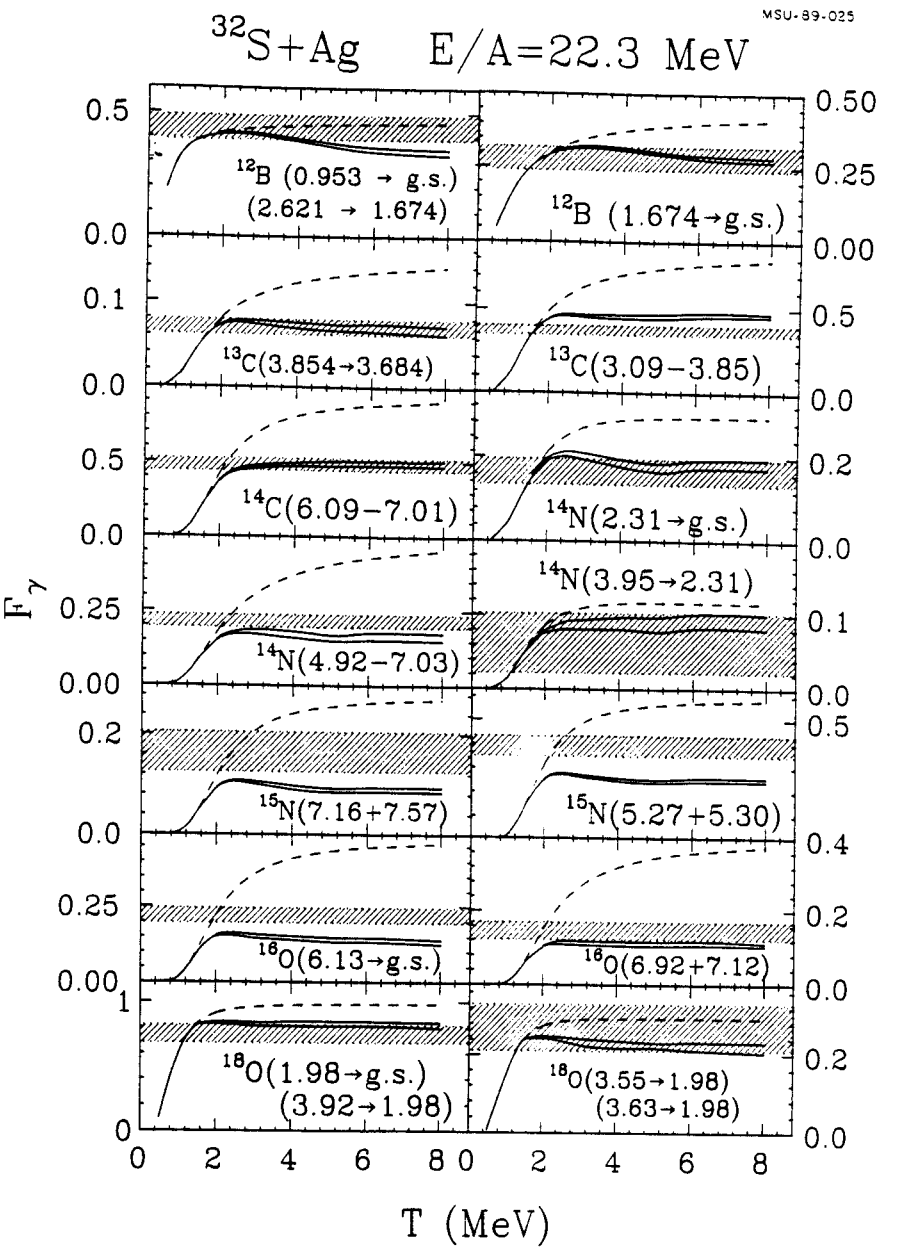

Figure 4.5: The solid curves indicate the range of calculated fractions, F_γ, for fragments decaying through the designated γ-ray transition as a function of the emission temperature, T, which characterizes the ensemble of emitted fragments. (The values for F_γ on the curves are one theoretical standard deviation from the average value of F_γ provided by the calculations.) The dashed lines show the fractions calculated when feeding from particle stable states is included, but not feeding from particle unbound states. The horizontal bands indicate the measured values.

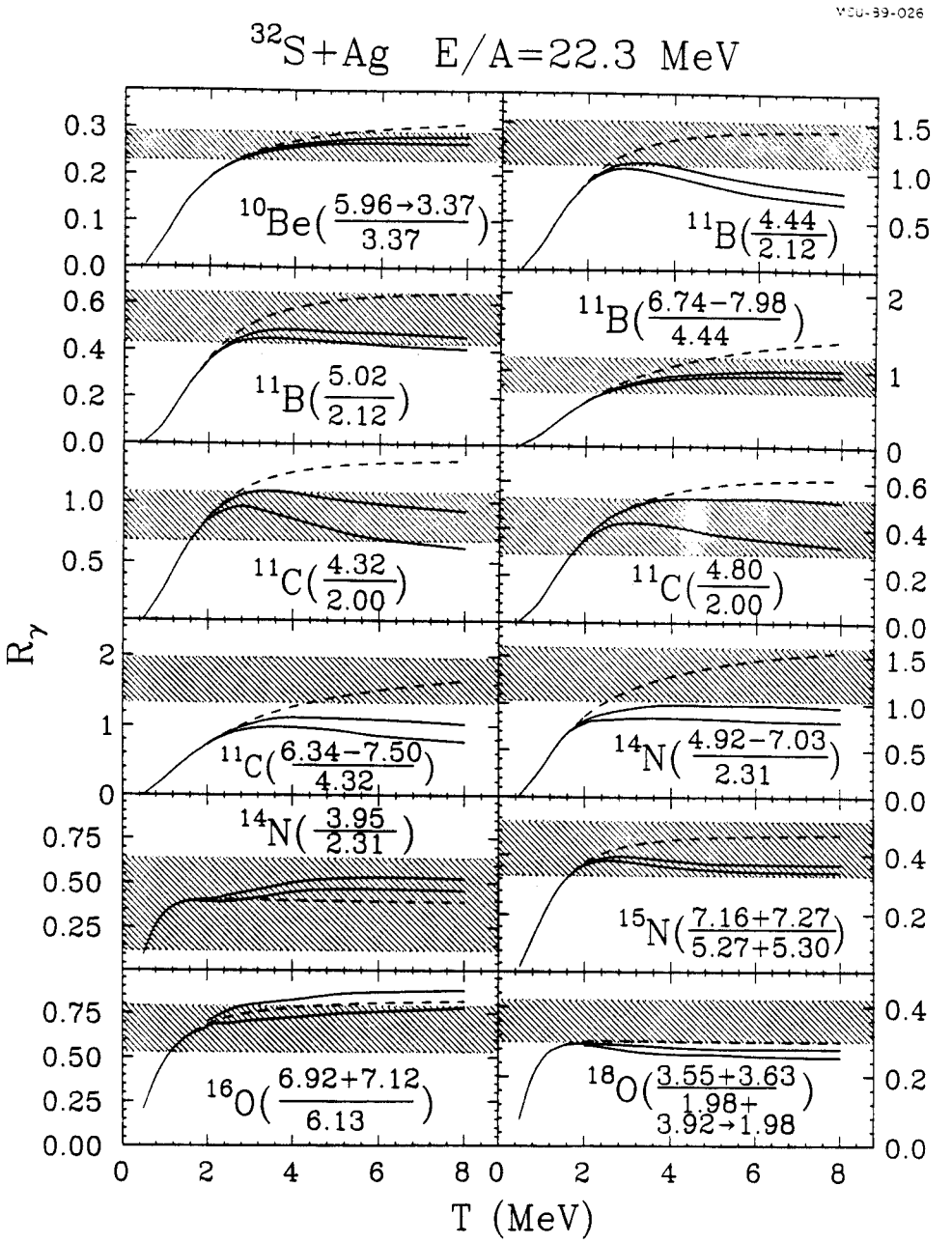

Figure 4.6: The solid curves indicate the range of calculated fractions, $R_\gamma = F_{\gamma 1}/F_{\gamma 2}$, of designated γ-ray transition probabilities as a function of the emission temperature, T, which characterizes the ensemble of emitted fragments. (The values for R_γ on the curves are one theoretical standard deviation from the average value of F_γ provided by the calculations.) The dashed lines show the ratios calculated when feeding from particle stable states is included, but not feeding from particle unbound states. The horizontal bands indicate the measured values.

calculation, we compute the function,

$$\chi^2_\nu = \frac{1}{\nu}\sum_{i=1}^{\nu}\frac{(y_{\mathrm{exp},i} - y_{\mathrm{cal},i})^2}{\sigma_i^2}. \tag{4.18}$$

where $y_{\mathrm{exp},i}$ and $y_{\mathrm{cal},i}$ are the i-th experimental and calculated values of the γ-ray fraction, F_γ, or the ratio of γ-ray fractions,R_γ; ν is the number of independent data points (ν=28 for F_γ's, and ν =12 for R_γ's); and σ_i, given by $\sigma_i^2 = \sigma_{\mathrm{exp},i}^2 + \sigma_{\mathrm{cal},i}^2$, is an uncertainty associated with the comparison for the i-th measured quantity. In the latter expression, $\sigma_{\mathrm{exp},i}$ is the experimental uncertainty; $\sigma_{\mathrm{cal},i}$ reflects the range of calculated values corresponding to the different assumptions for the spins, isospins and parities of low-lying states where this information is incomplete. $\sigma_{\mathrm{cal},i}$ was computed as the variance of the calculations indicated in Figs. 4.4-4.6.

Values for χ^2_ν calculated for the γ-ray fractions in Figures 4.4 and 4.5 are shown on the right side of Fig. 4.7. Values for χ^2_ν calculated for the ratios of γ-ray fractions given in Fig. 4.6 are shown on the left side of Fig. 4.7. The solid and open circles depict the values of χ^2_ν obtained for excitation energy cutoffs of μ = 3 and 5 MeV, respectively, when the unknown spectroscopic information for low-lying discrete states was chosen according to the noninteracting shell model. The open squares depict the values of χ^2_ν obtained for an excitation energy cutoff of μ = 3 MeV when the unknown spectroscopic information for low-lying discrete states was chosen according to the simpler 'flat spin distribution' described in section V. For all calculations, minimum values for χ^2_ν are observed in the region of T = 3-4 MeV for both sets of measurements. The comparison involving ratios of γ-ray fractions may be slightly more accurate because such ratios are insensitive to uncertainties in the ground state yields, for which much more sequential feeding contributions are observed in these and other similar calculations [Xu 86, Hahn 87, Fiel 87, Chen 88]. This argument is supported by the reduced values of χ^2_ν indicated in the figure. For the comparison involving ratios of γ-ray fractions, the minimum value of χ^2_ν approaches unity, cor-

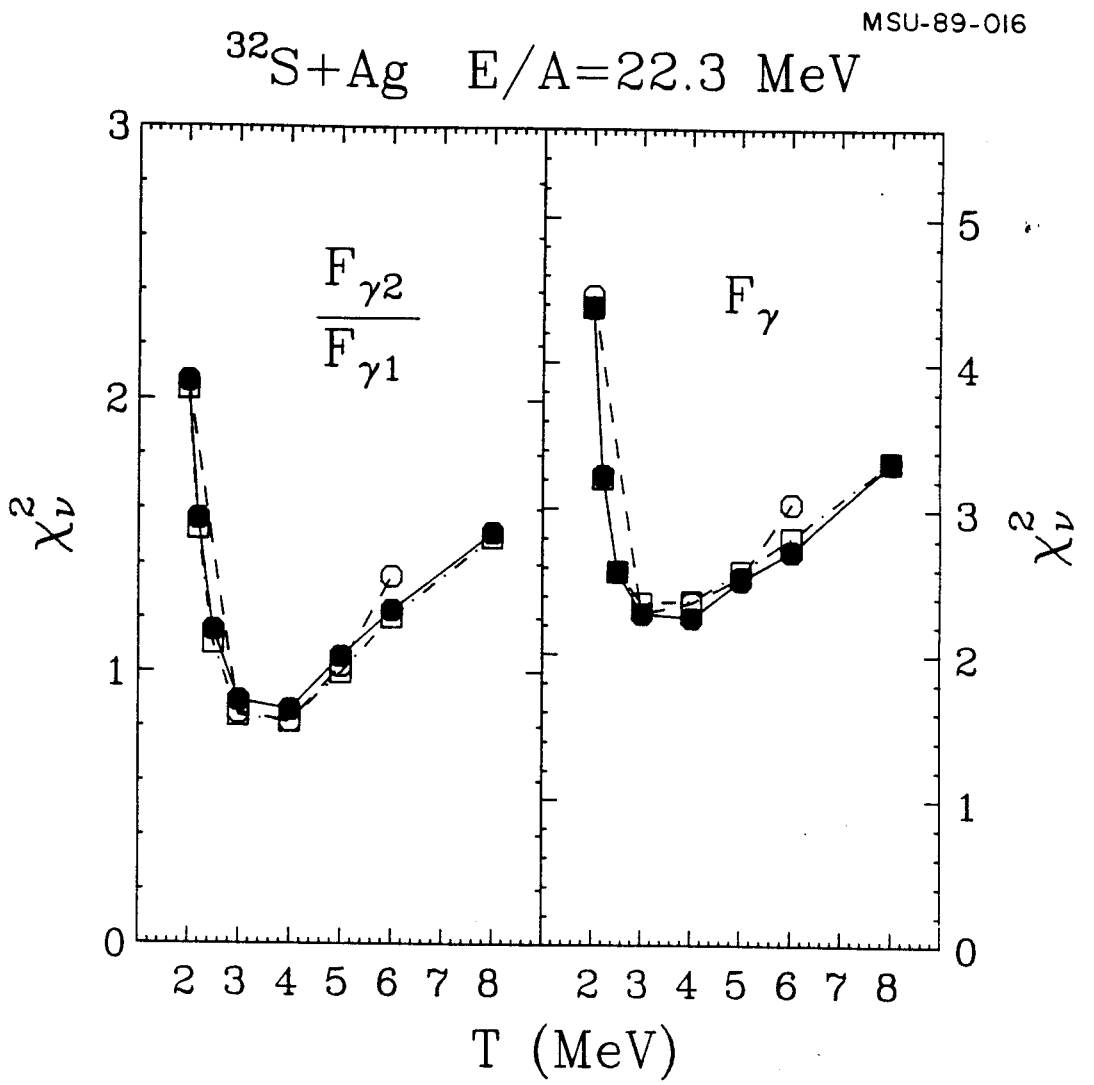

Figure 4.7: Left side: Results of the least squares analysis of the ratios of γ-ray fractions, R_γ. Right side: Results of the least squares analysis of the γ-ray fractions, F_γ. The solid and open circles depict the values for χ^2_ν obtained for excitation energy cutoffs of $\mu = 3$ and 5 MeV, respectively, when the unknown spectroscopic information for low-lying discrete states was chosen according to the noninteracting shell model. The open squares depict the values for χ^2_ν obtained for an excitation energy cutoff of $\mu = 3$ MeV when the unknown spectroscopic information for low-lying discrete states was chosen according to the simpler 'flat spin distribution' described in section V. The lines connecting respective points are used to guide eyes.

responding to statistical agreement between calculations and measurements. χ^2_ν is larger for comparisons involving γ-ray fractions alone. This larger value of χ^2_ν may be partly attributed to a small number of transitions where the disagreements between measured and calculated values of F_γ are especially large. Some of these transitions (e.g. in ^{8}Li, ^{15}N, and ^{16}O fragments) were identified previously. Both calculations appear to exclude temperatures much larger than 5 MeV or smaller than 3 MeV. The upper limit is, however, much less certain because the feeding corrections are larger and the measurements less sensitive to temperature at higher excitation energies.

IV Summary and Conclusions

We have investigated the emission of intermediate mass fragments for ^{32}S induced reactions on ^{nat}Ag at E/A=22.3 MeV. Inclusive energy spectra and angular distributions were measured for isotopically resolved fragments with Z=3-8. The energy spectra exhibit broad maxima at energies close to the exit channel Coulomb barriers and nearly exponential tails at higher energies. The slopes of the energy spectra become steeper at larger emission angles. The angular distributions of the emitted fragments are forward peaked in the center-of-mass frame indicating significant emission prior to the attainment of statistical equilibrium of the composite system.

Information about the populations of particle stable states of the emitted fragments was obtained by measuring their γ-ray decays with the Spin Spectrometer. A total of 28 independent γ-ray transition intensities were measured for fragments of mass A=7-18.

The effects of feeding from particle unbound states of fragments with $Z \leq 13$ were investigated by calculations in which the initial populations of particle bound and unbound states, both discrete and continuum, were assumed to be thermally

populated. The decay of these fragments was calculated by using experimentally known γ-ray branching ratios and particle decay branching rations. When branching ratios for the decays of particle unstable states were unknown, they were calculated from the statistical model. The primary fragment distributions were adjusted such that, after the decays of particle unstable states, the calculated final fragment yields were consistent with the measured yields. Unknown spins and parities of low-lying discrete particle unbound states were chosen randomly according to a distribution defined by the non-interacting shell model. Repeating the calculations with different choices for this spectroscopic information gave a range of calculated γ-ray fractions and ratios of γ-ray fractions. This provided a measure of the theoretical uncertainty associated with the lack of spectroscopic information. It remains an open question, however, whether a more accurate description of the isospin and parity dependence of the level densities could result in significantly different predictions for specific transitions.

No significant dependence of the measured γ-ray intensities upon the fragment energy or emission angle was observed. When the experimental data for all angles and energies were combined, a large number of γ-ray intensities could be rather well described by these calculations for emission temperatures ranging from 3-4 MeV. This result is significant since it allows the description of a large number of measured values in terms of a single parameter. This, ultimately, must be the experimental justification of statistical treatments. This result therefore adds support for statistical treatments of the fragmentation process and for a thermal description of the primary distribution. A few of the measured γ-ray intensities strongly disagree with the calculated γ-ray intensities at temperatures of about 3-4 MeV. Because all of the measured γ-ray transitions are strongly fed at high excitation energies, however, the present level of agreement between calculations and measurements may reflect more the accuracy of

the sequential decay calculations than the accuracy of the thermal description of the primary distribution.

Fig. 4.8 shows the emission temperature extracted in this dissertation (solid diamond), along with the emission temperature extracted by Nayak *et al* [Naya 90] from the relative populations of a large number of particle unstable states in the ^{14}N + ^{nat}Ag reactions at E/A=35 MeV (solid square), the emission temperatures extracted from pairs of widely separated particle unstable states of ^{5}Li (solid circles) and ^{6}Li (closed crosses) fragments obtained from ^{14}N + ^{197}AU reactions at E/A=35 MeV, ^{40}Ar + ^{nat}Ag reactions at E/A=60 MeV, and ^{16}O + ^{nat}Ag reactions at E/A=94 MeV [Chen 88a]. These measurements suggest a gradual increase in the emission temperature with the incident energy per nucleon. More detailed coincident measurements reveal little sensitivity to gates placed on the linear momentum transferred to the target residue [Chen 88a] or to the associated multiplicity of coincident charged particles detected at forward angles [Sain 88]. Similar temperatures have been obtained from the analyses of the kinetic energy spectrum of light particles emitted in ^{40}Ar + U collisions at E/A=27 MeV [Jacq 84] or deduced from the neutron multiplicities observed in ^{40}Ar + ^{232}Th collisions at various incident energies [Jian 89]. In this latter case, a level density parameter of a=A/8 MeV $^{-1}$ was assumed.

Such a gradual dependence of the emission temperature on incident energy could arise from expansion of the emitting system [Bond 85, Gros 86, Frie 88, Snep 88] and suggests that thermal freezeout occurs at a nearly constant temperature, rather than at constant density as is frequently assumed. A number of dynamical calculations of expanding nuclear systems arrived at qualitatively similar conclusions [Schl 87, Boal 89, Snep 88]. Surprisingly, some of these dynamical calculations predict that all fragments, including a target-like residue, are emitted at a constant temperature [Boal 89, Schl 87].

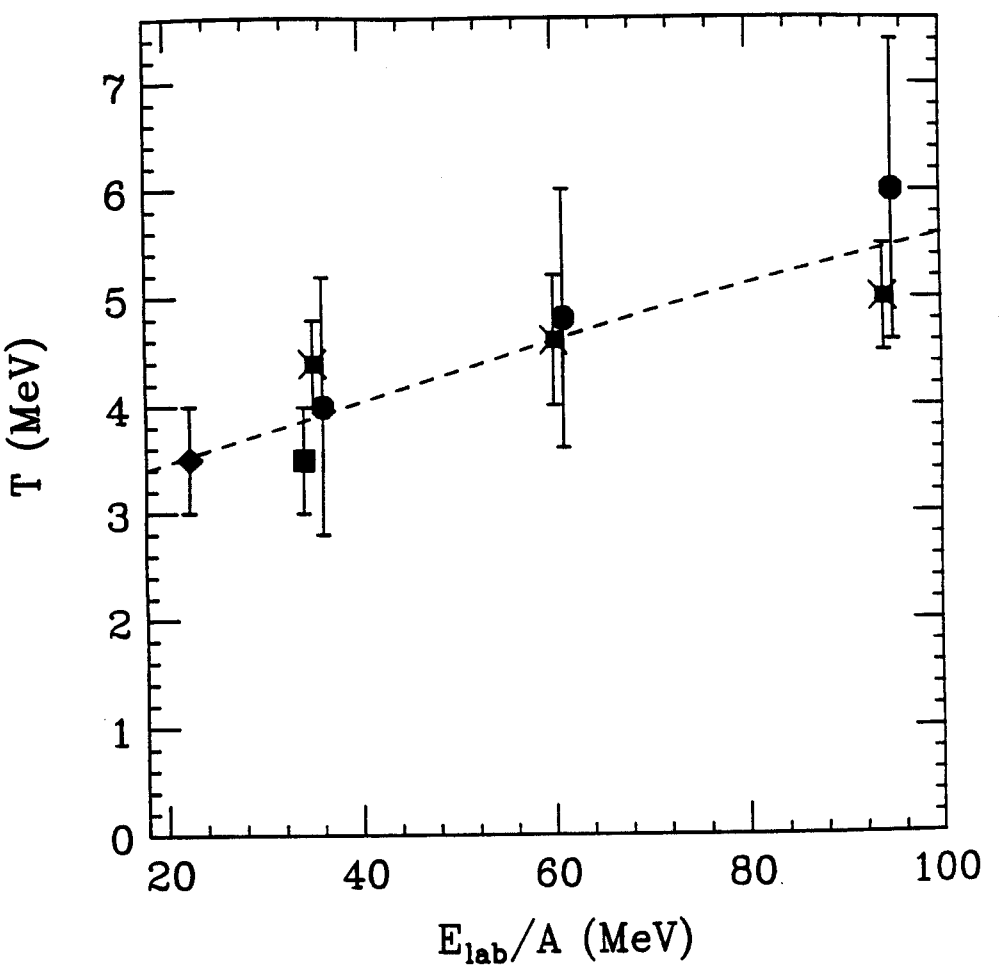

Figure 4.8: Summary of the emission temperature extracted from recent experiments. The sold diamond is the experimental result of this dissertation. The solid square is taken from ref. [Naya 90] which is derived from a large number of particle unstable states. The solid circles and solid crosses are results of excited states of ^{5}Li and ^{6}Li, respectively [Chen 88a]. The dashed lines are used to guide the eyes.

Little is known concerning the relationship between the impact parameter or the choice of model assumptions in these dynamical calculations and the values of the temperatures these models predict. The existence of a strong sensitivity of freezeout temperature to important issues like the low density EOS could serve to stimulate more detailed experimental investigations of the emission temperature. The second half of the dissertation is motivated by a desire to determine whether there exists such a strong theoretical motivation for emission temperature measurements.

Chapter 5

BUU Equation in the Lattice Hamiltonian Approximation

Starting from this chapter, we will try to address the the second important question mentioned in the introduction, i.e., do the values of emission temperature T $\sim 3-4$ MeV hold any implications about basic quantities such as the nuclear equation of state or the in-medium nucleon-nucleon cross section.

In principle, one should examine this issue theoretically by calculating the excitation energies of intermediate mass fragments produced in heavy-ion collisions. At present, such information may be obtained from molecular dynamics calculations. However, the theoretical justification for applying molecular dynamics to heavy-ion collisions remains unclear. For this reason, it is uncertain how much one can learn about the nuclear mean field at low density from such calculations. The connection to nuclear mean field is somewhat better established for models based on the Boltzmann-Uehling-Uhlenbeck equation. These approaches, however, do not incorporate sufficient fluctuations of the mean field and therefore do not allow the calculations of cluster emission and excitation energies of intermediate mass fragments. Nonetheless, it is possible to study the excitation energy of the heavy residues predicted by the BUU calculations. Since molecular dynamical calculations predict that

the average excitation energy per nucleon is approximately the same for all fragments produced in the reaction. One may hope that the information about the excitation energies of the intermediate mass fragments may be obtained by studying the excitation energies of heavy residues produced in BUU calculations. To explore this issue, we have therefore performed BUU calculations to investigate the sensitivity of the residue excitation energies to the equation of state and the in-medium nucleon cross section.

In this chapter, we will discuss numerical details of the Lattice Hamiltonian Method used to solve the Boltzmann-Uehling-Uhlenbeck equation. As first shown by Lenk and Pandharipande, this method provides a more accurate algorithm for the treatment of the nuclear mean field and the equations of motion. Consistent with Lenk and Pandharipande, we found that the total energy is well conserved in our numerical calculations. In the following sections, we give a detailed descriptions of the BUU equation followed with a discussion of the numerical details of its solution. Some numerical tests of stability of the nuclei in their ground states and energy conservation are also presented.

I The Formalism

A The BUU equation

We solve the Boltzmann-Uehling-Uhlenbeck equation [Bert 84, Aich 85, Bert 88]

$$\frac{\partial f_1}{\partial t} + \vec{v}\cdot\nabla_r f_1 - \nabla_r U\cdot\nabla_p f_1 = \frac{4}{(2\pi)^3}\int d^3k_2 d^3k_3 d\Omega \frac{d\sigma_{nn}}{d\Omega} v_{12}$$
$$\times[f_3 f_4(1-f_1)(1-f_2) - f_1 f_2(1-f_3)(1-f_4)]\delta^3(\vec{k}_1+\vec{k}_2-\vec{k}_3-\vec{k}_4), \qquad (5.1)$$

where $f = f(\vec{r},\vec{p},t)$ is the Wigner transformation of the one body density matrix and $\frac{d\sigma_{nn}}{d\Omega}$ and v_{12} are the in-medium cross section and relative velocity for the colliding nucleons. In Eq. (5.1), U is the total mean-field potential parameterized as

$$U = V_C + U_n + U_{sym}, \tag{5.2}$$

here V_C, U_n and U_{sym} represent the Coulomb potential, the isoscalar nuclear potential and the symmetry energy, respectively. In our simulation, the isoscalar mean-field potential U_n (in MeV) is approximated [Bert 84, Aich 85, Bert 88] by

$$U_n = A\rho/\rho_0 + B(\rho/\rho_0)^\gamma, \tag{5.3}$$

where $\rho_0 = 0.017(fm)^{-3}$ is the saturation value of the nuclear matter density and $\rho = \rho(\vec{r})$ is the local density of nuclear matter. Values of $A = -356$ MeV, $B = 303$ MeV, and $\gamma = 7/6$ correspond to a soft nuclear matter equation of state (EOS) with compressibility coefficient $K = 200$ MeV; while $A = -124$ MeV, $B = 70.5$ MeV and $\gamma = 2$ correspond to a stiff EOS with $K = 375$ MeV. The symmetry potential U_{sym} is represented by:

$$U_{sym} = C[(\rho_n - \rho_p)/\rho_0]\tau_z. \tag{5.4}$$

where, ρ_n and ρ_p are the neutron and proton matter densities and τ_z is the isospin operator with eigenvalues $+1$ and -1 for neutrons and protons, respectively. C is a constant with a value C=32 MeV. For simplicity, $\sigma_{NN} = \int d\Omega \frac{d\sigma_{nn}}{d\Omega}$ is chosen to be isotropic and energy independent. The mean-field and the Pauli-blocking factors in the collision integral are averaged over an ensemble of 80 parallel simulations (for details, see section II).

B The Lattice Hamiltonian Method

The Boltzmann-Uehling-Uhlenbeck equation, given in Eq. (5.1), is most frequently solved by the *test particle* method [Wong 82, Bert 84, Aich 85, Bert 88], in which the Wigner function f is approximated by

$$f(\vec{r},\vec{p},t) = \frac{(2\pi\hbar)^2}{N_{test}} \sum_i \delta(\vec{r} - \vec{r}_i(t))\delta(\vec{p} - \vec{p}_i(t)), \tag{5.5}$$

here, N_{test} is the number of parallel ensembles and δ is the Dirac delta function. In the test particle approach, f solves the BUU equation provided $\vec{r}_i$ and $\vec{p}_i$ are themselves the solutions of equations of motion for test particles in a self consistent mean field [Wong 82, Bert 84, Aich 85, Bert 88]. This mean field is calculated on a lattice on which the local density is evaluated by integrating Eq. (5.5) over the momentum. In the early BUU calculations, the test particles propagated according to Newtonian mechanics

$$\dot{\vec{r}}_i = \frac{\partial H}{\partial \vec{p}_i} = \frac{\vec{p}_i}{m}, \qquad \dot{\vec{p}}_i = -\nabla_i U, \tag{5.6}$$

where the the mean field U was defined on a lattice. The gradient could be evaluated by taking a difference between the mean field at the neighboring points, given below,

$$(-\nabla_i U)_x = \frac{1}{2l}[U(\rho(k_1 - 1, k_2, k_3)) - U(\rho(k_1 + 1, k_2, k_3))] \tag{5.7}$$

where l was the lattice spacing, and k_1, k_2, k_3, are the the coordinates of the lattice point where the particle is located.

The numerical techniques outlined above did not conserve energy because Eqs. (5.6) and (5.7) do not take the influence of the lattice properly into account. As a result, spurious emission of free nucleons could be so large that the total energy would be increased by as much as 1 MeV per nucleon over a period of 100 fm/c [Bert 88]. To calculate the excitation energies of the order of $\sim 2 - 3$ MeV per nucleon, a more accurate energy conservation is required. Lenk and Pandharipande recently [Lenk 89] demonstrated that excellent energy conservation could be obtained if adequate attention was paid to the role of the lattice upon which the density and therefore the mean field were calculated.

Following Lenk and Pandharipande, we evaluate the average density ρ_L at lattice location α by smearing out the test particle with a form factor S,

$$\rho_L(\vec{r}_\alpha) \equiv \sum_{i=1}^{AN_{test}} S(\vec{r}_\alpha - \vec{r}_i), \tag{5.8}$$

where $\vec{r}_\alpha$ is the position of lattice point α, $\vec{r}_i$ the position of particle i, and N_{test} the number of parallel ensembles. The the form factor S has the form

$$S(\vec{r}) = \frac{1}{N_{test}(nl)^6} g(x)g(y)g(z), \tag{5.9}$$

$$g(q) = (nl - |q|)\Theta(nl - |q|). \tag{5.10}$$

Here, l is the lattice spacing, and $\Theta(x)$ is the step function with values of 1 for $x \geq 0$ and 0 for $x < 0$; n is an integer which determines the range of S. Following ref. [Lenk 89], we also take $n = 2$ in our calculations. The specific choice of the form factor $S(\vec{r})$ in Eq. (5.9) satisfies the normalization condition

$$l^3 \sum_\alpha S(\vec{r}_\alpha - \vec{r}) = \frac{1}{N_{test}}, \tag{5.11}$$

independent of $\vec{r}$, and therefore the total number of particles is exactly conserved:

$$l^3 \sum \rho_L(\vec{r}_\alpha) = A. \tag{5.12}$$

It is simple to show the potential energy density at $\vec{r}$ is given by

$$v(\vec{r}) = \frac{A\rho_0}{2}(\frac{\rho}{\rho_0})^2 + \frac{B\rho_0}{\gamma+1}(\frac{\rho}{\rho_0})^{\gamma+1} + \frac{1}{2}\rho_p V_C + \frac{C\rho_0}{2}(\frac{\rho_p - \rho_n}{\rho_0})^2, \tag{5.13}$$

where A, B, C, and γ are parameters of the mean field. The total potential energy can be calculated by summing over the lattice points,

$$V = l^3 \sum_\alpha v_\alpha. \tag{5.14}$$

and the total 'lattice' Hamiltonian (or total energy) for a classical system of $N_{test}A$ test particles is given by

$$H = \sum_{i=1}^{AN_{test}} \frac{p_i^2}{2m} + N_{test}V \tag{5.15}$$

With this Hamiltonian, it's straight forward to derive the Hamilton's equations of motion for the individual test particles:

$$\dot{\vec{r}}_i = \frac{\partial H}{\partial \vec{p}_i} = \frac{\vec{p}_i}{m}, \tag{5.16}$$

$$\begin{aligned} \dot{\vec{p}}_i = -\nabla_i H = -N_{test}\nabla_i V = -N_{test}\sum_\alpha \frac{\partial V}{\partial \rho_\alpha}\nabla_i \rho_\alpha \\ = -N_{test}\sum_\alpha U(\rho_\alpha)\nabla_i \rho_\alpha. \end{aligned} \tag{5.17}$$

If the trajectories of test particles satisfy Hamilton's equations, it is trivial to verify that the Hamiltonian given in Eq. (5.15)is a conserved quantity. It interesting to note the force on the right hand side of Eq. (5.17) is more complex than that given in Eq. (5.6). Further numerical details to implement Eqs. (5.8)-(5.17) are derived in the next section.

II Numerical Realizations of the BUU with the LHM

We now discuss the numerical procedure for our improved BUU calculations. There are basically 3 steps in the program flow: 1) the initialization of positions and momenta for test particles in both the projectile and target; 2) the propagation of test particles according to a mean field dynamics; 3) the checking of collisions and the modification of momenta if a collision is not Pauli-blocked. After initialization, the program alternates between step 2 and 3 until the final step, given by inputs, is

reached. For most collisions presented in this study, we follow a time evolution of $t = 240$ fm/c, though most of the interesting observables are evaluated at an earlier time.

In the following subsections, we provide details of the initialization procedure in subsection A. Details concerning the density evaluation and the equations of motion are derived in subsections B and C, respectively. Two-body collisions and the Pauli-blocking algorithm are discussed in subsections D and E, respectively.

A Initialization

The calculation starts by initiating the projectile and target with their surface separated by 4 fm. In total, there are $(Z_p + Z_t)N_{test}$ and $(N_p + N_t)N_{test}$ test particles, respectively, for protons and neutrons. Here, $A_p = Z_p + N_p$ and $A_t = Z_t + N_t$ are the masses for the projectile and target, respectively. For each nucleus, the test particles are distributed uniformly with a sphere of radius $R = 1.12A^{1/3}$, with A being A_p or A_t, according to

$$r = R(x_1)^{1/3} \tag{5.18}$$

$$\cos\theta = 1 - 2x_2 \tag{5.19}$$

$$\phi = 2\pi x_3 \tag{5.20}$$

where (r, θ, ϕ) are the spherical coordinates of the test particle with respect to the center-of-mass coordinates of projectile or target. x_1, x_2, x_3 are three random numbers uniformly distributed among $0 \leq x_i \leq 1$. Using the test particle spacial distributions, the local proton and neutron density are calculated on the lattice according an algorithm to be discussed in the next section. The momentum of the test particle is then assigned stochastically within a local momentum sphere with its radius given by

$$p_f^{\mu}(\vec{r}) = (3\pi^2\rho^{\mu}(\vec{r}))^{1/3}\hbar \tag{5.21}$$

where p_f^μ and ρ^μ are the local fermi momentum and density and the index, $\mu = 1, 2$, denotes protons and neutrons respectively. Finally, the momentum of test particles in the projectile and target are boosted towards each other with their respective c.m. momenta determined from the incident energy and the masses of the projectile and target.

B Density evaluation

The neutron and proton densities as well as the mean field potential are calculated in a lattice of dimension $32fm \times 34fm \times 48fm$ with a lattice spacing of $l = 1fm$. The neutron and proton densities on these lattice points are computed by summing over the contributions from all individual test particles. The contribution of test particle i to the density [from Eq. (5.9)] at lattice point $\vec{r}_K$ is computed by the form factor

$$S(\vec{r}_K - \vec{r}_i) = \frac{1}{2^6 N_{test}} \prod_{\mu=1}^{3} (2 - |r_{i\mu} - K_\mu|) \tag{5.22}$$

where $K_\mu = (K_1, K_2, K_3)$ denote the Cartesian coordinates of the lattice point $\vec{r}_K$. Each test particle contributes to 64 neighboring lattice points positioned from $K_\mu = r^0_{i\mu} - 1$ to $r^0_{i\mu} + 2$ with $\mu = 1, 2, 3$, respectively. Here, $r^0_{i\mu} = (r^0_{i1}, r^0_{i2}, r^0_{i3})$ represent the integer truncations of the coordinates $\vec{r}_i = (r_{i1}, r_{i2}, r_{i3})$ for test particle i.

It is perhaps useful to note that this method to distribute the density creates an effective surface with an average skin thickness of $r_s \simeq 2.5$ fm as shown in Fig. 5.1 for both ^{40}Ca (top) and ^{124}Sn (bottom) nuclei. This value of skin thickness agrees with the empirical value of $r_{emp} \simeq 2.4$ fm [deSh74]. In Fig. 5.2, we plot the binding energy per nucleon predicted by LHM for a wide range of masses $A \simeq 30 - 200$ on the valley of beta-stability. The solid line is calculated from the liquid drop mass formula [Myer 66]

$$B(N, Z) = a_V A + a_S A^{2/3} + a_C \frac{Z^2}{A^{1/3}} + a_I \frac{(N - A)^2}{A} \tag{5.23}$$

with

$$a_V = 15.68; \quad a_S = -18.56; \quad a_C = -0.717; \quad a_I = -28.1; \quad [MeV]. \tag{5.24}$$

For A $\geq$ 30, nuclei bound by the soft EOS (designated by open circles) are in good agreement with the liquid drop formula. For nuclei bound by the stiff EOS (solid circles), the binding energy/nucleon of nuclei in this mass range is 0.4 - 0.8 MeV less than that with the soft EOS, mainly because the surface energy coefficient for the stiff EOS is somewhat larger.

C Equation of Motion

Between successive collisions, the test particles are propagated according to classical equations of motion. To preserve the accuracy to $O(\delta t^3)$, each test particle i is propagated by the simple algorithm

$$\vec{r}_i(t + \frac{1}{2}\delta t) = \vec{r}_i(t - \frac{1}{2}\delta t) + \delta t \frac{\vec{p}_i(t)}{m} \tag{5.25}$$

$$\vec{p}_i(t + \delta t) = \vec{p}_i(t) + \delta t \vec{F}_i(\vec{r}_i, t + \frac{1}{2}\delta t) \tag{5.26}$$

where δt is time step size and $\vec{F}_i$ is the force on particle i derived from Eq. (5.17). In all our calculations we use $\delta t = 0.5 fm/c$. We note here the positions and momenta given by Eqs. (5.25)-(5.26) are not evaluated at the same time but at times differing by $\delta t/2$. This algorithm is essential to preserve a good numerical accuracy and its convergence to $O(\delta t^3)$ can be verified, from Eq. (5.25), by performing a Taylor expansion,

$$\vec{r}_i(t + \frac{1}{2}\delta t) = \vec{r}_i(t) + \dot{\vec{r}}_i(\frac{1}{2}\delta t) + \frac{\ddot{\vec{r}}_i}{2!}(\frac{1}{2}\delta t)^2 + \frac{1}{3!}\frac{d^3\vec{r}_i}{dt^3}(\frac{1}{2}\delta t)^3 + \cdots \tag{5.27}$$

$$\vec{r}_i(t - \frac{1}{2}\delta t) = \vec{r}_i(t) + \dot{\vec{r}}_i(-\frac{1}{2}\delta t) + \frac{\ddot{\vec{r}}_i}{2!}(-\frac{1}{2}\delta t)^2 + \frac{1}{3!}\frac{d^3\vec{r}_i}{dt^3}(-\frac{1}{2}\delta t)^3 + \cdots \tag{5.28}$$

subtraction of Eq. (5.27) by Eq. (5.27), one obtains

$$\vec{r}_i(t + \frac{1}{2}\delta t) - \vec{r}_i(t - \frac{1}{2}\delta t) \quad = \dot{\vec{r}}_i(t)\delta t + \tfrac{1}{4!}\tfrac{d^3\vec{r}_i}{dt^3}(\delta t)^3 + \cdots$$

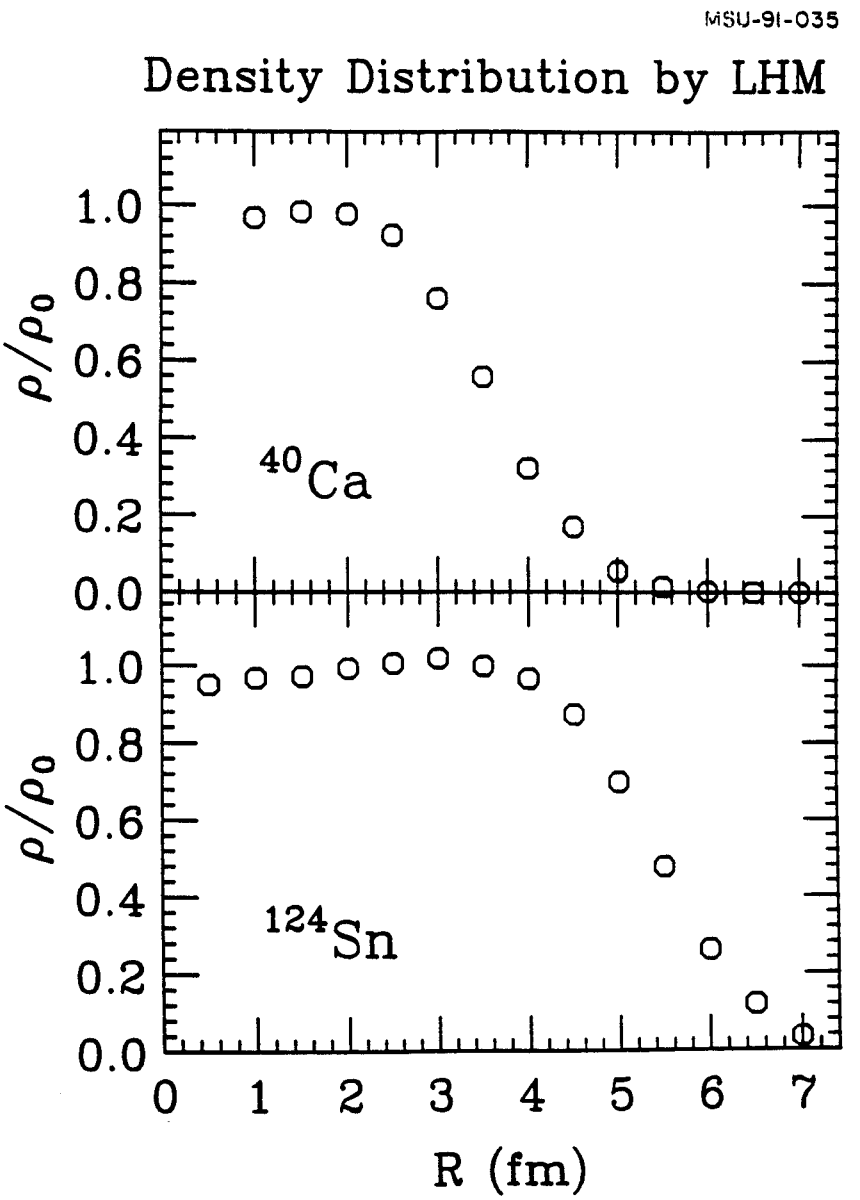

Figure 5.1: The density distributions as functions of the radius for both ^{40}Ca (top window) and ^{124}Sn (bottom window) nuclei.

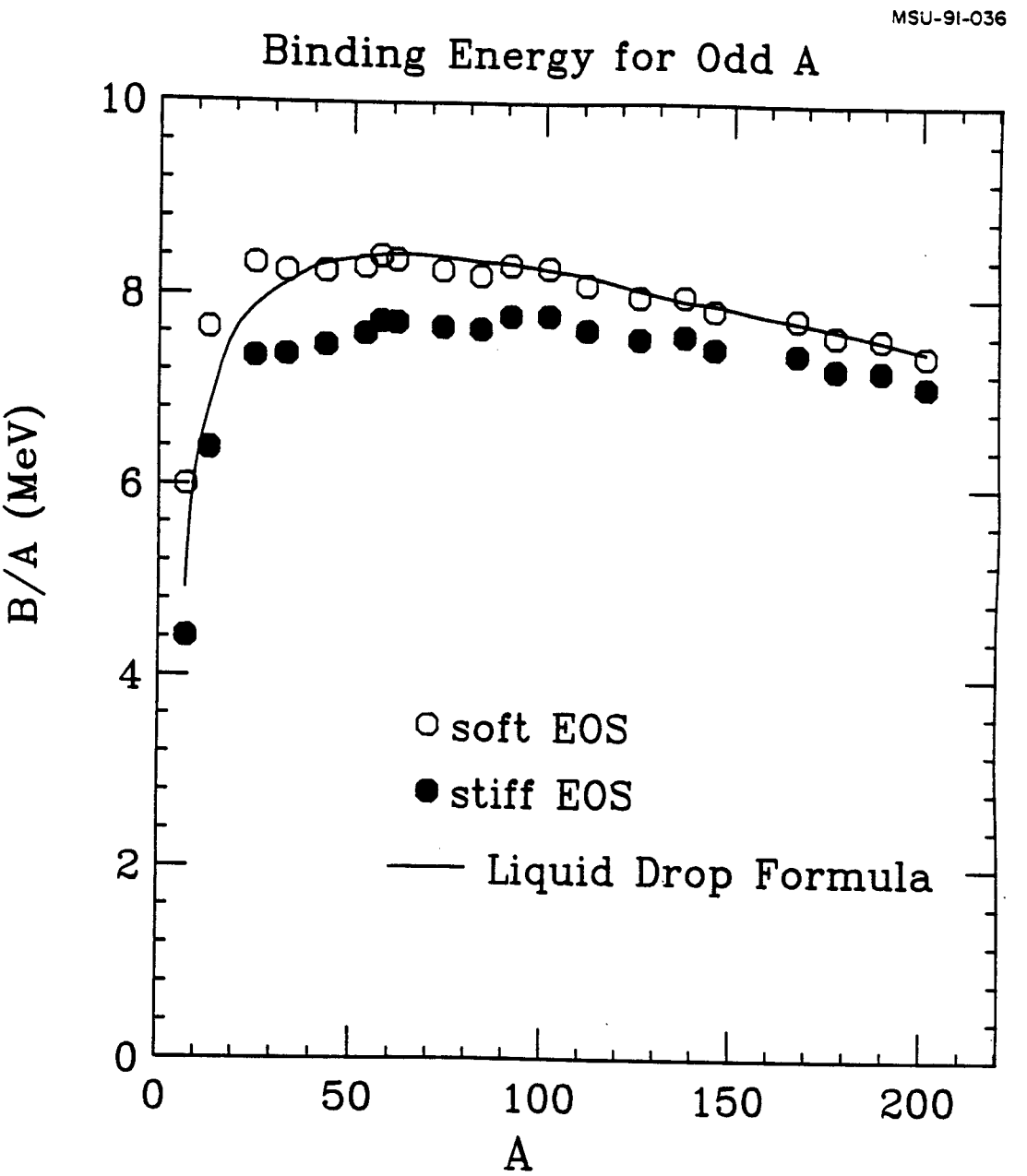

Figure 5.2: The binding energy per nucleon for the mass range $30 \leq A \leq 200$ initialized at the beginning of the BUU calculations for both the stiff (circles) and the soft (squares) equations of state. The solid line indicates the results from the liquid drop mass formula.

$$= \dot{\vec{r}}_i(t)\delta t + O(\delta t^3) + \cdots$$

$$= \delta t \frac{\vec{p}_i(t)}{m} + O(\delta t^3) + \cdots \tag{5.29}$$

a similar exercise can be performed to check the accuracy of Eq. (5.26) as well.

The force F_i, given in Eq. (5.26) must be derived from Eq. (5.17). It has the form, for example, for x-component F_{i1},

$$F_{i1} = -\sum_{K_2=r^0_{i2}-1}^{r^0_{i2}+2}\sum_{K_3=r^0_{i3}-1}^{r^0_{i3}+2}\frac{1}{2^6}\prod_{\mu=2}^{3}(2-|r_{i\mu}-K_\mu|)[U(r^0_{i1}-1,K_2,K_3)$$

$$+U(r^0_{i1},K_2,K_3)-U(r^0_{i1}+1,K_2,K_3)-U(r^0_{i1}+2,K_2,K_3)] \tag{5.30}$$

where U is the mean field potential given by Eq. (5.2). The other notations were given in the previous subsection. By similar equations, one can compute the other two components F_{i2}, F_{i3}. clearly, $\vec{F} \neq -\nabla_i U$ as was the approximation used in early calculations [see also (5.7)]. The precise calculation of Eq. (5.30) requires information about the mean field from 64 neighboring lattice points and this slows down the calculation of the force term considerably.

During the simulation, the positions $\vec{r}_i$ and momenta $\vec{p}_i$ of the test particles are known at times which differ by $\delta t/2$. On the other hand, when one wants to calculate the total energy and various contributions to the excitation energy, one needs to know the positions and momenta at the same time. To achieve this in our simulation, we branch out from the main flow of the test particle propagation and move the position one half time step forward using a equation similar to Eq. (5.25) to match the time at which the momentum is known. Then we calculate the quantities of interest. The dependence of the conservation of energy on time step size δt, as well as the stability of the nucleus propagated by the mean field, is discussed in section III.

D Two-Body Collisions

Collisions between two test particles are only allowed to occur for test particles within the same ensemble. This reduces the number of computations and allow us to use the collision cross section σ_{nn} without reduction [Bert 88]. Successful collisions are allowed if the two test particles are close enough and if their momenta after scattering are not Pauli-blocked. If one of the test particles are Pauli-blocked, the original momenta of both test particles are restored. Details of the Pauli-blocking will be discussed in subsection E.

To check whether particles are close enough, let us consider two test particles at $(\vec{r}_1, \vec{p}_1; \vec{r}_2, \vec{p}_2)$. The two test particles follow straight line trajectories between successive time steps. For a collision to occur, the two test particles must pass by each other the point of the closest approach within a collision radius defined by $r_{nn} = (\sigma_{nn}/\pi)^{1/2}$. This condition can be expressed by the following two equations

$$|\frac{\delta\vec{r}_{21} \cdot \delta\vec{v}_{21}}{\delta v_{21}}| \leq \delta v_{21} \cdot \frac{\delta t}{2} \tag{5.31}$$

$$|\delta\vec{r}_{21}|^2 - |\frac{\delta\vec{r}_{21} \cdot \delta\vec{v}_{21}}{\delta v_{21}}|^2 \leq r_{nn}^2 = \frac{{\sigma_{nn}}^2}{\pi} \tag{5.32}$$

Where $\delta\vec{r}_{21} = \vec{r}_2 - \vec{r}_1$, $\delta\vec{v}_{21} = \vec{v}_2 - \vec{v}_1$ and $\delta v_{21} = |\vec{v}_2 - \vec{v}_1|$.

If the pair of test particles satisfies both Eq. (5.32) and Eq. (5.31), the momenta of the two particles are changed from $(\vec{p}_1; \vec{p}_2)$ to $(\vec{p}_1\,'; \vec{p}_2\,')$ with $\vec{p}_1\,'$ and $\vec{p}_2\,'$ given by

$$\vec{p}_1\,' = \vec{p}_{c.m.} + \frac{1}{2}\delta\vec{p}\,'_{21} \tag{5.33}$$

$$\vec{p}_2\,' = \vec{p}_{c.m.} - \frac{1}{2}\delta\vec{p}\,'_{21} \tag{5.34}$$

where $\vec{p}_{c.m.} = \frac{1}{2}(\vec{p}_1 + \vec{p}_2)$ is the nucleon c.m. momentum and $\delta\vec{p}\,'_{21}$ is the relative momentum assigned randomly according to an isotropic distribution with a magnitude $\delta p_{21} = |\vec{p}_2 - \vec{p}_1|$. This algorithm clearly conserves both momentum and energy.

Although it violates in principle the conservation of angular momentum for each individual pair of test particles, our numerical simulations indicate that its influence to the total angular momentum is negligible.

E Pauli-blocking

After the pairs get their respective new momenta, it is checked whether the collision violates the Pauli principle. To do this, we build of sphere of radius r around $\vec{r}_1$ and a sphere of radius p around $\vec{p}_1{}'$ so that n_0 test particles inside the phase-space means full occupation. Scaling with ground states (a phase-space of $(\frac{4\pi}{3})^2 R^3 P_F^3$ is fully occupied by $N_{test}A$ test particle) and with the relation $r/p = R/P_F$ one can get r and p, respectively, once n_0 is given. Thus the occupation probability is calculated by

$$f_1(\vec{r}_1, \vec{p}_1) = \frac{n_1}{n_0}, \tag{5.35}$$

where n_1 is the number of test particles inside the phase-space volume not including the test particle being checked at $(\vec{r}_1, \vec{p}_1{}')$. Similarly, one can calculate the probability f_2. The probability for this pair to collide successfully is calculated by

$$P = (1 - f_1)(1 - f_2). \tag{5.36}$$

In our calculations, we choose $n_0 = 4$ and thus, the radii of the spheres are $r = 0.60 fm$ and $p = 0.904 fm^{-1}$, respectively. This yields about a 80% blocking probability for the ground states of ^{40}Ca and ^{124}Sn nuclei. Probability closer to 100% would be preferred. Most of the collisions allowed for the ground states of ^{40}Ca and ^{124}Sn nuclei occur between test particles near the phase space boundaries of the nuclei. There, the Pauli blocker samples regions of phase space in which no test particles are found. Clearly, additional work on the Pauli blocking algorithm is needed.

III Ground State Stability and Conservation of Energy

To check the stability of ground states produced by the Lattice Hamiltonian Method, we have performed extensive calculations for ^{40}Ca and ^{124}Sn nuclei. We start the calculation by providing a nucleus in its ground state using the algorithm as described in section II (A). We then let the individual test particles (nucleons) propagate according to their mean field for a period of 300 fm/c with the step size $\delta t = 0.5$ fm/c. Figs. 5.3 shows projections of the nuclear densities in the $x - z$ plane for ^{40}Ca (left two columns) and ^{124}Sn (right two columns) ground state nuclei as a function of time in steps of 40 fm/c. In all our calculations the full potential includes the Coulomb field and the symmetry terms in addition to the isoscalar mean field. As shown in these figures, only a few test particles escape from the mean field over a period of of 160 fm/c.

A more quantitative analysis of the calculations is shown in Fig. 5.4. The left column is the results obtained for ^{40}Ca and the right is that for ^{124}Sn. The top windows display the binding energy per nucleon predicted by both the soft equation of state (open circles) and the stiff equation of state (open crosses) calculated from Eq. (5.15). One can see that both equations of state produce an effective binding energy B/A $\simeq$ 8 MeV. The binding energy obtained for calculations with the soft equation of state is somewhat larger since the corresponding potential is deeper at low densities. The number of escaped particles $A_{escaped}$ and the root-mean-square radius R_{rms} for both nuclei are plotted, respectively, in the bottom windows. The escaped particles are defined as those having a local density lower than $7\%\rho_0$. The root-mean-square radius includes all test particles.

Once nucleon-nucleon collisions are turned on, spurious emission of nucleons oc-

curs due to the insufficient Pauli-blocking at the nuclear surface. With a nucleon-nucleon cross section of $\sigma_{nn} = 41$ mb, the average emission rate is less than 8% over a period of 160 fm/c. The total energy is, nonetheless, well conserved. The dependence of the conservation of energy on the time step size δt has been extensively investigated. In Fig. 5.5, we show the results for ^{40}Ca+^{40}Ca collisions using the mean field given by Eq. (5.2) with the soft EOS parametrization. ΔH is the energy difference calculated between $t = 140$ fm/c and $t = 0$. For $\delta t \leq 0.5$ fm/c, the total energy changes by less than 0.1 MeV/A during this time interval. We have chosen $\delta t = 0.5$ fm/c in all our calculations.

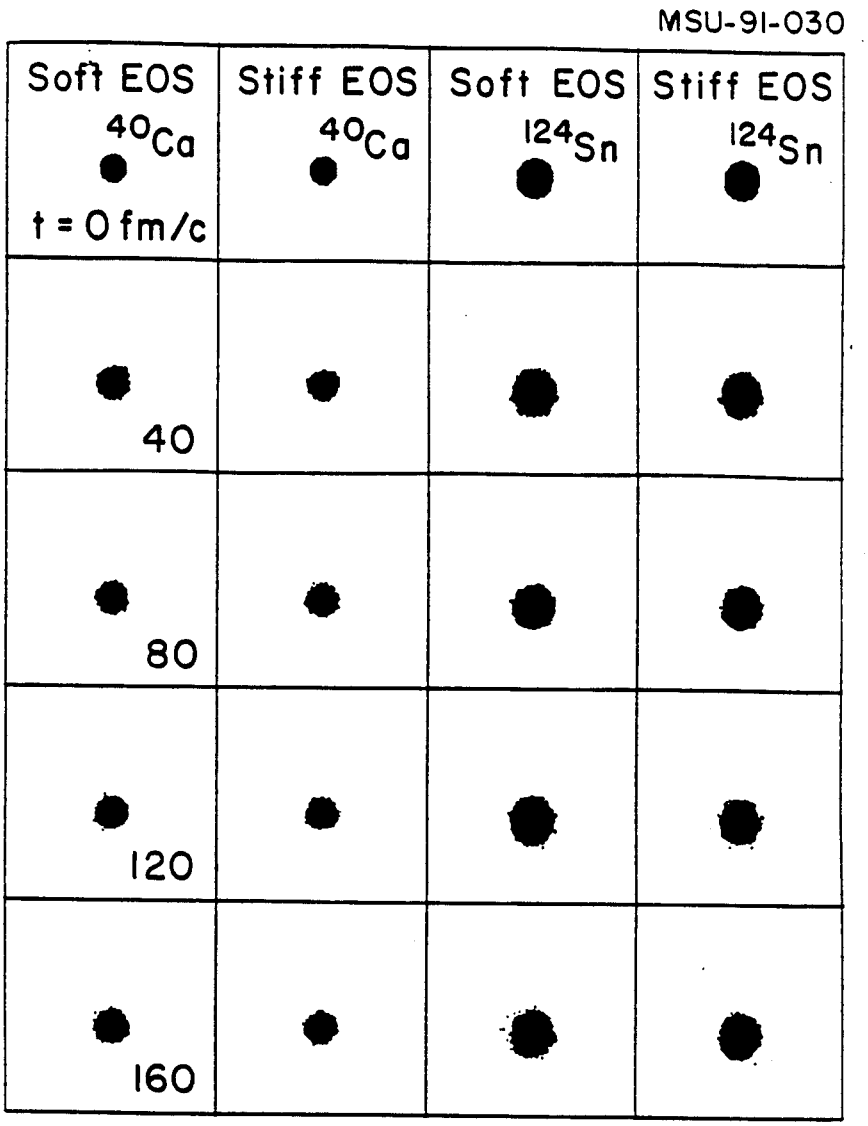

Figure 5.3: The time evolution of ^{40}Ca (left-hand two columns) and ^{124}Sn (right-hand two columns) ground state nuclei projected in the $x-z$ plane in step of 40 fm/c. The equations of state and the time at which the density is plotted are already indicated in the figure.

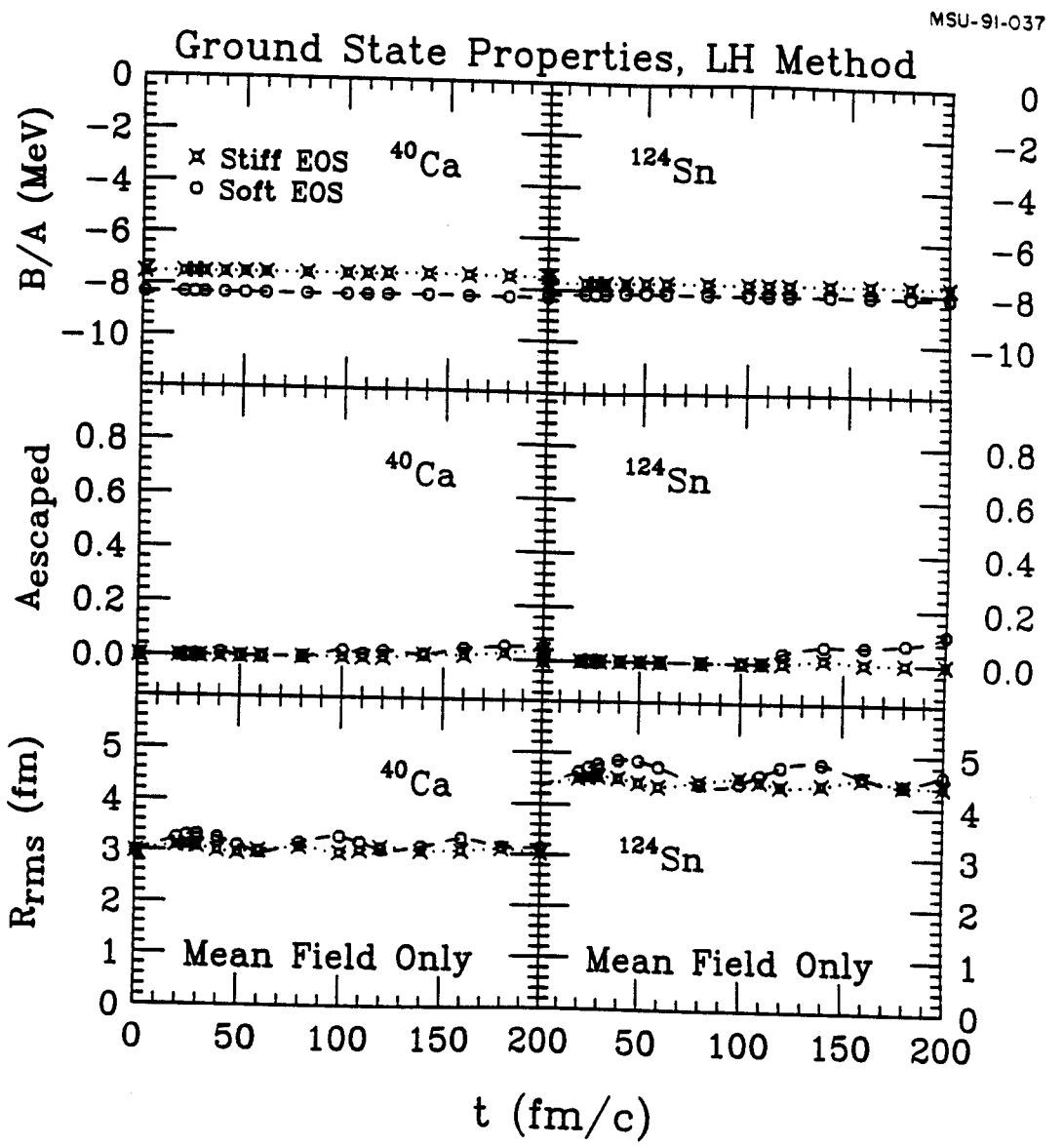

Figure 5.4: Stability tests and the conservation of energy for the ground states of ^{40}Ca (left column) and ^{124}Sn (right column) nuclei. the top and the central windows display, respectively, the number of escaped particles $A_{escaped}$ and the root-mean-square radius R_{rms} (see the text). The bottom windows display the binding energy per nucleon predicted by both the soft equation of state (open circles) and the stiff equation of state (open crosses) calculated from Eq. (5.15).

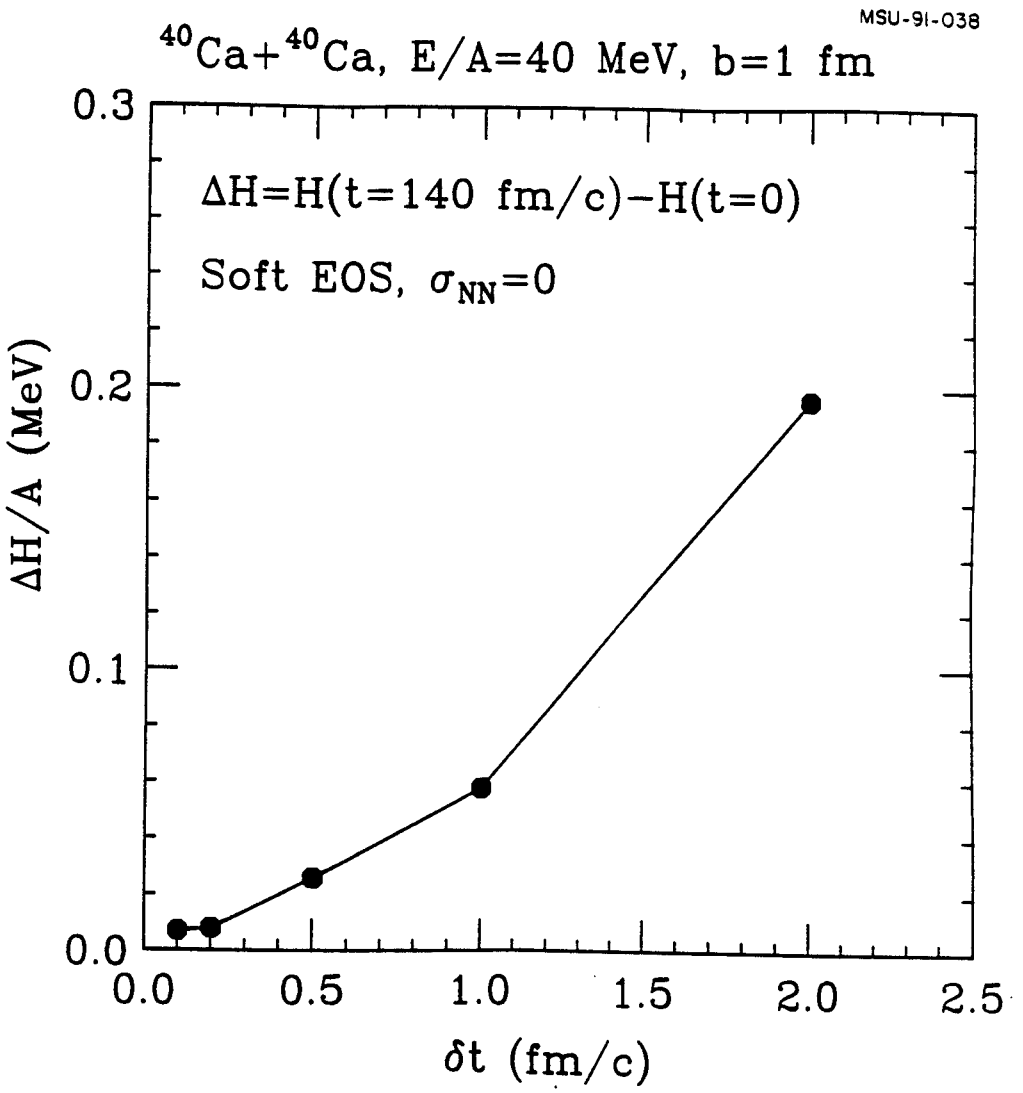

Figure 5.5: The step size dependence of the conservation of the total energy for ^{40}Ca+^{40}Ca collisions with the soft equation of state. ΔE is the energy difference calculated between $t = 140$ fm/c and $t = 0$.

Chapter 6

The Disappearance of Fusion-Like Processes and the Nuclear Equation of State

Hot nuclei can be readily formed by the incomplete fusion of projectile and target nuclei in a heavy ion reaction. For moderate incident energies, the excitation energies of fusion-like residues increase with incident energy. At incident energies in excess of about E/A = 35-40 MeV, however, vanishing cross sections for fusion-like residues have been reported, and interpreted as a manifestation of a bulk instability of nuclei at high temperatures. This interpretation may be unwarranted if very hot nuclei decay via unexpected decay modes, or if the reaction dynamics preclude the formation of very highly excited residues.

Although this issue is not directly related to the questions raised in the experimental study of this dissertation, early results of the Lattice Hamiltonian code prompted us to direct some efforts to the understanding of the dynamical limits to the residue formation. In this chapter, we will attempt to address 1) what can be learned about the nuclear equation of state and the in-medium nucleon-nucleon cross section from measurements of fusion-like residues; and 2) what are the dynamical limitations to the formation of hot composite nuclei. For such purposes, heavy residue cross sections

were calculated for ^{40}Ca + ^{40}Ca and ^{40}Ar + ^{27}Al collisions using the Boltzmann equation. Qualitatively consistent with experimental observations, the calculated heavy residue cross sections decrease rapidly to zero for E/A $\geq 35 - 40$ MeV. The decrease in cross section does not appear related to a bulk instability of nuclei at high temperature. The calculated cross sections are quite sensitive to the in-medium nucleon-nucleon cross section and the nuclear equation of state (EOS) at sub-nuclear density.

I Fusionlike Cross Sections and the Equation of State

A ^{40}Ca+^{40}Ca Collisions at E/A =40 MeV

The formation and decay of heavy residues is an important process at energies E/A $\leq$ 40 MeV. To illustrate our calculations for heavy residue cross section, we consider first the calculations for the ^{40}Ca + ^{40}Ca system at E/A = 40 MeV, performed for an isotropic nucleon-nucleon cross section of $\sigma_{nn} = 41$ mb and for both soft and stiff equations of state. Figs. 6.1 and 6.2 show the projections of test particles on the $x - z$ plane as functions of time for both stiff and soft EOS. For calculations with the stiff EOS and b=2 fm, one obtains a single fusionlike residue. For the soft EOS, on the other hand, one obtains two residues. The impact parameter dependences of the calculations for the two equations of state are shown in the left column of Fig. 6.3 where we plot the masses (upper left panel) and the component of velocity parallel to the beam axis (lower left panel) of heavy residues produced in the calculations. Two residues with $30 \leq A \leq 40$ are produced at large impact parameters, $b \geq$ 3.3 fm, in calculations with the stiff EOS (open points) and the soft EOS (open squares). A single heavy residue is observed at small impact parameters, $b \leq 3.3$ fm, in calculations with the stiff EOS (solid points). For small impact parameters with the soft EOS, however, the projectile and target simply pass through each other, with

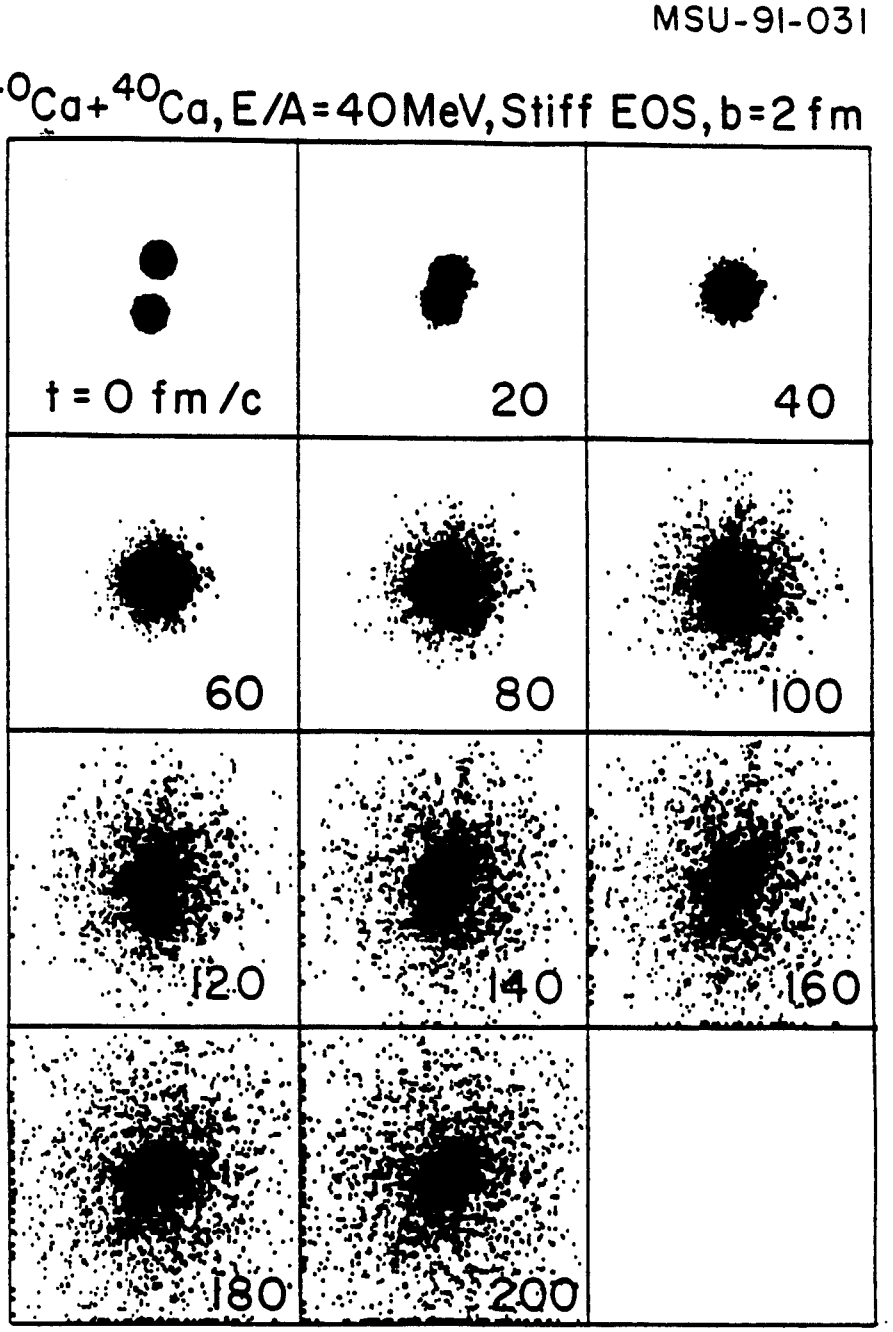

Figure 6.1: The time evolution of test particles for ^{40}Ca+^{40}Ca collisions at E/A=40 MeV and b=2 fm with the stiff EOS and $\sigma_{nn} = 41$ mb projected in the $x - z$ plane in step of 20 fm/c.

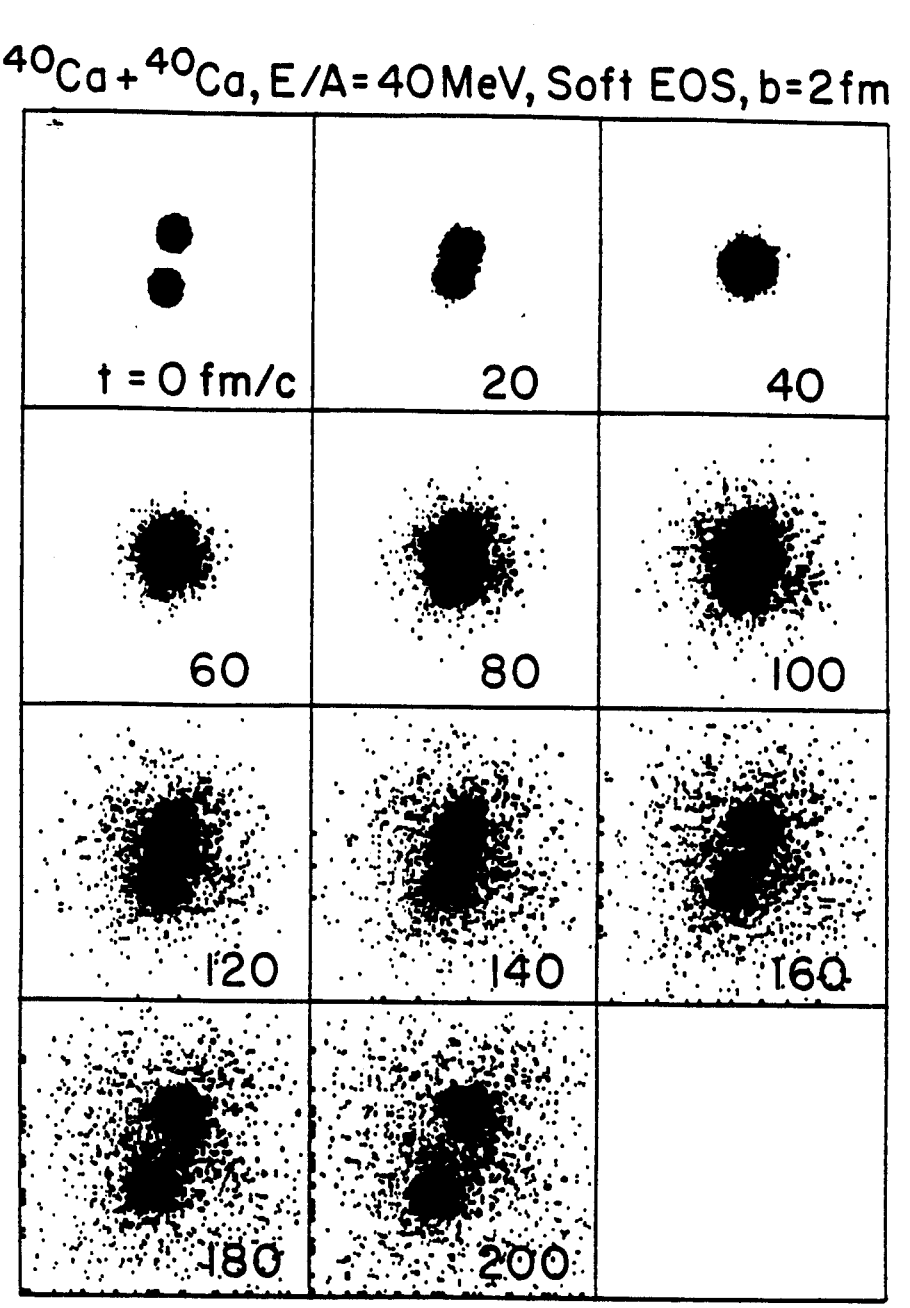

Figure 6.2: The time evolution of test particles for ^{40}Ca+^{40}Ca collisions at E/A=40 MeV and b=2 fm with the soft EOS and $\sigma_{nn} = 41$ mb projected in the $x - z$ plane in step of 20 fm/c.

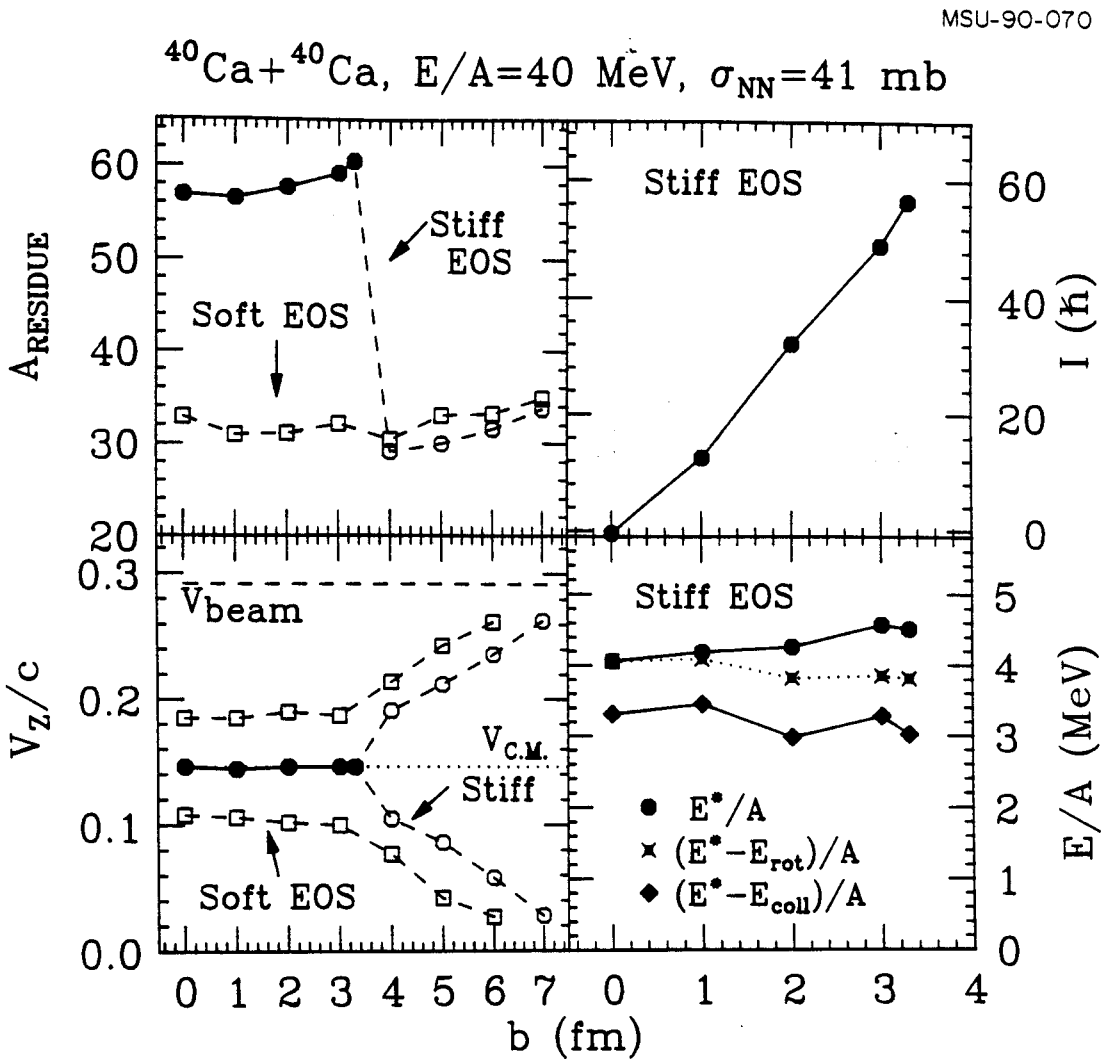

Figure 6.3: Observables calculated for the ^{40}Ca+ ^{40}Ca system at E/A=40 MeV assuming $\sigma_{nn} = 41$ mb. Upper left: Mean residue masses. Lower left: Component of the mean residue velocity parallel to the beam. Upper right: Mean residue angular momentum for the stiff EOS. Lower right: Mean residue total excitation energy/nucleon (solid points), after subtracting the rotational energy (crosses), and after subtracting the total collective energy (solid diamonds) for calculations with the stiff EOS. The lines are drawn to guide the eye.

their velocities and masses reduced due to insufficient nuclear stopping for the soft EOS at this energy. The right-hand panels of this figure will be discussed in the next section.

B Sensitivity of Fusionlike Cross Sections to The Equation of State

The energy dependences of the heavy residue cross sections for ^{40}Ca+^{40}Ca collisions with soft and stiff equations of state are indicated respectively by the solid squares and solid points in the upper half of Fig. 6.4. Each symbol (square or point) is obtained from the largest calculated impact parameter b_{max} which yields massive fusion-like residues; the upper edge of each vertical bar corresponds to the smallest calculated impact parameter b_{II} which yields distinct projectile- and target-like residues. These critical parameters, b_{max} and b_{II} , are listed in Table 6.1. As an example, Fig. 6.5 shows the time evolution of the bound test particles for ^{40}Ar +^{27}Al collisions at E/A=30 MeV at the critical parameters, b_{max} = 4.3 fm (left two columns) and b_{II} = 4.5 fm (right two columns). For a constant nucleon-nucleon cross section of 41 mb, the cross sections for fusion-like residues are larger for calculations with the stiff EOS.

To see which part of the equation of state is responsible for the varying fusion cross sections, we performed calculations at E/A = 40 MeV with equations of state having variable low- and high-density behavior. For example, we define a soft-stiff equation of state which follows the soft EOS at low density and the stiff EOS at high density. The parameterizations for this and the analogous stiff-soft equation of state are given in Table 6.2. The ^{40}Ca+^{40}Ca heavy residue cross sections obtained with these EOS's, 330 $\pm$ 30 mb for stiff-soft and 120 $\pm$ 20 mb for soft-stiff, show that the residue cross section depends mainly on the low density EOS.

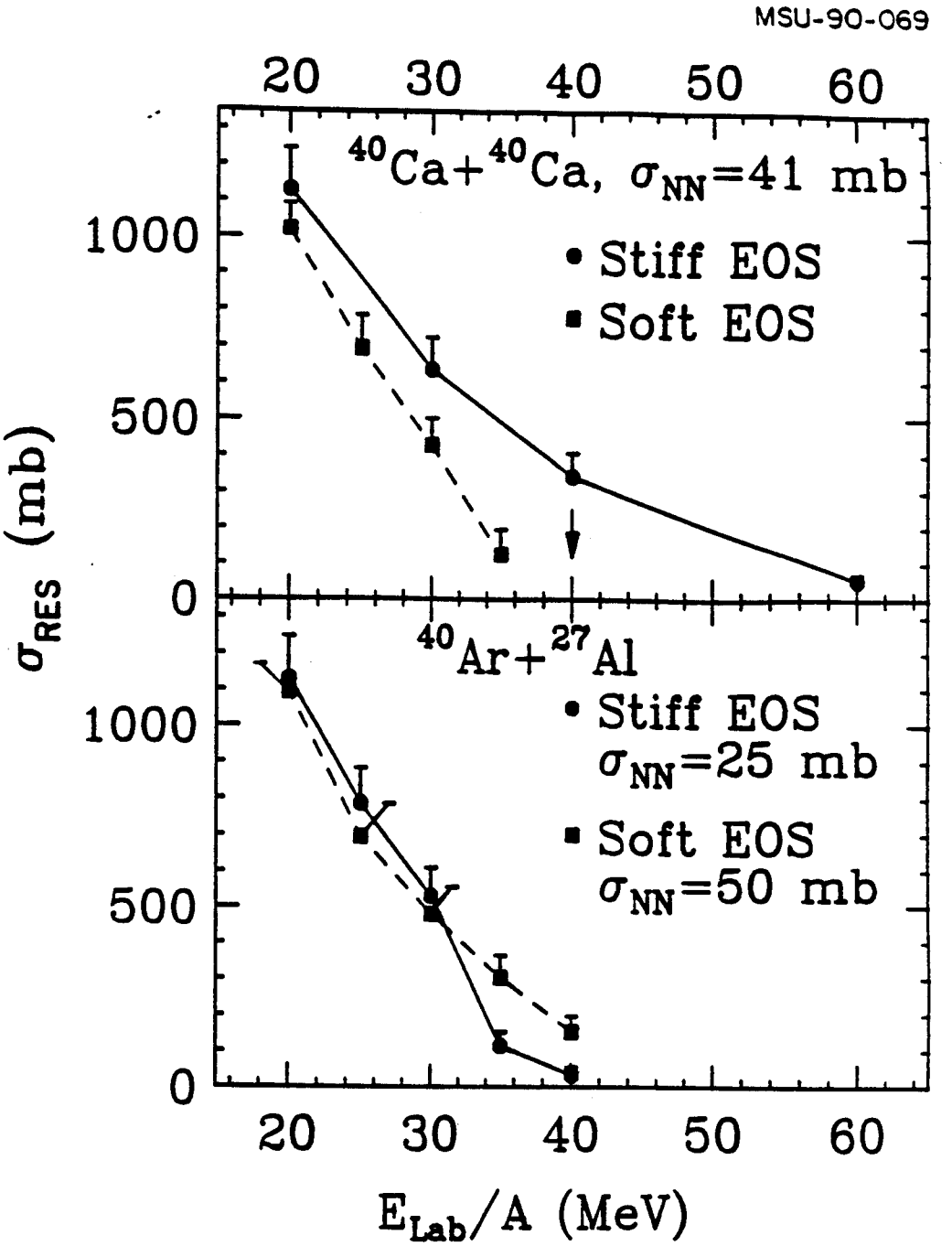

Figure 6.4: Upper half: Residue cross sections for ^{40}Ca+ ^{40}Ca collisions. The arrow indicates zero cross section for soft EOS. Lower half: Residue cross sections for ^{40}Ar+^{27}Al collisions. The solid points and solid squares describe calculations with the stiff and soft equations of state, respectively. The lines are drawn to guide the eye.

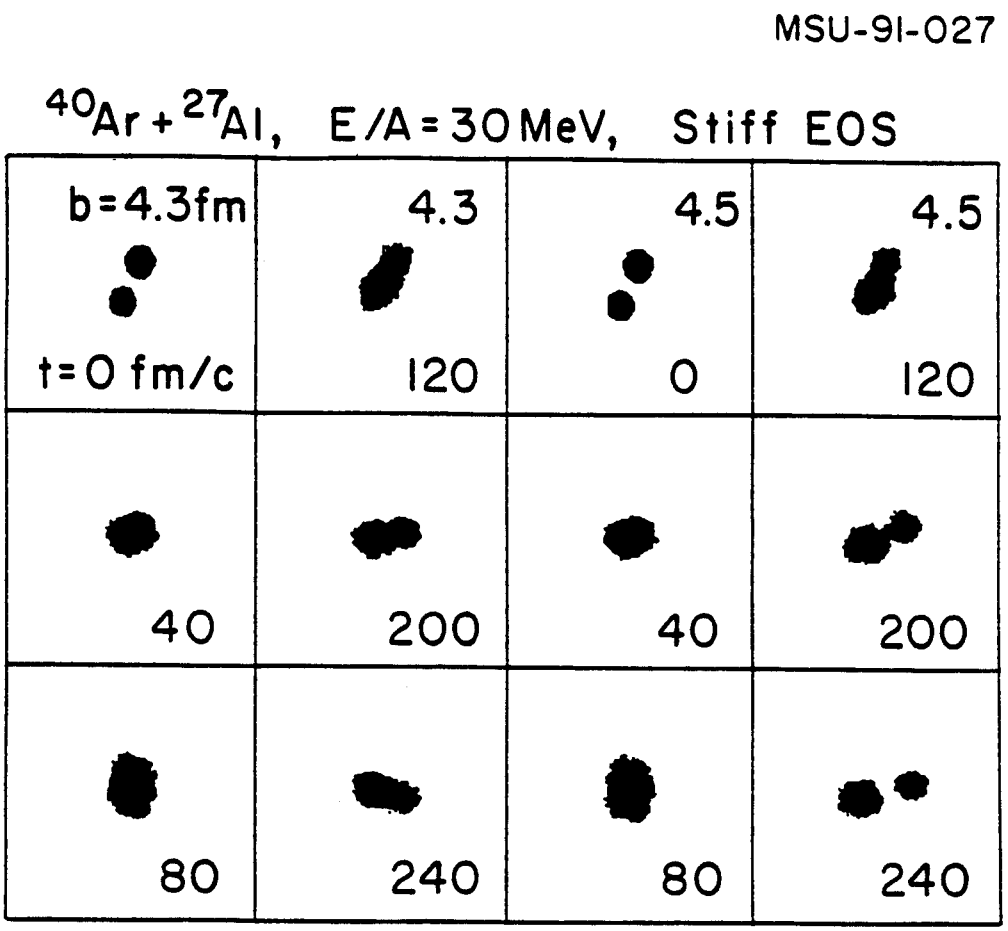

Figure 6.5: The time dependent spatial evolution of ^{40}Ar+^{27}Al collisions at E/A= 30 MeV at the critical impact parameters, $b_{max} = 4.3$ fm (left two columns) and $b_{II} = 4.5$ fm (right two columns). The time at which the density is plotted is indicated in the each panel. The free particles have been suppressed.

This sensitivity to the low-density EOS could have been anticipated from the qualitative study of ref. [Bert 78]. There it is shown that compression of nuclear matter in one-dimensional collisions is followed by a rarefaction, and the maximum tensile strength of the nuclear matter in the low-density phase depends on the EOS. Stiffer equations of state have higher tensile strengths, and so the tendency of the system to breakup into two or more fragments is less.

A possible determination of the low-density EOS on the basis of the cross sections for residue formation is hindered by the fact that these cross sections are also sensitive to σ_{nn}. To illustrate the possible theoretical ambiguities, calculations were performed for the ^{40}Ar+ ^{27}Al system in which the value for σ_{nn} was adjusted separately for calculations with both stiff and soft equations of state to obtain residue cross sections of about 500 mb at E_{lab}/A = 30 MeV. These choices, (1) σ_{nn}= 25 mb and a stiff EOS and (2) σ_{nn} =50 mb and a soft EOS, provide essentially equal residue cross sections at E/A $\leq$ 30 MeV. The critical parameters are listed in Table 6.3. The energy dependence of the residue cross sections predicted by both calculations is qualitatively consistent with experimental observations. Differences between the two sets of calculations at $E_{lab}/A \geq$ 30 MeV may not be large enough to discriminate between different equations of state. One must also assess the differences that could arise from variations in the energy dependence in the in-medium nucleon-nucleon cross section.

Table 6.1: The critical parameters for fusionlike reactions in ^{40}Ca+^{40}Ca collisions. The nucleon-nucleon cross section are taken to be $\sigma_{nn} = 41$ mb for both calculations.

EOS	E/A (MeV)	b_{max} (fm)	b_{II} (fm)
stiff	20	6.0	6.3
	30	4.5	4.8
	40	3.3	3.5
	60	1.3	1.5
soft	20	5.8	5.9
	25	4.8	5.0
	30	3.7	4.0
	35	2.0	2.5

Table 6.2: Parameters used for the isoscalar nuclear Mean Field

Set	Label	range	A(MeV)	B(MeV)	γ	K($\rho = \rho_0$)(MeV)
1	soft	$0 < \rho/\rho_0 < B$	356	303	7/6	200
2	stiff	$0 < \rho/\rho_0 < B$	124	70.5	2	375
3	soft-stiff	$\rho/\rho_0 < 1.024$	356	303	7/6	
		$1.024 < \rho/\rho_0$	124	70.5	2	
4	stiff-soft	$\rho/\rho_0 < 1.024$	124	70.5	2	
		$1.024 < \rho/\rho_0$	356	303	7/6	

Measurements of additional observables may help to reduce these ambiguities. For example, the top panel in Fig. 6.6 shows the corresponding predictions for the ratio of the yield of nucleons emitted in the reaction plane over the yield emitted out of the reaction plane for center of mass angles, $30° \leq \theta_{c.m.} \leq 150°$, and energies, $E_{c.m.} \geq 20$ MeV . Calculations with the soft EOS and $\sigma_{nn} = 50$ mb are more isotropic. The greater isotropy of calculations with larger σ_{nn} is also manifested in the dependence of the mean transverse momentum of emitted nucleons upon rapidity, shown in the bottom panel of Fig. 6.6. Significantly larger transverse momenta are predicted at $Y \leq Y_{beam}$ for calculations with smaller values for σ_{nn}. Even larger anisotropies would be expected for deuterons, tritons or α particles within the coalescence approximation for cluster emission. Given advances in the treatment of cluster production, such large anisotropies in the emission of the heavier hydrogen and helium isotopes could provide significant constraints on σ_{nn} and consequently, on the EOS, if anisotropy measurements are combined with heavy residue cross sections.

Some caution must be exercised when comparing these residue cross sections to experimental data. Since the BUU equation is a one-body theory and it does not have sufficient fluctuations, it can only calculate the average trajectories and cannot fully handle the subsequent decay of the residues formed during the collisions. Therefore, all residue decay channels, including the binary emission of heavy fragments, [Plag 89, Frie 80, More 72] must be experimentally measured and summed before comparisons to the calculated cross sections of Fig. 6.4 can be made. Additional investigations are necessary to assess whether prompt multi-fragmentation processes, not considered by the present Boltzmann code, remove flux from the reaction trajectories that lead to heavy residue formation in the present calculations. Investigations are also required to assess the sensitivity of the residue cross sections to details of the Pauli-blocking algorithm and the surface energies of the computational nuclei.

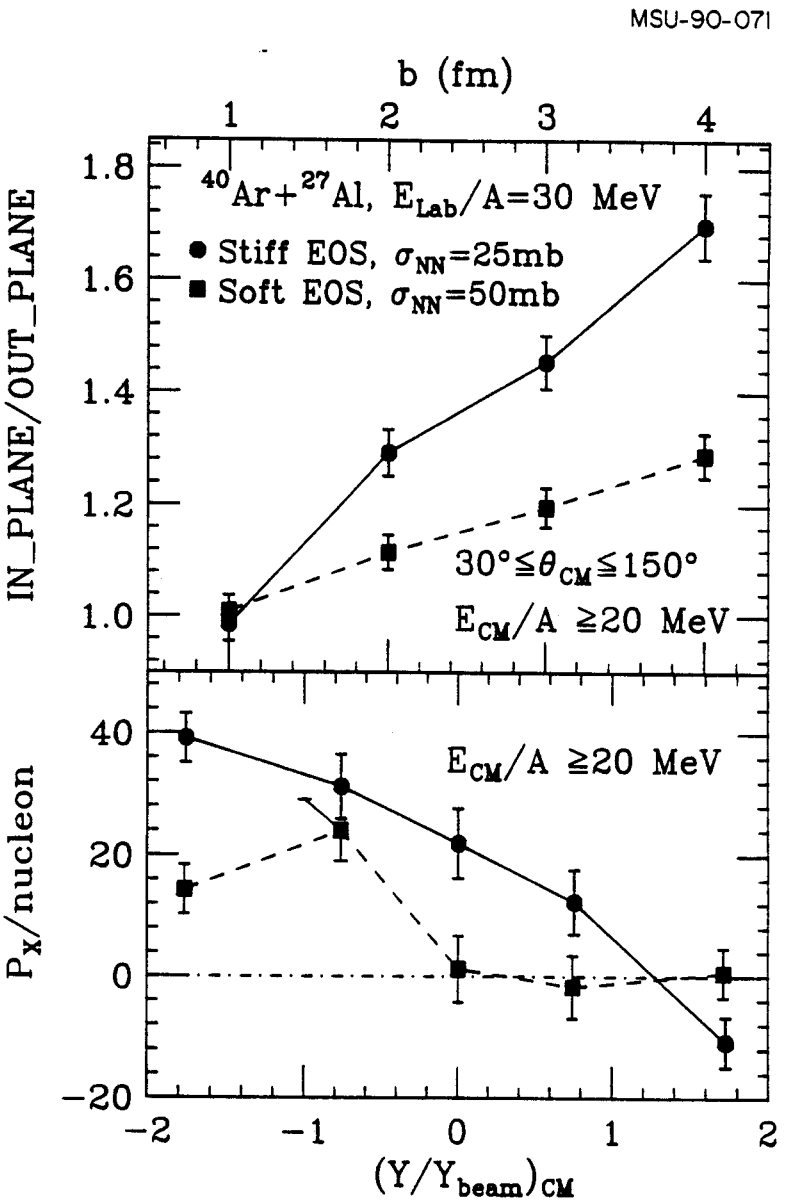

Figure 6.6: In/out-of-plane ratios and mean transverse momenta for unbound nucleons with $E_{c.m.} \geq 20$ MeV from calculations for the $^{40}Ar+^{27}Al$ system at E/A = 30 MeV for σ_{nn} =25 mb with a stiff EOS (solid points) and σ_{nn} =50 mb with a soft EOS (solid squares). Upper half: Ratios of the nucleon yield in the reaction plane (azimuthal angles $-30° < \phi < 30°$ and $150° < \phi < 210°$ to the nucleon yield out of the reaction plane ($60° < \phi < 120°$ and $240° < \phi < 300°$) for the polar angles $30° < \theta_{c.m.} < 150°$ Lower half: The component of the mean transverse momentum of unbound nucleons in the reaction plane as a function of rapidity. A weighted sum over impact parameters $b \leq 4$ fm has been performed. The lines are drawn to guide the eye.

Table 6.3: The critical parameters for fusionlike reactions in ^{40}Ar+^{27}Al collisions. Two sets parameters, (1) stiff EOS and σ_{nn} = 25 mb; and, (2) soft EOS and σ_{nn} = 50 mb, are used to produced the same fusion cross section at E/A=30 MeV.

EOS	E/A (MeV)	b_{max} (fm)	A_{max} (a.m.u.)	I_{max} (a.m.u.)$\cdot fm^2$	J_{max} ($\hbar$)	b_{II} (fm)	I_{II} (a.m.u.)$\cdot fm^2$	J_{II} ($\hbar$)
stiff	20	6.0	60	1118	75	6.3	1381	79
	25	5.0	58	980	64	5.3	1204	69
	30	4.3	56	1141	57	4.5	1298	64
	35	2.0	54	972	25	2.2	1170	31
	40	1.2	50	953	15	1.3	1084	18
soft	20	6.0	58	1277	68	6.1	1495	71
	25	4.7	54	1006	52	5.0	1215	57
	30	4.0	52	1081	46	4.2	1314	51
	35	3.3	49	1116	37	3.4	1203	43
	40	2.4	44	800	21	2.5	1213	28

II Entrance Channel Effects and the Formation of Hot Nuclei

In this section, we will examine in further detail the possible origins for the dynamical limitations to the formation of fusionlike residues. For such purpose, we present the excitation energies and the angular momenta for the fusionlike residues formed in ^{40}Ar+^{27}Al collisions. In this study, we will continue to use the following two sets of parameters: (1) σ_{nn}= 25 mb and a stiff EOS and (2) σ_{nn} =50 mb and a soft EOS, with which almost equal fusion cross sections have been produced at E/A$\simeq 25-40$ (see the last section).

A Decomposition of the Excitation Energy

Since the residue continues to decay after its formation, the residue masses, excitation energies and angular momenta are sensitive to the freezeout time at which observables are evaluated. To indicate how this freezeout time was chosen and how to estimate the thermal energy of the residue, we decompose the total energy E_{tot}, calculated from Eq. (5.15), into collective E_{coll} and internal E_{int} components,[Rema 88]

$$E_{tot} = H = E_{coll} + E_{int}. \tag{6.1}$$

the collective energy is estimated by

$$E_{coll} = \frac{1}{2} m \int \frac{\vec{j}^2(\vec{r})}{\rho(\vec{r})} d^3r, \tag{6.2}$$

where $\rho(\vec{r})$ and $\vec{j}(\vec{r})$ are the local density and local collective current field defined as

$$\rho(\vec{r}) = \frac{1}{(2\pi\hbar)^3} \int f(\vec{r},\vec{p},t) d^3p, \tag{6.3}$$

$$\vec{j}(\vec{r}) = \frac{1}{(2\pi\hbar)^3} \int \frac{\vec{p}}{m} f(\vec{r},\vec{p},t) d^3p, \tag{6.4}$$

The internal energy E_{int} can be decomposed into a thermal excitation energy E^*_{the} and a "cold" internal energy $E_{int}(T=0, A_{res})$:

$$E_{int} = E^*_{the} + E_{int}(T=0, A_{res}), \tag{6.5}$$

where A_{res} denotes the residual mass of interest, and, $E_{int}(T=0, A_{res})$, obtained for a cold nucleus with the same density distribution $\rho(\vec{r})$, includes both the kinetic energy density $\tau(\vec{r})$ due to Fermi motion (required by the Pauli exclusive principle) and the potential energy density $v(\vec{r})$:

$$E_{int}(T=0, A_{res}) = \int [\tau(\vec{r}) + v(\vec{r})] d^3r. \tag{6.6}$$

in the Thomas-Fermi limit $\tau(\vec{r})$ has the form

$$\tau(\vec{r}) = \frac{3}{10}(3\pi^2)^{2/3}\frac{\hbar^2}{m}[\rho_p^{5/3}(\vec{r}) + \rho_n^{5/3}(\vec{r})], \tag{6.7}$$

and, the potential energy density $v(\vec{r})$, given by Eq. (5.13), includes both nuclear and Coulomb interactions.

It is instructive to consider the various excitation energy components contained in Eqs. (6.1)-(6.6) for the case of an isolated nucleus at its ground state. Obviously such a nucleus should have no collective energy, $E_{coll} = 0$, and no thermal excitation energy, $E^*_{the} = 0$. The total energy E_{tot} is therefore equal to the internal energy $E_{int}(T=0, A_{res})$ of a ground state nucleus with a central density $\rho = \rho_0$. (In our later discussions, we denote this energy of ground state by $E_{g.s.}(A_{res})$. Obviously, $E_{g.s.}(A_{res})/A_{res}$ has an average value of about -8 MeV as shown in Fig. 5.2). In numerical computations, however, particular care has to be taken to eliminate spurious contributions due to finite statistics of test particles. Because of finite number of test particles at each lattice point, calculations of the local current $\vec{j}(\vec{r})$ via Eq. (6.4) would yield non-zero values even if the whole nucleus is at rest. This would yield a

positive value for the collective energy E_{coll} by using Eq. (6.2). This effect, due to finite statistics, can be analyzed using techniques similar to those developed by Goldhaber in his treatment of projectile fragmentation [Gold 74]. We have compared the Goldhaber technique with a more direct approach discussed in Appendix A, and we find that both methods give essentially the same values. By subtracting this spurious contribution from the collective energy, we checked that the application of equations (6.1)-(6.6) always yields zero collective energy for an isolated nucleus in its ground state. Such corrections to the collective energy have been taken into account in all our calculations.

In analyzing the excitation energy at different stages of nucleus-nucleus collisions, it is frequently useful to separate the test particles bound in a residue from those which are free. The analysis of the free test particles is simple. Following our previous decomposition, free test particles have no thermal excitation energy $E^*_{the} = 0$ and no cold Fermi energy (since $\rho = 0$). Their contribution to the total energy E_{tot} consists of only their kinetic energies which appear, in our analysis, as a contribution to E_{coll} following Eq. (6.2). For later reference, we separate out this collective (or total) energy of free particles and denote it by $E_{nucleon}$.

When the local density of a given test particle exceeds $\rho \geq 7\%\rho_0$, we consider this test particle to be part of a bound cluster. Bound test particles contribute to all terms of Eqs. (6.1)-(6.6). The total mass A_{res} and the total energy E_{tot} of a composite residue can be determined by

$$A_{res}(t) = \int_C \rho(\vec{r}) d^3r \tag{6.8}$$

$$E_{tot}(A_{res}) = \int_C d^3r \{\frac{1}{(2\pi\hbar)^3}[\int \frac{p^2}{2m} f(\vec{r},\vec{p},t) d^3p] + v(\vec{r})\} \tag{6.9}$$

Here, $v(\vec{r})$ is the potential energy density given by Eq. (5.13). We define the total *excitation* energy of the residue to be the difference between $E_{tot}(Ares)$ and the energy

$E_{g.s.}(A_{res})$ of a computational nucleus of the same mass A_{res} in its ground state and moving at the same c.m. velocity:

$$E^* = E_{tot}(A_{res}) - E_{g.s.}(A_{res}) - \frac{1}{2}A_{res}mV_{res}^2 \tag{6.10}$$

where V_{res} is the c.m. velocity of the residue and m is the mass of a nucleon. We are especially interested in the portion of excitation energy which can be considered thermal in origin. For this purpose, it is useful to separate out the two non-thermal contributions, E^*_{coll} and E_{comp}, from the total excitation energy $E_{tot}(A_{res})$. Here, the first contribution E^*_{coll} is the collective energy of the residue as observed at the rest frame of the residue. It can be evaluated easily by performing the integral in Eq. (6.2) over the volume, yielding E_{coll}, and subtracting from it the translational energy of the c.m. motion of the residue:

$$E^*_{coll} = E_{coll} - \frac{1}{2}A_{res}mV_{res}^2 \tag{6.11}$$

The compression energy E_{comp} is the difference between the internal energy of a cold nucleus with density distribution $\rho(\vec{r},t)$ and that of the corresponding g.s. nucleus

$$E_{comp} = E_{int}(T=0, A_{res}) - E_{g.s.}(A_{res}) \tag{6.12}$$

Obviously, E_{comp} is non-zero only when the density distribution of the residue differs significantly from that of the corresponding g.s. nucleus. Subtracting E^*_{coll} and E_{comp} from E^*, one can obtain the thermal energy E^*_{the} of the residue

$$E^*_{the} = E^* - E_{comp} - E^*_{coll} \tag{6.13}$$

To understand the dynamics governing the formation of the residues, it is sometimes instructive to decompose the collective energy E^*_{coll} of the residue, see Eq. 6.13, into a rotational component E_{rot} and a non-rotational component $E_{n.r.}$,

$$E^*_{coll} = E^*_{rot} + E^*_{n.r.} \tag{6.14}$$

Here, the rotational energy E^*_{rot} is estimated by

$$E^*_{rot} = \frac{J^2}{2I} \tag{6.15}$$

where J is the angular momentum of the residue A_{res} calculated by

$$\vec{J} = \frac{1}{(2\pi\hbar)^3}\int_C (\vec{r}' \times \vec{p}')f(\vec{r}', \vec{p}')d^3r'd^3p' \tag{6.16}$$

and $\vec{r}'$ and $\vec{p}'$ are defined in a coordinate system centered at center of mass of the residue. In our simulations, we choose the $x-z$ plane as the reaction plane and therefore the total angular momentum lies along the y axis. For the residue nucleus, we also found that the angular momentum of the residue are nearly parallel to the y-axis. We therefore neglect rotations about the x and y axis axis and we approximate the rigid body moment of inertia by

$$I \approx I_{yy} = \int_C (x^2 + z^2)\rho d^3r \tag{6.17}$$

Examples of values of I and J calculated in this approximation for ^{40}Ar+^{27}Al collisions were listed in Table 6.3.

After the decomposition of Eq. (6.14), the total excitation energy E^* now has the following components

$$E^* = E^*_{coll} + E^*_{the} + E_{comp} = E^*_{rot} + E^*_{n.r.} + E_{comp} + E^*_{the} \tag{6.18}$$

Since the rotational energy E^*_{rot} is associated with the motion in the tangential direction, the non-rotational energy $E^*_{n.r.}$ is therefore primarily associated with radial motion. This non-rotational energy could originate from the excitation of giant resonances, with dominant contribution, argued by Remaud *et al*, from monopole oscillations [Rema 88].

Using Eqs. (6.1)-(6.18), we can explore how one may define an appropriate time for thermal freezeout. The decomposition by Eq. (6.9)-(6.18) can also provide information concerning the dynamics for the formation of the heavy residues. In the next few subsections, we will use the decomposition to consider whether the rotations or thermal instabilities place limitations on the formation of heavy residues.

B Freezeout Conditions

Since the pre-equilibrium and equilibrium emissions are both present in intermediate nucleus-nucleus collisions, one needs to know whether the thermal freezeout is indeed reached and whether one can define a freezeout time unambiguously. To investigate this, we describe, in the following three subsections, three distinctive criteria used to define the thermal freezeout time. Two of these criteria, the emission rate and the thermal excitation energy, were found to give consistent freezeout times. The third criterion, the quadrupole moment of the momentum distribution, did not provide a clear signature for the freezeout time, but was not inconsistent with the freezeout time determined from the other two criteria.

Emission Rate

In Fig. 6.7, we display the emission rate of nucleons as functions of time for ^{40}Ar+^{27}Al collisions at E/A=30 MeV. The solid and open circles in the figure depicted the calculations with the stiff and soft equations of state, respectively. The corresponding nucleon-nucleon cross sections are indicated in the figures. For all calculations, one observes large emission rates at t $\simeq$ 60$-$80 fm/c. These large emission rates reflect the fast pre-equilibrium emission of nucleons before the system reach equilibrium. The emission rate, at $t \geq$ 100 fm/c for stiff EOS, and $t \geq$ 120 fm/c, is significantly reduced and changes very slowly, suggesting a slow statistical emission from the reaction

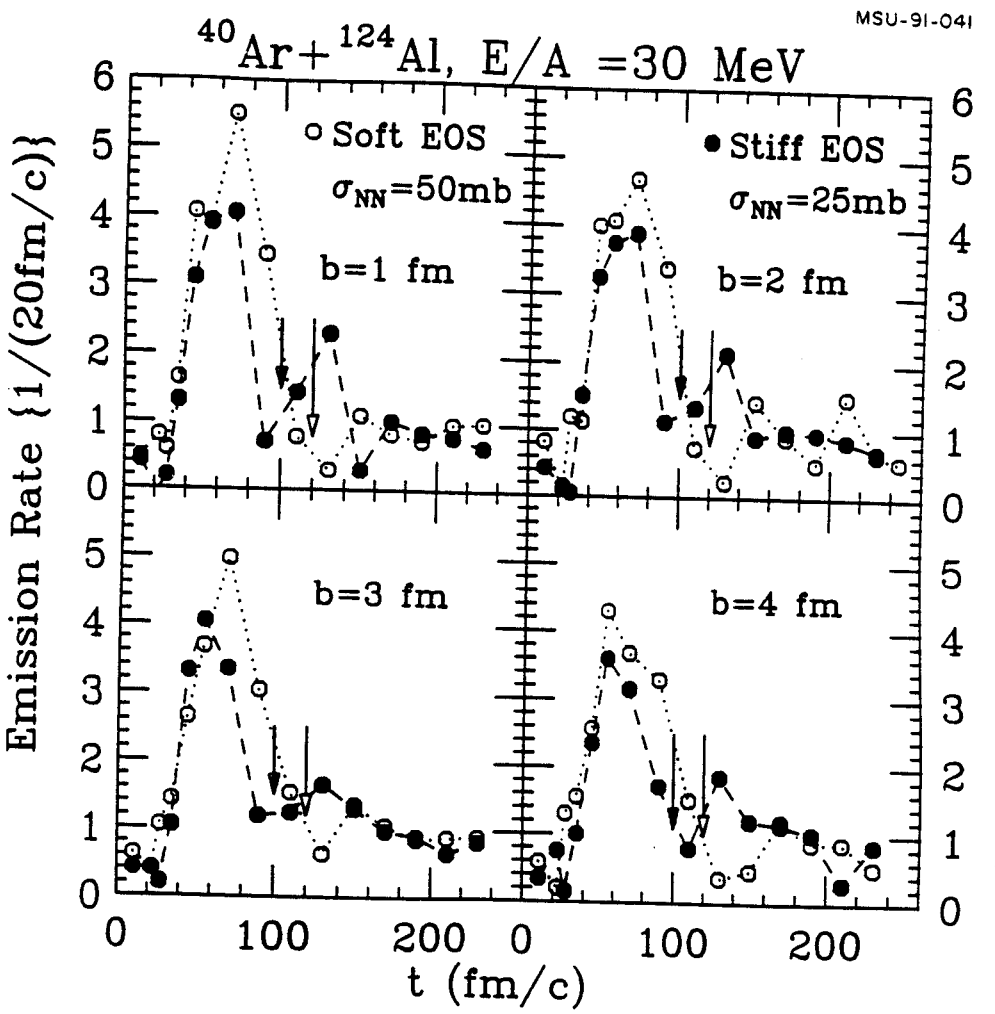

Figure 6.7: The emission rates of ^{40}Ar+^{27}Al collisions at E/A=30 MeV for impact parameters b=1-4 fm. The solid circles are results with stiff EOS and σ_{NN} = 25mb. The open circles are results with soft EOS and σ_{NN} = 50mb. The corresponding freezeout times are indicated by the arrows (solid for stiff EOS and open for soft EOS). The respective lines are used to guide the eyes.

residue. The emission at later times is modulated by the influence of macroscopic vibrations which can be clearly seen in the Qzz plot (Fig. (6.10)). We will come back to this point. The solid and open arrows in Fig. 6.7 indicate the freezeout times selected by this criterion for the calculations with the stiff and soft equations of state. These freezeout times are consistent with the freezeout times obtained from the thermal excitation energy of the residues described below.

Thermal Excitation Energies

In general, one expects the temperature or the thermal excitation energy of a hot equilibrated nucleus to decrease with time via evaporative cooling. Assuming this evaporative cooling is properly described by sequential decay calculations like those described in chapter 4, the emission temperature should depend on the maximum thermal energy at the end of the preequilibrium stage of the reaction. This provides a second criterion for choosing the freezeout time. In Figs. 6.8-6.9, we display the various contributions to the excitation energy for ^{40}Ar+^{27}Al collisions at E/A=30 MeV assuming a soft EOS (Fig. 6.8) and a stiff EOS (Fig. 6.9), respectively. Several features of the reaction dynamics are immediately apparent. First, from the time dependence of potential energy (bottom curve), it is clear that the system undergoes a compression during first 40 fm/c, and afterwards an expansion between 40 fm/c $\leq t \leq$ 80 fm/c, and finally a relaxation to a more tightly bound state at 120 fm/c (100 fm/c for stiff EOS). The binding energy $E_{int}(T = 0)$ (third curve from the bottom) exhibits a similar behavior at a smaller scale. Second, the energy of free particles increases rapidly after $t \geq$ 40 fm/c, suggesting much of the collective energy E_{coll} is taken away by particle emission. Finally, the thermal energy E^*_{the}, which is of our particular interest, exhibits two maxima: one global maximum at t$\approx$ 40fm/c and one local maximum at t_{fre} = 120 fm/c (t_{fre} = 100 fm/c for stiff EOS). The maximum at t$\approx$

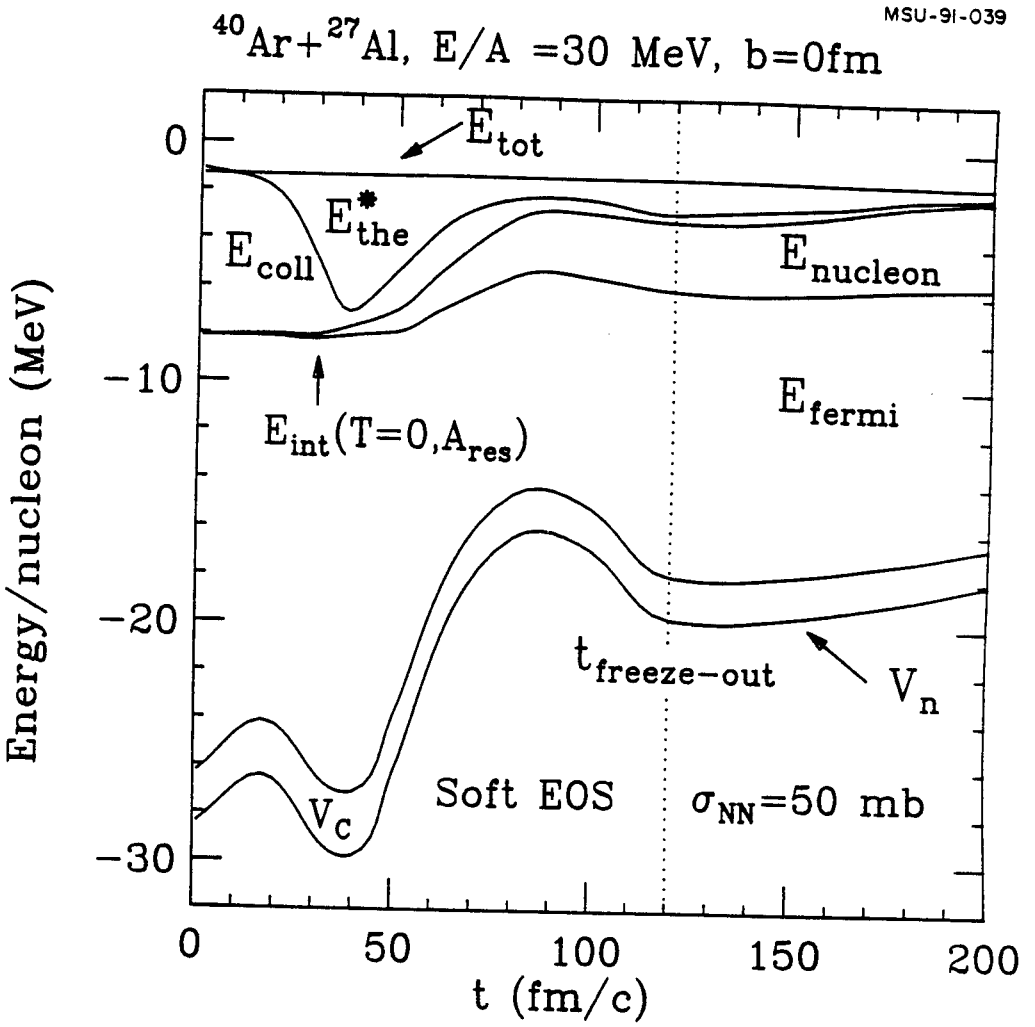

Figure 6.8: Decomposition of the various excitation energies as a function of time for ^{40}Ar+^{27}Al collisions with the soft equation of state at E/A=30 MeV, b=0 fm. The bottom line is the nuclear potential energy. From this bottom line up are,respectively, Coulomb energy (difference between the second and the bottom lines), Fermi energy required by the Pauli exclusion principle (difference between the third and second lines), kinetic energy of emitted particles (difference between the fourth and third lines), collective energy of bound nucleons (difference between the fifth and fourth lines) and thermal energy (difference between the top and fifth lines). The freezeout time is indicated by the dotted line.

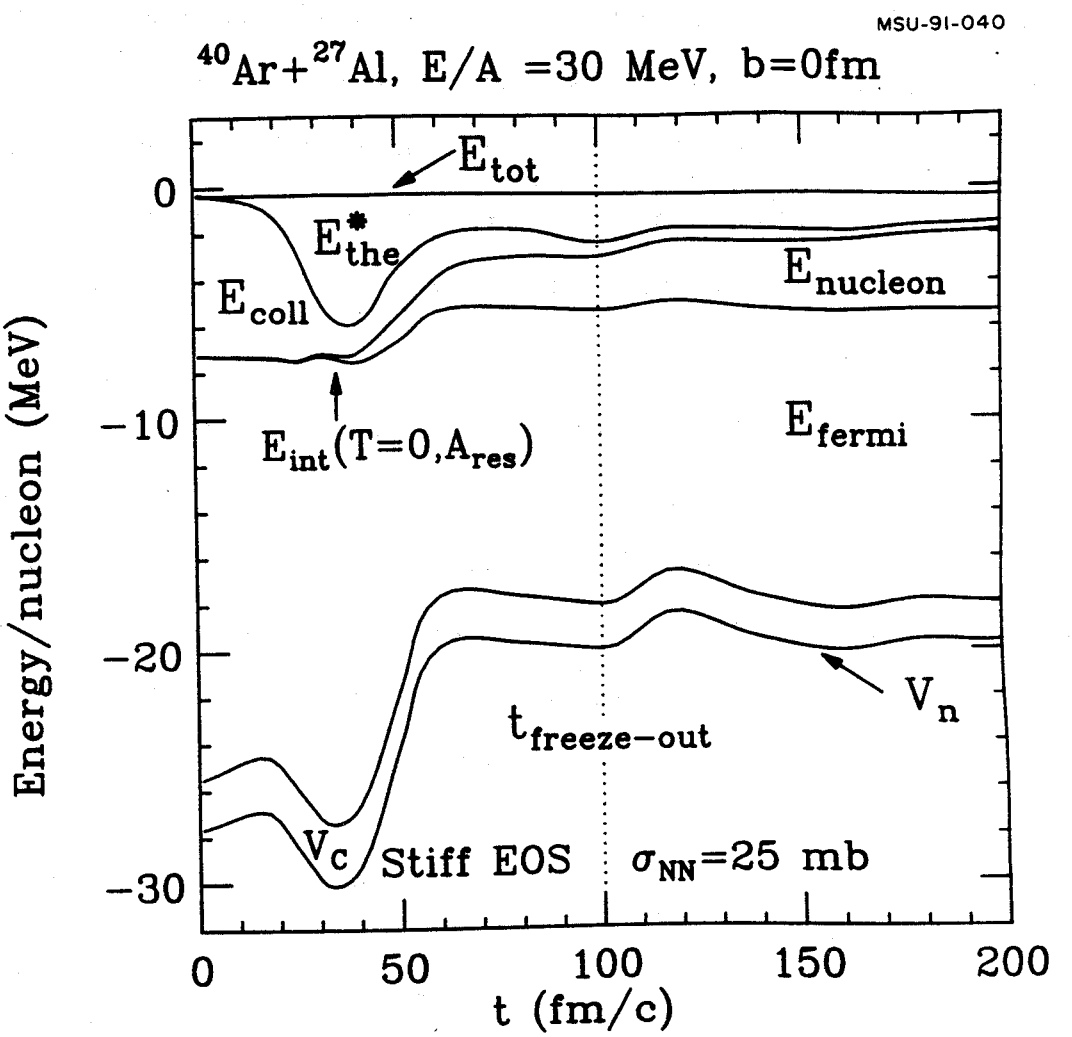

Figure 6.9: Decomposition of various excitation energies as a function of time for ^{40}Ar+^{27}Al collisions with the stiff equation of state at E/A=30 MeV, b=0 fm. The bottom line is the nuclear potential energy. From this bottom line up are,respectively, Coulomb energy (difference between the second and the bottom lines), Fermi energy required by the Pauli exclusion principle (difference between the third and second lines), kinetic energy of emitted particles (difference between the fourth and third lines), collective energy of bound nucleons (difference between the fifth and fourth lines) and thermal energy (difference between the top and fifth lines). The freezeout time is indicated by the dotted line.

40fm/c is an artifact of the initial momentum distributions, in which the longitudinal velocities of the projectile and the target nuclei cancel each other, causing a minimum in the computation of the collective energy. At the second maximum, the initial preequilibrium stages have finished and residue has already contracted to a more compact spacial configuration and the thermal energy at its local maximum. After this time, the thermal energy gradually decreases. Due to the evaporative cooling, we take the freezeout time to be the time of the second maximum in the thermal energy. This time is consistent with the time determined by the change in the nucleon emission rate shown in Fig. 6.7.

It is interesting to note that the freezeout time is largely determined by the relaxation time of the surface of the residue. Residues calculated with stiff equation of state, which has a larger restoring force and a larger sound speed, contracts to a compact configuration more rapidly than the residues calculated with soft equation of state. The excitation energies left in the residues are higher for residues characterized by a stiff EOS because they have less time for preequilibrium cooling.

Momentum Distributions

A third measure for defining the freezeout time may be obtained by the quadrupole moment of momentum distribution [Cass 87, Baue 87]:

$$Q_{zz}(t) = \frac{1}{(2\pi\hbar)^3} \int d^3r d^3p (2p_z^2 - p_x^2 - p_y^2) f(\vec{r}, \vec{p}, t) \tag{6.19}$$

This criterion is motivated by the belief that a system in thermal equilibrium should satisfy $Q_{zz} = 0$. To see how this variable changes with time, we plot Q_{zz} in the bottom panels of Fig. 6.10 as a function of time for ^{40}Ar+^{27}Al collisions at b=0 fm. For comparison, we show the emission rates in the top panels. The left hand panels show results obtained with the stiff equation of state. The right hand panels show

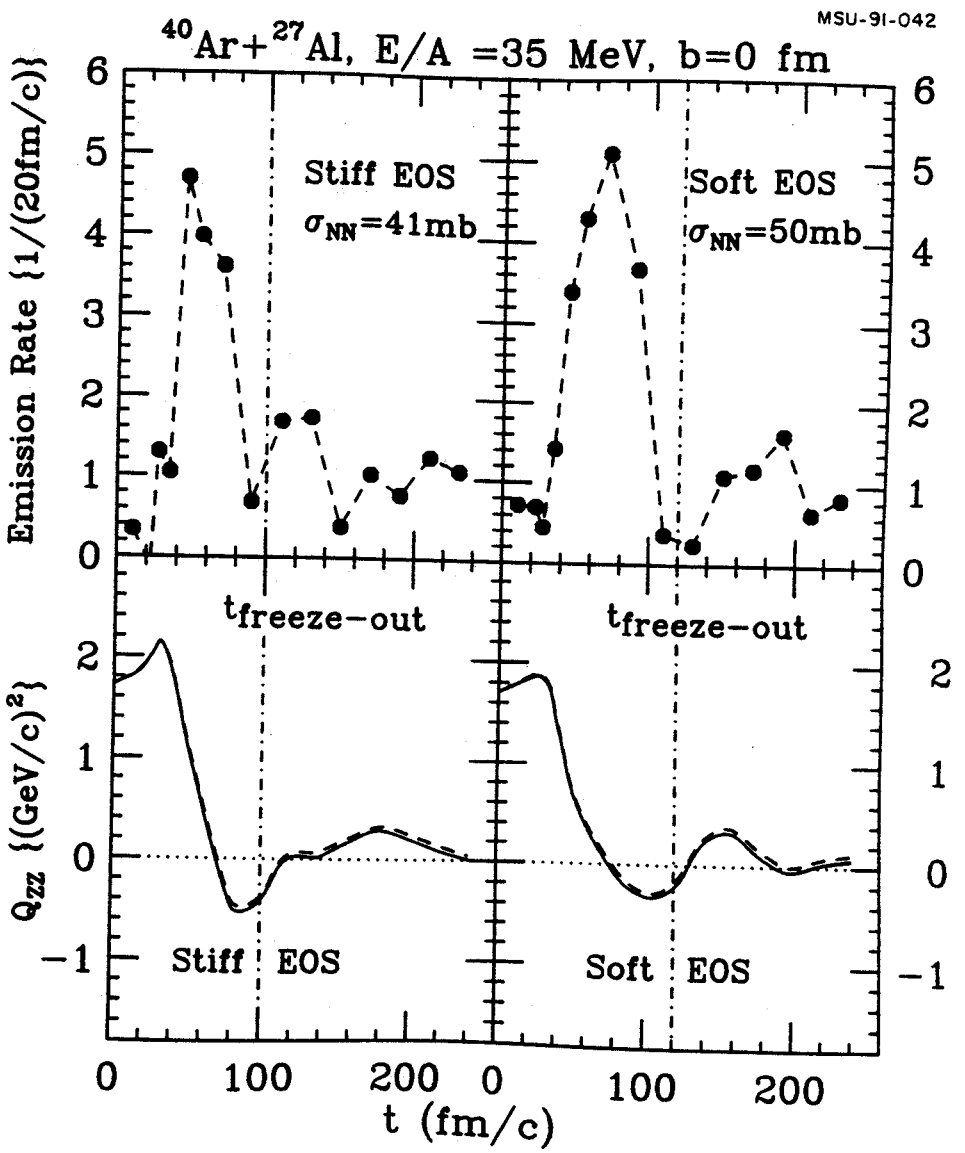

Figure 6.10: The emission rates of nucleons (top panels) and the quadrupole momentum distributions Q_{zz} (bottom panels), defined by Eq. (6.19), for ^{40}Ar+^{27}Al collisions at E/A=30 MeV, b=0 fm. The left panels (right panels) show the results for the stiff EOS (soft EOS). The vertical dot-dash lines indicate the freezeout time discussed in the text. The dashed lines in the bottom panels include the calculations for all nucleons, while the solid lines include only nucleons in the bound residues.

those from the soft equation of state. The dashed lines include all nucleons while the solid lines include the nucleons bound in the residual nuclei. Clearly at the t_{fre} defined previously, Q_{ZZ} is significantly reduced from its initial value at t=0. However, the values of Q_{ZZ} continue to oscillate about zero for a long time after thermal freezeout, reflecting the existence of macroscopic quadrupole vibrations. Such long term *collective* vibrations render Q_{ZZ} less useful in defining the *thermal* freezeout time.

In summary, a consistent freezeout time was obtained by checking three different variables. In the next few subsections, we will study the excitation energies and the angular momenta of residual nucleus at freezeout.

C Collisions at E/A=30 MeV

In Fig. 6.11, we show different contributions to the excitation energies of residues at freezeout as functions of the impact parameter for ^{40}Ar+ ^{27} Al collisions at E/A=30 MeV assuming alternatively the stiff (lower panel) or the soft (upper panel) equations of state. (A similar analysis was shown in lower right hand panel of Fig. 6.3 for ^{40}Ca+^{40}Ca system at E/A=40 MeV assuming stiff EOS.) The solid symbols in the figure represent the calculations in which a single heavy residue is observed in the final state. The open symbols represent calculations at larger impact parameters in which the system breaks up into projectile-like and target-like residues at a later time. The total excitation energy E^* (solid circles), calculated from Eq. (6.10) increases slightly with impact parameter. This increase can be partly attributed to the collective rotation. The crosses in Fig. 6.11 depict the excitation energy after the rotational energy E^*_{rot}, see Eq. (6.15), has been subtracted. The remaining part, $E^* - E^*_{rot}$, becomes constant for the central collisions where heavy composite residues were formed. We note here that the rotational energy E^*_{rot}, indicated by the difference

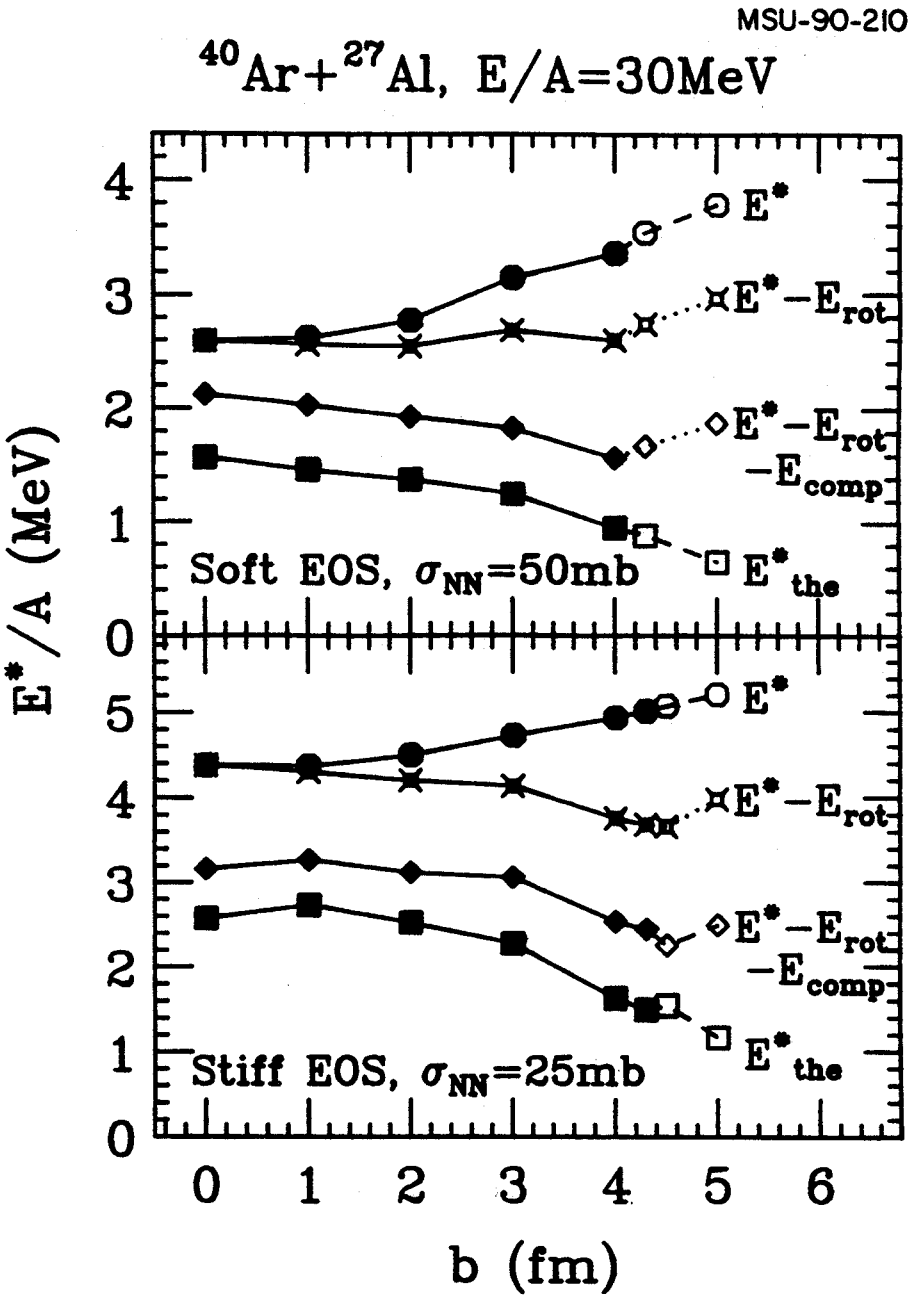

Figure 6.11: Decomposition of the predicted excitation energy at freezeout for different impact parameters in ^{40}Ar+^{27}Al collisions at E/A =30 MeV, assuming the soft EOS, (top panel) or the stiff EOS (lower panel). The solid and open symbols are explained in the text. The solid lines are drawn to guide the eye.

between the points and crosses, increases with impact parameter until reaching the maximum impact parameters for fusion, it then becomes constant at larger impact parameters. The constant behavior of E^*_{rot} at large impact parameters can be expected since the moment of inertia I scales as $I \sim b^2$, and the angular momentum J scales as $J \sim b$ at large impact parameters. Thus from Eqs. (6.15)-(6.17), one would expect constant values of E^*_{rot} at larger impact parameters.

The compressional energy, which corresponds to the difference between the crosses and the diamonds shown in Fig. 6.11, exhibits little dependence on the impact parameter. The collective energy $E^*_{n.r.}$, indicated by the difference between the diamonds and the squares, remains roughly constant for central fusionlike reactions at impact parameters at $b \leq 4$ fm. This constant value for fusionlike residues reflects the energy stored in macroscopic vibrations which may have a significant monopole components [Rema 88]. At larger impact parameters, $b \geq 4$ fm, the collective energy $E^*_{n.r.}$ increases with impact parameter suggesting an incomplete dissipation of the incident collective motion of projectile and target nucleons. It is this incomplete stopping, not the thermal instability, which cause a decrease in the residue cross section as the incident energy is raised.

The thermal excitation energy E^*_{the}, designated by the squares in Fig. 6.11, decreases slightly with impact parameter. Thus in these dynamical calculations, the formation of heavy residues for ^{40}Ar + ^{27}Al at E/A $\leq$ 30 MeV does not appear to be limited by the stability of the residual nucleus at high temperature. Indeed, in larger impact parameter collisions, where the residue formation is less likely, the intrinsic thermal energies are somewhat smaller.

Experimental investigation of excitation energy have been based on the massive transfer models [Lera 86, Auge 85, Nife85, Goni 89, Wada 89, Deco 90, Grif 90, Fahl 86, Bour 85, Gali 88] in which the measured residual velocities were used to es-

timate the excitation energies. In Fig. 6.12, we show the comparisons of the massive transfer models with the BUU calculations. The open points depict the results of massive transfer models (for details, see Appendix B) using the residue velocity from the BUU calculations. The massive transfer models significantly over-estimate the total excitation energy, suggesting the present BUU calculations are inconsistent with expectations of massive transfer models.

D Limiting Angular Momenta

Fig. 6.13 shows the total angular momenta for residues, obtained for both the stiff equation of state (solid circles) and the soft equation of state (squares), as a function of impact parameter for ^{40}Ar +^{27}Al collisions at E/A=30 MeV. The angular momentum increases linearly with impact parameter to a value of J_{max} ≈58 $\hbar$ at b=4.3 fm for stiff EOS (J_{max} ≈44 $\hbar$ at b = 4 fm for soft EOS), comparable to the maximum orbital angular momentum predicted by the liquid-drop model [Cohe 74, Ring 80] for mass A=56 (A=52 for soft EOS). Similar results were shown in the upper right panel of Fig. 6.3 for ^{40}Ca +^{40}Ca collisions with a stiff EOS. This suggests that the formation of a residue at E/A = 30 MeV may be partially limited by the maximum angular momentum that a nucleus can sustain.

To examine how the maximum angular momentum evolves with incident energy, we display, in Fig. 6.14, the energy-dependent residue masses (top windows) and the maximum angular momenta (bottom windows) for both the soft equation of state (right-hand side) and the stiff equation of state (left-hand side). At each energy, the solid symbol corresponds the maximum angular momentum J_{max} which occurred at the largest impact parameter b_{max} for which a fused residue is observed in the final state. The open symbol corresponds to the minimum angular momentum J_{II} calculated at slightly higher impact parameter b_{II} for which the system breaks up

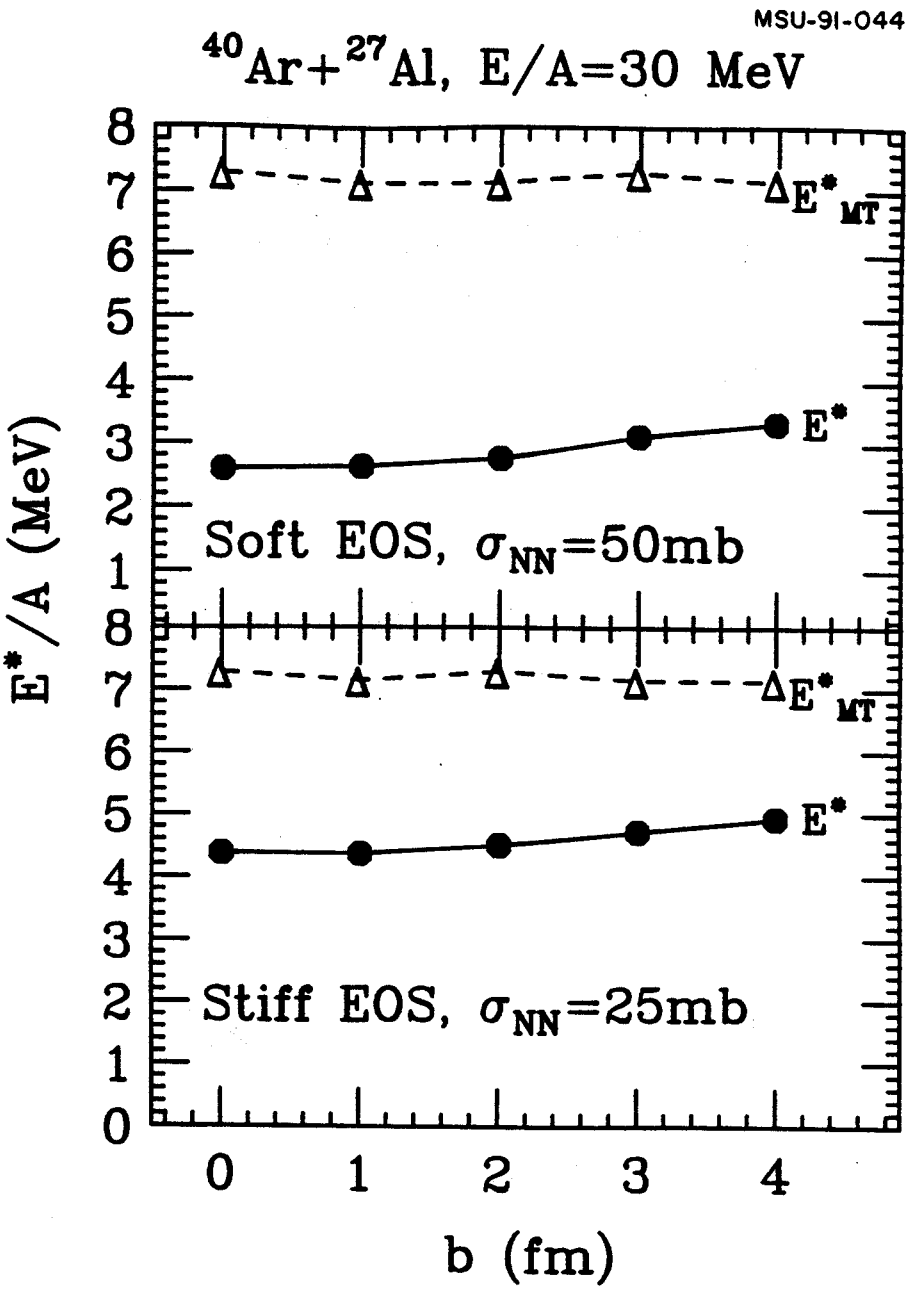

Figure 6.12: Comparisons of the total energy from BUU with that from massive transfer models in ^{40}Ar+^{27}Al collisions at E/A =30 MeV, see the text for the details

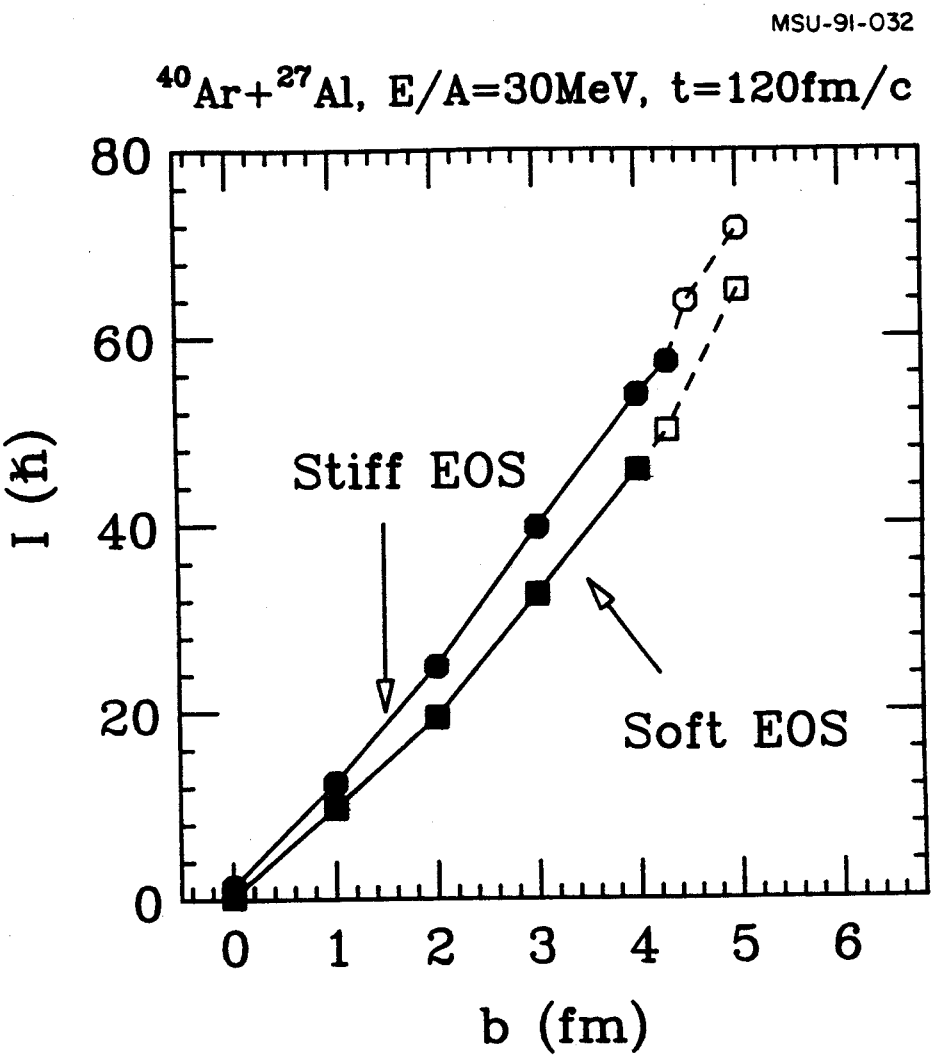

Figure 6.13: Angular momenta of residues as a function of impact parameter for calculations with the soft EOS (squares) and the stiff EOS (circles). The solid and open symbols are discussed in the text

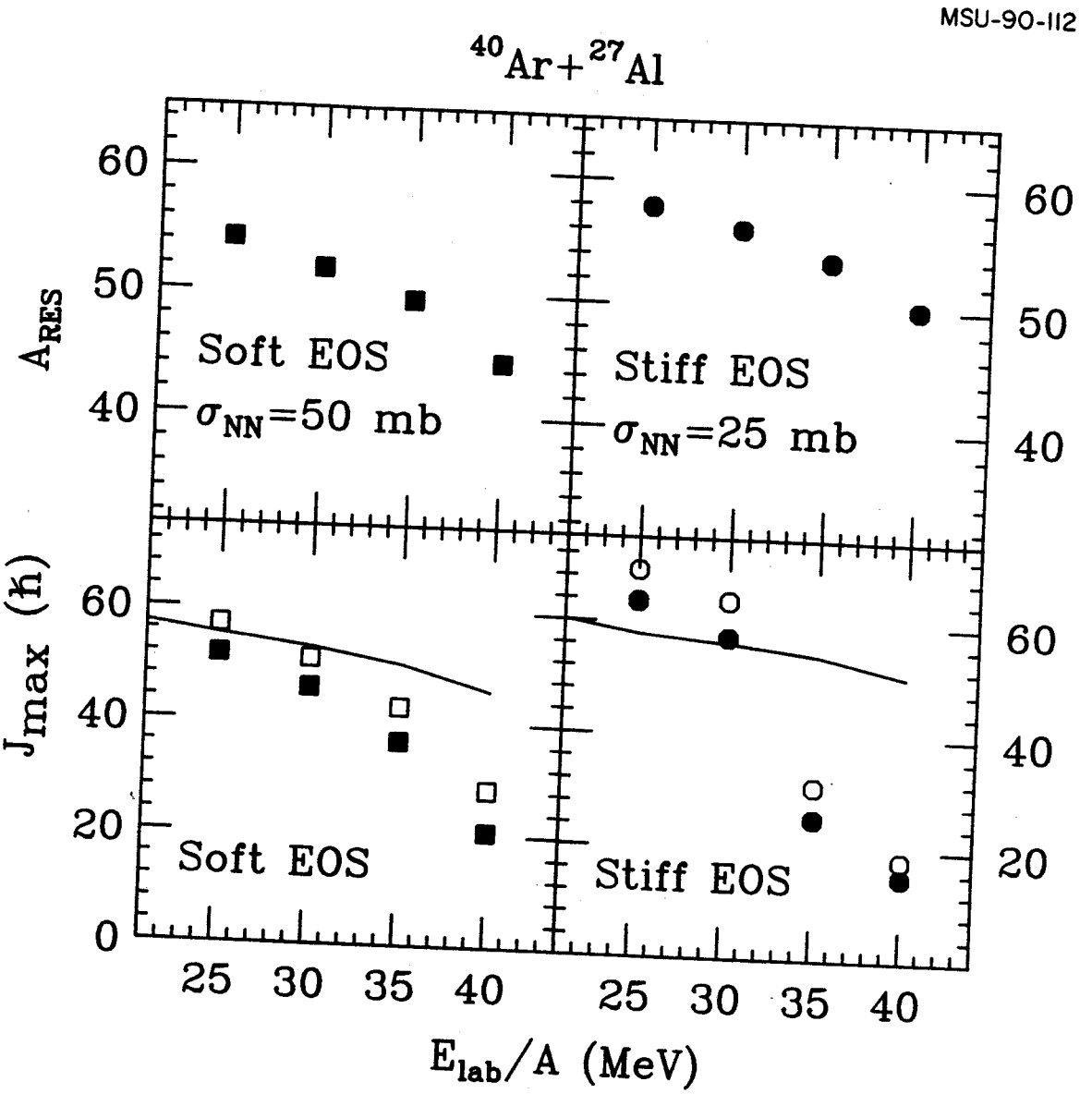

Figure 6.14: Residual masses (top) and angular momenta (bottom) at the freezeout as functions of the incident energy for calculations with the soft (right side) and the stiff EOS (left side). The curves and the open and close symbols are explained in the text.

eventually into two pieces. These boundary values, b_{max}, A_{max}, I_{max} and J_{max}, and, b_{II}, I_{II} and J_{II}, were listed in Table 6.3.

For both sets of equations of states, the fusion-like residues are comparable to the maximum angular momenta (solid curves in Fig. 6.14) predicted by liquid-drop models [Cohe 74] at E/A $\leq$ 30 MeV. At higher energies, E/A$\geq$35 MeV, however, the maximum angular momenta from BUU calculations decrease more rapidly than that expected from liquid-drop model calculations, suggesting that the liquid- drop model calculations provide little theoretical guidance at high energy collisions.

E Limiting Excitation Energy

Much effort has been devoted to the determination of the maximum excitation energy that a metastable composite nucleus can sustain. To learn about the possible dynamical limitations to the residue excitation energy, it is interesting to see how the calculated total excitation energy evolves with the incident energy in fusionlike collisions. On the left hand side of Fig. 6.15, we show the decomposition of the excitation energy for central collisions as a function of incident energy for the soft EOS (top panel) and the stiff EOS (bottom panel). On the right hand side, we provide the corresponding calculations for the maximum impact parameters b_{max} that lead to residue formation. With both equations of state, the calculated total excitation energy and the thermal excitation energy increase slightly with incident energy, a phenomenon also predicted in other simulations of light systems. [Snep 88, Boal 88a, Boal 88b]. The calculated excitation energies are generally larger for calculations with the stiff EOS, a trend also predicted by static models, [Levi 84] even though σ_{nn} was adjusted to make equal residue cross sections for the two sets of parameters. The total excitation energy for the stiff EOS increases gradually from E*/A= 3.8 MeV at E/A=25 MeV to E*/A=5.5 MeV at E/A=40 MeV; the thermal energy increases correspondingly

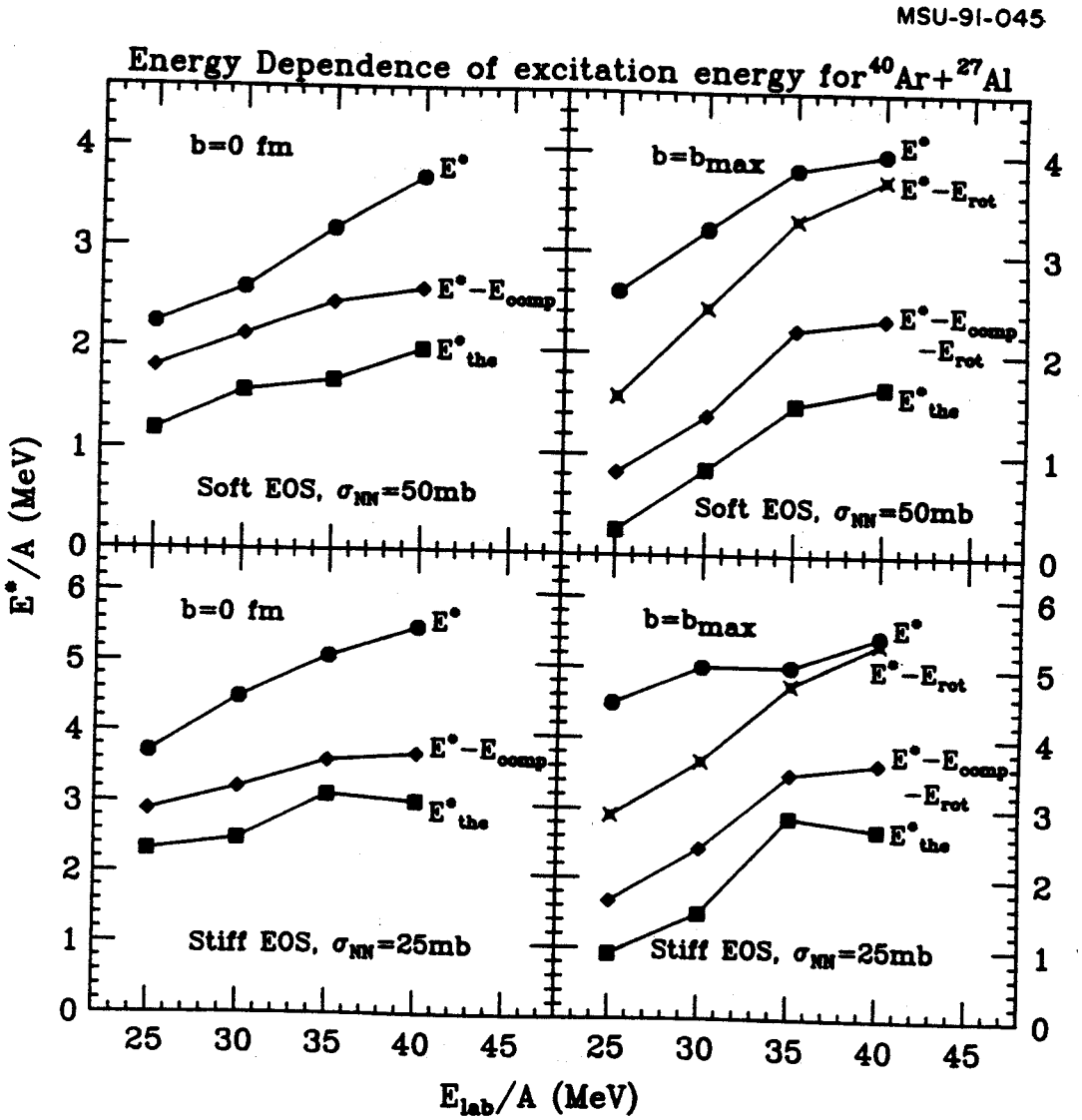

Figure 6.15: Decomposition of the excitation energy at freezeout for b=0 fm (left side), b=b$_{max}$ (right side), soft EOS (top panel) and stiff EOS (lower panel) as functions of incident energies in $^{40}Ar+^{27}Al$ collisions. Here, the solid circles and squares denote the total and thermal excitation energies, respectively. For other symbols, see the text and the figure caption of Fig. 6.11. The values of B$_{max}$ were listed in Table 6.3.

from E^*_{the}/A= 2.4 to 2.8 MeV. The maximum predicted thermal energy, E^*_{the}/A =2.8 MeV, is not small compared to predictions for the maximum excitation energy that a non-rotating nucleus can sustain. Thus it is possible that, besides limited by dynamic effects in large impact collisions, additional reductions in the calculated residue cross sections may occur for central collisions at the highest energies due to thermal instabilities [Boal 88a, Boal 88b, Levi 84, Saga 85, Gros 88] of the hot residues which are not considered by our calculations.

Similar excitation energies have been estimated from the experimentally measured residue velocity distributions using massive transfer models. An analogous procedure using the calculated residue velocity provides the open points in Fig. 6.16. As also shown in Fig. 6.12, application of the massive transfer to BUU calculations greatly model overestimates the residue excitation energy of this light symmetric system at all energies because it underestimates the cooling due to preequilibrium emission. Part of this discrepancy may also be due to the fact that the present calculations seem to lead to residue velocities which are smaller (for reverse kinematics) than the measured ones. This discrepancy could be reduced by choosing smaller values of nucleon-nucleon cross section that lead to residue velocities which are more similar to the measured ones. A detailed study of this issue would require a large amount of computer CPU time and it is beyond the scope of the present study.

III Conclusions

In summary, calculations have been performed with the Boltzmann equation to assess the sensitivity of heavy residue cross sections to the EOS and the in-medium nucleon-nucleon cross section. For specific choices of σ_{nn} and the nuclear EOS, the calculated residue cross sections decrease and eventually vanish for incident energies

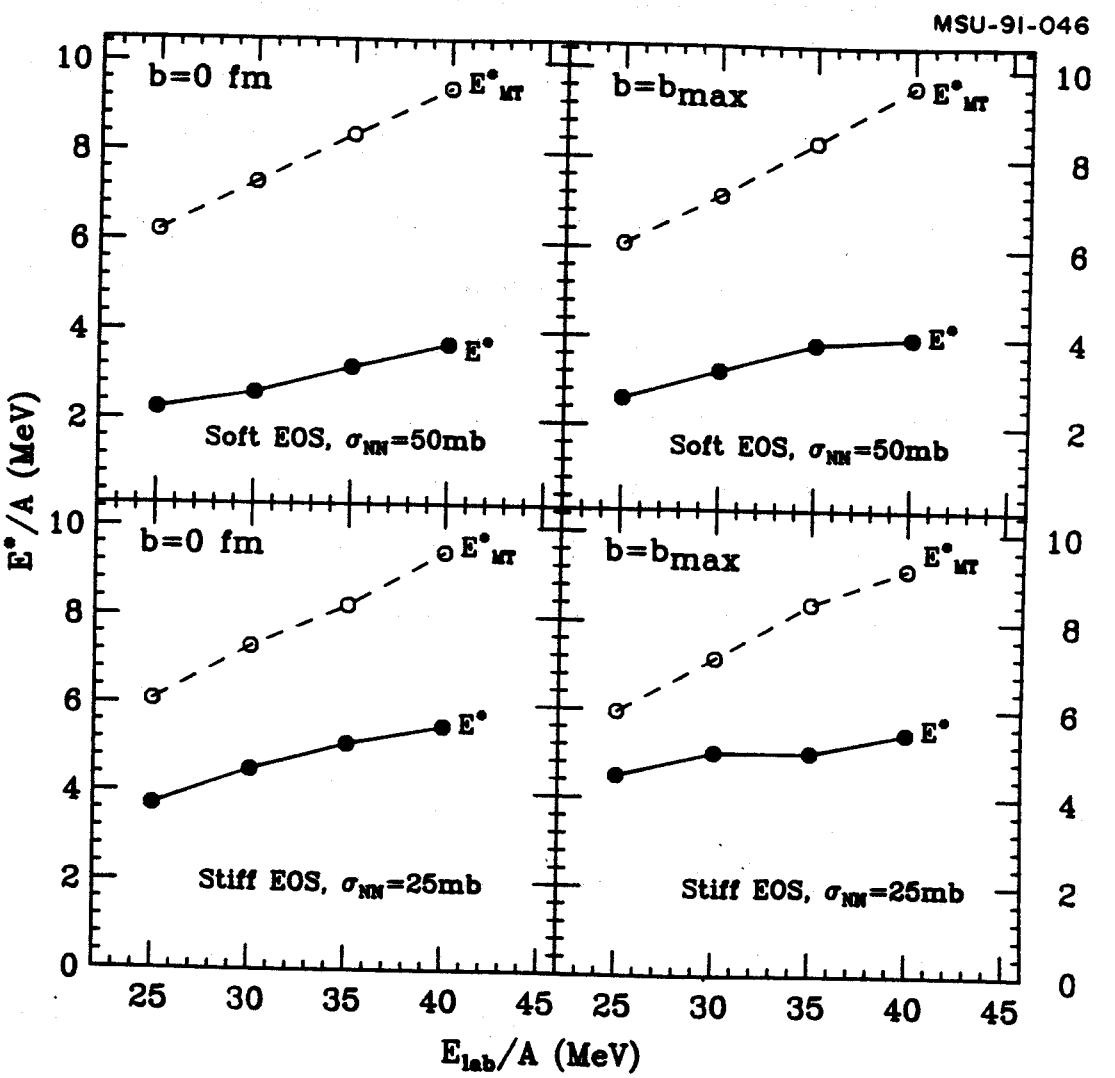

Figure 6.16: Comparisons of the total energy from BUU with that from massive transfer models in ^{40}Ar+^{27}Al collisions at freezeout for b=0 fm and b=b_{max} with the soft EOS and the stiff EOS as a function of incident energy. see the text for the details

above E/A $\geq$ 35 MeV, consistent with experimental observations. This decrease in cross section does not seem to be related to a bulk instability of nuclei at high temperature. The calculated residue cross sections are sensitive to both the nuclear EOS and the nucleon-nucleon cross section. This dual sensitivity constitutes an ambiguity which may be reduced or eliminated by measurements of observables like the in/out-of-plane ratio and the mean transverse momentum that are related to the isotropy of the emission patterns of coincident light particles.

By using a decomposition technique for the excitation energy, we have investigated in detail the thermal and dynamical limitations for the formation of heavy residues formed in the ^{40}Ar+^{27}Al collisions. For a given incident energy of E/A $\leq$ 30 MeV, the calculated excitation energy is slightly lower than the maximum values extracted from experiments and the cross sections are mainly limited by dynamical considerations in large impact parameter collisions. At higher energies, however, the calculated maximum angular momentum decreases much faster than that predicted by static model calculations, indicating large dynamical effects. Moreover, the thermal energy increases from E^*_{the}/A= 2.4 to 2.8 MeV as the incident energy is raised from E/A=25 to 40 MeV. The maximum predicted thermal energy, E^*_{the}/A =2.8 MeV, is comparable to predictions for the maximum excitation energy that a non-rotating nucleus can sustain. Thus it is possible that, besides limited by dynamic effects in large impact collisions, additional reductions in the calculated residue cross sections may occur for central collisions at the highest energies due to thermal instabilities [Boal 89, Levi 84, Saga 85, Gros 88] of the hot residues which are not considered by our calculations.

The present calculation has several limitations. Because the theory has insufficient fluctuations, it can not predict, for example, under what conditions and how the hot residues will disassemble. Even within the model itself, there are considerable uncertainties concerning the nuclear EOS and in-medium nucleon-nucleon cross sec-

tion. Further investigations are also required to assess the sensitivity of the calculated observables to the detailed algorithm for Pauli- blocking and to the surface energies of the computational nuclei.

Chapter 7

Nuclear Temperature and Nuclear Equation of State

In the preceeding chapters, we presented experimental measurements of emission temperature obtained from the relative population of excited states of intermediate mass fragments. In chapter 5 and 6, we discussed BUU calculations which were undertaken to determine whether excitation energies of residues are sensitive to theoretical quantities such as the nuclear equation of state and in-medium nucleon-nucleon cross section. Some sensitivity of the excitation energies to these quantities was obtained for light systems and they were presented in chapter 6. Such light systems may not be ideally suited to address our original questions about limiting temperatures since the residues formed in such light systems do not survive collisions for incident energies in excess of E/A $\approx$ 40 MeV. Emission temperatures, on the other hand, have been obtained for heavy asymmetric systems at incident energies up to E/A=94 MeV [Chen 88a]. Here we present Boltzmann-Uehling-Uhlenbeck (BUU) calculations for the asymmetric ^{40}Ar+^{27}Al and ^{40}Ar+^{124}Sn system. We show that the calculated thermal temperature for the residual nucleus is sensitive to the nuclear equation of state, as well as the impact parameter, and surprisingly, in-sensitive to the in-medium nucleon-nucleon cross section.

This chapter is organized as follows. In section I, we check whether the criteria used to define the freezeout time are also satisfied for this heavy asymmetric system. We discuss the dependence of the total excitation energy on incident energy and compare the results with the predictions of massive transfer models in Section II. In Section III, we consider a simple model for extracting the emission temperature from the thermal excitation energy. Some conclusions are drawn in Section IV.

I Freezeout Conditions

Before we present the calculated excitation energies and temperatures, we would like to check whether the freezeout conditions discussed in the previous chapter give consistent freezeout times for ^{40}Ar+^{124}Sn collisions.

Figs. 7.1-7.4 show the decomposition of the excitation energy using Eqs. (6.1)-(6.6) for ^{40}Ar+^{124}Sn collisions at b=0 fm. In Figs. 7.5-7.6, we display the emission rate of nucleons as functions of time for ^{40}Ar+^{124}Sn collisions at E/A=35 MeV and 65 MeV, respectively. The solid (open) circles depicted the calculations with the stiff (soft) equation of state. Both calculations are performed assuming an isotropic in-medium nucleon-nucleon cross section of 41 mb. Similar to ^{40}Ar +^{27}Al collisions shown in the last chapter, one sees a prompt non-equilibrium peak at t $\simeq 60-80$ fm/c followed by a lower emission rate characteristic of slow statistical evaporation from a equilibrated system. The solid arrows in the figures indicate the freezeout times we choose for the stiff EOS while the open arrows indicate the freezeout time for the soft EOS. By examining the thermal excitation energies shown Figs. 7.1-7.4 and the emission rates shown in Figs. 7.5-7.6, consistent freezeout times were achieved. The freezeout time t_{fre} for ^{40}Ar+^{124}Sn collisions at b=0 fm are, respectively, $t_{fre} \approx 140$ ($t_{fre} \approx 120$) at E/A =35 MeV; and $t_{fre} \approx 160$ ($t_{fre} \approx 120$) at E/A=65 MeV; for

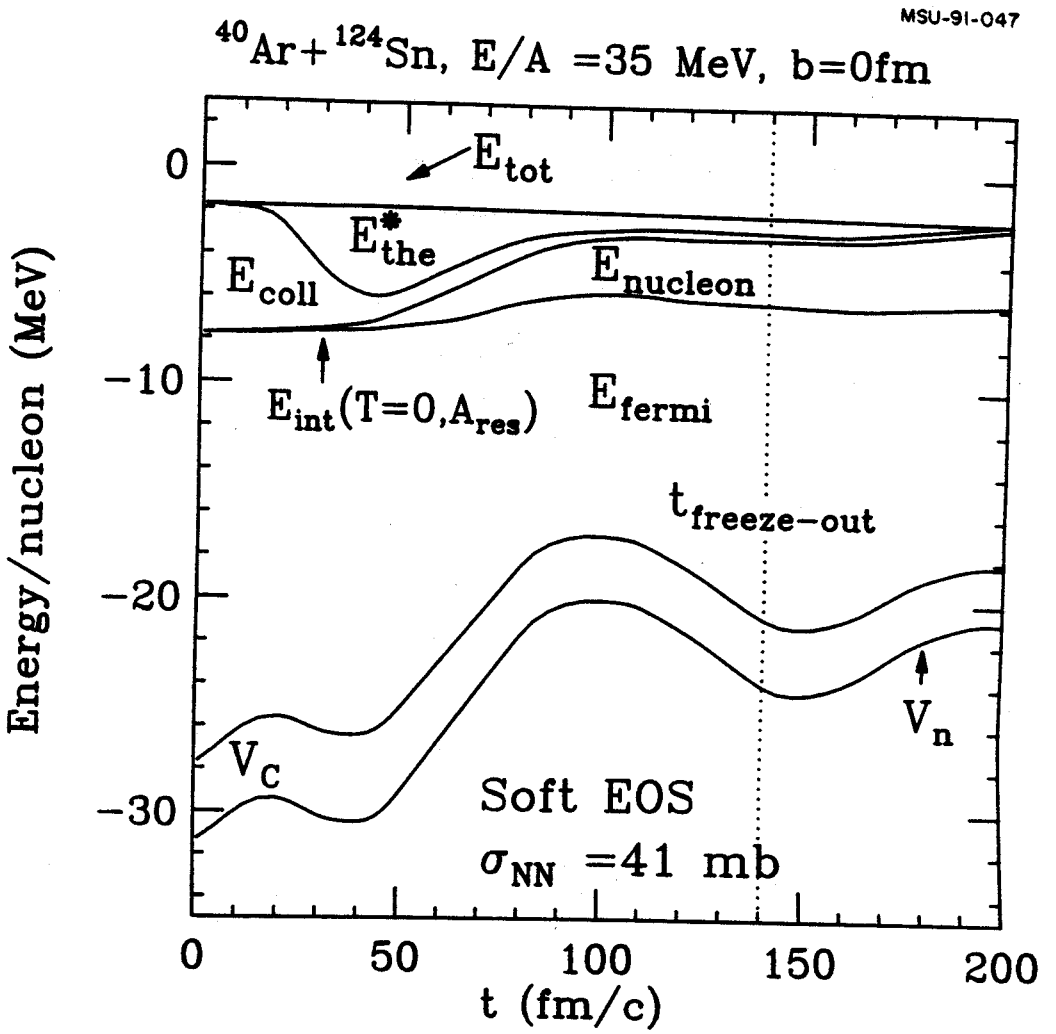

Figure 7.1: Decomposition of various excitation energies as a function of time for ^{40}Ar+^{124}Sn collisions with the soft equation of state at E/A=35 MeV, b=0 fm. The bottom line is the nuclear potential energy. From this bottom line up are,respectively, Coulomb energy (difference between the second and the bottom lines), Fermi energy required by the Pauli exclusion principle (difference between the third and second lines), kinetic energy of emitted particles (difference between the fourth and third lines), collective energy of bound nucleons (difference between the fifth and fourth lines) and thermal energy (difference between the top and fifth lines). The freezeout time is indicated by the dotted line.

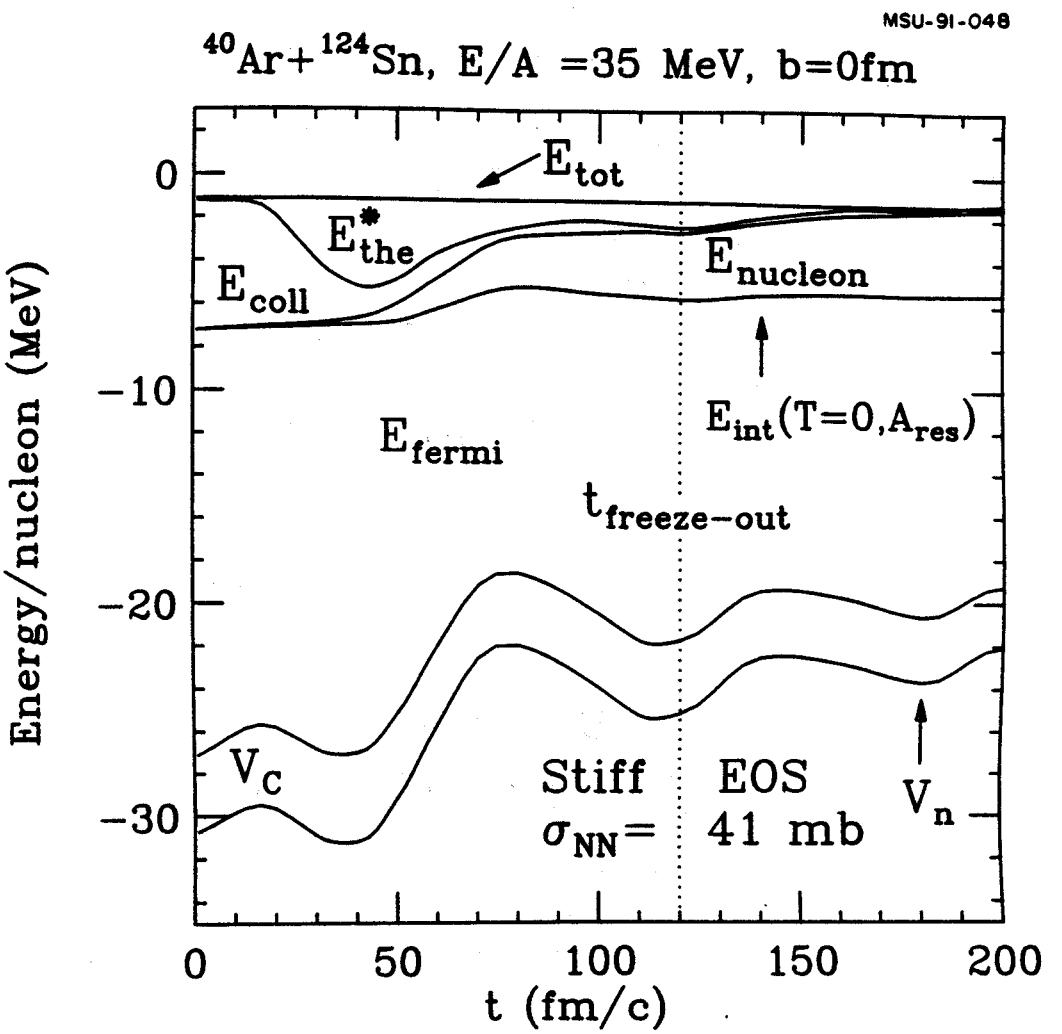

Figure 7.2: Same as Fig. 7.1, but for ^{40}Ar+^{124}Sn collisions with the stiff EOS at E/A=35 MeV, b=0 fm.

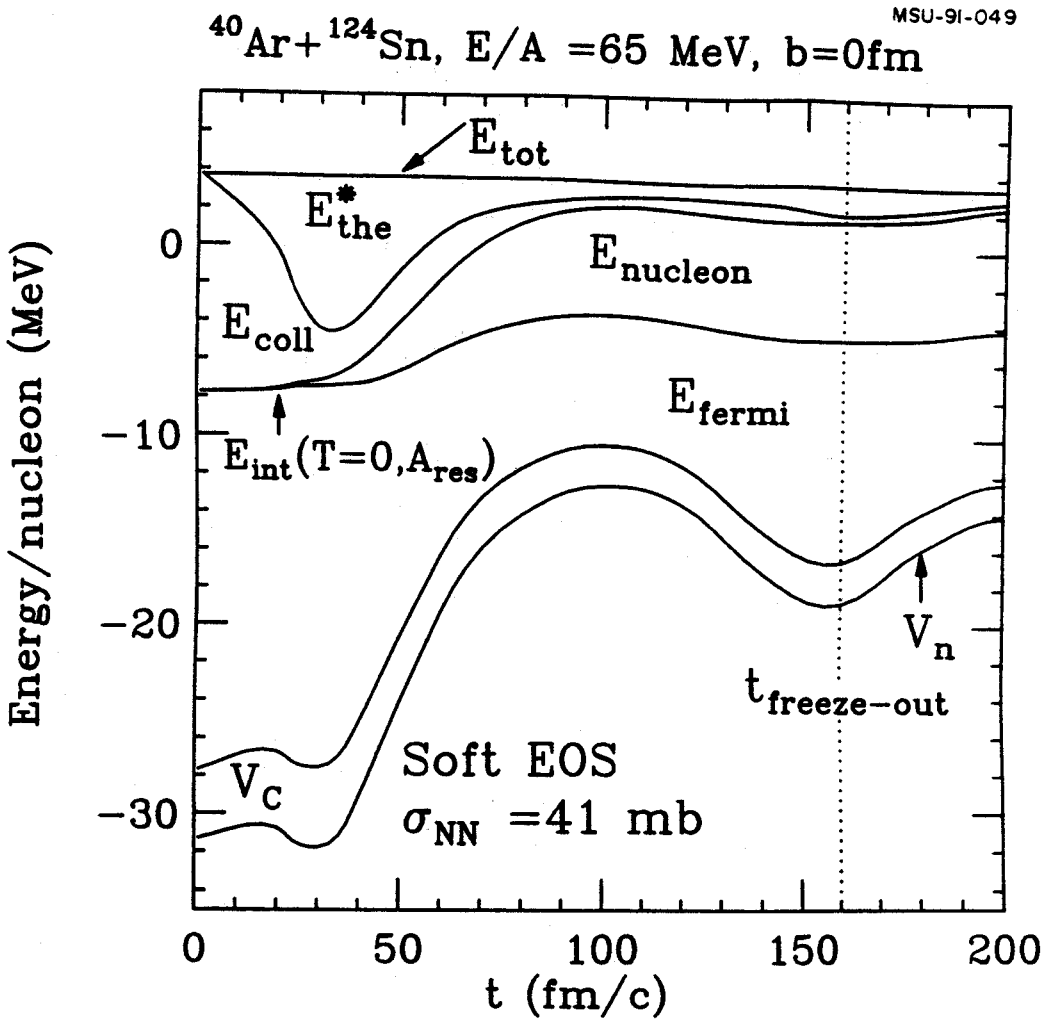

Figure 7.3: Same as Fig. 7.1, but for ^{40}Ar+^{124}Sn collisions with the soft EOS at E/A=65 MeV, b=0 fm.

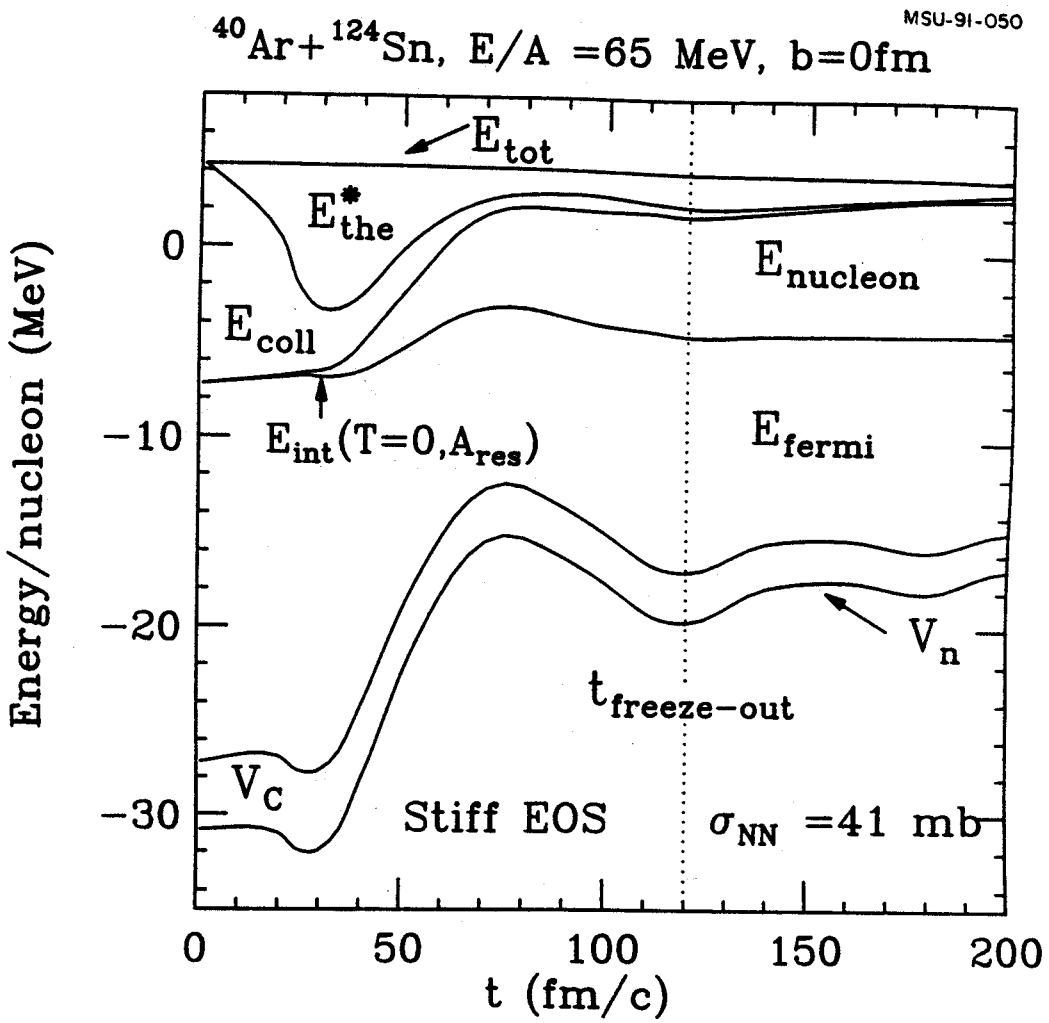

Figure 7.4: Same as Fig. 7.1, but for ^{40}Ar+^{124}Sn collisions with the stiff EOS at E/A=65 MeV, b=0 fm.

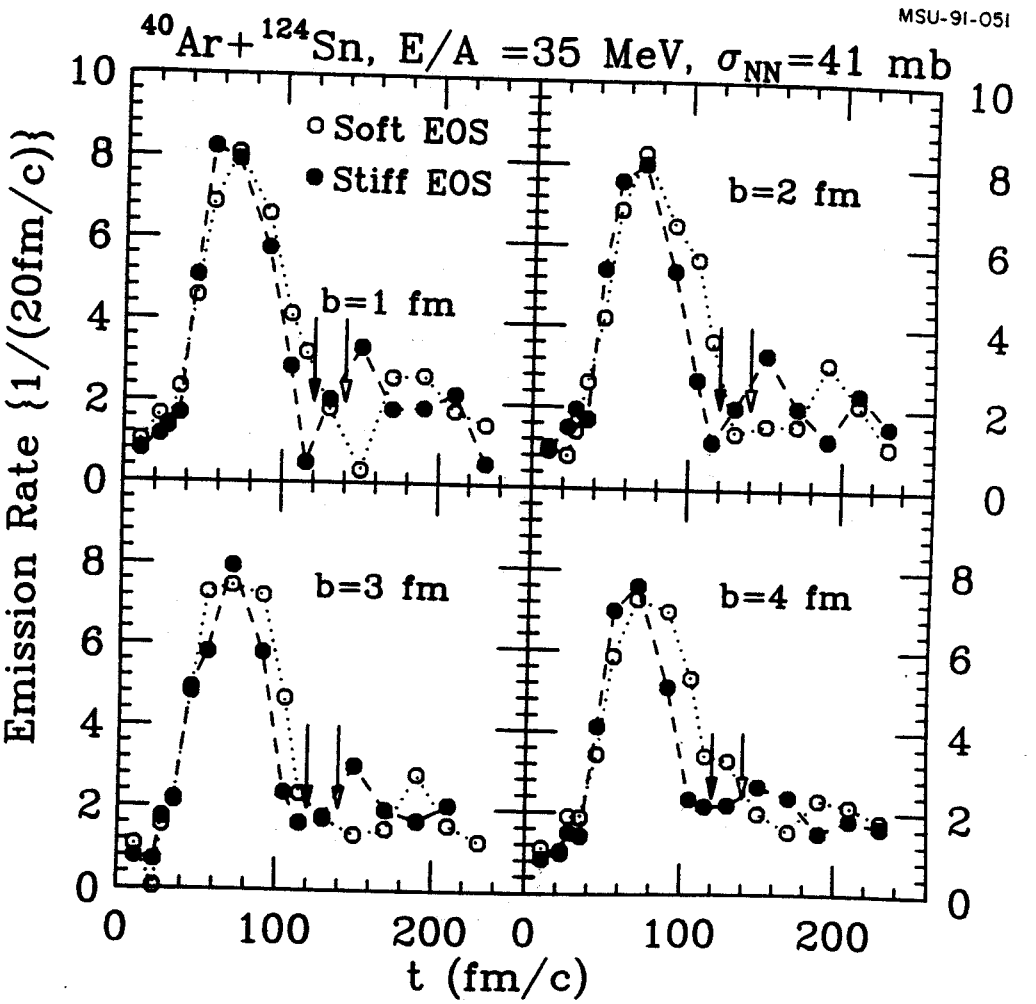

Figure 7.5: The emission rates of ^{40}Ar+^{124}Sn collisions at E/A=35 MeV for impact parameters b=1 – 4 fm. The solid circles are results with stiff EOS and the open circles are results with soft EOS. The corresponding freezeout times are indicated by the arrows (solid for stiff EOS and open for soft EOS). The respective lines are used to guide the eyes.

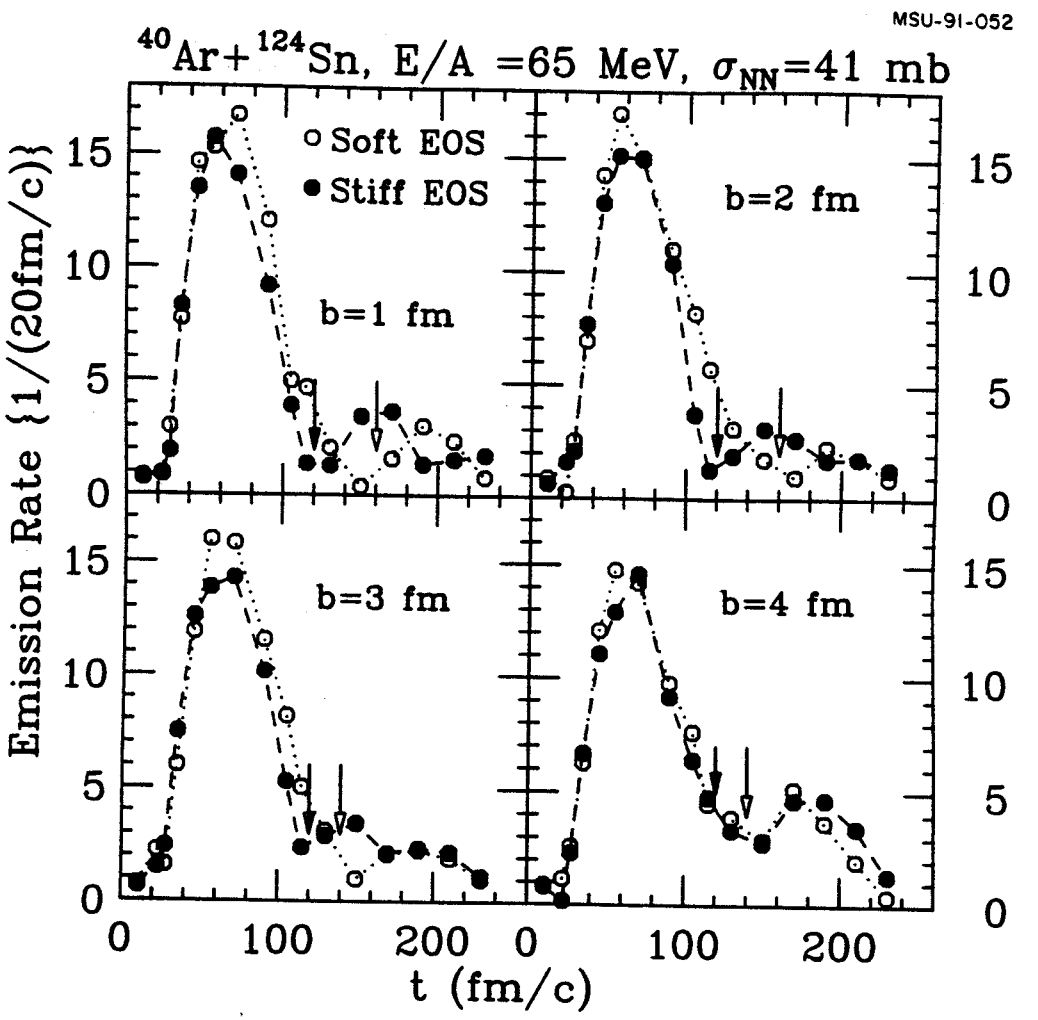

Figure 7.6: The emission rates of ^{40}Ar+^{124}Sn collisions at E/A=65 MeV for impact parameters b=1 – 4 fm. The solid circles are results with stiff EOS and the open circles are results with soft EOS. The corresponding freezeout times are indicated by the arrows (solid for stiff EOS and open for soft EOS). The respective lines are used to guide the eyes.

soft (stiff) EOS. In general, the freezeout time reached with our criteria are slightly shorter for stiff EOS compared to that obtained for soft EOS. More detailed studies also indicates that the freezeout time does not depend on the impact parameter at E/A=35 MeV for either stiff or soft equation of state. However, at higher energies, E/A=65 MEV, the freezeout time depends very sensitively on the impact parameter, particularly for the soft EOS. With $\sigma_{NN} = 41$ mb, the freezeout time decreases from $t_{fre} \approx 160$ fm/c at b=0 fm to $t_{fre} \approx 120$ fm/c at b=6 fm for the soft EOS; and the freezeout time decreases from $t_{fre} \approx 120$ fm/c at b=0 fm to $t_{fre} \approx 100$ fm/c at b=6 fm.

The bottom panels of figs. 7.7-7.8 show the quadrupole momentum distributions as a function of time for ^{40}Ar+^{124}Sn collisions at b=0 fm. For comparison, the emission rates at $b = 0$ are presented in the top panels. Similar to ^{40}Ar +^{27}Al collisions discussed in the previous chapter, Q_{ZZ} does not provide accurate freezeout time due to complications from quadrupole vibrations.

The final spatial configurations at freezeout depend very much on the incident energy. Figs. 7.9-7.13 show the final spatial distributions for ^{40}Ar+^{124}Sn collisions at E/A=35 MeV and 65 MeV with soft or stiff EOS. At E/A=35 MeV, one always see a single well defined residue at the freezeout time, even for the larger impact parameter collisions in which the bound residue decays into distinctive projectile-like and target-like residues at a later time. In contrast, at E/A=65 MeV and impact parameters greater than $b \approx 2 - 3$ fm, the projectile-like and target-like residues (sometimes more than two residues) at freezeout appear to be more distinct. This indicates that the time scale for breakup in high energy collisions becomes shorter than the time scale for relaxation and equilibration of the extended residues. We also note here that at E/A=35 MeV, the residues appear to distribute over a larger volume for the calculations with $\sigma_{NN} = 20$ mb (Fig. 7.10) than the corresponding

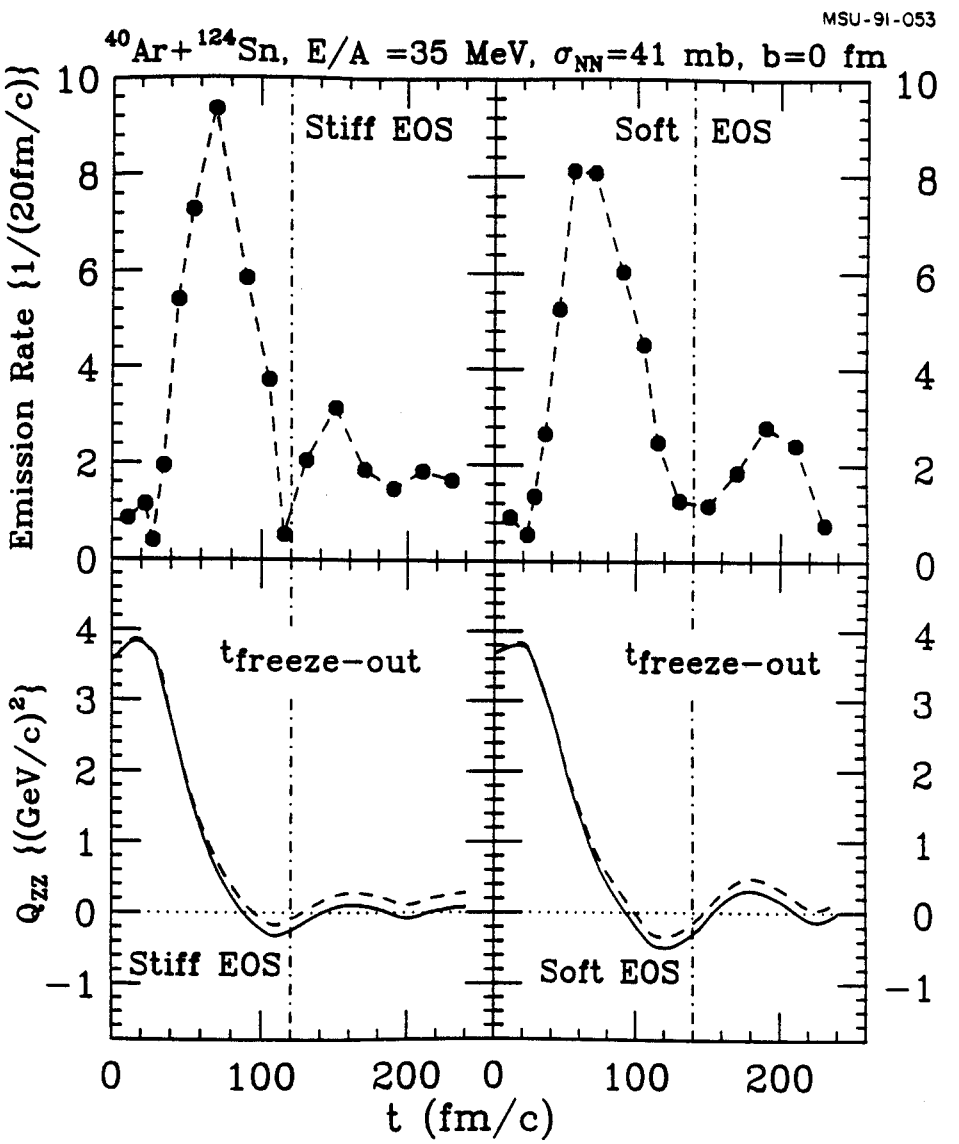

Figure 7.7: The emission rates of nucleons (top panels) and the quadrupole momentum distributions Q_{zz} (bottom panels), defined by Eq. (6.19), for ^{40}Ar+^{124}Sn collisions at E/A=35 MeV, b=0 fm. The left panels (right panels) show the results for the stiff EOS (soft EOS). The vertical dot-dash lines indicate the freezeout time discussed in the text. The dashed lines in the bottom panels include the calculations for all nucleons, while the solid lines include only nucleons in the bound residues.

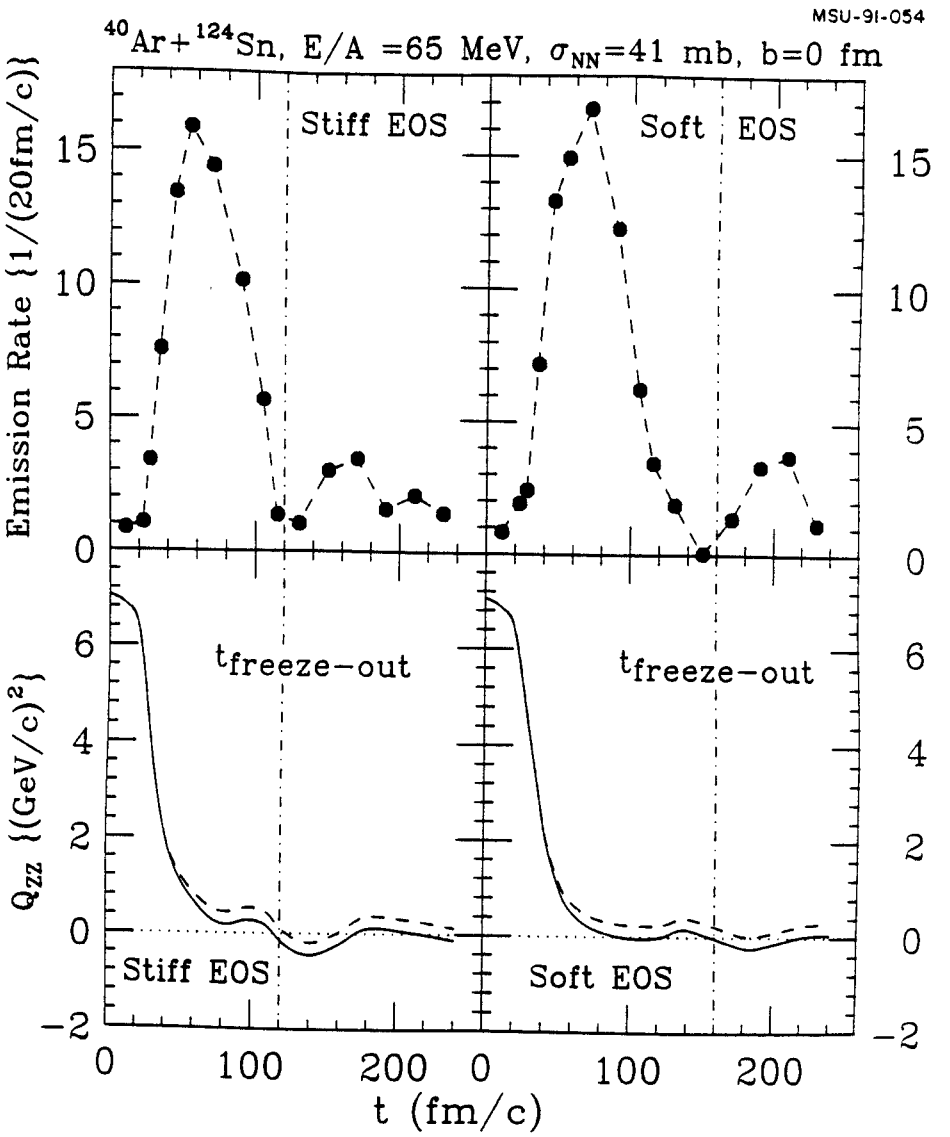

Figure 7.8: The emission rates of nucleons (top panels) and the quadrupole momentum distributions Q_{zz} (bottom panels), defined by Eq. (6.19), for ^{40}Ar+^{124}Sn collisions at E/A=65 MeV, b=0 fm. The left panels (right panels) show the results for the stiff EOS (soft EOS). The vertical dot-dash lines indicate the freezeout time discussed in the text. The dashed lines in the bottom panels include the calculations for all nucleons, while the solid lines include only nucleons in the bound residues.

calculations with $\sigma_{NN} = 41$ mb (Fig. 7.9). We will come back to this point when we evaluate the density dependent level density parameter.

II The Excitation Energy at Freezeout

A Excitation Energies

In Fig. 7.14, we display the decomposition of the excitation energy at freezeout using Eq. (6.18) for ^{40}Ar +^{124}Sn collisions at E/A=35 MeV. The freezeout configuration at this energy consists of a single bound system, similar to those obtained for ^{40}Ar +^{27}Al system at E/A=30 MeV and the qualitative behavior of various contributions to the excitation energy is also similar.

At higher incident energies, E/A =65 MeV, the freezeout configurations shown in Figs. 7.12-7.13 are more complex. The left hand panels of Fig. 7.15 display the decomposition of the excitation energy if *all* the residues are included in the calculation. The right hand panels show the corresponding decomposition if only the largest residue (target-like residue) is analyzed. In addition to the density requirement for the bound residues, a sphere of adjustable radius with its origin at the center of the target-like residue is used to separate the target-like residue from other bound clusters. Applying our analysis at large impact parameters, $b \geq 3$ fm, to the entire system yields a total excitation energy per nucleon which is significantly larger than that for the target-like residue alone. These large values for the excitation energies are a consequence of the large relative velocities between the various residues. These large relative velocities could be responsible for the significant increase in the non-rotational collective energies, $E^*_{n.r.}$, denoted by the difference between the diamonds and squares of the left hand panels of Fig. 7.15, at larger impact parameters. The thermal energy per nucleon (squares), however, is practically the same if one considers

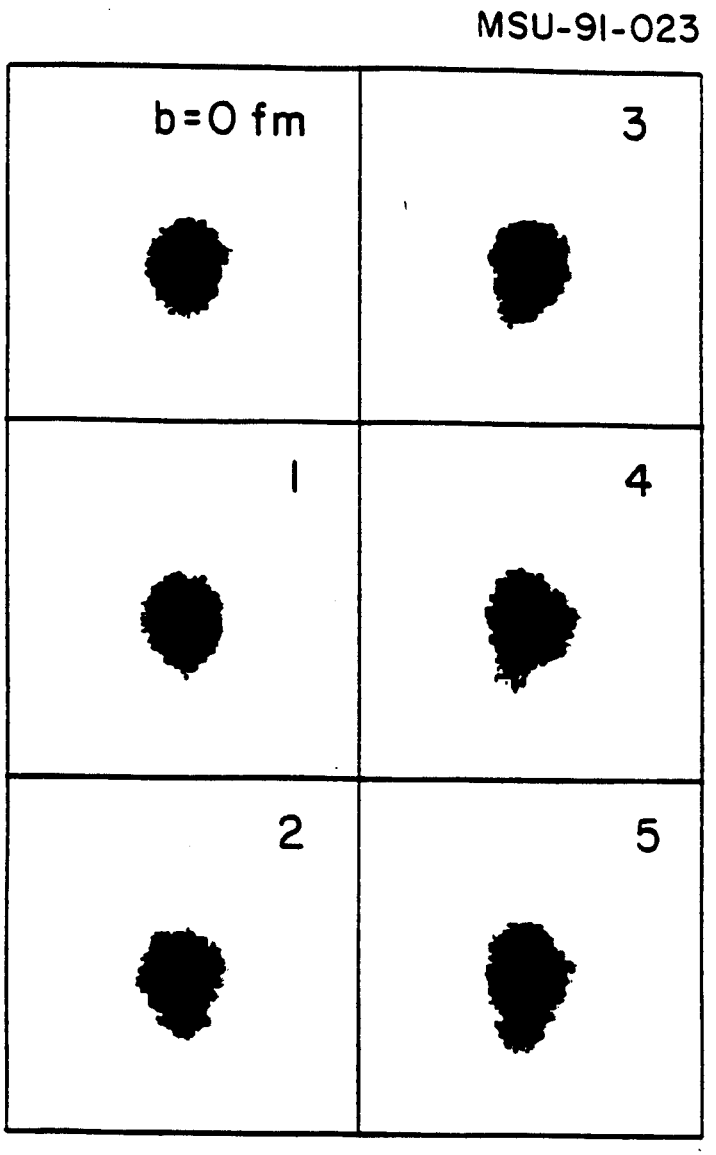

Figure 7.9: The spatial distributions at the freezeout time for ^{40}Ar+^{124}Sn collisions at E/A=35 MeV with the soft EOS and $\sigma_{NN} = 41$ mb. The values of impact parameters are indicated in each corresponding panel. The beam directions is in the vertical direction (projectile moves from top to bottom).

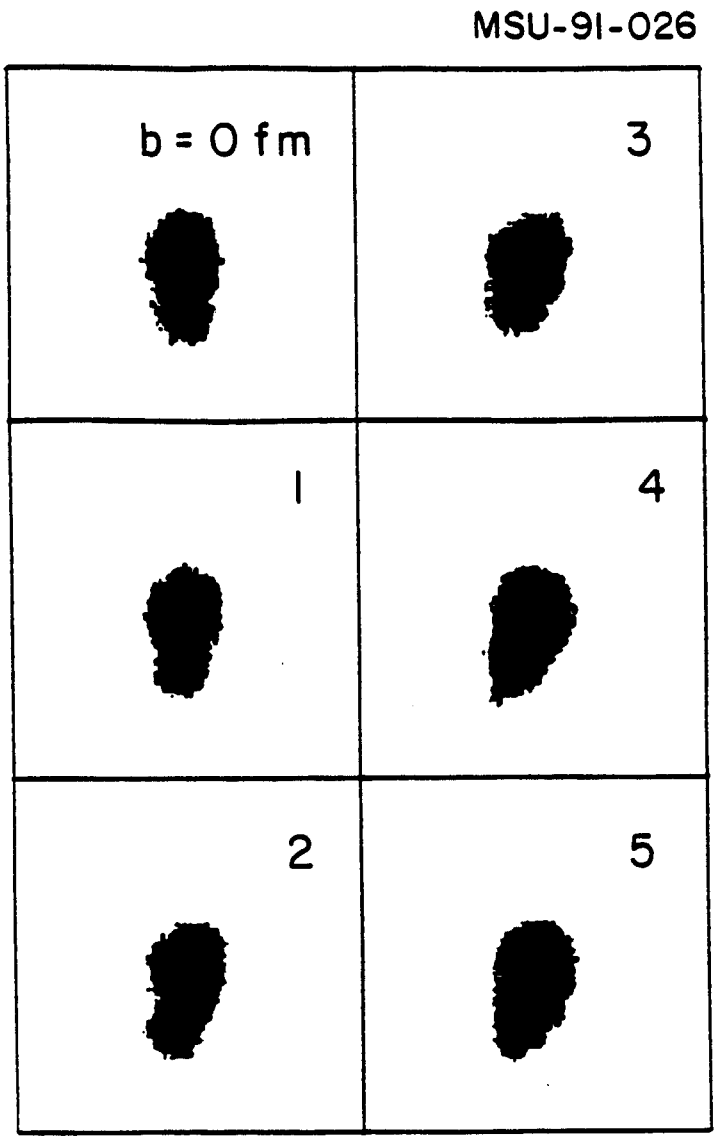

Figure 7.10: The spatial distributions at the freezeout time for ^{40}Ar+^{124}Sn collisions at E/A=35 MeV with the soft EOS and $\sigma_{NN} = 20$ mb. The values of impact parameters are indicated in each corresponding panel. The beam directions is in the vertical direction (projectile moves from top to bottom).

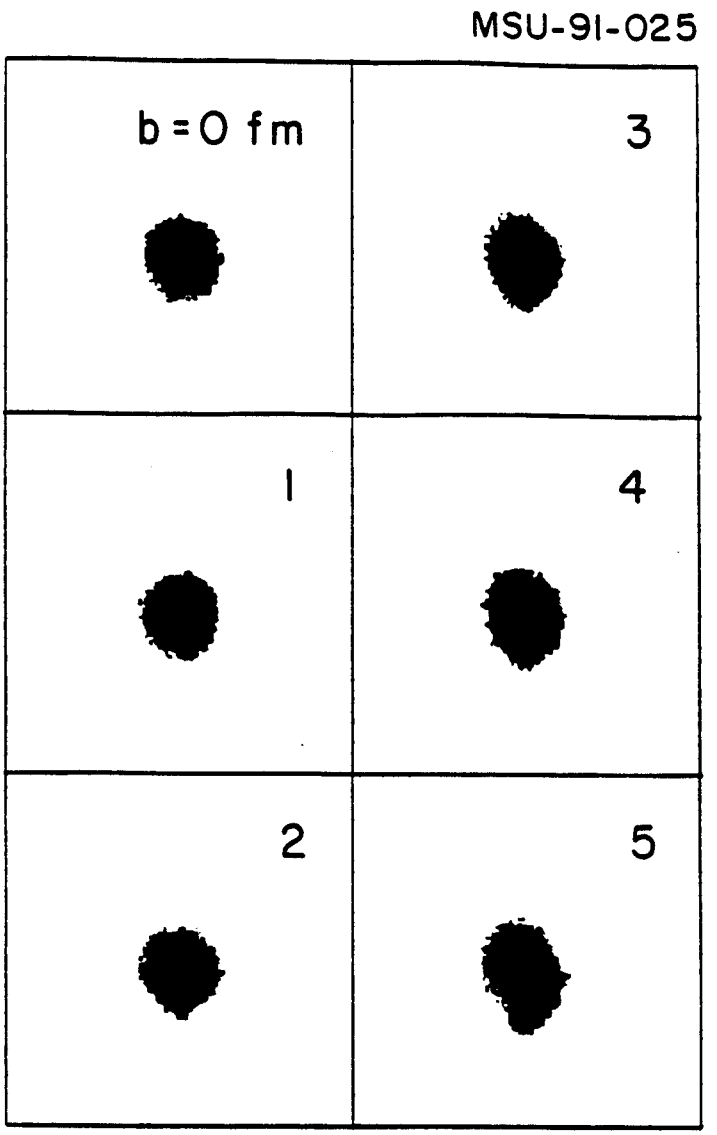

Figure 7.11: The spatial distributions at the freezeout time for ^{40}Ar+^{124}Sn collisions at E/A=35 MeV with the stiff EOS and $\sigma_{NN} = 41$ mb. The values of impact parameters are indicated in each corresponding panel. The beam directions is in the vertical direction (projectile moves from top to bottom).

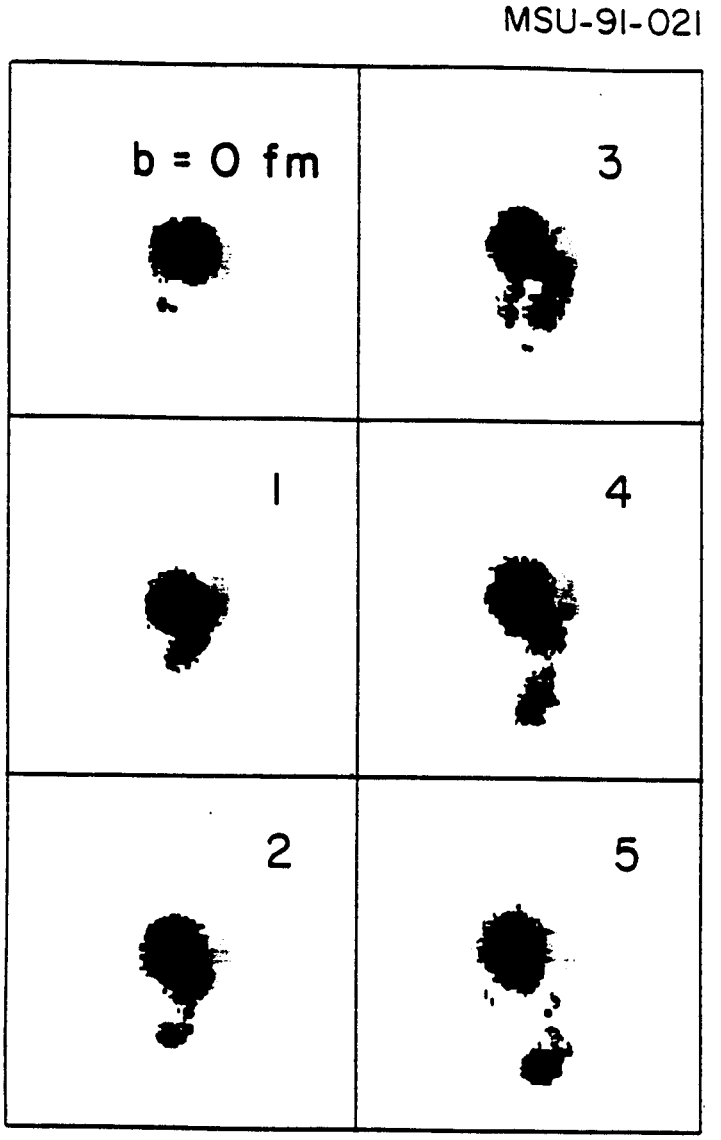

Figure 7.12: The spatial distributions at the freezeout time for ^{40}Ar+^{124}Sn collisions at E/A=65 MeV with the soft EOS and $\sigma_{NN} = 41$ mb. The values of impact parameters are indicated in each corresponding panel. The beam directions is in the vertical direction (projectile moves from top to bottom).

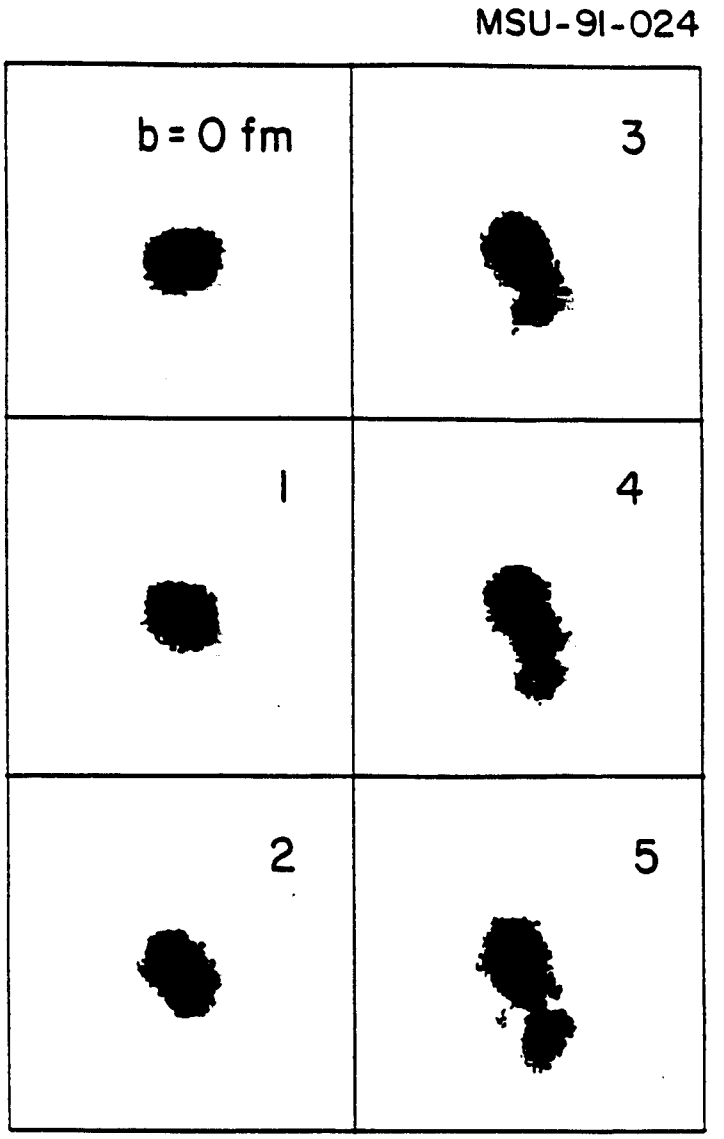

Figure 7.13: The spatial distributions at the freezeout time for ^{40}Ar+^{124}Sn collisions at E/A=65 MeV with the stiff EOS and $\sigma_{NN} = 41$ mb. The values of impact parameters are indicated in each corresponding panel. The beam directions is in the vertical direction (projectile moves from top to bottom).

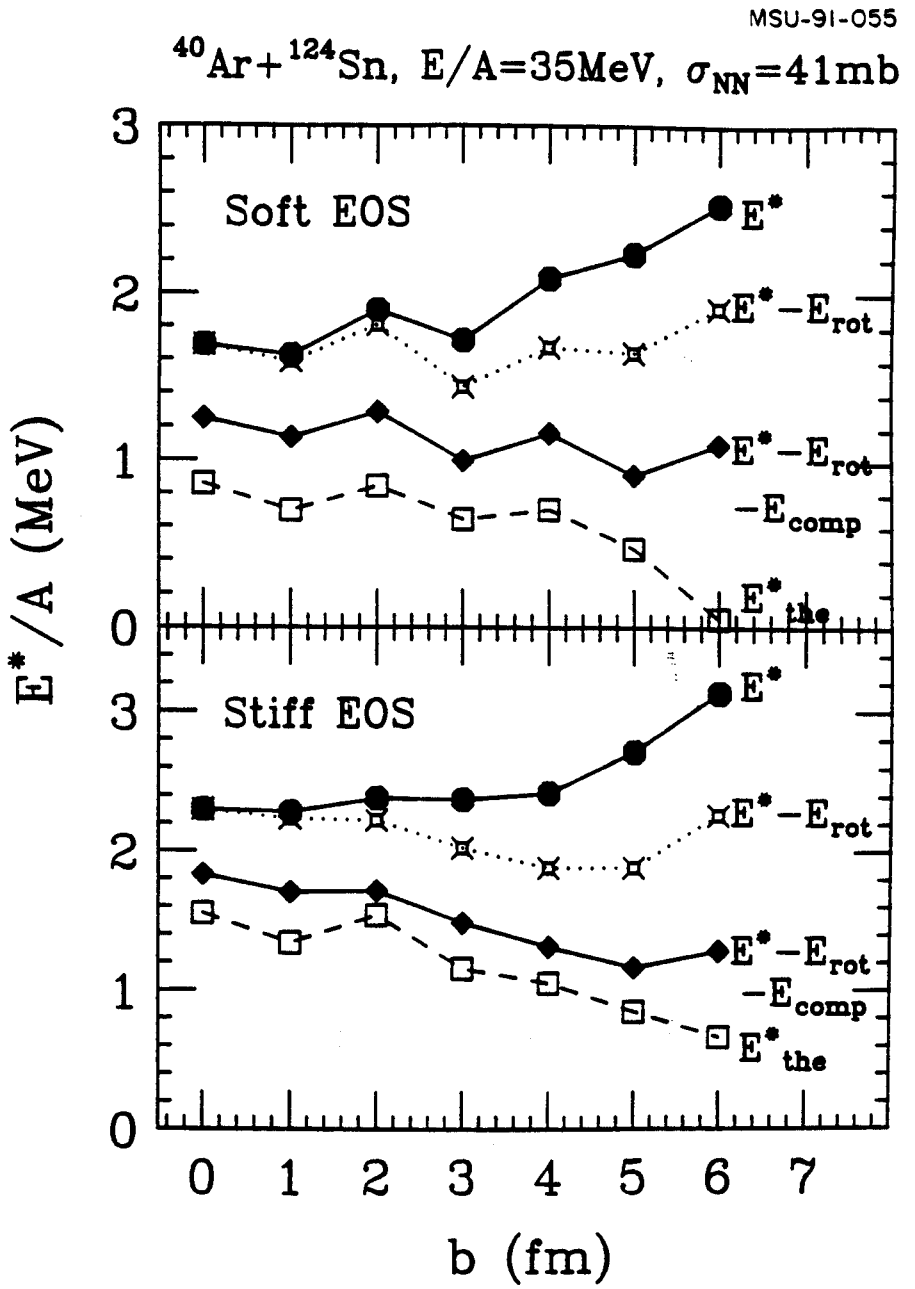

Figure 7.14: Decomposition of the excitation energy at freezeout for ^{40}Ar+^{124}Sn collisions at E/A =35 MeV, assuming the soft EOS, (top panel) or the stiff EOS (lower panel). The respective symbols indicated in the figure are the different components by using Eq. (6.18). The lines are drawn to guide the eye.

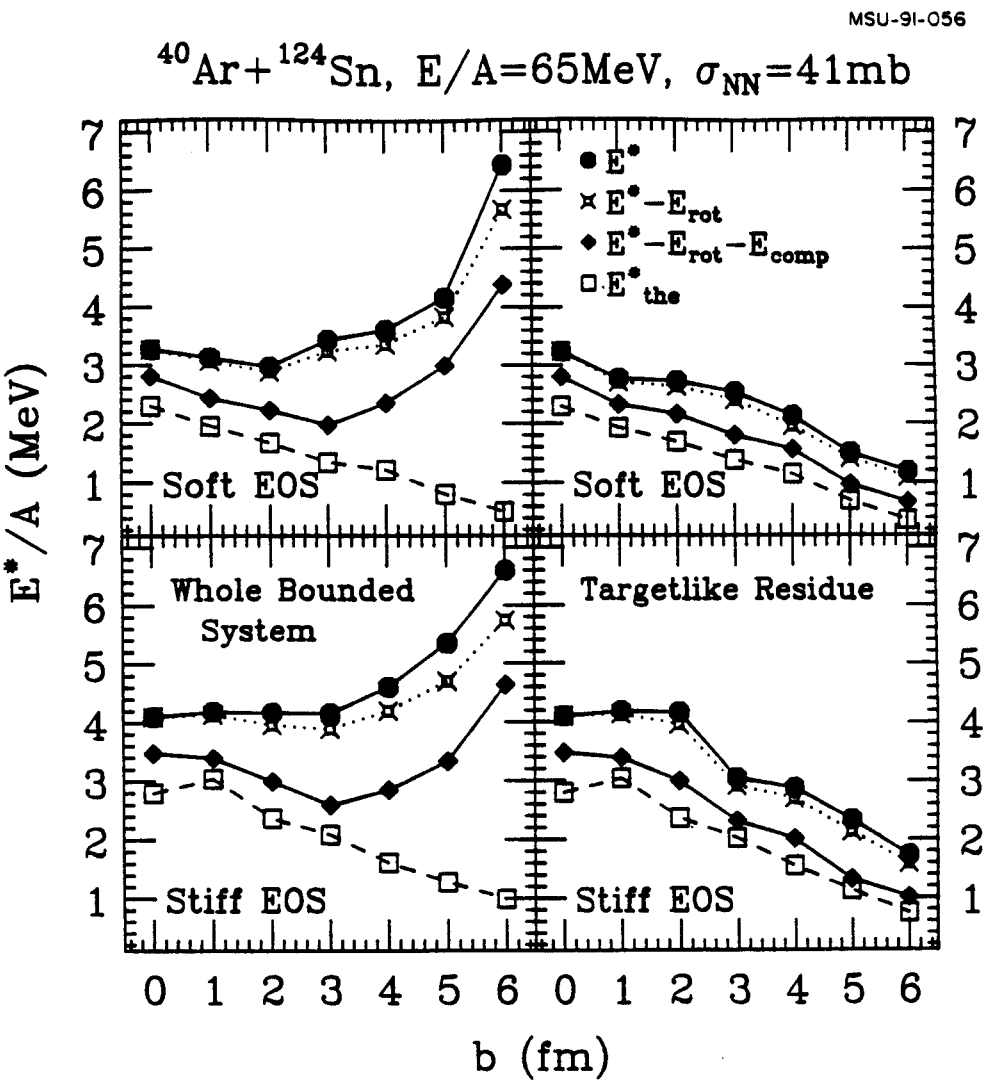

Figure 7.15: Decomposition of the excitation energy at freezeout for ^{40}Ar+^{124}Sn collisions at E/A =65 MeV, assuming the soft EOS, (top panels) or the stiff EOS (lower panels). The left hand panels display the decomposition of the excitation energy when *all* the residues are included. The right hand panels show the corresponding results when one includes only the largest residue (target-like residue). The respective symbols indicated in the figure are the different components by using Eq. (6.18). The lines are drawn to guide the eye.

the whole bounded system (left hand panels) or if one simply considers a single target-like residue (right hand panels). This result is consistent with the assumption that the thermal excitation energies per nucleon are the same for all clusters.

On the left panels of Fig. 7.16, we show the decomposition of excitation energies with soft EOS and $\sigma_{NN} = 20$ mb at E/A=35 MeV (top panel) and 65 MeV (bottom panel) at freezeout time. For comparison, the corresponding calculations for $\sigma_{NN} = 41$ mb are re-plotted on the right panels. The qualitative behavior with both values of σ_{NN} is very similar, indicating that no significant dependence of excitation energies on nucleon-nucleon cross sections. Indeed, one might expect that a larger nucleon-nucleon cross section could generate more excitation and therefore a larger excitation energy. However, this effect is partly compensated by the fact that the calculations with smaller σ_{NN} tend to freezeout earlier. In fact, the thermal excitation energy and the non-rotational collective excitation energy (the difference between the diamonds and the squares) at E/A =35 MeV calculated with $\sigma_{NN} = 20$ mb are slightly higher than those calculated with $\sigma_{NN} = 41$, since the systems freezeout at $t_{fre} \approx 120$ fm/c, earlier than $t_{fre} \approx 140$ fm/c obtained with $\sigma_{NN} = 41$ mb. we will come back to this point when we evaluate the temperatures.

In the bottom window of Fig. 7.17, we show the energy dependences of the total excitation energy (circles) and thermal energy (squares) per nucleon for ^{40}Ar +^{124}Sn collisions at b=0 fm. The corresponding residue mass is shown in the top window. For both the stiff EOS (solid symbols) and the soft EOS (open symbols), the excitation energy increases with incident energy. However, this increase with energy becomes more gradual at energies E/A $\geq$ 65 MeV, indicating that the excitation energy per nucleon may be reaching a saturation value. The difference between the excitation energies for different equations of state is of the order of $\approx$ 1 MeV per nucleon at all energies. For comparison, the solid diamonds depict the excitation energies deduced

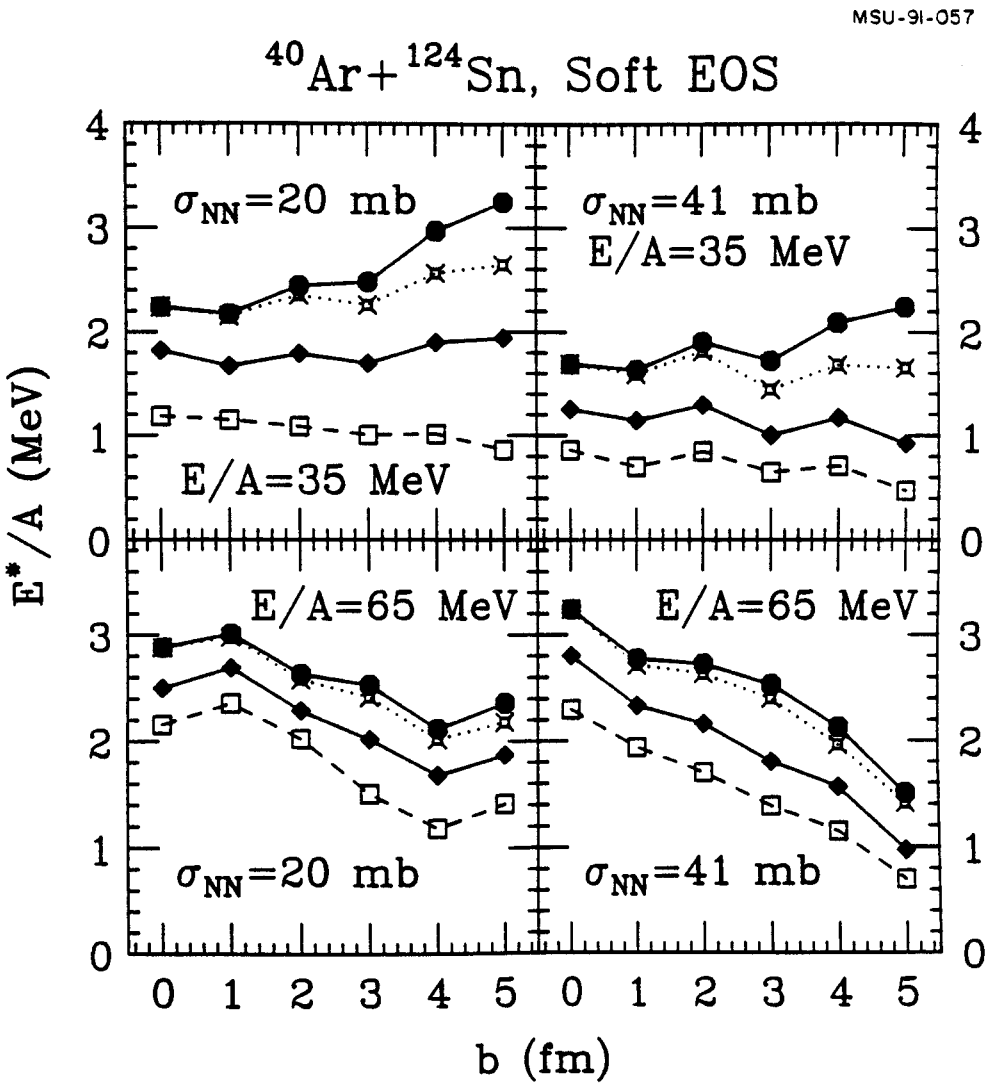

Figure 7.16: The dependences of the excitation energies on σ_{NN} for ^{40}Ar+^{124}Sn collisions at E/A=35 (top panels) and 65 MeV (bottom panels) with soft EOS. The left hand panels are results with σ_{NN} = 20 mb and the right hand panels are results with σ_{NN} = 41 mb. the excitation energies indicated by respective symbols are the same as those shown in Fig. 7.15. The lines are used to guide the eyes

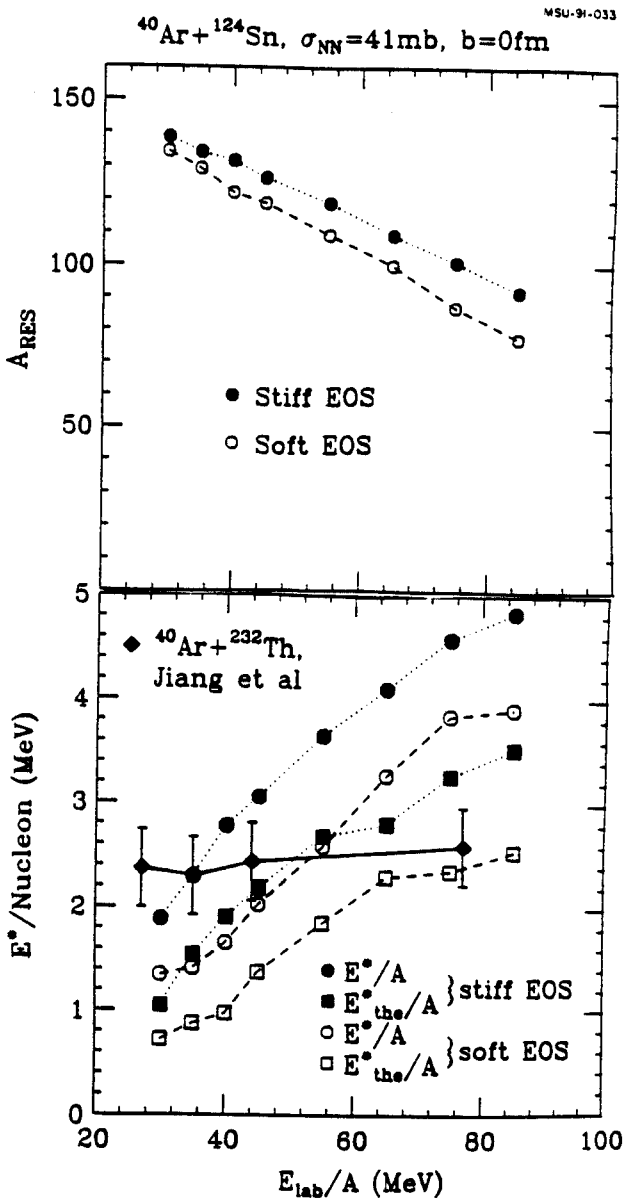

Figure 7.17: The dependence of residual mass (top window), the total energy and the thermal energy (bottom window) on the incident energy for ^{40}Ar+^{124}Sn collisions at b=0 fm. The solid symbols represent the results with the stiff EOS and the open ones represent the results with the soft EOS. The total energy and the thermal energy are indicated by the circles and squares, respectively. The diamonds are extracted from ref [Jian 89] for ^{40}Ar+^{232}Th collisions. The lines are used to guide the eyes

from neutron multiplicity measurements for the ^{40}Ar +^{232}Th system [Jian 89]. In ref. [Jian 89], only the total excitation energies were given. For simplicity, we have assumed the residue mass A_{res} = 272 for the ^{40}Ar +^{232}Th system. If the residue mass for this heavier system decreases with the incident energy as dramatically as we have calculated for ^{40}Ar + ^{124}Sn system, the excitation energy *per nucleon* of the residues for the ^{40}Ar +^{232}Th system would actually be increasing with incident energy. With the present calculations, we have not attempted to determine the EOS from the available data though the calculated excitation energies per nucleon are closer to the predictions for soft EOS than for stiff EOS.

To further illustrate the difficulties in making these comparisons more quantitative at present, we show the total excitation energies of these systems. The total calculated excitation energies predicted for ^{40}Ar+ ^{124}Sn are lower than those determined experimentally for ^{40}Ar+ ^{232}Th system. Clearly, to extrapolate our calculations to the ^{40}Ar +^{232}Th system, we need to know more about how the residue excitation energies depend on the target mass. The calculations do show that the total excitation energies predicted by both equations of state appear to be in-sensitive to the incident energy at E/A $\geq$ 40 MeV, similar to the insensitivities demonstrated by the experimental data. This result indicates that, because the residue mass is decreasing with incident energy, the total excitation energy may even saturate at energies where the excitation energy per nucleon shown in Fig. 7.17 is still increasing.

B Massive Transfer Models

Experimental studies of residue excitation energies are frequently based on analysis of residue velocities using massive transfer models. Such models assume that part of the projectile 'fuses' with the target, while the remaining part of the projectile escapes with the beam velocity. Using this simple assumption, it is easy to deduce the

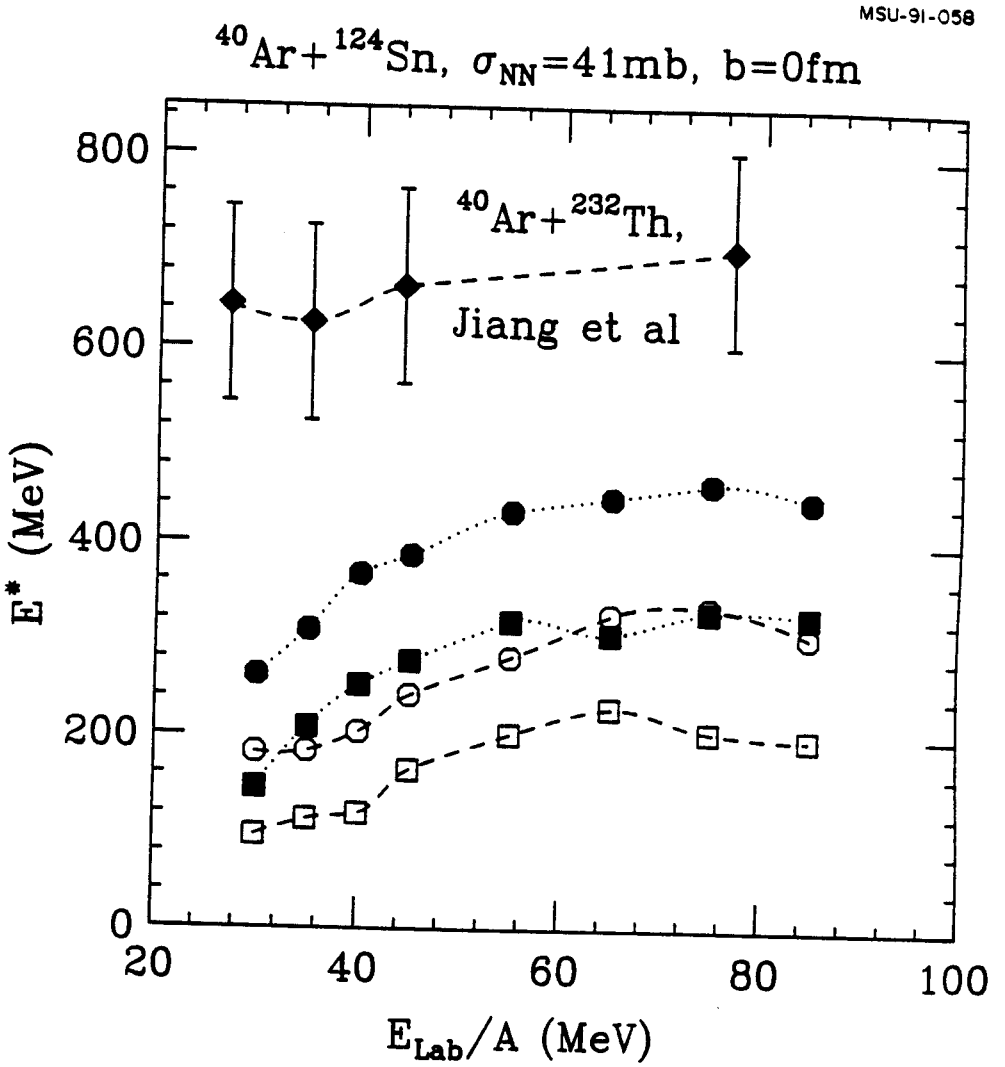

Figure 7.18: The dependence of the total energy and the thermal energy on the incident energy for ^{40}Ar+^{124}Sn collisions at b=0 fm and and for ^{40}Ar+^{232}Th extracted experimentally. The solid symbols represent the results with the stiff EOS and the open ones represent the results with the soft EOS. The total energy and the thermal energy are indicated by the circles and squares, respectively. The lines are used to guide the eyes.

excitation energy from the measured residue velocity (see Appendix B for details). To examine whether our BUU calculations are consistent with massive transfer models, we show in Fig. 7.19 the residue velocities (top panels) and the total excitation energies predicted by the BUU and the excitation energies extrapolated from the residue velocities (bottom panels) according to the massive transfer assumption. The left hand panels show the results for $^{40}Ar + ^{124}Sn$ collisions at E/A =35 MeV and the right hand panels show the results for E/A=65 MeV. The circles in the bottom panels depict the excitation energy extracted from the calculated residue velocity using the massive transfer models. The squares depict the total excitation energies obtained directly from the BUU calculations. Both the residual velocities and the excitation energies are determined for the targetlike residues which have survived the collisions.

At E/A=35 MeV, the predicted residue velocity by BUU is slightly less than the velocity of the center of mass and shows little dependence on impact parameter. In contrast, the velocity at E/A=65 MeV depends significantly on the impact parameter. At both incident energies and at all impact parameters, the massive transfer model significantly overestimates the excitation energy for the largest residue. The discrepancy is largest for the central collisions. In our simulations, the massive transfer model fails because it significantly underestimates the cooling due to preequilibrium emission and because the pre-equilibrium particles have velocities which are significantly less than the beam velocity, inconsistent with massive transfer models where the pre-equilibrium particles have the beam velocity. Caution must be taken when interpreting the calculated residual velocity because we have not adjusted σ_{NN} to reproduce the experimental data. Smaller discrepancies will occur for smaller values of σ_{NN}. Additional uncertainties may arise because the BUU models only predicts the average trajectory and can not accurately predict the multifragment breakup, due to the suppression of fluctuations by the ensemble averaging in the calculations.

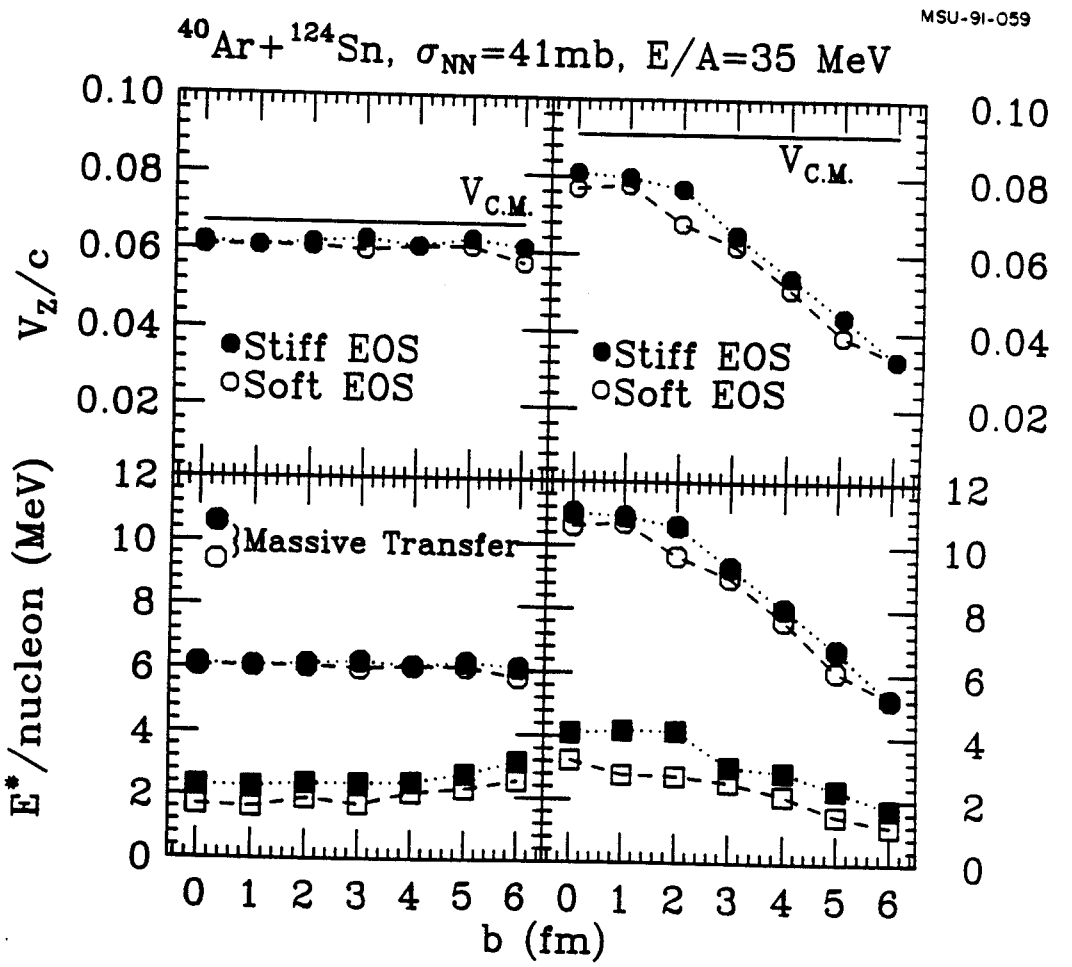

Figure 7.19: Comparison of BUU results with that from massive transfer models for ^{40}Ar+^{124}Sn collisions at E/A=35 MeV (left hand panels) and 65 MeV (right hand panels). The top panels show the residual velocities and the bottom panels show the comparison of the excitation energy. The details are discussed in the text. The lines are used to guide the eyes

Pre-equilibrium emission of complex fragments via multifragment breakup could reduce the velocity of the residue, and therefore might reduce the excitation energy estimated by the massive transfer model.

III Nuclear temperatures of the Residues

A Formalism

To allow a comparison with experimental emission temperatures, one must relate the excitation energies of the residues to the corresponding temperatures. For our computational residues, the level densities are sensitive to the density distributions and thermal energies of the residues and not solely to the total excitation energy, because there are sizable non-thermal collective energies and because the density distributions of the residues may retain some memory of the collision dynamics. We estimate the temperatures of the residues by integrating the Fermi-gas expression $\varepsilon^*(T, \varepsilon_F(\rho(\vec{r})))$ for the excitation energy per nucleon over the nuclear density and equating this value to the thermal energy provided by the numerical simulations, as follows.

$$E^*_{the} = \int_C d^3r \{\rho_p \cdot \varepsilon^*(T, \varepsilon_F(\rho_p)) + \rho_n \cdot \varepsilon^*(T, \varepsilon_F(\rho_n))\} \tag{7.1}$$

Here, ρ_p and ρ_n are the matter densities for neutrons and protons, respectively. For simplicity, we approximate $\varepsilon^*(T, \varepsilon_F(\rho))$ by its low temperature limit, and thus Eq. (7.1) becomes

$$E^*_{the} = aT^2 \tag{7.2}$$

with a, the level density parameter, given by

$$a = \frac{m}{3\hbar^2}(\frac{3\pi^2}{2})^{1/3} \int_C d^3r \rho^{1/3}(\vec{r}) \tag{7.3}$$

In expressions 7.2 and 7.3, we have assumed equal Fermi energies for protons and neutrons, and have used the local density approximation,

$$\varepsilon_F(\rho) = \frac{\hbar^2}{2m} \cdot (\frac{3\pi^2\rho}{2})^{2/3} \tag{7.4}$$

In our calculation, the level density parameter is evaluated from the density distribution produced from BUU calculations at freezeout. Since we already calculated the thermal energy, we can calculate the temperature from Eq. 7.2. The results are discussed in the following subsections.

B Results

^{40}Ar+^{27}Al collisions

Fig. 7.20 shows the predicted temperature at freezeout as a function of impact parameter for ^{40}Ar+^{27}Al collisions at E/A=30 MeV. The solid symbols indicates the calculations where a single fused residue is produced while the open ones correspond to the calculations in which two residues are observed in the final states. For both the stiff (circles) and soft (squares) equations of state, the predicted temperature decreases slightly with impact parameter. At larger impact parameters where no fusions occur, the predicted temperatures are smaller, thus indicating that, at E/A=30 MeV, the fusion cross sections are not limited by thermal instability at high temperatures. For all impact parameters, the temperatures predicted by the stiff EOS are much higher than that predicted by the soft EOS, even though the nucleon cross sections with the stiff EOS has been adjusted to produce similar fusion cross section as that of the soft EOS. The predicted values, T$\approx 3-5$, are comparable to inclusive experimental observations.

To indicate the range of the level density parameter, the different curves in Fig. 7.20 are the results obtained by Eq. (7.2), with respective values of a indicated in

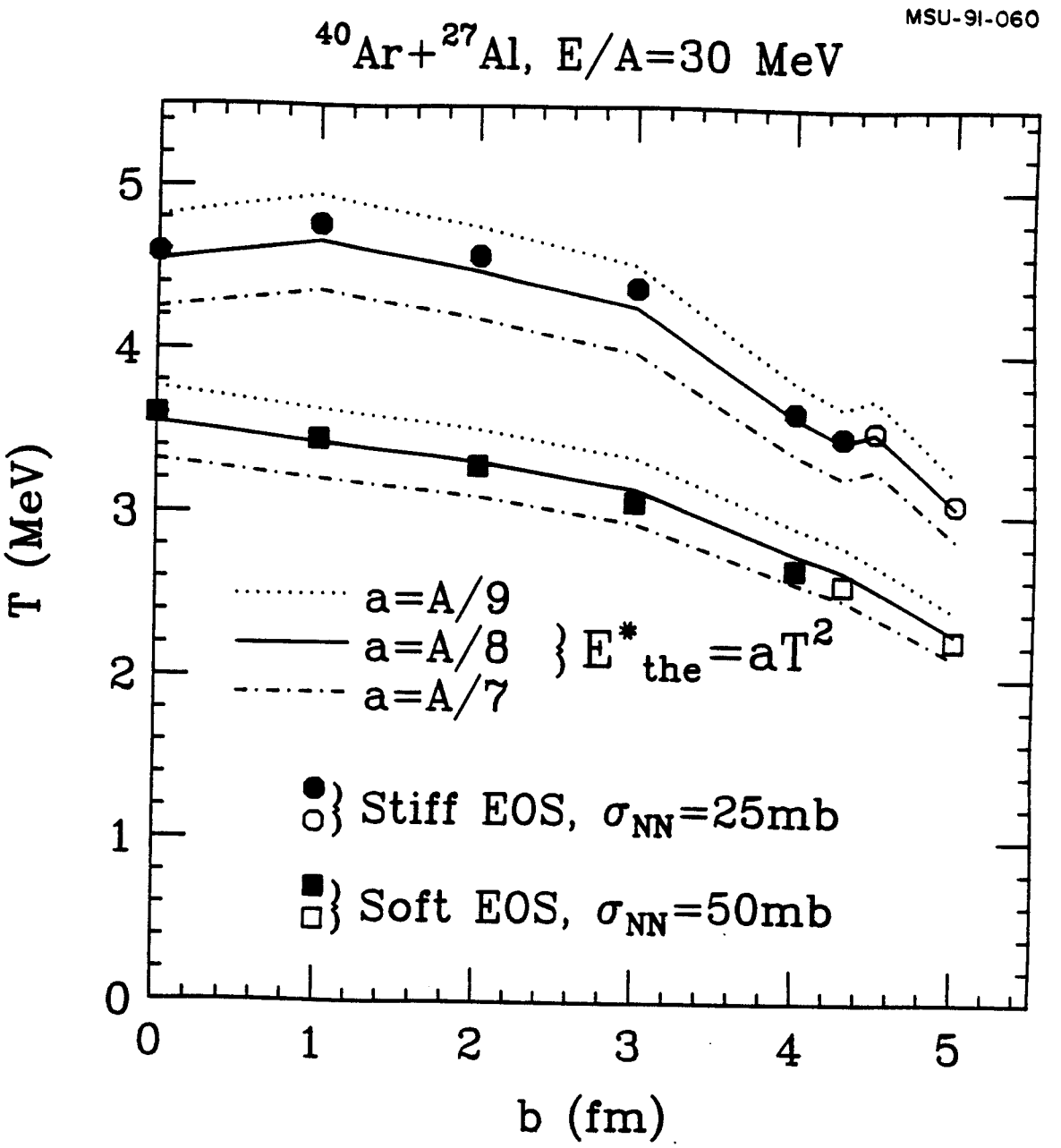

Figure 7.20: Dependence of the temperature on the impact parameter for ^{40}Ar+^{27}Al at E/A=35 MeV. The circles are results with the stiff EOS and σ_{NN} = 25 mb. The squares are results with the soft EOS and σ_{NN} = 50 mb. The solid and open symbols are discussed in the text. The respective lines are calculations by $E^* = aT^2$ with corresponding values of a indicated in the figure.

the figure. The predicted values of the level density parameter show little sensitivity to the nuclear equation of state. These in-sensitivities of the level density parameter to the nuclear EOS may indicate that rather similar freezeout density distributions are produced by both equation of state. We note here that although the values of the level density parameter, $a \approx A/7 - A/9$, are similar to the empirical values of A/8 commonly used to relate the total excitation energy to the temperature via the relation $E^* = aT^2$, it is important to recall that we are using the level density parameter to describe the thermal excitation energy and the temperature.

The dependence of temperature on incident energy is shown in Fig. 7.21. The left hand side is the calculations at b=0 and the right hand side is at $b = b_{max}$, the maximum impact parameter for fusion. The predicted temperature at $b = 0$ for both equations of state increases slightly with energy, a trend also seen experimentally [Chen 87c]. In all energies presented here, the calculations with the stiff EOS are ~ 1 MeV higher than that with the soft EOS, though the corresponding σ_{NN} is half as large. At lower energies, $E/A \approx 25-30$ MeV, the values of T at b_{max} are smaller than that at $b = 0$. At higher energies, $E/A \approx 30 - 40$ MeV, the values of temperature at b_{max} approach those at $b = 0$ fm, reflecting the fact that $b_{max} \rightarrow$ with increasing incident energy.

Based on the calculations on ^{40}Ar+ ^{27}Al collisions, it is possible to extract the information concerning both the equation of state and σ_{NN}, if the observables for experiments are properly selected. At low energies, for example, at E/A=30 MeV, the temperature at most central collisions, $b \leq 3$ fm, are relatively insensitive to impact parameter, but very sensitive to the nuclear equations of state (Fig. 7.20), even if the corresponding nucleon-nucleon cross sections are constrained to yield equal fusion cross sections. Thus it may be possible that, by measuring the fusion cross section, and by measuring the excitation energy or temperature for central collisions, one

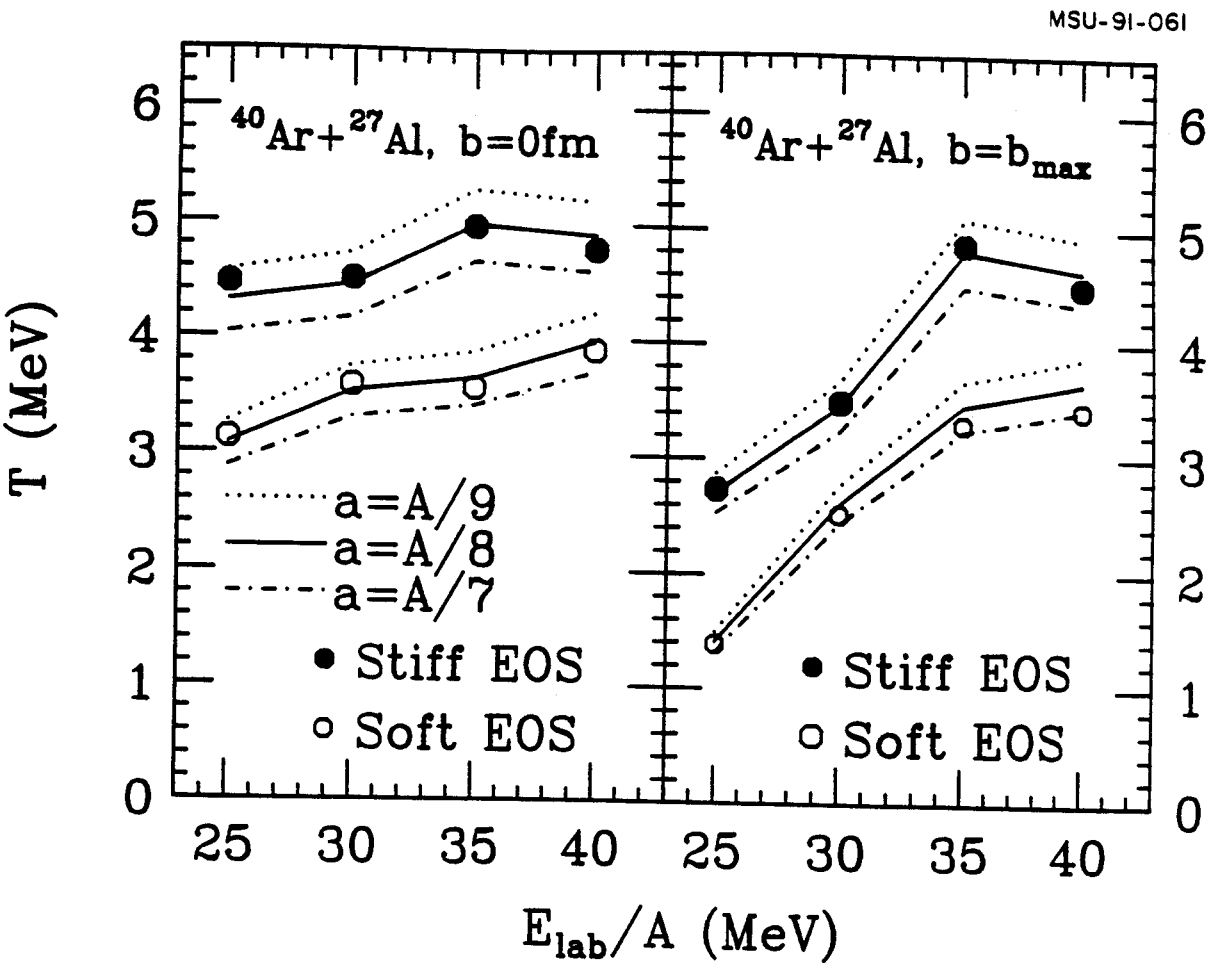

Figure 7.21: Dependence of the temperature on the incident energy for ^{40}Ar+^{27}Al. The left hand window is calculations at b=0 and the right hand window is the calculations at b_{max}, the maximum impact parameter for fusion. The solid circles are results with the stiff EOS and σ_{NN} = 25 mb. The open circles are results with the soft EOS and σ_{NN} = 50 mb. The respective lines are calculations by $E^* = aT^2$ with corresponding values of a indicated in the figure.

may obtain the minimum two constraints needed to separate the dual dependences of the observables on the nuclear EOS at low density and σ_{NN}. The emission pattern of coincident light particles, discussed in Chapter 6, can also provide additional information about σ_{NN}.

^{40}Ar+^{124}Sn collisions

Fig. 7.22 shows the predicted temperature as a function of impact parameter for ^{40}Ar+^{124}Sn collisions at E/A=35 MeV (top window) and E/A=65 MeV (bottom window), respectively. The dependence of the temperature on nuclear equation of state is shown in the left-hand panels. The solid circles in the left hand panels depict the results obtained for the stiff EOS, while the open ones depict the results for the soft EOS. For comparison, the respective curves are the results obtained with Eq. (7.2), and a constant level density parameter a with its value indicated in the figure. At E/A=35 MeV and central collisions, b$\leq$ 4 fm, the predicted temperature depends weakly on impact parameter, but depends sensitively on nuclear equation of state. In contrast, the temperature depends rather strongly upon the impact parameter at higher energies, E/A =65 MeV.

The sensitivities to nucleon-nucleon cross sections are shown on the right hand panels of Fig. 7.22. The predicted temperatures show surprisingly little sensitivity to the nucleon-nucleon cross section. This result is due to the fact that the calculations with smaller nucleon cross sections yield earlier freezeout times by using the criteria of nucleon emission rates and the thermal energies. For example, at E/A=35 MeV, the freezeout times with soft EOS and σ_{NN} = 20 mb are about $t_{fre} \approx$ 120 fm/c in contrast to $t_{fre} \approx$ 140 fm/c for the corresponding calculations with σ_{NN} = 41 mb. We also note here that the predicted level density parameters for the soft EOS and σ_{NN} = 20 mb at E/A=35 MeV, are higher than that for other calculations shown

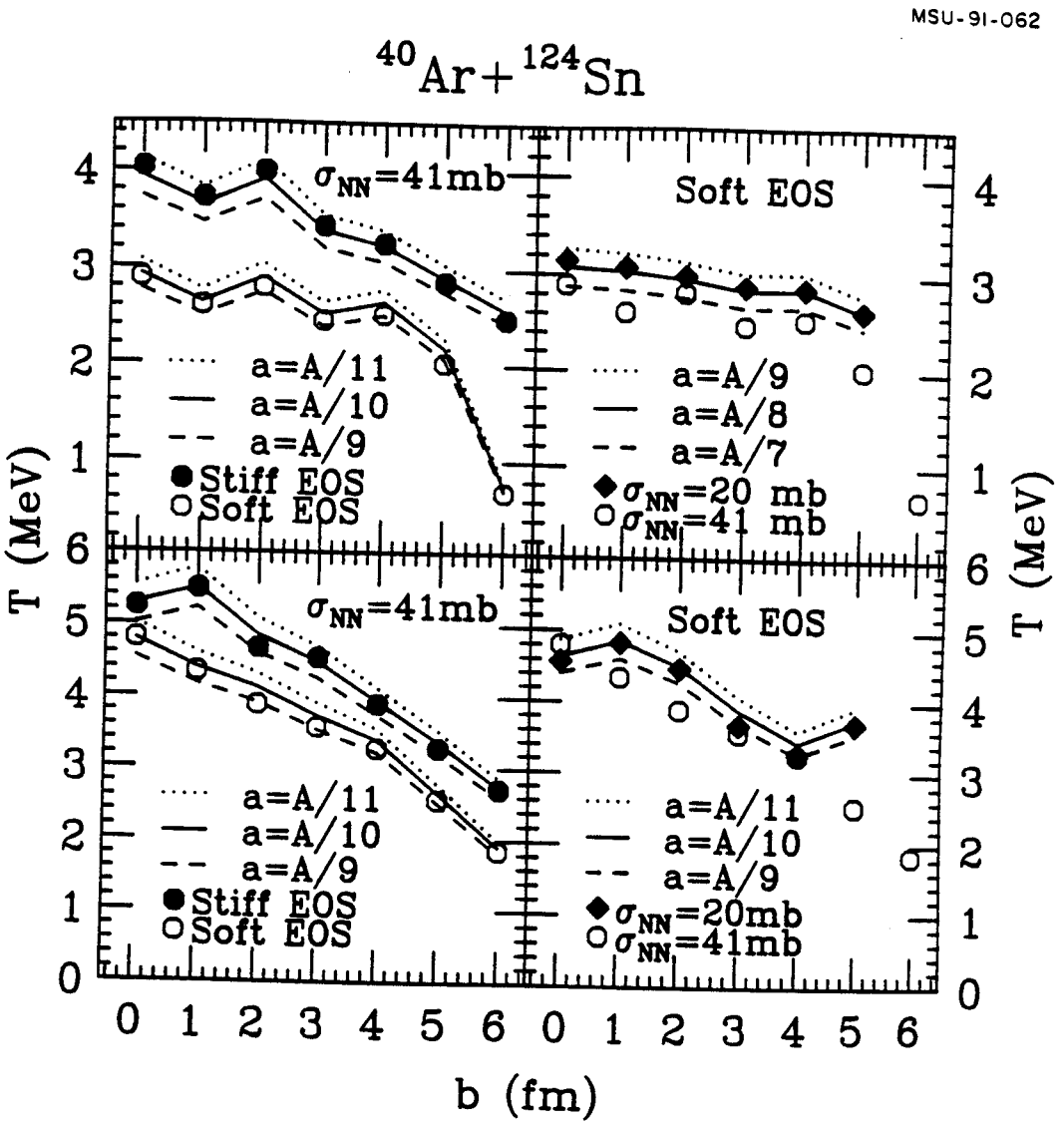

Figure 7.22: Dependence of the temperature on the impact parameter for ^{40}Ar+^{124}Sn collisions at E/A=35 MeV (left hand window) and 65 MeV (right hand window). The solid circles are results with the stiff EOS and the open circles are results with the soft EOS. The respective lines are calculations by $E^* = aT^2$ with corresponding values of a indicated in the figure.

in the figure. This occurs because the densities at freezeout for this calculation are distributed over a more extended volume than those for the other calculations.

Fig. 7.23 shows the energy dependence of the temperature for the ^{40}Ar+^{124}Sn system at b=0 fm. The experimental values of the emission temperature obtained in this dissertation study, along with other experimental results [Poch 85a, Poch 87, Chen 88a, Naya 90], are depicted by the squares. Both equations of state predict a gradual increase in temperature as the incident energy was raised from E/A=30 MeV to 55 MeV. The stiff EOS predicts consistent larger values of temperature at all incident energies. At higher incident energies, E/A $\geq$ 65 MeV, however, the temperature increases very little, suggesting a possible saturation in the temperature with incident energy. At all energies, our calculated temperatures are similar to experimental ones. Due to large uncertainties in the choice of the impact parameter averaging and the uncertainties in the Pauli-blocking and nucleon-nucleon cross section, we can not make more quantitative conclusions concerning the compressibility of the EOS at low density from our present comparisons.

IV Summary

In summary, guided by numerical solution of an improved BUU equation, we have studied the global features of the reaction dynamics for ^{40}Ar+^{124}Sn collisions. Using various criteria, we found that consistent freezeout times could be defined. The predicted thermal temperature for the heavy residues at freezeout is comparable with experimental measurements.

Our studies indicates that the extraction of information concerning the equation of state and the in-medium nucleon-nucleon cross sections is not trivial. Although the predicted excitation energies and emission temperatures display a significant sen-

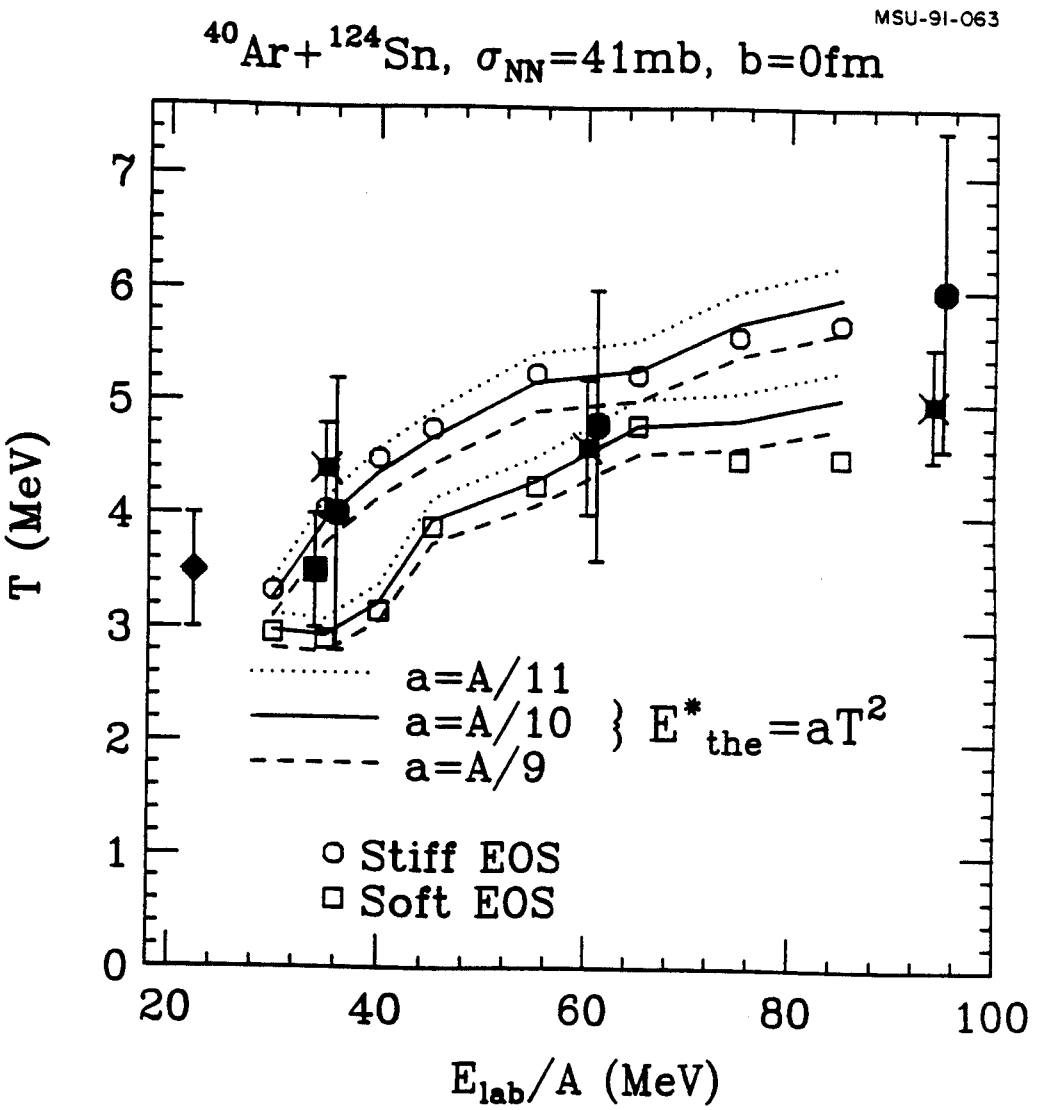

Figure 7.23: Dependence of the temperature on the incident energy for ^{40}Ar+^{124}Sn collisions at b=0 fm. The open circles are results with the stiff EOS and the open squares are results with the soft EOS. The respective lines are calculations by $E^*_{the} = aT^2$ with corresponding values of a indicated in the figure. The sold diamond is the experimental result of this dissertation. The solid square is taken from ref. [Naya 90] which is derived from a large number of particle unstable states. The solid circles and solid crosses are results of excited states of ^{5}Li and ^{6}Li, respectively [Chen 88a].

sitivity to the nuclear equation of state, a comparable sensitivity to impact parameter is also observed, particularly at higher energies. Fortunately, our calculations show that the predicated thermal excitation energies and the temperatures are relatively in-sensitive to in-medium nucleon-nucleon cross section, reducing the possibility of ambiguities in the interpretation of emission temperatures.

Chapter 8

Conclusion

In this dissertation, we have measured the average emission temperature for a large number of particle stable states of intermediate mass fragments for ^{32}S induced reactions on ^{nat}Ag at the incident energy of E/A=22.3 MeV. To assess if measurements of nuclear temperature can provide information concerning the nuclear equation of state and the in-medium nucleon-nucleon cross section, we have performed dynamical calculations based on the Boltzmann-Uehling-Uhlenbeck (BUU) equation.

To test the statistical assumptions for the fragment emission and to check the degrees of thermalization and the internal consistency of thermal assumptions, 28 independent γ-ray transition intensities were measured using the Spin Spectrometer [Jaas 83]. The measured relative populations of these states were compared to those calculated from a thermal model which include sequential feeding from higher lying states. This comparison indicated an average emission temperature of T$\approx 3-4$ MeV. This result is consistent with the trends established by measurements of the particle unstable states of ^{4}He, ^{5}Li, ^{6}Li, and, ^{8}B nuclei [Poch 85a, Poch 87, Chen 88a]. It is also consistent with the results of a recent investigation of large number of particle unstable states of intermediate mass fragments in ^{14}N induced reactions on Ag at E/A=35 MeV [Naya 90]. Putting together these results suggests that the emission temperature increases gradually with incident energy from values of $T \approx 3-4$ MeV

at E/A $\approx$ 23 MeV to $T \approx 5 - 6$ MeV at E/A=94 MeV.

To study whether the emission temperature can provide any information about the nuclear equation of state and the in-medium nucleon-nucleon cross section, we have performed dynamical calculations based on the Boltzmann-Uehling-Uhlenbeck (BUU) equation. Since the BUU equation is an one-body theory, it does not have the many-body fluctuations required to produce the intermediate mass fragments. We therefore attempted to study the excitation energy and the emission temperature of the heavy residues. We believe this approach may be justified because molecular dynamics calculations [Lenk 86, Schl 87] indicate that all reaction products, regardless of their masses, could be characterized by a common temperature. This result indicates that the information concerning the emission of intermediate mass fragments may be obtained from the emission temperatures of heavy residues predicted by BUU calculations.

To improve the stability of the ground-state nucleus and the conservation of energy during nucleus-nucleus collisions, we have used a Lattice Hamiltonian method to solve the BUU equation. With this improved code, consistent thermal freezeout times are obtained from the emission rates of nucleons and the thermal excitation energies of the heavy residue produced in ^{40}Ar +^{27}Al and ^{40}Ar +^{124}Sn collisions. The predicted total excitation energies and emission temperatures at freezeout are comparable with those obtained from experiments. These predicted values for the excitation energies and temperatures are quite sensitive to the equation of state. Surprisingly, little sensitivity of the emission temperature to the in-medium nucleon-nucleon cross section is observed. Unfortunately, the predicted emission temperatures are also sensitive to the impact parameter, particularly at high incident energies, making it difficult to determine the EOS and σ_{NN} from inclusive measurements.

Calculations for ^{40}Ca+^{40}Ca and ^{40}Ar+^{27}Al collisions also indicate that the residue

cross section is rather sensitive to both the equation of state at sub-nuclear density and the in-medium nucleon-nucleon cross section. This result provides another observable which may be used to obtain information concerning the equation of state at the *low* densities. We also demonstrate that measurements of the emission pattern of the coincident light particles may provide information concerning the in-medium nucleon-nucleon cross section.

The dynamical limitations to the formation of fusionlike residue are investigated by calculating the excitation energies and the total angular momenta for the residues formed in $^{40}Ar + {}^{27}Al$ collisions. These calculations indicate that the dynamics, not the Coulomb or thermal instability [Levi 84, Besp 89, Gros 82, Ban 85, Gros 86, Gros 88, Bond 85, Mekj 90], plays a decisive role in limiting the production of fusion-like residues at energies $E/A \leq 30$ MeV. At higher energies, $E/A \geq 35$ MeV, dynamics are still important, but we can not rule out additional reductions of the residue cross sections due to instabilities of hot nuclei at high temperature.

Based on our theoretical study, it is possible to extract information concerning the nuclear equation of state at sub-nuclear density and the in-medium nucleon-nucleon cross section from exclusive investigations of emission temperatures, cross sections of fusionlike residues, and the emission pattern of light particles [Xu 90, Tsan 89]. Additional theoretical work is needed to check the sensitivity of experimental observables to momentum dependent interactions as well as to the details of the Pauli-blocking algorithm.

Appendix A

Correction of Finite Statistics to the Collective Excitation Energy

In this appendix, we discuss two methods used to correct for spurious contributions to the collective energy due to finite number of test particles.

I The Goldhaber's Problem

To illustrate the finite particle number effects, we first consider the problem of projectile fragmentation. In order to understand the projectile fragmentation in relativistic heavy ion collisions, Goldhaber [Gold 74] considered the following question: Suppose that A nucleons are assembled with a zero net momentum, $\vec{p}_A = 0$. If K of these nucleons are chosen at random and are emitted as a single fragment, what would be the mean square total momentum p_K^2 of this fragment?

Goldhaber [Gold 74] solved this problem by the following arguments. By assumption, the total momentum of A nucleons has

$$< p_A^2 >=< (\sum_i \vec{p}_i)^2 >= 0, \tag{A.1}$$

and, in consequence,

$$A < p^2 > + \sum_{i \neq j} < \vec{p}_i \cdot \vec{p}_j >= 0, \tag{A.2}$$

or

$$\ll \vec{p}_i \cdot \vec{p}_j \gg = - < p^2 > /(A-1), \tag{A.3}$$

where $< p^2 >$ is the mean square nucleon momentum and the double bracket denotes an average over all $i \neq j$. A similar exercise applied to the momentum of K nucleons yields

$$< p_K^2 > = \ll (\sum_{i=1}^{K} \vec{p}_i)^2 \gg = K < p^2 > + K(K-1) \ll \vec{p}_i \cdot \vec{p}_j \gg \tag{A.4}$$

Here, the double bracket indicates an average over all possible choices of the K nucleons from given A nucleons. Substituting Eq. (A.3) into Eq. (A.4), one obtains

$$\begin{aligned} < p_K^2 > &= K < p^2 > - K(K-1) < p^2 > /(A-1) \\ &= K(A-K) < p^2 > /(A-1) \end{aligned} \tag{A.5}$$

Goldhaber used a Fermi gas value for $< p^2 >$ and was able to interpret quite successfully the mass dependent fragmentation spectra with Eq. (A.5). In the limit $A \to \infty$, $(A-K)/(A-1) \approx 1$, thus Eq. (A.5) becomes

$$< p_K^2 > \approx K < p^2 > \tag{A.6}$$

As we will see later, this expression is very close to the spurious collective momentum of K test particles located at a given lattice point in the hot residue.

II Correction of Finite Statistics to the Collective Excitation Energy

In our calculations, the collective excitation energy is obtained by summing up contributions from individual lattice cells in which the collective current are evaluated. Let's look at a given lattice cell with K test particles. Suppose this cell has a true collective momentum of $\vec{p}_{coll}$ per nucleon in the continuum limit (an infinite number

of test particles). The true collective excitation energy of K test particles can be represented by

$$E^0_{coll} = \frac{Kp^2_{coll}}{2m}. \tag{A.7}$$

Here m is the nucleon mass. In practice, this true collective energy is not known. Instead, we calculate the apparent collective energy E^a_{coll}

$$E^a_{coll} = < \frac{(\sum_i^K \vec{p}_i)^2}{2Km} > . \tag{A.8}$$

Rewriting $\vec{p}_i = \vec{p}_i\,' + \vec{p}_{coll}$ (here , $\vec{p}_i\,'$ is zero on the average),

$$E^a_{coll} = \frac{< [\sum_i^K (\vec{p}_i\,' + \vec{p}_{coll})]^2 >}{2Km}$$

$$= \frac{1}{2Km}[K^2 p^2_{coll} + (\sum_{i=1}^{K} \vec{p}_{coll}) \cdot < \sum_{i=1}^{K} \vec{p}_i\,' > + < (\sum_{i=1}^{K} \vec{p}_i\,')^2 >], \tag{A.9}$$

In our simulations, the second term can be ignored, since the vector sum satisfies $(\sum_{i=1}^K \vec{p}_i\,') \approx 0$, when summing over all possible ensembles or over all lattice points. The third term, however, is non-zero and has a value corresponding to Eq. (A.6). Using this expression, Eq. (A.9) becomes

$$E^a_{coll} \approx \frac{Kp^2_{coll}}{2m} + \frac{< p'^2 >}{2m}$$

$$= E^0_{coll} + \frac{< p'^2 >}{2m}. \tag{A.10}$$

Thus the apparent collective energy is larger than the true collective energy by a value of $\frac{<p'^2>}{2m}$. Rewriting Eq. (A.10) in terms of the true collective excitation energy per nucleon, one gets

$$\frac{E^0_{coll}}{K} = \frac{E^a_{coll}}{K} - \frac{1}{K} \cdot \frac{< p'^2 >}{2m}$$

$$= \frac{E^a_{coll}}{K} - \varepsilon_{corr}, \tag{A.11}$$

with

$$\varepsilon_{corr} = \frac{1}{K} \cdot \frac{< p'^2 >}{2m}. \tag{A.12}$$

This correction to the collective excitation energy is due to the finite number of test particles. We note here that p'^2 is viewed in the frame of the true local velocity and is not known. In the following two subsections, we describes two different ways to estimate $< p'^2 >$.

A Thomas-Fermi Approximation

Since $\vec{p}'$ is evaluated in a frame moving with local current, one may estimate ε_{corr} in the local Thomas Fermi approximation. Using this assumption, Eq. (A.12) becomes

$$\varepsilon_{corr} = \frac{1}{K} \cdot \frac{< p'^2 >}{2m} \approx \frac{1}{K} \frac{3}{5} \epsilon_F, \tag{A.13}$$

here the local Fermi energy ϵ_F is given by

$$\epsilon_F = \frac{p_F^2}{2m}, \tag{A.14}$$

with

$$p_F = \hbar (\frac{3\pi^2 \rho}{2})^{1/3}. \tag{A.15}$$

In these expressions, we have assumed that the proton and neutron have the same local Fermi energy.

For a lattice cell of size 1 fm^{-3}, with local density of $\rho_0 = 0.17 fm^{-3}$ and $N_{test} = 80$, one would obtains $K \approx 14$, thus the correction to collective energy would be $\varepsilon_{corr} \approx 1.7$ MeV/nucleon. This is clearly a non-negligible correction. As we discussed in Chapter 6, we have calculated the collective energy for a nucleus in its ground state. After correcting the local energy by a term given by Eq. (A.13), one indeed obtains a zero collective energy (for details, see the discussions in Chapter 6).

B Local Momentum Analysis

Another way of calculating $< p'^2 >$ in Eq. (A.12) is to try to relate it in terms of momentum $\vec{p}_i$ which is known. For this purpose, we use the identity

$$\sum_{i\neq j}(\vec{p}_i - \vec{p}_j)^2 = \sum_{i\neq j}(\vec{p}_i\,' - \vec{p}_j\,')^2. \tag{A.16}$$

Averaging over ensembles, the right hand of this equation becomes

$$< \sum_{i\neq j}(\vec{p}_i\,' - \vec{p}_j\,')^2 >= 2K(K-1) < p'^2 > -2K(K-1) \ll \vec{p}_i\,' \cdot \vec{p}_j\,' \gg, \tag{A.17}$$

Using Eq. (A.3), this equation becomes

$$\begin{aligned} < \sum_{i\neq j}(\vec{p}_i\,' - \vec{p}_j\,')^2 >&= 2K(K-1) < p'^2 > +2K(K-1) \cdot \frac{< p'^2 >}{A-1} \\ &= 2K(K-1) \cdot \frac{A}{A-1} \cdot < p'^2 > \\ &\approx 2K(K-1) < p'^2 >; \end{aligned} \tag{A.18}$$

in the limit of large A. Similarly, the left hand side of Eq. (A.16) has the form

$$< \sum_{i\neq j}(\vec{p}_i - \vec{p}_j)^2 >= 2(K-1)\sum_{i=1}^{K} < p_i^2 > -2 < \sum_{i\neq j} \vec{p}_i \cdot \vec{p}_j >, \tag{A.19}$$

Using the identity

$$< \sum_{i\neq j} \vec{p}_i \cdot \vec{p}_j >=< (\sum_{i=1}^{K} \vec{p}_i)^2 > - < \sum_{i=1}^{K} p_i^2 >, \tag{A.20}$$

we can rewrite (A.19) into

$$\begin{aligned} < \sum_{i\neq j}(\vec{p}_i - \vec{p}_j)^2 >&= 2K[\sum_{i=1}^{K} < p_i^2 > -K < (\frac{\sum_{i=1}^{K} \vec{p}_i}{K})^2 >] \\ &= 2K < \sum_{i=1}^{K}[p_i^2 - (\frac{\sum_{i=1}^{K} \vec{p}_i}{K})^2] >; \end{aligned} \tag{A.21}$$

Here the term $\frac{1}{2m}(\frac{\sum_{i=1}^{K} \vec{p}_i}{K})^2$ is the apparent collective energy. Equating Eq. (A.18) and Eq. (A.21), one obtains

$$\varepsilon_{corr} = \frac{1}{2m} \cdot \frac{1}{K(K-1)} \cdot < \sum_{i=1}^{K}[p_i^2 - (\frac{\sum_{i=1}^{K} \vec{p}_i}{K})^2] > . \tag{A.22}$$

which can be evaluated at each lattice point. This expression corrects for all spurious collective motion coming from the Fermi motion and the thermal motion. In our calculations, We have evaluated numerically the corrections given by Eq. (A.13) and by Eq. (A.22), and they essentially give the same results, indicating the dominant contribution from the Fermi motion. Further discussions are presented in Chapter 6.

Appendix B

Massive Transfer Model

In this appendix, we present the basic formula of massive transfer models which are commonly used to estimate the excitation energy in incomplete fusion reactions. For convenience, we start by considering reactions leading to complete fusion.

I Complete Fusion

Suppose a projectile of mass m_p with beam velocity $\vec{v}_p$ is fused completely with a target of mass m_t, the residue velocity $\vec{v}_r$ of the fused composite system satisfies

$$\vec{v}_r = \frac{m_p \vec{v}_p}{m_p + m_t}. \tag{B.1}$$

Neglecting the ground state Q-values, the total excitation energy E^* has the form

$$\begin{aligned} E^* &= \frac{1}{2} m_p v_p^2 - \frac{1}{2}(m_p + m_t) v_r^2 \\ &= \frac{1}{2} \cdot \frac{m_t(m_p + m_t)}{m_p} \cdot v_r^2. \end{aligned} \tag{B.2}$$

Eqs. (B.1)-(B.2) are constantly used in estimation of the excitation energies for reactions leading to complete fusion.

II Incomplete Fusion

The massive transfer models are referred to the following assumption used in incomplete fusion reactions. For a normal kinematics in which $m_p < m_t$, the massive transfer models assume that a fraction, f, of the projectile mass fuses completely with the target, with the remaining fraction, $1 - f$, escaped with beam velocity. The excitation of the composite system can therefore be evaluated from the measured residue velocity. Under this assumption, one has

$$(fm_p + m_t)v_r = fm_p v_p, \tag{B.3}$$

or

$$f = \frac{m_t v_r}{m_p(v_p - v_r)}, \tag{B.4}$$

and similar as Eq. (B.2), the excitation energy E^* are given by

$$E^* = \frac{1}{2} \cdot \frac{m_t(fm_p + m_t)}{fm_p} \cdot v_r^2. \tag{B.5}$$

From Eqs. (B.4)-(B.5), one may obtain the fraction f and the excitation energy E^* once the residue velocity is measured.

Similar exercise can be performed for reverse kinematics ($m_p > m_t$). In this case, the projectile fuses with part of the target f. The expressions for f and E^* are given by

$$f = \frac{m_p(v_p - v_r)}{m_t v_r}, \tag{B.6}$$

$$E^* = \frac{1}{2} \cdot \frac{fm_t(m_p + fm_t)}{m_p} \cdot v_r^2. \tag{B.7}$$

Using these equations, We have calculated the excitation energies from the residue velocities predicted by BUU calculations. The results are discussed in Chapter 6 and Chapter 7.

References

[Aich 85] J. Aichelin and G. Bertsch, Phys. Rev. **C331**, 1730 (1985).

[Aich 87] J. Aichelin, A. Rosenhauer, G. Peilert, H. Stöcker, and W. Greiner, Phys. Rev. Lett. **58**, 1926(1987).

[Aich 88] J. Aichelin, G. Peilert, A. Bohnet, A. Rosenhauer, H. Stocker and W. Greiner, Nucl. Phys. **A488**, 437c-450c (1988), and references contained therein.

[Ajze 82] F. Ajzenberg-Selove, Nucl. Phys. A**375** (1982) 1.

[Ajze 84] F. Ajzenberg-Selove, Nucl. Phys. A**413** (1984) 1.

[Ajze 85] F. Ajzenberg-Selove, Nucl. Phys. A**433** (1985) 1.

[Ajze 86a] F. Ajzenberg-Selove, Nucl. Phys. A**449** (1986) 1.

[Ajze 86b] F. Ajzenberg-Selove, Nucl. Phys. A**460** (1986) 1.

[Ajze 87] F. Ajzenberg-Selove, Nucl. Phys. A**475** (1987) 1.

[Ajze 88] F. Ajzenberg-Selove, Nucl. Phys. A**490** (1988) 1.

[Alek 90] K. Aleklett, W. Loveland, M. de Saint-Simon, L. Sihver, J.O. Lilienzin, G.T. Seaborg, Phys. Lett. **B236**, 404 (1990)

[Auge 85] G. Auger, D. Jouan, E. Plagnol, F. Pougheon, F. Naulin, H . Doubre, and Ggrégoire, Z. Phys. **A321** (1985) 243.

[Auge 86] G. Auger, E. Plagnol, D. Jouan, C. Guet, D. Heuer, M. Maurel, H. Nifenecker, C. Ristori, F. Schussler, H. Doubre, and C. Gregoire, Phys. Lett. **169B**, 161(1986).

[Ban 85] S. Ban-Hao and D. H. E. Gross, Nucl. Phys. A**437** (1985) 643.

[Barz 89] H.W. Barz, H. Schulz, and G.F. Bertsch, Phys. Lett. **217** (1989) 397.

[Baue 87] W. Bauer, et al, Phys. Rev. Lett. 58 (1987) 863.

[Baue 88] W. Bauer, Phys. Rev. Lett. **61**, 2534 (1988)

[Baue 90] W. Bauer, Michigan State University report MSUNSCL-699.

[Bert 78] G. Bertsch and D. Mundinger, Phys. Rev. C17,1646 (1978).

[Bert 83] G. Bertsch and P.J. Siemens, Phys. Lett. **126B** (1983) 9.

[Bert 84] G.F. Bertsch, H. Kruse, and S. Das Gupta, Phys. Rev. C29, (1984) 673.

[Bert 87] G.F. Bertsch, W.G.Lynch, and M.B. Tsang, Phys. Lett. B 189, (1987) 384.

[Bert 88] G. F. Bertsch and S. Das Gupta, Phys. Reports **160** (1988) 189; and references contained therein.

[Besp 89] J. Besprosvany and S. Levit, Phys. Lett. **B217**, 1 (1989).

[Bhat 89] S. Bhattacharya, J.N. De, K. Krishan, and S.K. Samaddar, Phys. Rev. Lett. **62**, (1989) 2589.

[Birk 79] J.R. Birkelund, L.E. Tubbs, J.R. Huizenga, J.N. De, and D. Sperner, Phys. Rep. **56**, 107 (1979)

[Bloc 86] C. Bloch, W. Benenson, E. Kashy, D. J. Morrissey, R. A. Blue, R. M. Ronningen, and H. Utsunomiya, Phys. Rev. C **34** (1986) 850.

[Bloc 87] C. Bloch, W. Benenson, A.I. Galonsky, E. Kashy, J. Heltsley, L. Heilbronn, M. Lowe, B. Remington, D.J. Morrissey, and J. Kasagi, Phys. Rev. **C36**, 203 (1987).

[Boal 84] David Boal, Phys. Rev. **C30**, 119 (1984).

[Boal 88a] D.H. Boal and J.N. Glosli, Phys. Rev. **C37**, 91 (1988).

[Boal 88b] D.H. Boal and J.N. Glosli, Phys. Rev. **C38**, 1870 (1988).

[Boal 89] D. H. Boal, J. N. Glosli, and C. Wicentowich Phys. Rev. C **40** (1989) 601.

[Boal 89a] D. H. Boal and J. N. Glosli, and C. Wicentowich Phys. Rev. Lett. **62** (1989) 737.

[Bohn 90] W.Bohne, et al, Phys. Rev. C41 (1990) R5.

[Bond 78] J.P. Bondorf, S.I.A. Garpman, and J. Zimanyi, Nucl. Phys. **A296**, 320 (1978).

[Bond 85] J. Bondorf *et al*, Phys. Lett. **162B**, 30 (1985); Nucl. Phys. **A443**,321 (1985).

[Bord 85] B. Borderie and M.F. Rivet, Z. Phys. **A321**, 703 (1985)

[Boug 87] R. Bougault, D. Horn, C.B. Chitwood, D.J. Fields, C.K. Gelbke, D.R. Klesch, W.G. Lynch, M.B. Tsang, and K. Kwiatkowski, Phys. Rev. **C36**, 830 (1987).

[Bour 85] B. Bourderie and M.F. Rivet, Z. Phys. A321 (1985) 703.

[Brau 87] P. Braun-Munzinger and J. Stachel, Ann. Rev. Nucl. Part. Sci. **37**, 97 (1987).

[Brow 88] B. A. Brown, Private Communication

[Cass 87] W. Cassing, Z. Phys. **A327**, 447(1987).

[Cass 88] W. Cassing, Z. Phys. **A329**, 487(1988).

[Cass 89] Proceedings of the International Workshop on Nuclear Dynamics at Medium and High Energies, Bod Honnef, Fed. Rep. Germany, Oct. 10-14, 1988, Edited by W. Cassing and U. Mosel; Nucl. Phys. A495 (1989) 1c.

[Cebr 90] D.A. Cebra, S. Howden, J. Karn, A. Nadasen, C.A. Ogilvie, A. Vander Molen, G.D. Westfall, W.K. Wilson, J.S. Winfield, and E. Norbeck, Phys. Rev. Lett. **64**, 2246 (1990).

[Chen 87a] Z. Chen, C. K. Gelbke, J. Pochodzalla, C. B. Chitwood, D. J. Fields, W. G. Lynch, and M. B. Tsang, Phys. Lett. **184B** (1987) 280.

[Chen 87b] Z. Chen, C. K. Gelbke, J. Pochodzalla, C.B. Chitwood, D.J. Fields, W. G. Gong, W. G. Lynch, and M. B. Tsang, Nucl. Phys. A**473** (1987) 564.

[Chen 87c] Z. Chen, C. K. Gelbke, W. G. Gong, Y. D. Kim, W. G. Lynch, M. R. Maier, J. Pochodzalla, M. B. Tsang, F. Saint-Laurent, D. Ardouin, H. Delagrange, H. Doubre, J. Kasagi, A. Kyanowski, A. Peghaire, J. Peter, E. Rosato, G. Bizard, F. Lefebvres, B. Tamain, J. Quebert and Y. P. Viyogi, Phys. Rev. C **36** (1987) 2297.

[Chen 87d] Z. Chen, C.K. Gelbke, W.G. Gong, Y.D. Kim, W.G. Lynch, M.R. Maier, J. Pochodzalla, M.B. Tsang, F. Saint-Laurent, D. Ardouin, H. Delagrange, H. Doubre, J. Kasagi, A. Kyanowski, A. Peghaire, J. Peter, E. Rosato, G. Bizard, F. Lefebvres, B. Tamain, J. Quebert, and Y.P. Viyogi, Phys. Lett. **B199**, 171 (1987).

[Chen 88] Z. Chen, C. K. Gelbke, Phys. Rev. C **38** (1988) 2630.

[Chen 88a] Z. Chen, Ph. D. Thesis, Michigan State University.

[Chit 83] C.B. Chitwood, D.J. Fields, C.K. Gelbke, W.G. Lynch, A.D. Panagiotou,

3. p. 1.

[Fabr 87] D. Fabris, et al, Nucl. Phys. A471 (1987) 351c.

[Fahl 86] A. Fahli, J.P. Coffin, G. Guillaume, B. Heusch, F. Jundt, F. Rami, P. Wagner, P. Fintz, A.J. Cole, S. Kox, and Y. Schutz, Phys. Rev. **C34**, 161 (1986).

[Fai 82] G. Fai and J. Randrup, Nucl. Phys. A**381** (1982) 557.

[Faty 87a] M. Fatyga, K. Kwiatkowski, V.E. Viola, W.G. Wilson, M.B. Tsang, J. Pochodzalla, W.G. Lynch, C.K. Gelbke, D.J. Fields, C.B. Chitwood, Z. Chen, and T. Nayak, Phys. Rev. Lett. **58**, 2527 (1987).

[Faty 87b] M. Fatyga, R.C. Byrd, K. Kwiatkowski, W.G. Wilson, L.W. Woo, V.E. Viola, Jr., H.J. Karwowski, J. Jastrzebski, and W. Skulski, Phys. Lett. **B185**, 321 (1987).

[Finn 82] J. E. Finn, S. Agarwal, A. Bujak, J. Chuang, L. J. Gutay, A. S. Hirsch, R. W. Minich, N. T. Porile, R. P. Scharenberg, B. C. Stringfellow, and F. Turkot, Phys. Rev. Lett. **49** (1982) 1321.

[Fiel 84] D. J. Fields, W. G. Lynch, C. B. Chitwood, C. K. Gelbke, M.B. Tsang, H. Utsunomiya, and J. Aichelin, Phys. Rev. C **30** (1984) 1912.

[Fiel 86a] D. J. Fields, W. G. Lynch, T. K. Nayak, M. B. Tsang, C. B. Chitwood, C. K. Gelbke, R. Morse, J. Wilczynski, T. C. Awes, R. L. Ferguson, F. Plasil, F. E. Obenshain, and G. R. Young Phys. Rev. C **34** (1986) 536.

[Fiel 86b] D. J. Fields, Ph.D. Thesis, Michigan state University, 1986.

[Fiel 87] D. J. Fields, C. K. Gelbke, W. G. Lynch, and J. Pochodzalla, Phys. Lett. **187B** (1987) 257.

[Fiel 89] D. E. Fields, K. Kwiatkowski, D. Bonser, R. W. Viola, V. E. Viola, W. G. Lynch, J. Pochodzalla, M. B. Tsang, C. K. Gelbke, D. J. Fields, and S. M. Austin, Phys. Lett. **220B** (1989) 356.

[Fran 81] K.A. Frankel and J.D. Stevenson, Phys. Rev. **C23**, 1511 (1981).

[Frie 80] W.A. Friedman and W.G. Lynch, Phys. Rev. C28 (1980) 950.

[Frie 83] W. A. Friedman and W. G. Lynch, Phys. Rev. C **28** (1983) 16, ibid. 950.

[Frie 89] W. A. Friedman, Phys. Rev. C **40** (1989) 2055.

[Frie 90a] W. A. Friedman, Phys. Rev. C **42** (1990) 667.

[Frie 90b] W. A. Friedman, Phys. Lett. **B242** (1990) 309.

[Frie 88] W. A. Friedman, Phys. Rev. Lett. **60** (198) 2125.

[Gale 87] G. Gale, G. Bertsch, and S. Das Gupta, Phys. Rev. C **35**, 1666(1987).

[Gale 90] G. Gale, G.M. Welke, M. Prakash, S.J. Lee and S. Das Gupta, Phys. Rev. C **41**, 1545(1990).

[Gali 88] J. Galin, Nucl. Phys. **A488**, 297c (1988).

[Galo 87] A. Galonsky, G. Caskey, L. Hilbronn, B. Remington, H. Schelin, F. Deak, A. Kiss, Z. Seres, and J. Kasagi, Phys. Lett. **B197**, 511 (1987).

[Gelb 87a] Proceedings of the Symposium on Central Collisions and Fragmentation Processes, ed. C.K. Gelbke, Nucl. Phys. A**471**, 1c-451c (1987).

[Gelb 87b] C. K. Gelbke and D.H. Boal, Prog. Part. Nucl. Phys. **19** (1987) 33; and references contained therein.

[Gilb 65a] A. Gilbert, F. S. Chen, A G. W. Cameron, Canadian Journal of Physics, **43** (1965) 1248.

[Gilb 65b] A. Gilbert, A G. W. Cameron, Canadian Journal of Physics, **43** (1965) 1446.

[Glas 74] D. Glas and U Mosel, Phys. Rec. **C10**, 2620 (1974).

[Gold 74] A.S. Goldhaber, Phys. Lett. **53B**, 306 (1974).

[Gome 88] J. Gomez Del Campo, J. L. Charvet, A. D'Onofrio, R. L. Auble, J. R. Beene, M. L. Halbert, and H. J. Kim, Phys. Rev. Lett., **61** (1988) 290.

[Gong 90] W.G. Gong, *et al*, Phys. Rev. Lett. (in press)

[Goni 88] M. Gonin, J.P. Coffin, G. Guillaume, F. Jundt, P. Wagner, P. Fintz, B. Heusch, A. Malki, A. Fahli, S. Kox, F. Merchez, and J. Mistretta, Phys. Rev. C38 (1988) 135.

[Goni 89] M. Gonin, L. Cooke, K. Hagel, Y. Lou, J.B. Natowitz, R.P. Schitt, B. Srivastava, W. Turmel, H. Utsunomiya, R. Wada, B. Fornal, G. Nardelli, G. Nebbia, G. Viesti, R. Zanon, G. Prete, P. Gonthier, and B. Wilkins, Phys. Lett. **B217**, 406 (1989).

[Gree 80] R.E.L. Green and R.G. Korteling, Phys. Rev. **C22** (1980) 1594.

[Gree 80] R.E.L. Green and R.G. Korteling, Phys. Rev. **C22** (1980) 1594.

[Grif 90] K.A. Griffioen, R.J. Meijer, P.F. Box, P. Decowski, G.J. Van Nieuwenhuizen, R. Kamermans, H.W. Wilschut, A. Giorni, C. Morand, A. Demeyer and D. Guinet, Phys. Lett. B237 (1990) 24

[Gros 88] D.H.E. Gross, *et al*, Phys. Lett. **B203**, 26 (1988).

[Gros 82] D. H. E. Gross, L. Satpathy, Mang Ta-Chung, and M. Satpathy, Z. Phys. **A309** (1982) 41.

[Gros 86] D. H. E. Gross, Zhang Xiao-ze, and Xu Shu-yan, Phys. Rev. Lett. **56** (1986) 1544.

[Guer 89] D. Guerreau, Lectures at the International School on Nuclear Physics "Nuclear Matter and Heavy Ion Collisions", Les Houches, Feb., 1989; GANIL Preprint P98-07.

[Hage 88] K. Hagel, *et al*, Nucl. Phys. **A486**, 429 (1988).

[Hako 82] B. Jakobsson, G. J;nsson, B. Lindkvist, and A. Oskarsson, Z. Phys. **A307**, 293 (1982).

[Hahn 87] D. Hahn and H. Stocker, Phys. Rev. C **35** (1987) 1311.

[Haus 52] W. Hauser and H. Feshbach, Phys. Rev. **87** (1952) 366.

[Hirs 84] A.S. Hirsch, A. Bujak, J.E. Finn, L.J. Gutay, R.W. Minich, N.T. Porile, R.P. Scharenberg, B.C. Stringfellow, and F.Turkot, Phys. Rev. **C29** (1984) 458.

[Huan 63] K. Huang, Statistical Mechanics (Wiley, New York, 1963), p. 310.

[Hyde 71] E.K. Hyde, G.W. Butler, and A.M. Poskanzer, Phys. Rev. **C4** (1971) 1759.

[Jaas 83] M. Jaaskelainen, D.G. Sarantites, R. Woodward, F.A. Dilmanian, J.T. Hood, R. Jaaskelainen, D.C. Hensley, M.L. Halbert, and J.H. Barker, Nucl. Instr. and Meth. **204** (1983) 385.

[Jaca 83] B.V. Jacak, G.D. Westfall, C.K. Gelbke, L.H. Harwood, W.G. Lynch, D.K.Scott, H. Stocker, M.B. Tsang, and T.J.M. Symons, Phys. Rev. Lett. **51**, 1846 (1983).

[Jaca 87] B.V. Jacak, G.D. Westfall, G.M. Crawley, D. Fox, C.K. Gelbke, L.H. Harwood, B.E. Hasselquist, W.G. Lynch, D.K. Scott, H. Stocker, M.B. Tsang, G. Buchwald, and T.J.M. Symons, Phys. Rev. **C35**, 1751 (1987).

[Jacq 84] D. Jacquet, E. Duek, J.M. Alexander, B. Borderie, J. Galin, D. Gardes, D. Guerreau, M. Lefort, F. Monnet, M.F. Rivet, and X. Tarrago, Phys. Rev. Lett. **53**, 2226(1984).

[Jian 89] D.X. Jiang, *et al*, Nucl. Phys. **A503**, 560 (1989).

[Krof 89] D. Krofcheck, W. Bauer, G.M. Crawley, C. Djalali, S. Howden, C.A. Ogilvie, A. Vander Molen, G.D. Westfall, W.K. Wilson, R.S. Tickle, and C. Gale, Phys. Rev. Lett. **63**, 2028 (1989).

[Krus 85] H. Kruse, B.V. Jacak, and H. Stöcker, Phys. Rev. Lett. **54**, 289(1985).

[Kwia 86] K.Kwiatkowski, J. Bashkin, H. Karwowski, M. Fatyga, and V.E. Viola, Phys. Lett. **B171**, 41 (1986).

[Land 80] L. D. Landau and E. M. Lifshitz, "Course of Theoretical Physics : Statistical Mechanics", Pergamon, New York (1980) Vol. 5, Pt. 1, page 236.

[Lenk 86] R.J. Lenk and V.R. Pandharipande, Phys. Rev. **C34**, 177 (1986).

[Lenk 89] R.J. Lenk and V.R. Pandharipande, Phys. Rev. C **39**, 2242(1989).

[Lera 86] S. Leray, in Proc. HICOFED 86, J. Phys. (Paris), Colloq. **47**, C4-275(1986), and references therein.

[Levi 84] S. Levit and P. Bonche, Nucl. Phys. **A437**, 426(1984).

[Lope 84b] J. A. Lopez and P.J. Siemens, Nucl. Phys. A**431** (1984) 728.

[Lync 87] W.G. Lynch, Ann. Rev. Nucl. Sci. **37** (1987) 493; and references contained therein.

[Marm 69] P. Marmier and E. Sheldon, Physics of Nuclei and particles, Vol. 1, Academic Press (1969) 38.

[Maru 85] J. A. Maruhn, K.T.R. Davies, and M.R. Strayer, Phys. Rev. **C31**, 1289 (1985)

[Maru 90] T. Maruyama, A. Ohnishi, and H. Hiriuchi, Phys. Rev. **C42**, 386 (1990)

[Mekj 90] A.Z. Mekjian, Phys. Rev. Lett. **18**, (1990) 2125.

[Mini 82] R.W. Minich, S. Agarwal, A. Bujak, J. Chuang, J.E. Finn, L.J. Gutay, A.S. Hirsch, N.T. Porile, R.P. Scharenberg, B.C. Stringfellow, and F. Turkot, Phys. Lett. **118B** (1982) 458.

[Mitt 85] W. Mittig, A. Cunsolo, A. Foti, J.P. Wieleczko, F. Auger, B. Berthier, J.M. Pascaud, J. Quebert, and E. Plagnol, Phys. Lett. **154B**, 259 (1985).

[Moli 85a] J.J. Molitoris and H. Stöcker, Phys. Rev. C **32**, 346(1985).

[Moli 85b] J.J. Molitoris and H. Stöcker, Phys. Lett. **162B**, 47(1985).

[More 72] L.G. Moretto, Phys. Lett. B 40 (1972) 185.

[More 75] L. G. Moretto, Nucl. Phys. A**247** (1975) 211.

[Morr 84] D.J. Morrissey, W. Benenson, E. Kashy, B. Sherrill, A.D. Panagiotou, R.A. Blue, R.M. Ronningen, J. van der Plicht, and H. Utsunomiya, Phys. Lett. **148B** (1984) 423.

[Morr 85] D. J. Morrissey, W. Benenson, E. Kashy, C. Bloch, M. Lowe, R. A. Blue, R. M. Ronningen, B. Sherrill, H. Utsunomiya, and I. Kelson, Phys. Rev. C **32** (1985) 877.

[Morr 86] D.J. Morrissey, C. Bloch, W. Benenson, E. Kashy, R.A. Blue, R.M. Ronningen, and R. Aryaeinejad, Phys. Rev. C34, 761 (1986).

[Mura 89] T. Murakami, T. K. Nayak, W. G. Lynch, K. Swartz, Z. Chen, D. J. Fields, C. K. Gelbke, Y. D. Kim, M. R. Maier, J. Pochodzalla, M. B. Tsang, H. M. Xu, and F. Zhu, Nucl. Instrum. Method Phys. Res. **A275** (1989) 112.

[Myer 66] W.D. Myers and W.J. Swiatecki, Nucl. Phys. 81, 1 (1966); W.D. Myers and W.J. Swiatecki, Ann. Phys. 55, 186 (1969).

[Naya 89] T. K. Nayak, T. Murakami, W. G. Lynch, K. Swartz, D. J. Fields, C. K. Gelbke, Y. D. Kim, J. Pochodzalla, M. B. Tsang, F. Zhu, and K. Kwiatkowski, Phys. Rev. Lett. **62** (1989) 1021.

[Naya 90] T. K. Nayak, Ph.D. Thesis, Michigan State University, 1990.

[Nife85] H. Nifenecker, J. Blachot, J. Crancon, A. Gizon, and A. Lleres, Nucl. Phys. **A447**, 533c(1985).

[Niit 90] K. Niita, *et al* (unpublished).

[Ogil 89a] C.A. Ogilvie, D.A. Cebra, J. Clayton, P. Danielewicz, S. Howden, J. Karn, A. Nadasen, A. Vander Molen, G.D. Westfall, W.K. Wilson, and J.S. Winfield, Phys. Lett. **B231**, 35 (1989).

[Ogil 89b] C.A. Ogilvie, D.A. Cebra, J. Clayton, P. Danielewicz, S. Howden, J. Karn, A. Nadasen, A. Vander Molen, G.D. Westfall, W.K. Wilson, and J.S. Winfield, Phys. Rev. **C40**, 2592 (1989).

[Ogil 90] C.A. Ogilvie, W. Bauer, D.A. Cebra, J. Clayton, S. Howden, J. Karn, A. Nadasen, A. Vander Molen, G.D. Westfall, W.K. Wilson, and J.S. Winfield, Phys. Rev. **C42**, R10 (1990).

[Peil 89] G. Peilert, H. Stöcker, W. Greiner, A. Rosenhauer, A. Bohnet and J. Aichelin, Phys. Rev. C **39**, 1402(1989).

[Plag 89] E. Plagnol, L. Vinet, D.R. Bowman, Y.D. Chan, R.J. Charity, E. Chavez, S.B. Gazes, H. Han, W.L. Kehoe, M.A. Mcmahan, L.G. Moretto, R.G. Stokstad, G.K. Wozniak, and G. Auger, et al, Phys. Lett. B 221, 11 (1989).

[Poch 85] J. Pochodzalla, W.A. Friedman, C.K. Gelbke, W.G. Lynch, M. Maier, D. Ardouin, H. Delagrange, H. Doubre, C. Gregoire, A. Kyanowski, W. Mittig, A. Peghaire, J. Peter, F. Saint-Laurent, Y.P. Viyogi, B. Zwieglinski, G. Bizard, F. Lefebvres, B. Tamain, J. Quebert, Phys. Lett. **B161**, 275 (1985).

[Poch 85a] J. Pochodzalla, W. A. Friedman, C. K. Gelbke, W. G. Lynch, M. Maier, D. Ardouin, H. Delagrange, H. Doubre, C. Gregoire, A. Kyanowski, W. Mittig, A. Peghaire, J. Peter, F. Saint-Laurent, Y. P. Viyogi, B. Zwieglinski, G. Bizard, F. Lefebvres, B. Tamain and J. Quebert, Phys. Rev. Lett. **55** (1985) 177.

[Poch 85b] J. Pochodzalla, W. A. Friedman, C. K. Gelbke, W. G. Lynch, M. Maier, D. Ardouin, H. Delagrange, H. Doubre, C. Gregoire, A. Kyanowski, W. Mittig, A. Peghaire, J. Peter, F. Saint- Laurent, Y. P. Viyogi, B. Zwieglinski, G. Bizard, F. Lefebvres, B. Tamain, J. Quebert, Phys. Lett. **161B** (1985) 256.

[Poch 86a] J. Pochodzalla, C. B. Chitwood, D. J. Fields, C. K. Gelbke, W. G. Lynch, M. B. Tsang, D. H. Boal and J. C. Shillcock, Phys. Lett. **B174** (1986) 36.

[Poch 86b] J. Pochodzalla, C. K. Gelbke, C. B. Chitwood, D. J. Fields, W. G. Lynch, M. B. Tsang, and W. A. Friedman, Phys. Lett. **175B** (1986) 275.

[Poch 87] J. Pochodzalla, C. K. Gelbke, W. G. Lynch, M. Maier, D. Ardouin, H. Delagrange, H. Doubre, C. Gregoire, A. Kyanowski, W. Mittig, A. Peghaire, J. Peter, F. Saint-Laurent, B. Zwieglinski, G. Bizard, F. Lefebvres, B. Tamain, J. Quebert, Y. P. Viyogi, W. A. Friedman and D. H. Boal, Phys. Rev. C **35** (1987) 1695.

[Posk 78] A.M. Poskanzer, G.W. Butler, and E.K. Hyde, Phys. Rev. **C3** (1971) 882.

[Rand 81] J. Randrup and S. E. Koonin, Nucl. Phys. **A356** (1981) 223.

[Rema 88] B. Remaud, C. Gregoire, F. Sebille and P. Schuck, Nucl. Phys. **A488**, 423c (1988).

[Rema 86] B. Remaud, C. Gregoire, F. Sebille and L. Vinet, Phys. Lett. **B180**, 198 (1986)

[Ring 80] Peter Ring and Peter Schuck, 'The Nuclear Many-Body Problem', Published by Springer-Verlag New York Inc., P.4 (1980).

[Rive 88] M.F. Rivet, et al, Phys. Lett. B215 (1988) 55

[Rohr 73] U. Rohrer and L. Brown, Nucl. Phys. A**210** (1973) 465

[Saga 85] H. Sagawa, and G.F. Bertsch, Phys. Lett. **155B**, 11 (1985).

[Sain 88] F. Saint-Laurent, A. Kyanowski, D. Ardouin, H. Delagrange, H. Doubre, C. Gregoire, W. Mittig, A. Peghaire, J. Peter, G. Bizard, F. Lefebvres, B. Tamain, J. Quebert, Y.P. Viyogi, J. Pochodzalla, C.K. Gelbke, W. Lynch, and M. Maier, Phys. Lett. **B202**, 190 (1988).

[Sang 87] T.C. Sangster, A.T. Bujak, D.D. Carmony, Y.H. Chung, L.J. Gutay, A.S. Hirsch, M. Mahi, G.L. Paderewski, N.T. Porile, R.P. Scharenberg, and B.C. Stringfellow, Phys. Lett. B188, 29 (1987).

[Schl 87] T. J. Schlagel and V. R. Pandharipande, Phys. Rev. C **36** (1987) 162.

[Siem 79] P. J. Siemens, and J. O. Rasmussen, Phys. Rev. Lett. **42** (1979) 880.

[Snep 88] K. Sneppen and L. Vinet, Nucl. Phys. A**480** (1988) 342.

[Sobo 83] L. G. Sobotka, M. L. Padgett, G. J. Wozniak, G. Guarino, A. J. Pacheco, L. G. Moretto, Y. Chan, R. G. Stokstad, I. Tserruya, and S. Wald, Phys. Rev. Lett. **51** (1983) 2187.

[Sobo 84] L. G. Sobotka, M. A. McMahan, R. J. McDonald, C. Signarbieux, G. J. Wozniak, M. L. Padgett, J. H. Gu, Z. H. Liu, Z. Q. Yao, and L. G. Moretto, Phys. Rev. Lett. **53** (1984) 2004.

[Sobo 86] L. G. Sobotka, D. G. Sarantites, H. Puchta, F. A. Dilmanian, M. Jaaskelainen, M. L. Halbert, J. H. Barker, J. R. Beene, R. L. Ferguson, D. C. Hensley, and G. R. Young, Phys. Rev. C **34** (1986) 917.

[Stoc 81] H. Stocker, A.A. Ogloblin, and W. Greiner, Z. Phys. **A303** (1981) 259

[Stok 77] R. G. Stokstad, Proceedings of the Topical Conference on Heavy-Ion Collisions, held at Fall Creek Falls State Park, Tennessee, June 13-17, 1977, p. 22.

[Sura 89a] E. Suraud, M. Pi, P, Schuck, B. Remaud, F. Sébille, C. Grégoire and F. Saint-Laurent, Phys. Lett. **B229**, 359(1989).

[Sura 89b] E. Suraud, C. Gregoire, and B. Tamain, Prog. Part. Nucl. Phys., 23 (1989) 357.

[Sura 90] E. Suraud, Proceeding of the XXVIII International Winter Meeting on Nuclear Physics, Bormio, Italy, Jan. 22-26, 1990, and references therein.

[Sura 89c] E. Suraud, D. Cussol, Ch. Grégoire, D. Boilley, M. Pi, P, Schuck, B. Remaudm and F. Sébille, Nucl Phys. **A495** (1989) 73c.

[Tsan 84] M. B. Tsang, C. B. Chitwood, D. J. Fields, C. K. Gelbke, D. R. Klesch, W. G. Lynch, K. Kwiatkowski, and V. E. Viola, Jr., Phys. Rev. Lett. **52** (1984) 1967.

[Tsan 86] M. B. Tsang, R. M. Ronningen, G. Bertsch, Z. Chen, C. B. Chitwood, D. J. Fields, C. K. Gelbke, W. G. Lynch, T. Nayak, J. Pochodzalla, T. Shea, and W. Trautmann, Phys. Rev. Lett. **57** (1986) 559.

[Tsan 88] M. B. Tsang, W. G. Lynch, R. M. Ronningen, ' Z. Chen, C. K. Gelbke, T. Nayak, J. Pochodzalla, F. Zhu, M. Tohyama, W. Trautmann, and W. Dunnweber, Phys. Rev. Lett. **60** (1988) 1479.

[Tsan 89] M.B. Tsang, G.F. Bertsch, W.G. Lynch and Mitsuru Tohyama, Phys. Rev. **C40**, 1685(1989).

[Troc 86] R. Trockel, K.D. Hildenbrand, U. Lynen, W.F.J. Muller, H.J. Rabe, H. Sann, H. Stelzer, W. Trautmann, R. Wada, N. Brummund, R. Glasow, K.H. Kampert, R. Santo, D. Pelte, J. Pochodzalla, and E. Eckert, Hadronic Matter in Collision, edited by P. Carruthers and D. Strottman, World Scientific, Singapore 1986, p. 291.

[Vice 85] A. Vicentini, G, Jacucci, and V.R. Pandharipande, Phys. Rev. **C31**, 1783 (1985).

[Vola 87] C. Volant, M. Conjeaud, S. Harar, M. Mostefai, E.C. Pollacco, Y. Cassagnou, R. dayras, R. legrain, G. Klotz-Engmann, and H. Oeschler, Phys. Lett. **195B**, 22(1987).

[Wada 89] R. Wada, D. Fabris, K. Hagel, G. Nebbia, Y. Lou, M. Gonin, J.B. Natowitz, R. Billerey, B. Cheynis, A. Demeyer, D. Drain, D. Guinet, C. Pastor, L. Vagneron, K. Zaid, J. Alarja, A. Giorni, D. Heuer, C. Morand, B. Viano, C. Mazur, C. Ngô, S. Leray, R. Lucas, M.Ribrag, and E. Tomasi, Phys. Rev. **C39**, 497(1989).

[Waps 85] A. H. Wapstra and G. Audi, Nucl. Phys. A**432** (1985) 1.

[Warw 83] A.I. Warwick, H.H. Wieman, H.H. Gutbrod, M.R. Maier, J. Peter, H.G.Ritter, H. Stelzer, F. Weik, M. Freedman, D.J. Henderson, S.B. Kaufman, E.P. Steinberg, and B.D. Wilkins, Phys. Rev. **C27**, 1083 (1983).

[Welk 88] G.M. Welke, M. Prakash, T.T.S. Kuo, S. Das Gupta, and C. Gale, Phys. Rev. C **38**, 2101(1988).

[West 78] G.D. Westfall, R.G. Sextro, A.M. Poskanzer, A.M. Zebelman, G.W. Butler, and E.K. Hyde, Phys. Rev. **C17** (1978) 1368

[Wils 90] W.K. Wilson, W. Benenson, D.A. Cebra, J. Clayton, S. Howden, J. Karn, T. Li, C.A. Ogilvie, A. Vander Molen, G.D. Westfall, J.S. Winfield, B. Young, and A. Nadasen, Phys. Rev. **C41**, R1881 (1990).

[Wong 82] C.Y. Wong, Phys. Rev. **C25** (1982) 1460.

[Wozn 74] G.J. Wozniak, *et al*, Nucl. Inst. Meth. **120** (1974) 29.

[Xu 86] H. M. Xu, D. J. Fields, W. G. Lynch, M. B. Tsang, C. K. Gelbke, M. R. Maier, D. J. Morrissey, J. Pochodzalla, D. G. Sarantites, L. G. Sobotka, M. L. Halbert, D. C. Hensley, D. Hahn, and H. Stocker, Phys. Lett. **182B** (1986) 155.

[Xu 89] H. M. Xu, W. G. Lynch, C. K. Gelbke, M. B. Tsang, D. J. Fields, M. R. Maier, D. J. Morrissey, T. K. Nayak, J. Pochodzalla, D. G. Sarantites, L. G. Sobotka, M. L. Halbert, D. C. Hensley, Phys. Rev. C **40** (1989) 186.

[Xu 90] H.M. Xu, W.G. lynch, P. Danielewicz, and G.F. Bertsch, Phys. Rev. Lett. **65**, 843(1990).

$$E^*_{coll} = E^*_{rot} + E^*_{n.r.} \tag{6.14}$$

Here, the rotational energy E^*_{rot} is estimated by

$$E^*_{rot} = \frac{J^2}{2I} \tag{6.15}$$

where J is the angular momentum of the residue A_{res} calculated by

$$\vec{J} = \frac{1}{(2\pi\hbar)^3}\int_C (\vec{r}' \times \vec{p}')f(\vec{r}', \vec{p}')d^3r'd^3p' \tag{6.16}$$

and $\vec{r}'$ and $\vec{p}'$ are defined in a coordinate system centered at center of mass of the residue. In our simulations, we choose the $x - z$ plane as the reaction plane and therefore the total angular momentum lies along the y axis. For the residue nucleus, we also found that the angular momentum of the residue are nearly parallel to the y-axis. We therefore neglect rotations about the x and y axis axis and we approximate the rigid body moment of inertia by

$$I \approx I_{yy} = \int_C (x^2 + z^2)\rho d^3r \tag{6.17}$$

Examples of values of I and J calculated in this approximation for ^{40}Ar+^{27}Al collisions were listed in Table 6.3.

After the decomposition of Eq. (6.14), the total excitation energy E^* now has the following components

$$E^* = E^*_{coll} + E^*_{the} + E_{comp} = E^*_{rot} + E^*_{n.r.} + E_{comp} + E^*_{the} \tag{6.18}$$

Since the rotational energy E^*_{rot} is associated with the motion in the tangential direction, the non-rotational energy $E^*_{n.r.}$ is therefore primarily associated with radial motion. This non-rotational energy could originate from the excitation of giant resonances, with dominant contribution, argued by Remaud *et al*, from monopole oscillations [Rema 88].

Using Eqs. (6.1)-(6.18), we can explore how one may define an appropriate time for thermal freezeout. The decomposition by Eq. (6.9)-(6.18) can also provide information concerning the dynamics for the formation of the heavy residues. In the next few subsections, we will use the decomposition to consider whether the rotations or thermal instabilities place limitations on the formation of heavy residues.

B Freezeout Conditions

Since the pre-equilibrium and equilibrium emissions are both present in intermediate nucleus-nucleus collisions, one needs to know whether the thermal freezeout is indeed reached and whether one can define a freezeout time unambiguously. To investigate this, we describe, in the following three subsections, three distinctive criteria used to define the thermal freezeout time. Two of these criteria, the emission rate and the thermal excitation energy, were found to give consistent freezeout times. The third criterion, the quadrupole moment of the momentum distribution, did not provide a clear signature for the freezeout time, but was not inconsistent with the freezeout time determined from the other two criteria.

Emission Rate

In Fig. 6.7, we display the emission rate of nucleons as functions of time for ^{40}Ar+^{27}Al collisions at E/A=30 MeV. The solid and open circles in the figure depicted the calculations with the stiff and soft equations of state, respectively. The corresponding nucleon-nucleon cross sections are indicated in the figures. For all calculations, one observes large emission rates at t $\simeq$ 60$-$80 fm/c. These large emission rates reflect the fast pre-equilibrium emission of nucleons before the system reach equilibrium. The emission rate, at $t \geq$ 100 fm/c for stiff EOS, and $t \geq$ 120 fm/c, is significantly reduced and changes very slowly, suggesting a slow statistical emission from the reaction

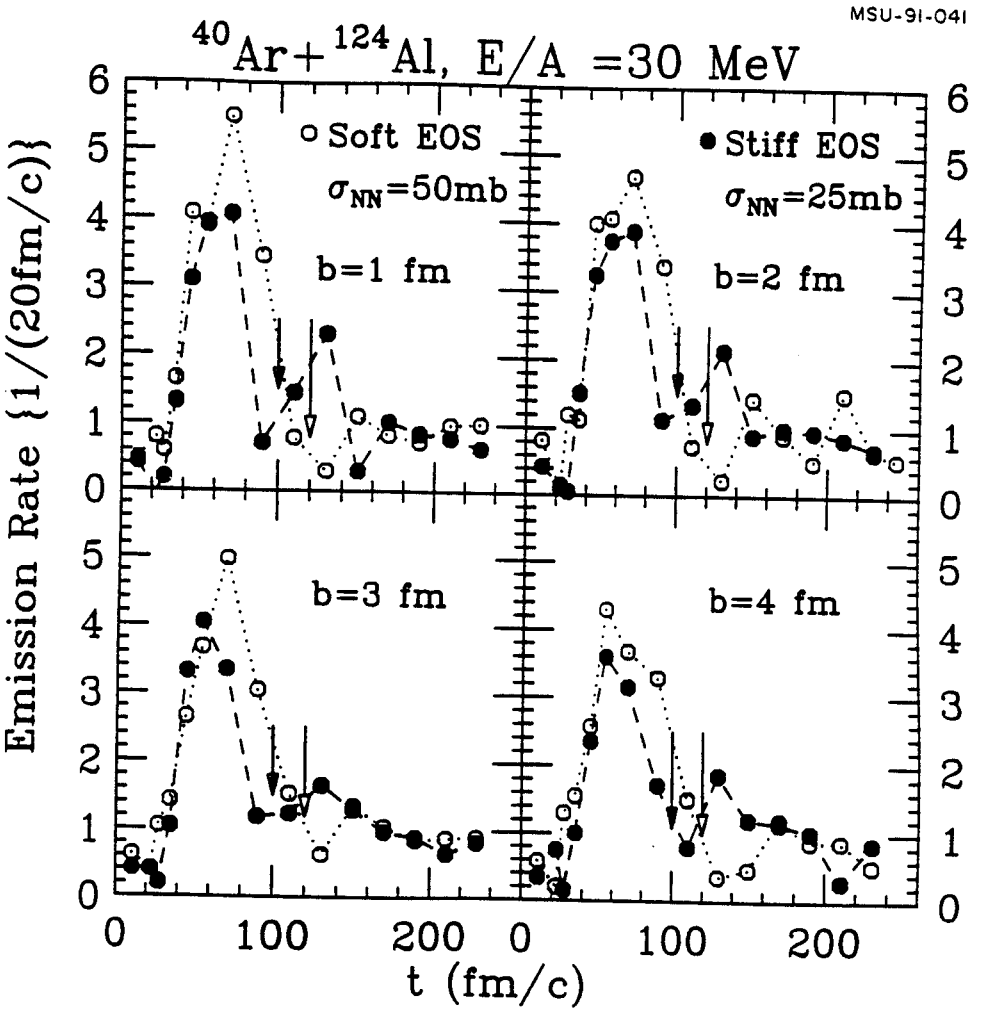

Figure 6.7: The emission rates of ^{40}Ar+^{27}Al collisions at E/A=30 MeV for impact parameters b=1-4 fm. The solid circles are results with stiff EOS and σ_{NN} = 25mb. The open circles are results with soft EOS and σ_{NN} = 50mb. The corresponding freezeout times are indicated by the arrows (solid for stiff EOS and open for soft EOS). The respective lines are used to guide the eyes.

residue. The emission at later times is modulated by the influence of macroscopic vibrations which can be clearly seen in the Q_{zz} plot (Fig. (6.10)). We will come back to this point. The solid and open arrows in Fig. 6.7 indicate the freezeout times selected by this criterion for the calculations with the stiff and soft equations of state. These freezeout times are consistent with the freezeout times obtained from the thermal excitation energy of the residues described below.

Thermal Excitation Energies

In general, one expects the temperature or the thermal excitation energy of a hot equilibrated nucleus to decrease with time via evaporative cooling. Assuming this evaporative cooling is properly described by sequential decay calculations like those described in chapter 4, the emission temperature should depend on the maximum thermal energy at the end of the preequilibrium stage of the reaction. This provides a second criterion for choosing the freezeout time. In Figs. 6.8-6.9, we display the various contributions to the excitation energy for ^{40}Ar+^{27}Al collisions at E/A=30 MeV assuming a soft EOS (Fig. 6.8) and a stiff EOS (Fig. 6.9), respectively. Several features of the reaction dynamics are immediately apparent. First, from the time dependence of potential energy (bottom curve), it is clear that the system undergoes a compression during first 40 fm/c, and afterwards an expansion between 40 fm/c $\leq t \leq$ 80 fm/c, and finally a relaxation to a more tightly bound state at 120 fm/c (100 fm/c for stiff EOS). The binding energy $E_{int}(T = 0)$ (third curve from the bottom) exhibits a similar behavior at a smaller scale. Second, the energy of free particles increases rapidly after $t \geq$ 40 fm/c, suggesting much of the collective energy E_{coll} is taken away by particle emission. Finally, the thermal energy E^*_{the}, which is of our particular interest, exhibits two maxima: one global maximum at t$\approx$ 40fm/c and one local maximum at t_{fre} = 120 fm/c (t_{fre} = 100 fm/c for stiff EOS). The maximum at t$\approx$

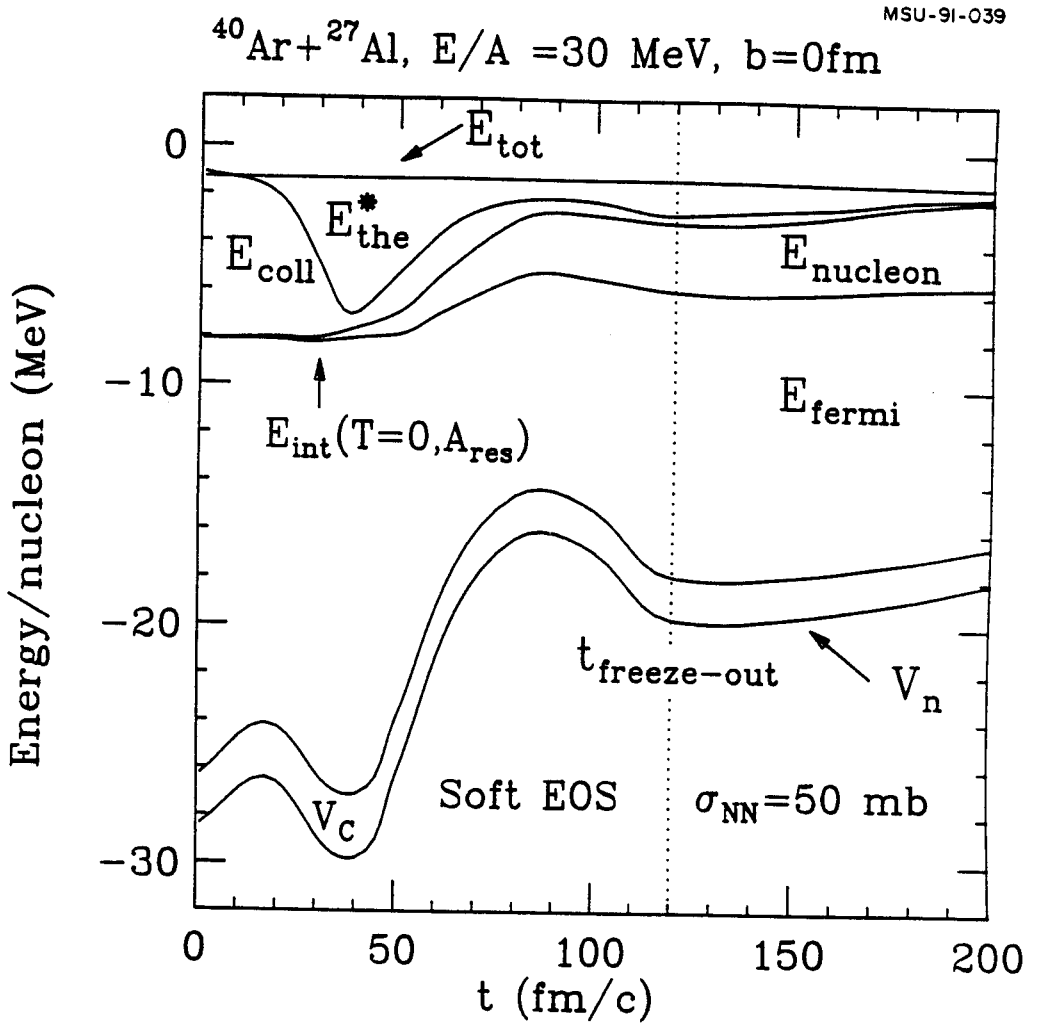

Figure 6.8: Decomposition of the various excitation energies as a function of time for ^{40}Ar+^{27}Al collisions with the soft equation of state at E/A=30 MeV, b=0 fm. The bottom line is the nuclear potential energy. From this bottom line up are,respectively, Coulomb energy (difference between the second and the bottom lines), Fermi energy required by the Pauli exclusion principle (difference between the third and second lines), kinetic energy of emitted particles (difference between the fourth and third lines), collective energy of bound nucleons (difference between the fifth and fourth lines) and thermal energy (difference between the top and fifth lines). The freezeout time is indicated by the dotted line.

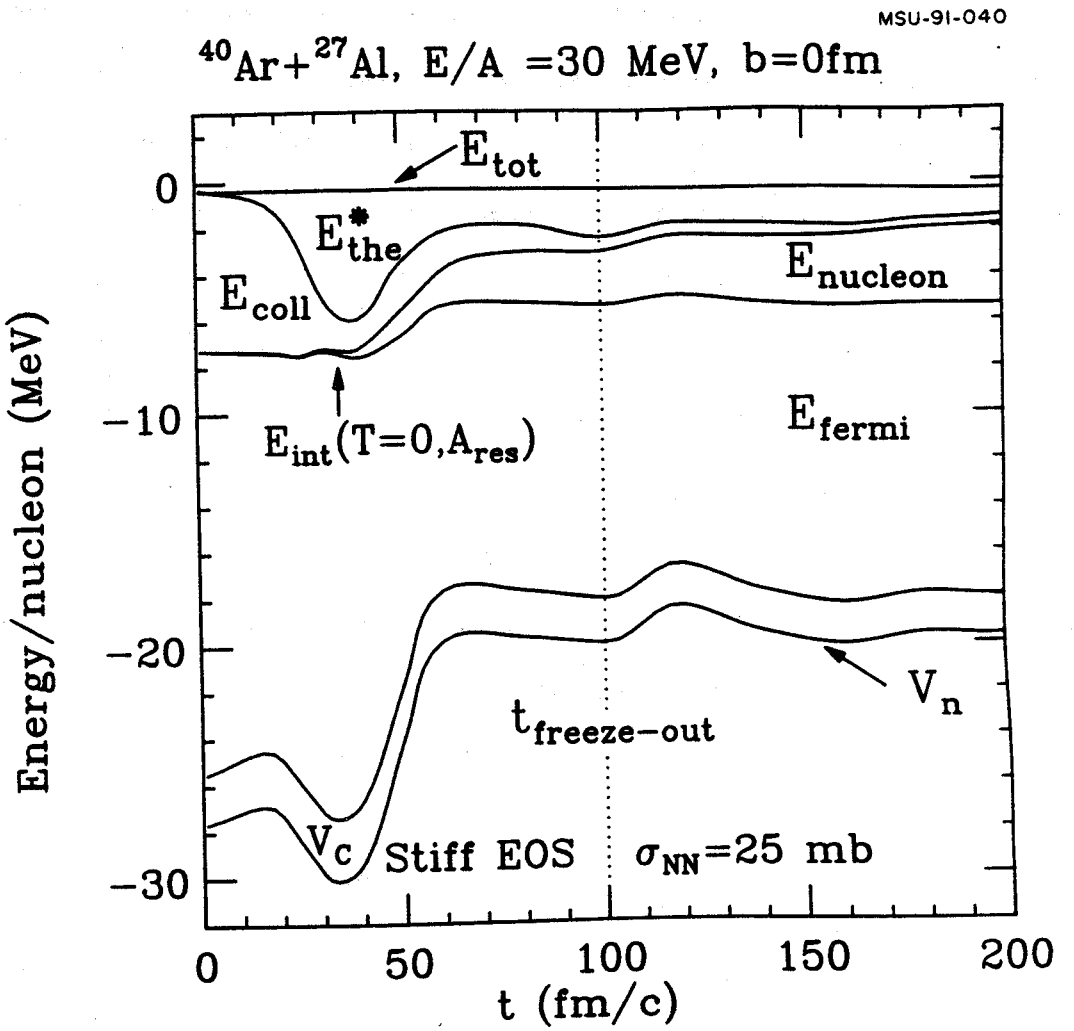

Figure 6.9: Decomposition of various excitation energies as a function of time for ^{40}Ar+^{27}Al collisions with the stiff equation of state at E/A=30 MeV, b=0 fm. The bottom line is the nuclear potential energy. From this bottom line up are,respectively, Coulomb energy (difference between the second and the bottom lines), Fermi energy required by the Pauli exclusion principle (difference between the third and second lines), kinetic energy of emitted particles (difference between the fourth and third lines), collective energy of bound nucleons (difference between the fifth and fourth lines) and thermal energy (difference between the top and fifth lines). The freezeout time is indicated by the dotted line.

40fm/c is an artifact of the initial momentum distributions, in which the longitudinal velocities of the projectile and the target nuclei cancel each other, causing a minimum in the computation of the collective energy. At the second maximum, the initial preequilibrium stages have finished and residue has already contracted to a more compact spacial configuration and the thermal energy at its local maximum. After this time, the thermal energy gradually decreases. Due to the evaporative cooling, we take the freezeout time to be the time of the second maximum in the thermal energy. This time is consistent with the time determined by the change in the nucleon emission rate shown in Fig. 6.7.

It is interesting to note that the freezeout time is largely determined by the relaxation time of the surface of the residue. Residues calculated with stiff equation of state, which has a larger restoring force and a larger sound speed, contracts to a compact configuration more rapidly than the residues calculated with soft equation of state. The excitation energies left in the residues are higher for residues characterized by a stiff EOS because they have less time for preequilibrium cooling.

Momentum Distributions

A third measure for defining the freezeout time may be obtained by the quadrupole moment of momentum distribution [Cass 87, Baue 87]:

$$Q_{zz}(t) = \frac{1}{(2\pi\hbar)^3} \int d^3r d^3p (2p_z^2 - p_x^2 - p_y^2) f(\vec{r}, \vec{p}, t) \tag{6.19}$$

This criterion is motivated by the belief that a system in thermal equilibrium should satisfy $Q_{zz} = 0$. To see how this variable changes with time, we plot Q_{zz} in the bottom panels of Fig. 6.10 as a function of time for ^{40}Ar+^{27}Al collisions at b=0 fm. For comparison, we show the emission rates in the top panels. The left hand panels show results obtained with the stiff equation of state. The right hand panels show

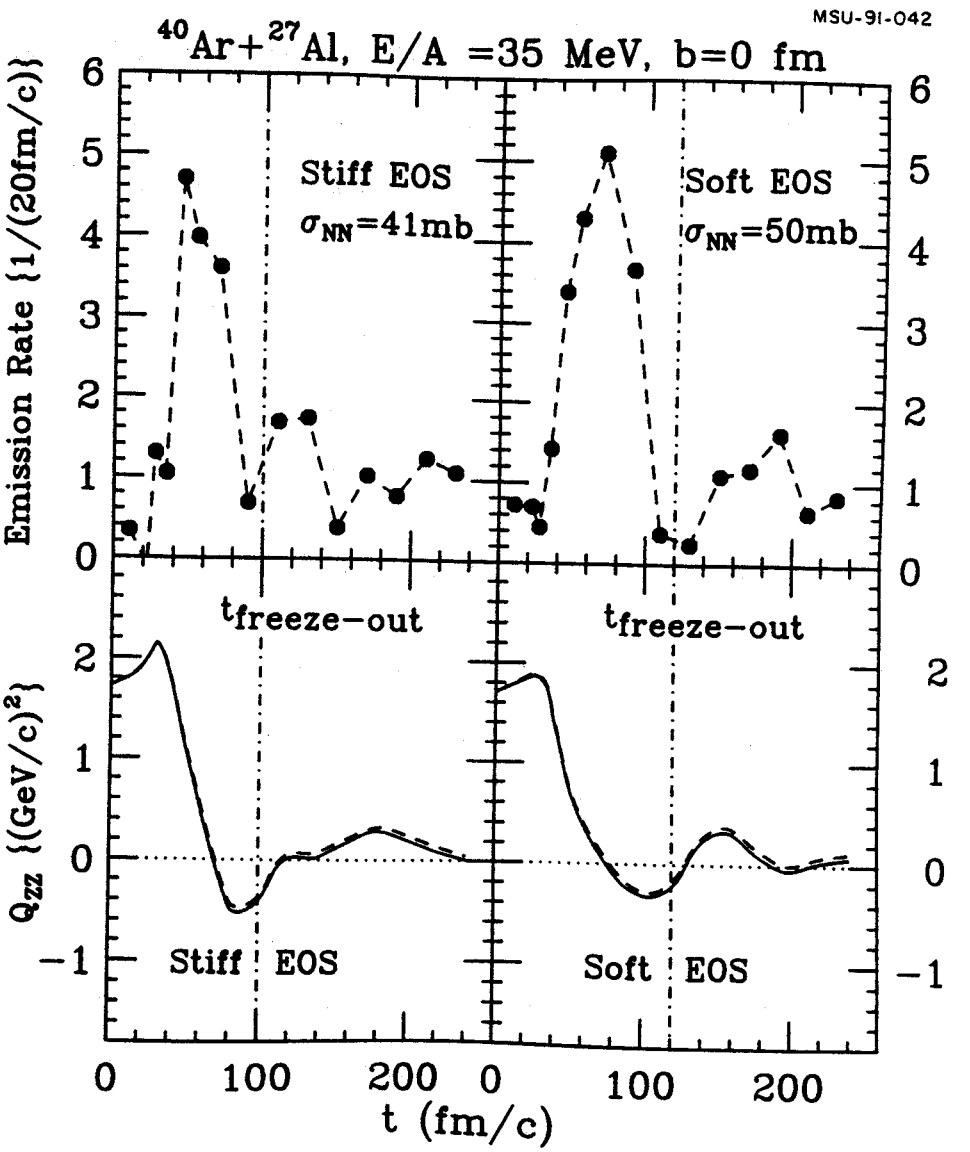

Figure 6.10: The emission rates of nucleons (top panels) and the quadrupole momentum distributions Q_{zz} (bottom panels), defined by Eq. (6.19), for ^{40}Ar+^{27}Al collisions at E/A=30 MeV, b=0 fm. The left panels (right panels) show the results for the stiff EOS (soft EOS). The vertical dot-dash lines indicate the freezeout time discussed in the text. The dashed lines in the bottom panels include the calculations for all nucleons, while the solid lines include only nucleons in the bound residues.

those from the soft equation of state. The dashed lines include all nucleons while the solid lines include the nucleons bound in the residual nuclei. Clearly at the t_{fre} defined previously, Q_{ZZ} is significantly reduced from its initial value at t=0. However, the values of Q_{ZZ} continue to oscillate about zero for a long time after thermal freezeout, reflecting the existence of macroscopic quadrupole vibrations. Such long term *collective* vibrations render Q_{ZZ} less useful in defining the *thermal* freezeout time.

In summary, a consistent freezeout time was obtained by checking three different variables. In the next few subsections, we will study the excitation energies and the angular momenta of residual nucleus at freezeout.

C Collisions at E/A=30 MeV

In Fig. 6.11, we show different contributions to the excitation energies of residues at freezeout as functions of the impact parameter for ^{40}Ar+ ^{27} Al collisions at E/A=30 MeV assuming alternatively the stiff (lower panel) or the soft (upper panel) equations of state. (A similar analysis was shown in lower right hand panel of Fig. 6.3 for ^{40}Ca+^{40}Ca system at E/A=40 MeV assuming stiff EOS.) The solid symbols in the figure represent the calculations in which a single heavy residue is observed in the final state. The open symbols represent calculations at larger impact parameters in which the system breaks up into projectile-like and target-like residues at a later time. The total excitation energy E^* (solid circles), calculated from Eq. (6.10) increases slightly with impact parameter. This increase can be partly attributed to the collective rotation. The crosses in Fig. 6.11 depict the excitation energy after the rotational energy E^*_{rot}, see Eq. (6.15), has been subtracted. The remaining part, $E^* - E^*_{rot}$, becomes constant for the central collisions where heavy composite residues were formed. We note here that the rotational energy E^*_{rot}, indicated by the difference

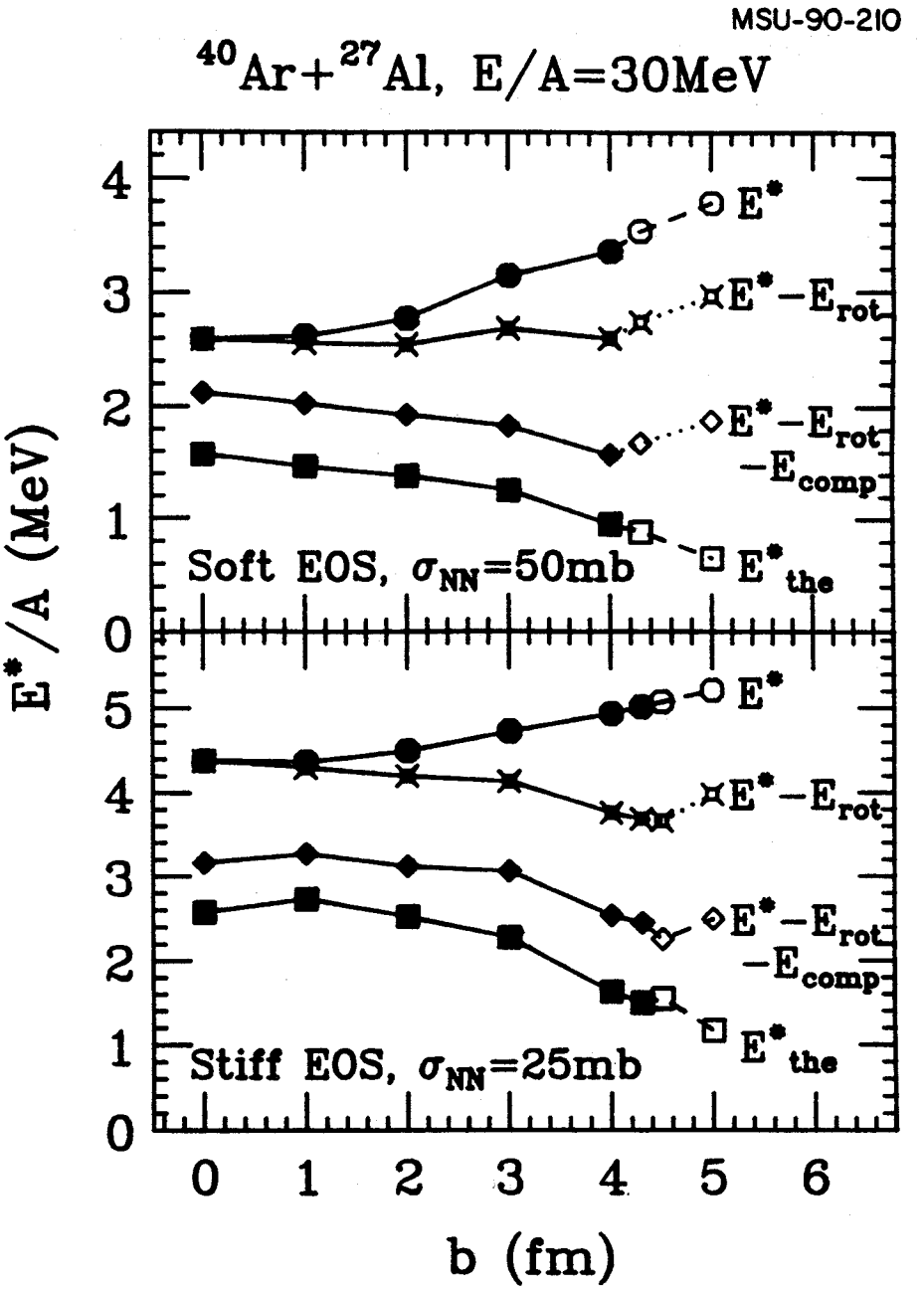

Figure 6.11: Decomposition of the predicted excitation energy at freezeout for different impact parameters in ^{40}Ar+^{27}Al collisions at E/A =30 MeV, assuming the soft EOS, (top panel) or the stiff EOS (lower panel). The solid and open symbols are explained in the text. The solid lines are drawn to guide the eye.